NUMERICAL AND EXPERIMENTAL EVALUATION OF SINUOUS ANTENNAS FOR REMOTE SENSING APPLICATIONS

A Dissertation
Presented to
The Academic Faculty

By

Dylan Andrew Crocker

In Partial Fulfillment
of the Requirements for the Degree
Doctor of Philosophy in
Electrical and Computer Engineering

School of Electrical and Computer Engineering
Georgia Institute of Technology
December 2019

NUMERICAL AND EXPERIMENTAL EVALUATION OF SINUOUS ANTENNAS FOR REMOTE SENSING APPLICATIONS

Approved by:

Dr. Waymond R. Scott Jr., Advisor
School of Electrical and Computer Engineering
Georgia Institute of Technology

Dr. Andrew F. Peterson
School of Electrical and Computer Engineering
Georgia Institute of Technology

Dr. Gregory D. Durgin
School of Electrical and Computer Engineering
Georgia Institute of Technology

Dr. Brett T. Walkenhorst
School of Electrical and Computer Engineering
Georgia Institute of Technology

Dr. Zhigang Peng
School of Earth and Atmospheric Sciences
Georgia Institute of Technology

Dr. Bernd H. Strassner
Electronic Systems Center
Sandia National Laboratories

Date Approved: November 1, 2019

To my wife Grace, our children Karis, Andrew, David, and Hope, and the memory of our baby Haven.

ACKNOWLEDGEMENTS

I would like to thank my Advisor Dr. Waymond Scott Jr., for all his encouragement, guidance, and support. His mentorship has meant a great deal to my professional and personal growth, for which I am very grateful. I would also like to thank my committee members, Dr. Andrew Peterson and Dr. Gregory Durgin, for their valuable work serving on my proposal, reading, and defense committees. Thank you also to Dr. Brett Walkenhorst, Dr. Zhigang Peng, and Dr. Bernd Strassner for their service on my final defense committee. Also, I would not be where I am today without the mentorship of Dr. Kristen Donnell, my MSEE thesis advisor. A special thank you to Dr. Strassner, who has also been a great mentor to me during my time at Sandia National Laboratories.

Thank you to Sandia National Laboratories for making it possible for me to attend graduate school at Georgia Tech through their Doctoral Studies Program. I also want to thank my co-workers at Sandia for their support and encouragement throughout my Ph.D. journey. Thanks to Wade Freeman, Ward Patitz, Troy Saterthwaight, Tyler LaPointe, and Dianna Frederick for their help with my "mad scientist" measurement setups in their labs and work-spaces as well as my antenna fabrication efforts. A thank you to Doug Brown for loaning me the use of his computing equipment. Thank you to my fellow student and co-worker Zach Silva for helping me to navigate Georgia Tech. Also, a special thanks to John Borchardt and Dr. Strassner for their time reviewing my publication drafts and providing valuable feedback. Additionally, I would not have been able to pursue the Ph.D. through Sandia's doctoral studies program without the support of my manager Kurt Sorenson. Thank you also to Janea Gomez and Bernadette Montano, in student programs, for helping me to get accepted and successfully complete Sandia's doctoral studies program. Finally, thank you to the many other colleagues who provided simple words of encouragement or helpful conversations that have meant much more than it might have seemed.

Thank you to my fellow lab-mates, Mark Reed and Dr. Yoni Gabbay, for their help and

encouragement. Also, thank you to Dr. Scott's past students Dr. Mike McFadden and Dr. James Sustman, whose Ph.D. work I relied upon heavily at times. Of course, I would not have been able to graduate on time without those in the ECE advising office—especially Dr. Daniela— helping me to keep all my academic "ducks in a row."

I want to thank my family and friends without whom I could not have accomplished this work. Thank you to my wife, Grace, who spent many long hours single-handedly caring for our family while I was busy with my research deadlines as well as providing support and encouragement when I really needed it. Without her, I could not have survived all the work and stress. Thank you to my four amazing children who have provided so much happiness and relief with their smiles and hugs! I would also like to thank my parents for their encouragement and all the hard work starting my academic journey with homeschooling 25 years ago. Also, my in-laws have given my family much support—especially traveling 14 hours to watch the kids while Grace and I flew to Atlanta for my Ph.D. proposal. Thank you to my siblings and siblings-in-law (all 17 of them!) for their support throughout my life and career. A special thank you to my brother-in-law Josh Mitchell who has been a friend, colleague, and fellow Georgia Tech grad student! Thank you to all our friends at Desert Springs Church for their prayers and support of my family during our time getting this degree. Most importantly, thank you to Jesus, who has saved me from myself and continues every day to make me in all ways a better person.

DISCLAIMER

This work was supported in part by Sandia National Laboratories, a multimission laboratory managed and operated by National Technology and Engineering Solutions of Sandia, LLC., a wholly-owned subsidiary of Honeywell International, Inc., for the U.S. Department of Energy's National Nuclear Security Administration under Contract DE-NA0003525. This dissertation describes objective technical results and analysis. Any subjective views or opinions that might be expressed in the dissertation do not necessarily represent the views of the U.S. Department of Energy or the United States Government.

TABLE OF CONTENTS

LIST OF TABLES

LIST OF FIGURES

SUMMARY

The research presented in this dissertation analyzes the operation of the sinuous antenna and seeks to overcome practical design challenges for radar applications. The sinuous antenna can operate over ultra-wide bandwidths while producing polarization diversity, which makes the antenna an attractive candidate for polarimetric radar. The specific application addressed in this work is the detection of targets close to the ground surface with ground-penetrating radar (GPR).

The sinuous antenna may suffer from unintended resonant modes which distort the radiation and will produce ringing when the antenna is used to transmit pulses. An investigation was performed to determine the correlation between design parameters and these resonant modes. Design guidance is presented, which mitigates the excitation of these modes. A new sinuous antenna outer truncation technique is also presented, which prevents low-frequency resonances. A sinuous antenna is designed, fabricated, and measured to validate the proposed design guidance.

Dispersion in sinuous antennas is another undesirable characteristic when radiating pulses. Since the active region on the antenna moves with frequency, the spectral content of the radiation is spread out over time. The original pulse may be reconstructed by applying a phase correction that compensates the dispersive effects. A simple dispersion model that is suitable for a fieldable system is proposed and implemented for both simulated and measured sinuous antennas. The dispersion is dependent on the sinuous antenna design variables. An optimization procedure is used to fit the model to the specific sinuous antenna. With the developed dispersion model, the sinuous antenna may be successfully used to transmit and receive temporally compact pulses.

When attempting to detect targets close to the ground surface, GPR systems often employ a bistatic antenna configuration. Such a configuration is used to improve the isolation between the transmit and receive channels; however, this leads to extreme bistatic angles

that often reduce system performance. The operation of the sinuous antenna as an array of closely spaced yet independent arms is investigated as a potential quasi-monostatic antenna with a low height profile. The quasi-monostatic configuration dramatically reduces the bistatic angles, which significantly improves performance for close-in targets while keeping the isolation to a manageable level. A prototype antenna is fabricated and integrated into a GPR testbed. The polarimetric nature of the antenna allows for the discrimination between linear and circular targets, which is demonstrated with measured data.

CHAPTER 1
INTRODUCTION AND BACKGROUND

The objective of Remote Sensing is to provide systems a means to determine or infer information about an object or location that may not be readily available for interrogation by natural human perception. Often, the use of electromagnetic waves, with frequencies lower than the visible spectrum, are used for such sensing since target information may be inferred by analyzing the scattering produced by an incident wave. This technique is referred to as radar[1] and has been in use since just prior to World War II [2]. Since its inception, radar engineers have sought continuously to extract additional target information with increasing accuracy from the scattered electromagnetic wave. This search has lead to many advances in both electromagnetics and signal processing. One such development is the exploitation of wave polarization to provide additional target information [3]. By detecting two orthogonal senses of polarization, additional target characteristics may be obtained and used for target classification, e.g., discriminating between human-made objects and naturally occurring ones.

Perhaps one of the most challenging applications of such electromagnetic sensing is that of detecting buried objects utilizing ground-penetrating radar (GPR) systems. Buried objects of interest include utilities, treasure, archaeological items, and buried hazards such as landmines. Not only is the unaided detection of such objects difficult since they are hidden by soil, but exploratory excavation may also represent significant safety risks. The successful implementation of a GPR system requires significant technical hurdles to be overcome. Not the least of which are unknown properties of the propagation medium, air-to-ground interface reflection, signal-path loss, and significant clutter due to unwanted

[1] The term radar is an acronym for RAdio Detection And Ranging (RADAR) [1]. However, capitalization is not used in the literature since the term is considered a common noun.

targets such as rocks, debris, and soil variations. Polarimetry may be used to overcome some of these obstacles by increasing the accuracy of target classification. However, almost all current GPR systems utilize singularly polarized antennas in order to reduce size and complexity.

Sinuous antennas provide both ultra-wide bandwidth (UWB) as well as polarization diversity. The four-arm sinuous antenna is capable of producing orthogonal sets of both linear and circular polarization depending on the feeding arrangement. Other wideband antenna designs provide similar capabilities; however, they require relatively large and often complex three-dimensional structures in order to produce orthogonal senses of polarization. Alternatively, the sinuous antenna may be implemented as a planar structure. These attributes have made the sinuous antenna useful in many applications such as electromagnetic pulse (EMP), human health monitoring, and radio astronomy. The combination of polarimetric capabilities with a low profile makes the sinuous antenna attractive to polarimetric remote-sensing applications, particularly, close-in sensing applications such as GPR.

The objective of this research is, in general, to utilize the sinuous antenna for polarimetric sensing. An emphasis will be placed on the application to polarimetric detection of subsurface targets, i.e., GPR. Sinuous antennas are particularly suited for such an application as they are capable of producing UWB radiation with polarization diversity in a low-profile form factor. However, there is limited information provided on sinuous antennas in the current literature. This research will provide detailed analysis, utilizing both simulation and measurement of the sinuous antenna resulting in design guidance for pulsed radar applications. Additionally, the operation of the sinuous antenna arms as four individual elements will be explored to realize a compact, quasi-monostatic, polarimetric GPR system.

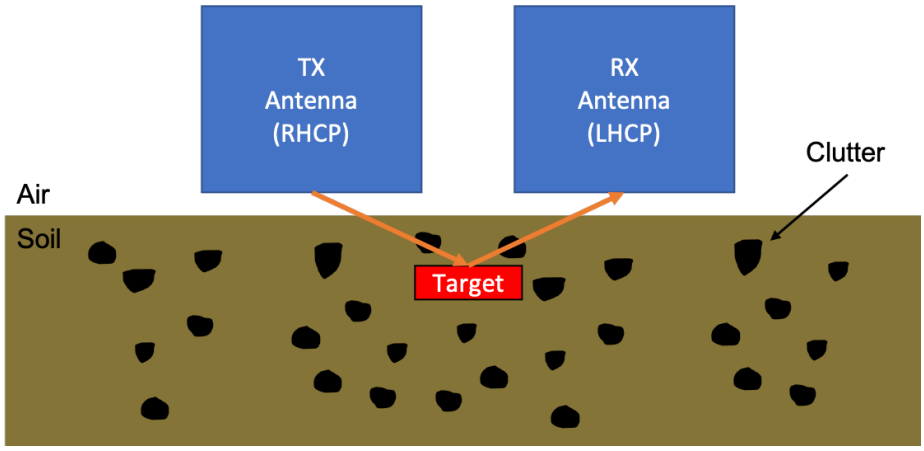

Figure 1.1: Illustration of basic GPR operation utilizing bistatic antennas.

1.1 GPR Antennas

Ground-penetrating radar (GPR) systems operate by coupling electromagnetic waves into the soil and measuring the resultant back-scattered signal produced by discontinuities in the subterranean material. These discontinuities (also referred to as targets) may be the result of buried human-made objects or natural phenomena such as rocks, soil strata, cavities, and others. The GPR processes the received signals in an effort to detect and classify targets of interest. The ability to reliably detect and classify subterranean targets is often hampered by a large amount of non-interest targets or "clutter." A typical GPR measurement setup is illustrated in Figure 1.1.

In order to correctly discriminate between desired targets and clutter, target information must be accurately inferred from the received signals. Target range information, i.e., depth and length, may be determined by coherently processing wide-signal bandwidths. Additionally, by coherently processing multiple measurements collected as the GPR is scanned along the soil surface, cross-range information may be inferred, i.e., cross-range position and width. This technique is referred to as Synthetic Aperture Radar (SAR) [4]. Finally, target shape information may be obtained by analyzing the polarization of the scattered wave relative to the polarization of the transmitted wave. This technique is referred to as polarimetry and has significant application in the classification of targets [5, 6]. However,

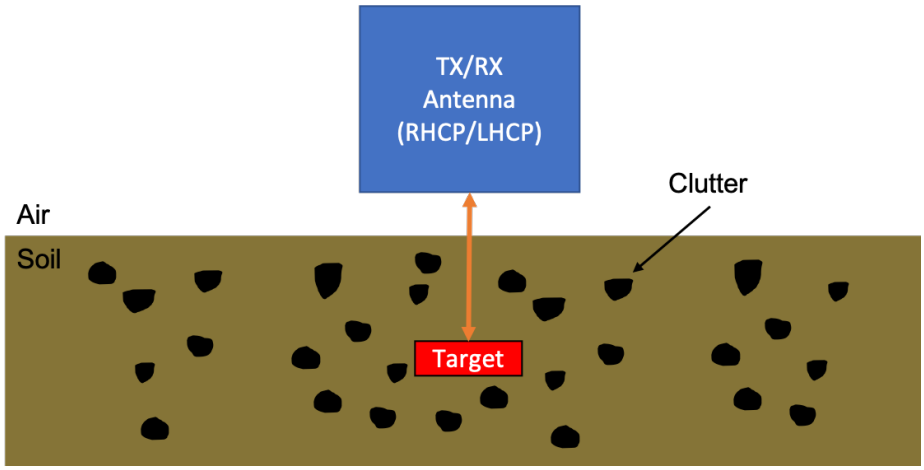

Figure 1.2: Illustration of basic GPR operation utilizing a monostatic antenna.

almost all current GPR systems utilize singularly polarized antennas to reduce the size and complexity of the system. Further, GPR antennas are usually operated bistatically to increase isolation between transmit and receive channels. This bistatic configuration often results in extreme bistatic angles, as illustrated in Figure 1.1. At such extreme angles, the antennas often have reduced polarization purity and pattern uniformity over the operating band, which may degrade system performance. Therefore, a polarimetric GPR operated in a configuration similar to that illustrated in Figure 1.2, is desired.

Recently, a polarimetric antenna based on resistive-vee elements was developed for GPR applications [7, 8]. The antenna's resistive-vee elements were interleaved to achieve smaller bistatic angles, i.e., quasi-monostatic (see Figure 1.3). While these antennas work well, the antenna structure is relatively large and complex. Additionally, such antennas may couple strongly to metal detector coils placed nearby if the GPR is used in conjunction with an electromagnetic induction (EMI) sensor [9, 10]. These issues may represent significant design hurdles for practical GPR systems. One example is the PSS-14 landmine detection system [11], shown in Figure 1.4[2], which employs both GPR and EMI sensors with the EMI coil surrounding the GPR antennas. As can be seen, sizeable and complex antenna structures which couple to nearby coils would be problematic. It is therefore de-

[2]PSS-14 photo used with permission, courtesy of Military.com.

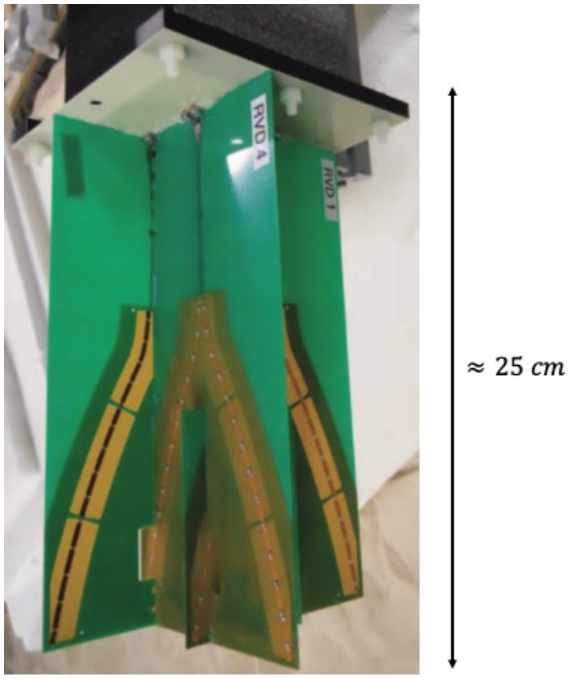

Figure 1.3: Polarimetric GPR antenna composed of resistive-vee elements. The resistive-vee elements are interleaved to achieve quasi-monostatic operation.

sired for GPR applications to obtain a low-profile antenna capable of transmitting multiple polarizations over ultra-wide bandwidths. Further, the ability to operate the antenna in a monostatic or quasi-monostatic system in order to achieve good antenna performance for close-in targets is also desired.

1.2 Sinuous Antenna Background

The sinuous antenna was first published in a patent by DuHamel in 1987. The patent describes the sinuous antenna as the combination of the frequency-independent spiral and log-periodic antenna (LPA) concepts [12]. Spiral antennas produce ultra-wideband (UWB) radiation but are limited to a single circular polarization depending on the winding. LPAs are inherently linearly polarized, and four-element LPAs may be designed to produce both dual-linear and dual-circular polarization from the same aperture [13]. However, LPAs result in apertures on the order of 2λ in circumference [13]—twice that of spiral antennas [14]. Comparatively, sinuous antennas are capable of producing ultra-wideband (UWB)

Figure 1.4: Soldier operating the PSS-14 landmine detector[1].

radiation with polarization diversity in a form factor smaller than an LPA (similar to that of a spiral) [12, 15].

These properties have made the sinuous antenna useful in many applications such as: wireless communications [16, 17], direction-finding [18, 19], human-health monitoring [20], radio astronomy [21, 22, 23, 24, 25], terahertz detectors [26, 27, 28, 29, 30], global positioning systems (GPS) [31], electromagnetic pulse (EMP) [32], and electronic warfare [33, 34]. Polarimetric radar systems [3] are an especially intriguing use case due to the ability of the four-arm sinuous antenna to produce dual-polarized radiation over wide bandwidths. Other wideband antenna designs such as quad-ridge horn [35], Vivaldi [36], and resistive-vee [7] antennas provide similar capabilities. However, they require relatively large and often complex three-dimensional structures in order to produce orthogonal senses of polarization. Alternatively, the sinuous antenna may be implemented as a planar structure. With these attributes, the sinuous antenna shows promise for many sensing applications—in particular, ground-penetrating radar (GPR). Although sinuous antennas

have been connected to GPR applications in the literature [37, 38], to the author's knowledge, system integration, and specific sinuous antenna design analysis has not been provided.

1.2.1 Design

Sinuous antennas are comprised of N arms each made up of P cells where the curve of the p^{th} cell is described in polar coordinates (r, ϕ) by[3]

$$\phi = (-1)^{p-1}\alpha_p \sin\left(\frac{\pi \ln(r/R_p)}{\ln(\tau_p)}\right) \pm \delta, \tag{1.1}$$

where $R_{p+1} \leq r \leq R_p$ [12]. In Equation 1.1, R_p controls the outer radius, τ_p the growth rate i.e., $R_{p+1} = \tau R_p$, and α_p the angular width of the p^{th} cell (see Figure 1.5). The argument of the $\sin$ function ranges from $\pi \rightarrow 0$ as r ranges from $\tau_p R_p \rightarrow R_p$. Thus, the sinusoidal component of Equation 1.1 provides half of a sinusoidal like curve (positive values only), as illustrated in Figure 1.6. Consequently, the sign term $(-1)^{p-1}$ is required in order for the curve to oscillate between $\pm\alpha_{p+1}$ and $\mp\alpha_p$. The curve is then rotated $\pm$ the angle δ in order to fill out the arm. In this analysis, the antennas are fed by a self-complementary arrangement of orthogonal bow-tie elements, each feeding a set of opposing sinuous arms (see Figure 1.5).

The angular width of the sinuous antenna metalization is controlled by the angle δ. When setting $\delta = 90^\circ/N$, the sinuous antenna structure is considered self-complementary, i.e., the metal and non-metal areas are identical only offset by a rotation. The parameter α does not affect this condition as only δ controls the metal to non-metal ratio. In the four-arm sinuous antenna case, δ equal to 22.5° results in a self-complementary structure,

[3] The astute reader will notice subtle differences between Equation 1.1 and that presented in [12]. The exponent of the sign component is arbitrary in that it must merely provide a sign difference between consecutive cells. Here $p-1$ was chosen in order to control the direction of the wrap for illustration purposes. Next, the value of π in the $\sin(...)$ function is replaced by 180 in the original equations. This is purely determined by the underlying implementation of the $\sin$ function. The $\sin$ functions that expect input argument to be in units of radians require π while those that expect degrees instead require 180.

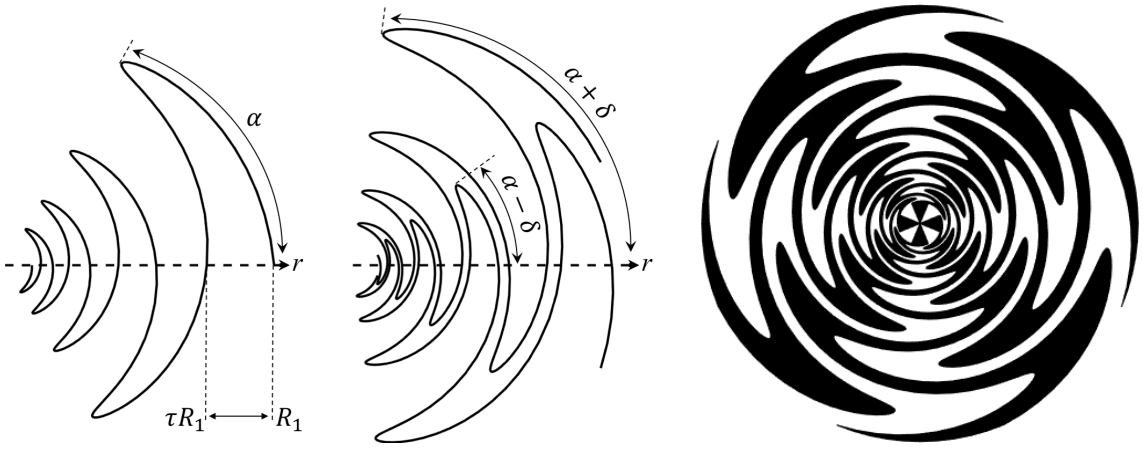

Figure 1.5: Illustration of sinuous antenna design parameters: (left) angular width α, expansion ratio τ, and outermost cell radius R_1; (center) curve rotation angle δ; (right) self-complementary sinuous antenna design having parameters $N = 4$, $P = 8$, $\alpha = 60°$, and $\tau = 0.75$ with bowtie feed.

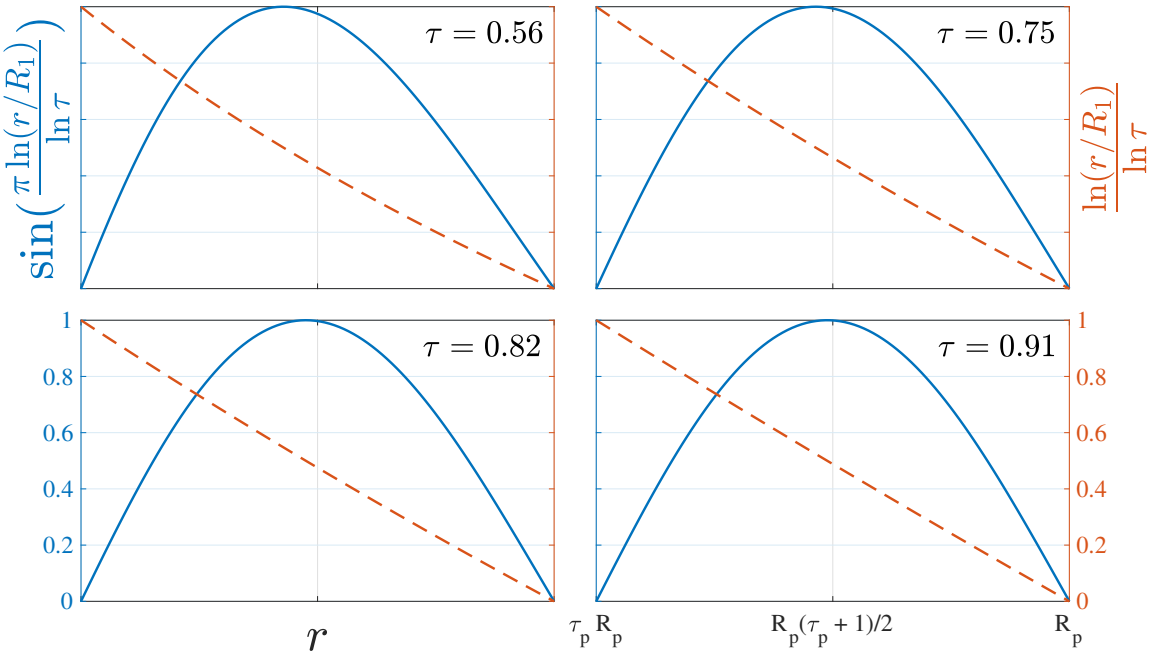

Figure 1.6: Illustration of the sinuous curve equation sinusoidal component for various values of the expansion ratio τ. Note that the curve is less skewed as τ approaches unity.

as illustrated in Figure 1.5. The self-complementary condition is desired since it helps to ensure the sinuous antenna's input impedance is both real and frequency independent [39, 40]. However, in [41], the authors broke the self-complementary condition near the feed to improve the match to a 100 Ω feed. Additionally, some have investigated using values of δ not equal to $90^\circ/N$ to improve bandwidth when the self-complementary condition has already been broken by the inclusion of a ground plane [22, 42] or in the case of a non-complementary two-arm sinuous antenna [34].

The number of arms in a sinuous antenna may vary depending on the application; the DuHamel patent describes both $N = 4$ and $N = 6$ designs [12]. Since the original intent of the antenna was to produce dual-circular polarization, DuHamel indicated N must be greater than two [12]. However, two-arm ($N = 2$) sinuous antennas have been investigated by several authors in the literature [34, 40, 43, 44, 45, 46]. Further, it has been shown that self-complementary two-arm sinuous antennas act like spirals with the sense of polarization oscillating between RHCP and LHCP depending on frequency [44]. Although not present in the literature, it may be possible to construct a single-arm sinuous antenna operated in a monopole fashion. Four-arm ($N = 4$) sinuous antennas, shown in Figure 1.5, are the most common variant as they represent the simplest version capable of producing two orthogonal senses of polarization.

As shown in Equation 1.1, both the expansion ratio τ and angular width α may vary from cell to cell [12]. Some have allowed τ to increase with r in order to achieve better power handling by preventing tiny trace widths near the feed [47, 48]. Maintaining α and τ constant for all cells results in a log-periodic structure [12]. For such a structure, the radiated fields at frequency f will repeat, since the structure repeats (scaled in size), at frequencies $\tau^n f$ where n is an integer [49]. Allowing either or both τ and α to vary between cells results in a quasi-log-periodic structure since the fields no longer repeat with a constant periodicity in log-space [12]. Theoretically, τ may vary over the range of $0 \rightarrow 1$; however, values larger than 0.56 are recommended for good pattern uniformity [12].

Moreover, the quality of the patterns increases as τ approaches unity, although this comes at lower efficiency due to increased conductor losses [33, 39]. Furthermore, larger values of τ result in thinner (harder to fabricate) traces [39] as well as increased dispersion in the antenna [50, 51]. Design equations in [12] relate α to both the beamwidth and bandwidth of the sinuous antenna. The low-frequency cutoff of the sinuous antenna is dependent on the total angular sweep of the arms at the outer radius, and the wavelength at cutoff can be approximated as

$$\lambda_L/4 = R_1(\alpha + \delta), \tag{1.2}$$

where α and δ are in radians [12]. Therefore, when designing a compact antenna for lower frequencies of operation, antenna designers may be motivated to choose large values for α. However, for large values of α, the sinuous begins to act like a spiral with alternating senses of circular polarization [17]. Published values of α range from 45° to 90° [44, 52] with some authors choosing 50° [17, 34] and 60° [53, 37, 51]. The vast majority of published sinuous antennas have α equal to 45° [54, 15, 27, 55, 26, 39, 56, 57, 58, 59, 48, 46, 30, 60, 61, 62, 63, 25, 45, 64, 33, 65] which is most likely attributed to design guidance provided in [66] which suggests $\alpha + \delta$ be kept to $\leq 70°$ "to ensure good efficiency and gain performance without dropouts over the frequency band." However, to the knowledge of the author, no additional analysis of the effects of both τ and α (and a combination thereof) on sinuous antenna performance is provided in the literature.

1.2.2 Radiation Characteristics

Radiation from a sinuous antenna, as described in [12], occurs at active regions which are formed when the length of a cell is approximately a multiple of $\lambda/2$. In this case, the current at the start and end of a cell are in phase due to the wrapping of the arm and $\lambda/2$ travel. Equation 1.2 is based on this mechanism. This concept is illustrated in Figure 1.7. Since the $\lambda/2$ distance moves with frequency, a variation or wobble in polarization with frequency is observed [22, 56, 64, 67]. Attempts have been made to correct this effect in processing

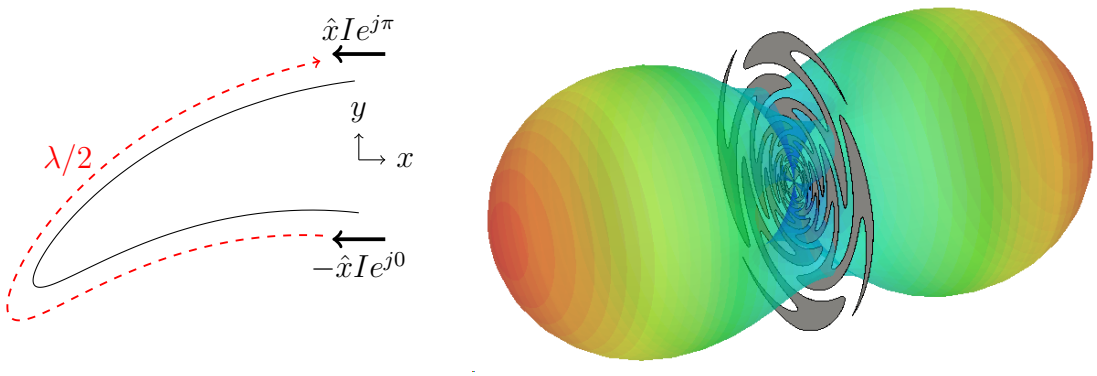

Figure 1.7: Sinuous antenna radiation: illustration of active region definition (left), and example radiation pattern (right).

[67] while others have attempted to exploit it for the detection of linear scatterers [68].

As illustrated in Figure 1.7, the sinuous antenna radiates bi-directionally; therefore, in order to prevent interference from structures behind the antenna, e.g., the mounting structure and feeding network, the back lobe is often removed by inclusion of an absorbing cavity [12, 52, 69, 70, 71, 34]. However, this attribute has been exploited for use in a frequency doubler apparatus [54]. Although the inclusion of an absorbing cavity results in an omnidirectional pattern, it reduces efficiency by 50% prompting many researchers to evaluate alternative methods [41]. Perhaps, one of the more exciting alternatives is an electromagnetic band-gap (EBG) structure which acts like a magnetic boundary that does not cause out of phase reflections [72]; however, these are hard to design over wide bandwidths reliably. Some have incorporated a ground plane [16, 73, 24, 22] or unloaded cavity [48, 74, 42] in order to reflect the back lobe and improve gain. However, these methods generally result in a significant decrease in bandwidth [70]. Alternatively, the antenna may be implemented on a cone, rather than a plane, which results in a more directive antenna [21, 22, 61, 63, 24, 75, 15, 76, 77, 23]. Although the back lobe still exists, it is significantly reduced. Some have combined the conical structure with a ground plane in order to achieve a fixed phase reference and omnidirectional pattern [22]. While not in an effort to reduce back-lobe radiation, some studies have been conducted on the performance of

sinuous antennas conformally mapped to other three-dimensional structures [61, 63].

The use of lenses has also been investigated as a method to increase directivity [56, 39, 78, 47, 30, 29, 25, 27]. Not only does a lens focus the radiation, but a larger portion of the fields are also contained in the lens dielectric, thereby reducing the back-lobe radiation. The use of a lens has been shown to reduce the back-lobe radiation to only 5% [56]. Additionally, lenses have the added benefit of reducing the radial size of the sinuous antenna [78]. Others have tried truncating the antenna in a ring to reduce the size [60]; however, this results in the ring radiating at the lower frequencies—the radiation is no longer characteristic of a sinuous antenna.

1.2.3 Feeding Mechanism

Developing a feed for the sinuous antenna is complicated by the fact that the input impedance at the terminals of the arms is not 50 Ω which is the impedance of most RF electronics. The feeding mechanism for sinuous antennas (and other similar antennas) has been an area of active research. In [42], four feed lines, all enclosed in a conducting cylinder, fed the sinuous antenna. Often tapered-microstrip baluns are used to transform from an unbalanced 50 Ω port to a balanced line of the appropriate impedance[4][79, 80, 64, 45, 60, 70, 81]. Both linear [82, 45] and non-linear [79, 64, 60, 70, 81] tapers have been investigated. While such structures are relatively simple, some research has sought to expand their functionality. The authors in [82] implemented a notch in the microstrip balun's frequency response in order to place a null in the antenna's gain at a specific frequency. Others have integrated a 90° coupler into the microstrip balun [83] intended for producing circular polarization with a single feed component. Tapered-microstrip baluns are relatively simple when feeding two antenna arms [79, 80, 60, 45] but become more complex when attempting to feed four arms [79, 83, 65]. A special version was developed to feed four arms in mode 2, where each set of opposing arms are driven together against

[4] The impedance of practical sinuous antennas varies (lower) from the theoretical (267 Ω) due to the inclusion of a dielectric substrate.

the other set of arms [81]. A novel photonic feed was developed which allowed for individual control of each sinuous antenna arm as a separate element [84]. This system is especially interesting since it provides a way to operate each arm of the sinuous antenna independently and with arbitrary phasing [84], which has significant potential for GPR applications and will be discussed further in a later chapter.

Although the original sinuous geometry was defined as a metalization on a dielectric substrate [12], the sinuous antenna can also be implemented as a slot [19, 74, 25, 48, 43, 34, 59, 85, 80]. The slot implementation has several advantages, such as better power handling [48] as well as reduced input impedance, which makes feeding by 50 Ω cables more feasible [85]. In [34], a two-arm slot antenna was fed by a coupled trace; however, the method used would not be viable for a four-arm design. While slot antennas change the target impedance, they still present feeding difficulties similar to sinuous antennas of the metalized variety.

1.2.4 Summary

As discussed, the sinuous antenna provides many capabilities that are desirable for wideband polarimetric remote sensing applications–particularly close-in sensing, e.g., GPR. Before evaluating the performance of a GPR with sinuous antenna(s), the required antennas must be designed and constructed. The proper design of a sinuous antenna requires an understanding of both the design equations themselves as well as the effects of the parameters on performance. While the sinuous antenna design equations are well documented, the effects and trade-offs of the parameters are not. In this work, analysis is provided that describes how the design parameters affect the performance. Specifically, solutions to limitations such as unintended resonate modes and dispersion are presented. Additionally, practical design problems will be discussed such as feeding arrangements and truncation.

1.3 Outline

The research presented in this dissertation intends to analyze, through simulation and measurement, the operation of the sinuous antenna and provide guidance for overcoming practical design challenges when utilizing the antenna for pulsed radar applications. The specific application investigated is the detection of close-in targets, e.g., landmines, with polarimetric GPR. The research is outlined as follows.

In Chapter 2, the excitation of unintended resonant modes on sinuous antennas will be investigated. Such resonances produce distortion in the radiation, which is particularly troublesome for pulsed applications. The relationship between the resonances and sinuous antenna design decisions will be established. Design guidance for the mitigation of the resonances will also be provided.

Dispersion in sinuous antennas will be considered in Chapter 3. A simple model for the correction of sinuous antenna dispersion—suitable for a real-world GPR system—is presented and applied to both measured and simulated antennas. It will be shown that the model may be successfully used to compress pulses dispersed by the antenna.

In Chapter 4, the theoretical input impedance of self-complementary sinuous antennas will be derived and discussed. The input impedance of practical sinuous antennas will deviate from the theoretical due to the finite size of the antenna and the use of dielectric substrates. Simulated results of the sinuous antenna input impedance on some common substrates will be provided. Finally, the effects of placing an absorber loaded cavity behind the antenna to absorb the back lobe of the radiation will be investigated.

A different method of driving the sinuous antenna for close-in sensing applications is proposed in Chapter 5. This new method operates each arm of the sinuous antenna as an independent element of a closely interleaved array. The input impedance, as well as the radiation characteristics of both four- and eight-arm sinuous antennas will be investigated. The development of a prototype antenna for evaluation will also be described.

Chapter 6 describes the experimental integration of the prototype unbalanced sinuous antenna (developed in Chapter 5) into a GPR testbed. The antenna is used to acquire polarimetric measured data from both symmetric and asymmetric targets. The polarimetric data is then utilized to discriminate between targets of differing symmetries.

Chapter 7 presents the conclusion which summarizes the contributions and publications of the research as well as describing future work. Appendix A provides details on the full-wave simulations performed for this research, and Appendix B describes the Gaussian pulses utilized in the analysis.

CHAPTER 2

MITIGATING UNINTENDED RESONANT MODES IN SINUOUS ANTENNAS

Although sinuous antennas provide the desirable properties described in Section 1.2, the antennas can suffer from unintended resonances that degrade performance. The sharp ends produced by the outer truncation of the antenna have been shown to resonate when their length is approximately $\lambda/2$ which produces both pattern distortion and ringing in the time domain [64, 58, 53, 37]. Furthermore, log-periodic resonances occurring internal to the sinuous arms have been observed and shown to produce additional ringing as well as deleterious effects on gain smoothness, polarization purity, and group delay [37, 51]. Such resonances may reduce the effectiveness of sinuous antennas, particularly when applied to remote-sensing applications that transform the data into the time domain. Techniques for their mitigation have been presented in the literature. The sharp ends may be empirically removed in order to prevent the associated resonance [64, 58, 53, 62, 69, 37, 22, 51]. Similarly, in [37, 51] the sinuous cell tips were clipped along the antenna arm to mitigate the log-periodic resonances. While these techniques have been successful, they require additional empirical design steps while destroying the self-complementary nature of the antenna—reducing both elegance and frequency independence.

In this chapter, a review of the proposed mitigation techniques in the literature, and a detailed investigation as to the correlation between the log-periodic resonances and the sinuous antenna design parameters will be presented. It will be shown that these resonances may be mitigated simply by selecting appropriate design parameters. In addition, a novel truncation method is proposed to remove the sharp-end resonance. Simulated and measured data is provided in order to develop and validate the design guidance. The simulations were performed using the time-domain solver in CST Microwave Studio [86]. More information about the simulations may be found in Appendix A.

Figure 2.1: Reference sinuous antenna design: $N = 4$ arms, $P = 8$ cells, $\tau = 0.75$, $\alpha = 60^{\circ}$, $R_T = R_1 = 5$ cm, with traditional truncation, i.e., sharp ends. Note that since α and τ are constant for all cells, the antenna is a log-periodic structure.

2.1 Unintended Resonances

In order to investigate the resonances, full-wave electromagnetic analysis of a log-periodic sinuous antenna (pictured in Figure 2.1) in free-space was conducted using the CST Microwave Studio [86] time-domain solver. Both pairs of opposing sinuous arms were terminated by an ideal port set to the theoretical impedance of 267 Ω [39]. A single pair was then driven, with the other pair remaining matched, to produce linearly polarized radiation. The resulting co-polarized realized gain and group delay are shown in Figure 2.2 and display prominent resonances. The resonance at approximately 1.7 GHz is attributed to the sharp-ends of the antenna [37] and will be removed by the outer truncation discussed in Section 2.4. The additional resonances starting at 2.9 GHz are log-periodic in frequency and attributed to interactions between adjacent arms. The log-periodic nature of these resonances is consistent with the work presented in [37] which showed each resonance could be attributed to a specific cell. It will be shown in Section 2.3 that these interactions may be mitigated by reducing the interleaving of adjacent arms, i.e., smaller values of α.

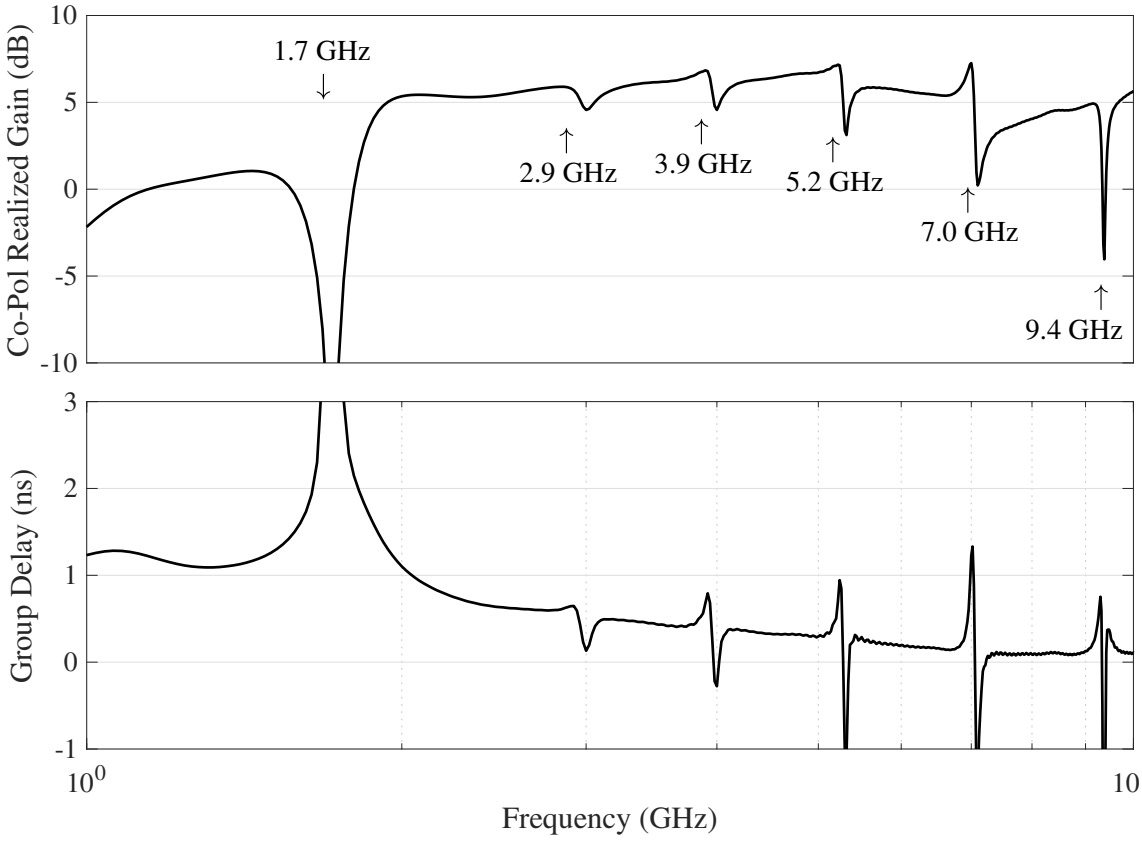

Figure 2.2: Simulated co-polarized (linear polarization) realized gain and group delay of the reference sinuous antenna design on a logarithmic frequency scale. Notice the sharp discontinuities in the radiation starting at 2.9 GHz are logarithmically periodic in frequency.

2.2 Previously Reported Log-Periodic Resonance Mitigation Techniques

The sharp ends produced at the outer truncation of the sinuous antenna can be removed in order to prevent them from resonating [64, 58, 53, 62, 69, 37, 22, 51]. Similarly, in [37, 51], the sinuous cell tips were trimmed along the antenna arm (in addition to the removal of the sharp ends) in order to mitigate the log-periodic resonances which were attributed to currents on the cell tips. These clipping techniques are demonstrated in Figure 2.3 alongside an unmodified version with identical design parameters. Section 2.4 provides further discussion on the sharp ends removal technique. In this section, the conclusions presented in [37, 51] for the mitigation of the log-periodic resonances are further investigated and applied to different sinuous antenna designs.

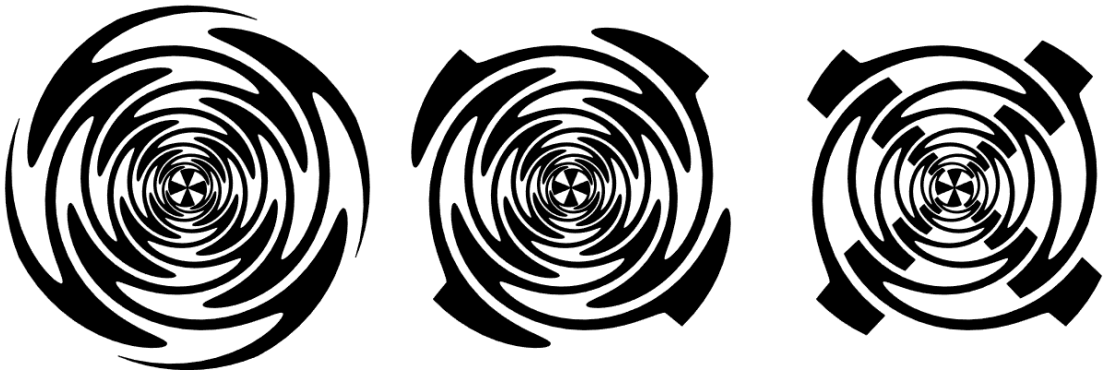

Figure 2.3: Sinuous antenna ends trimming proposed in the literature: (a) no trimming, (b) sharp ends removed, and (c) sharp ends removed and cell tips trimmed.

The initial sinuous antenna design investigated was similar to that evaluated in [37, 51] and is described by Figure 2.1. This antenna is referred to herein as the "Reference Design" and displays prominent resonances in the radiation (see Figure 2.2). For this analysis, the cell ends were clipped at a constant angle ϕ_{trim} and the sharp ends of the outermost cells were also removed as illustrated by Figure 2.4. A mathematical definition of sinuous antenna trimming techniques are not provided in the literature; however, a description of the method employed in this analysis follows. When trimming the ends (or bends) of a cell, define a trim angle ϕ_{trim}. The outside edge of a sinuous antenna cell at is maximum angle is equal to $\alpha+\delta$. The trim is then defined as the removal of any part of the arm that extends beyond the angle $\alpha + \delta - \phi_{trim}$. If it is desired to trim all cells in the antenna the same, ϕ_{trim} can be a constant–see illustration in Figure 2.4. In the more general case, ϕ_{trim} can be considered a vector, of length P, where each value $\phi_{trim}[p]$ specifies a trimming angle for the p^{th} cell.

Four values of ϕ_{trim} were investigated: 0°, 10°, 20°, and 30° with the sharp end removed for each. The trimmed antennas are compared in Figure 2.5 which shows that trimming the cell tips reduces the amount of overlap between adjacent arms. However, according to [12], the cell tips are necessary since they create a capacitance which prevents standing waves on the arms. Simulation results show the antenna match does degrade with

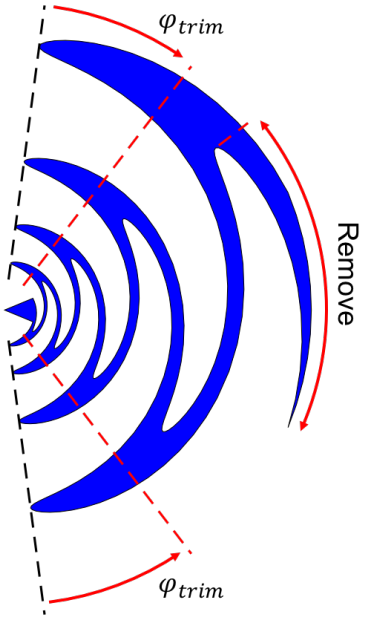

Figure 2.4: Illustration of sinuous antenna cell trimming methodology.

the trimming of the cell tips. The input impedance of the antenna shown in Figure 2.1 can be computed analytically since it is a self-complementary structure [39]. Following the derivation in [39], the impedance of a four-arm self-complementary structure is shown to be 267 Ω when the arms are driven in a balanced manner. It is this impedance to which the ports are referenced in the simulations and subsequently used for the computation of S_{11} shown in Figure 2.6. As expected, the match does deviate from the theoretical when the cell ends are trimmed. Increased clipping of the cell ends causes the impedance to become more frequency-dependent as is illustrated by the graphs of S_{11} in Figure 2.6 and

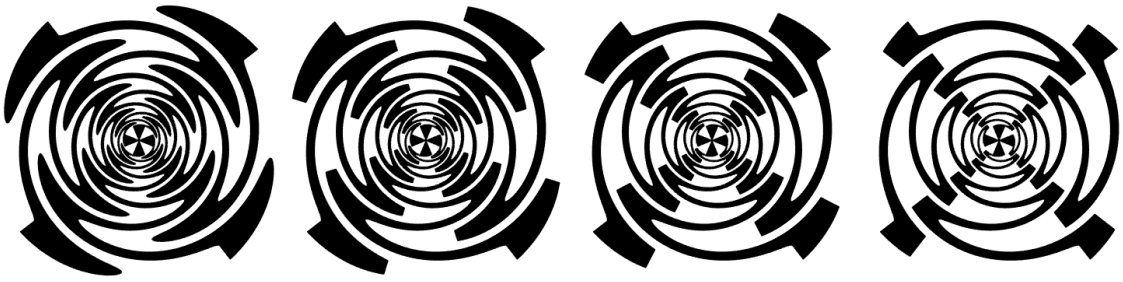

Figure 2.5: Trimmed sinuous antennas simulated: (a) $\phi_{trim} = 0°$, (b) $\phi_{trim} = 10°$, (c) $\phi_{trim} = 20°$, and (d) $\phi_{trim} = 30°$. Note, the sharp ends are also removed.

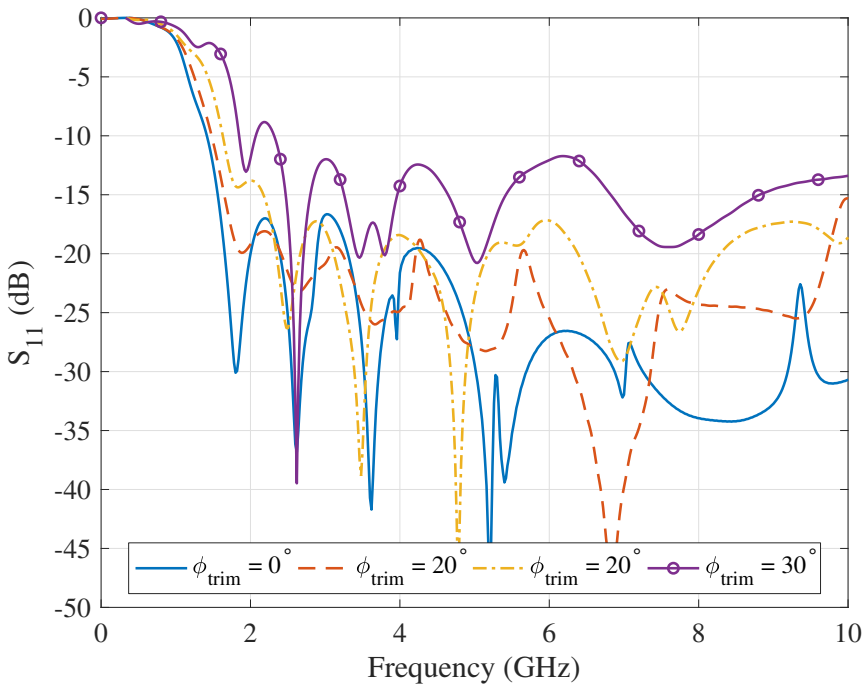

Figure 2.6: Simulated antenna match (S_{11}) for various cell trimming angles (ϕ_{trim}). Larger trim angles result in a reduced match, i.e., increased frequency dependence.

Figure 2.7. It can also be observed in Figure 2.6 that the antenna's low-frequency cutoff increases slightly with increased clipping. Such behavior is expected since trimming the arms effectively reduces their length, thereby making the antenna electrically smaller. Although a decrease in the antenna match may seem undesirable, improved performance in the radiation is obtained from the cell ends trimming.

Simulated boresight realized gain for the antennas with trimming applied (illustrated in Figure 2.5) is shown in Figure 2.8. It may be observed that radiation from the untrimmed sinuous antenna ($\phi_{trim} = 0°$) contains multiple sharp discontinuities due to the unintended resonances, which reduce the gain flatness over frequency. In comparison, trimming the cell ends is shown to mitigate the log-periodic resonances thereby producing smoother gain over frequency. For the $\phi_{trim} = 10°$ case, the resonances are reduced but their effects are still present. The resonances are effectively removed by trim angles of $20°$ and higher. Notice that the cross-polarized gain increases with frequency for all antennas considered. The bow-tie feed produces radiation polarized orthogonal to that of the sinuous arms and

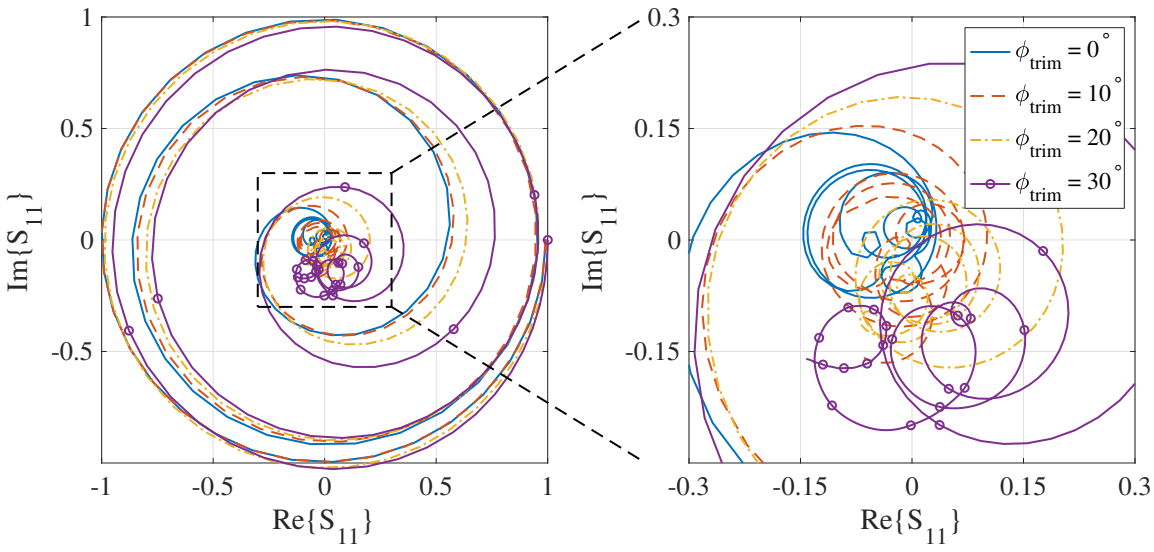

Figure 2.7: Simulated antenna match (S_{11}) for various cell trimming angles (ϕ_{trim}) plotted on the complex plane. Larger trim angles result in reduced match indicated by the increased deviation from $S_{11} = 0 + 0j$.

is responsible for the increase in cross-polarized gain.

In an effort to understand the unintended resonances, and the effects of trimming the cells, the currents excited on the antenna structures were investigated and are displayed in Figure 2.9 for the frequencies 6, 7, and 8 GHz. An unintended resonant mode is excited on the untrimmed antenna at 7 GHz, but not 6 and 8 GHz, as is evident by the current distributions. The current at 7 GHz is distributed over a larger region of the antenna including the adjacent arms. However, when the cell ends are trimmed ($\phi_{trim} = 20°$), the currents at the three frequencies shown behave as expected. The currents also indicate that the tips in the adjacent arms contribute to the unintended resonances.

Distortion in the gain of the sinuous antenna—due to the resonances—ultimately results in ringing when the antenna is used in pulsed type applications. Such ringing can be particularly troublesome for close-in sensing applications such as GPR. Examination of the radiated fields in the time domain is necessary to determine the extent of such ringing. The time-domain radiated pulse $E^x_{pulse}(r_p, t)$ for a given excitation $v_{pulse}(t)$ can be computed

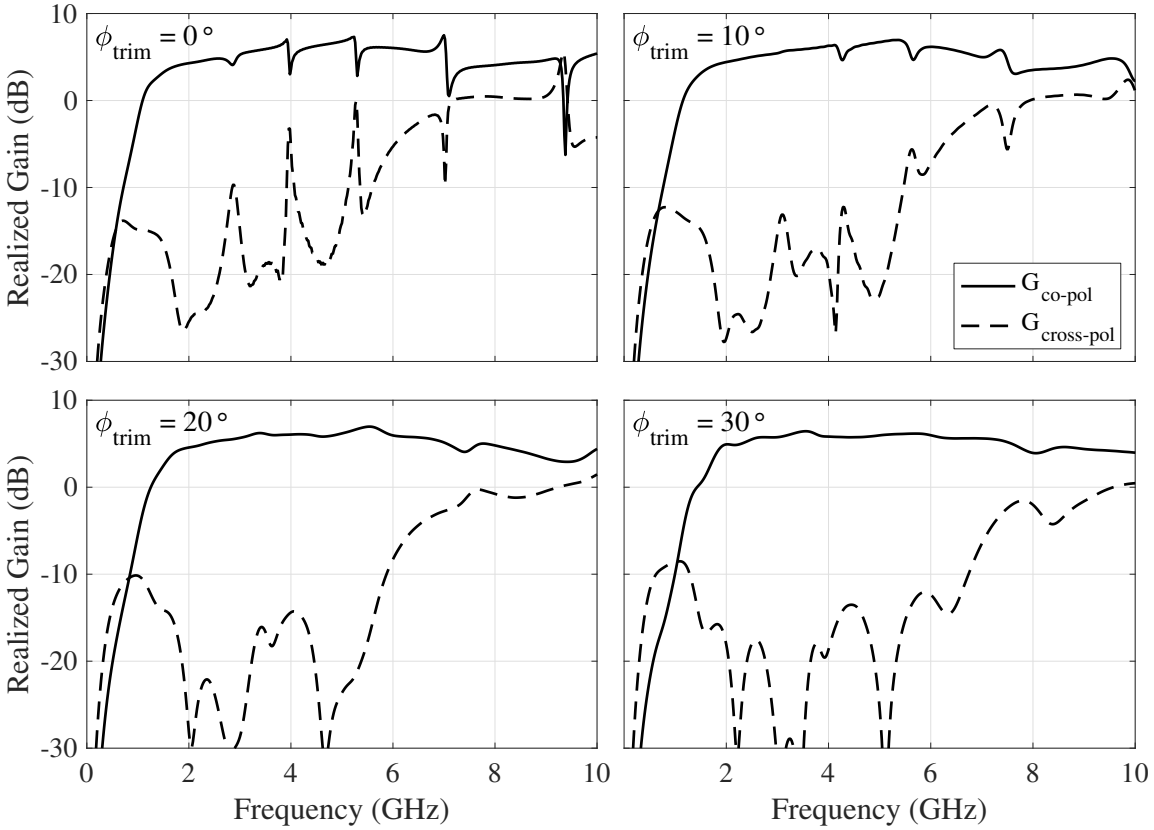

Figure 2.8: Simulated realized gain (on bore-sight) of the trimmed sinuous antennas.

from the frequency-domain radiated fields by

$$E^x_{pulse}(z_p, t) = \mathcal{F}^{-1}\left\{ \mathcal{F}[v_{pulse}(t)] \, \frac{E^x_{sim}(z_p, \omega)}{V_{sim}(\omega)} \right\} \tag{2.1}$$

where $V_{sim}(\omega)$ is the frequency-domain excitation in the simulation and $\mathcal{F}$ and $\mathcal{F}^{-1}$ represent the Fourier, and inverse Fourier transforms, respectively. The input pulse used is a differentiated Gaussian with 1 V peak voltage and maximum spectral energy at 3.2 GHz. The differentiated Gaussian pulse is further described in Appendix B. Both the time- and frequency-domain representation of the pulse are shown in Figure 2.10. Although small, some of the pulse's energy extends beyond 10 GHz. In order to prevent high-frequency content from square windowing the spectrum, the antennas were simulated at frequencies beyond that shown (>10 GHz) and the radiated pulses were then computed using the full spectrum. The computed radiated pulses are shown in Figure 2.11. From the results, it is

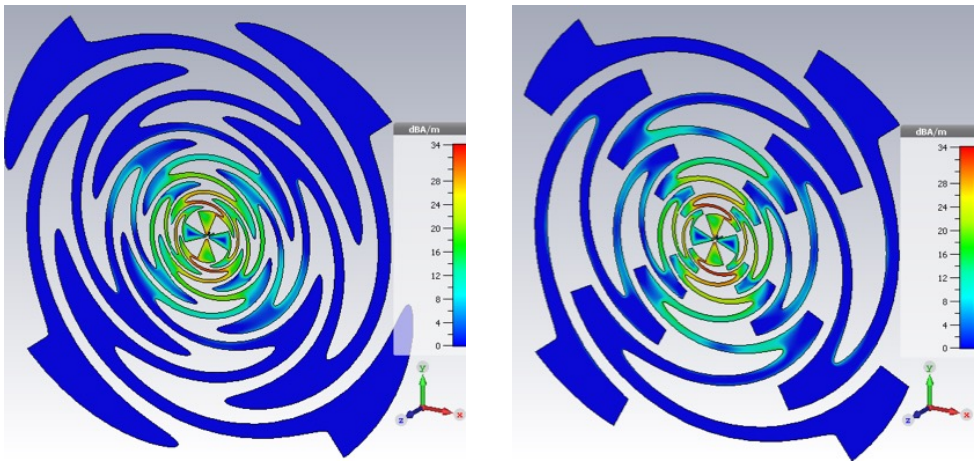

(a) $\phi_{trim} = 0°$ at 6 GHz

(b) $\phi_{trim} = 20°$ at 6 GHz

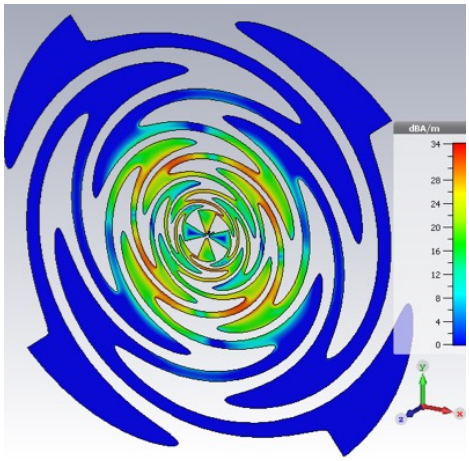

(c) $\phi_{trim} = 0°$ at 7 GHz

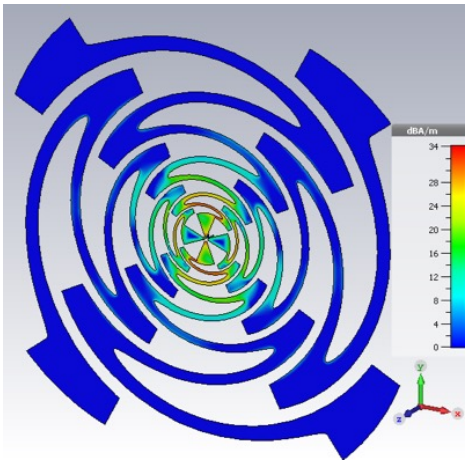

(d) $\phi_{trim} = 20°$ at 7 GHz

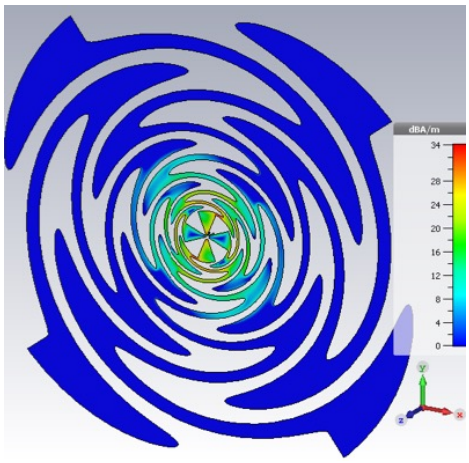

(e) $\phi_{trim} = 0°$ at 8 GHz

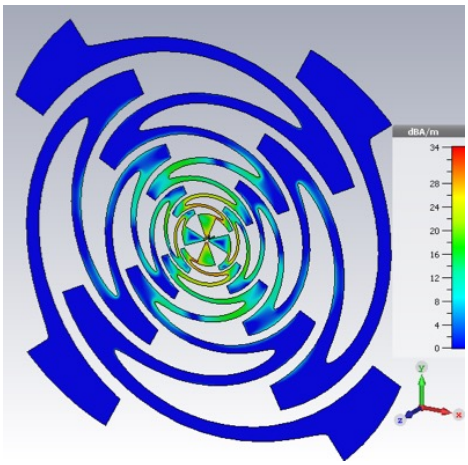

(f) $\phi_{trim} = 20°$ at 8 GHz

Figure 2.9: Pseudo-color graphs of the intensity of the simulated current on the antenna with and without cell ends trimming for three frequencies.

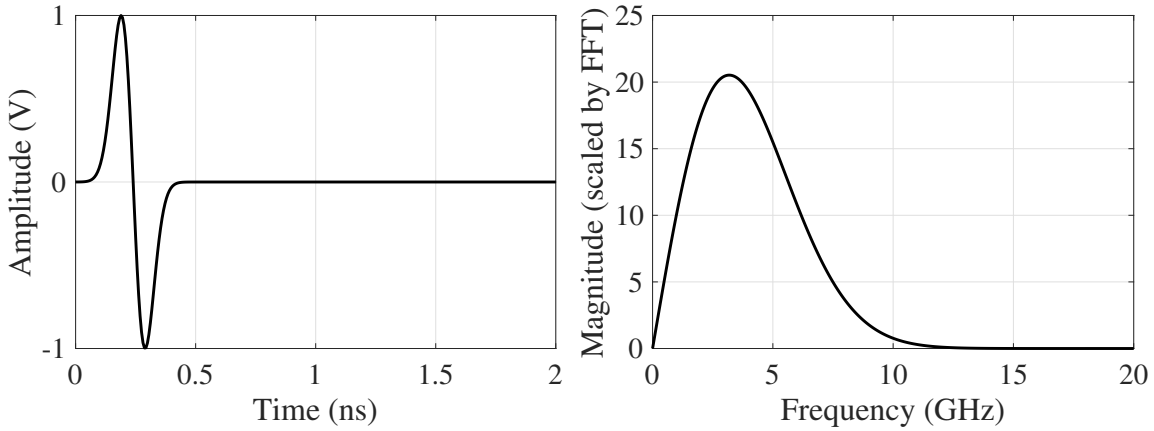

Figure 2.10: Differentiated Gaussian pulse used to compute the time domain radiated pulses. The pulse has 1 V peak voltage and maximum spectral energy at 3.2 GHz.

evident that as the ends are trimmed and the internal resonances are reduced, the radiated pules contain less ringing.

The radiated pulses shown in Figure 2.11 do not match the shape of the input pulse described by Figure 2.10. The distortion is due to the dispersive nature of the antenna, which will be discussed extensively in Chapter 3. The phase of the co-polarized complex radiated field $E^x_{sim}(\omega)$, probed at a boresight distance of $z_p = 2$ m (far-field), was propagated back to the origin by

$$\Phi^d_{sim}(\omega) = \arg\left[E^x_{sim}(z_p, \omega)\exp(jkz_p)\right], \tag{2.2}$$

for each simulated antenna. The remaining phase $\Phi^d_{sim}(\omega)$ is due to dispersion and is plotted in Figure 2.12. Notice that the antennas with trimmed cell ends have smoother unwrapped phase. This difference is even more pronounced when examining the antenna group delay (also plotted in Figure 2.12). The group delay quantifies the antenna dispersion and is computed as $-\frac{d}{d\omega}\Phi^d_{sim}(\omega)$. As can be seen, the non-trimmed sinuous antenna contains significant spikes in the group delay at the frequencies corresponding to the discontinuities in the gain shown in Figure 2.8. The delay may also be used to indicate the location of the resonances on the antenna. With the cell ends trimmed, the spikes are reduced which results in a much smoother group delay.

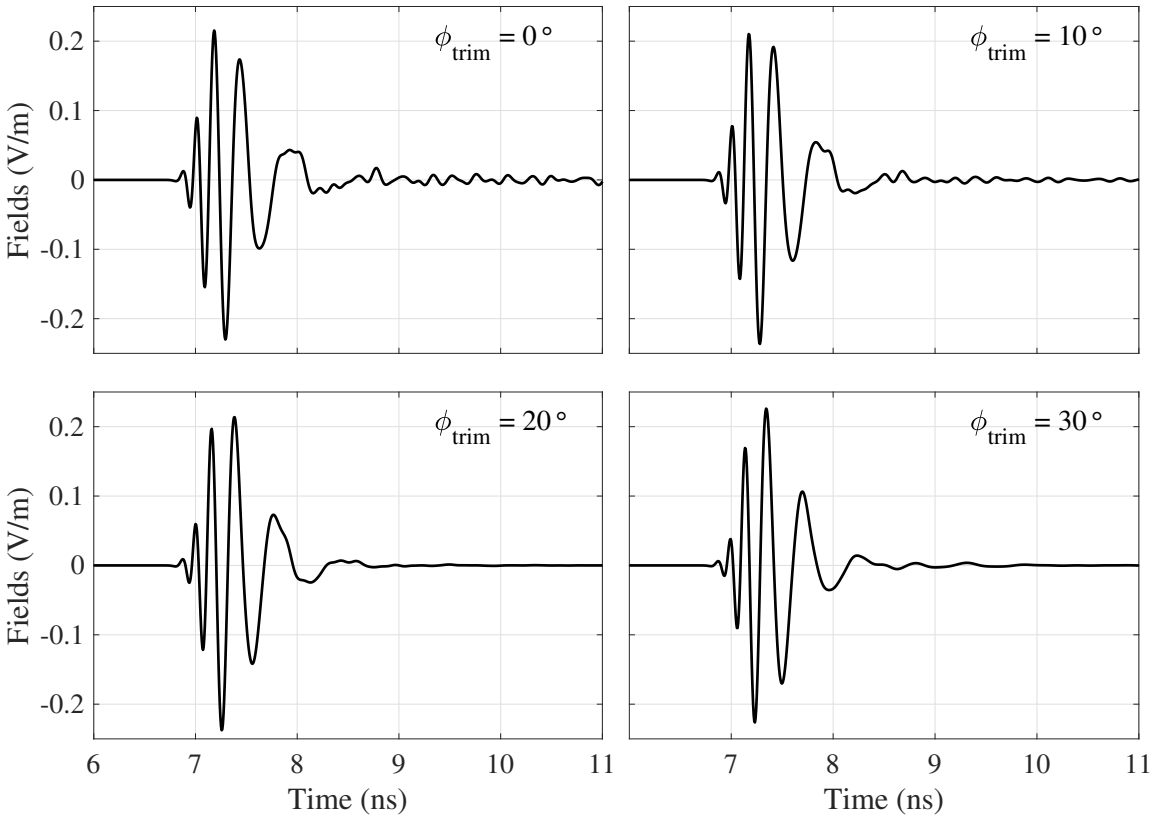

Figure 2.11: Simulated time-domain radiated pulses at 2m (on bore-sight) from the trimmed sinuous antennas.

The resonances also affect polarization metrics, such as the axial ratio (AR). In general, radiated electric fields may be considered to be elliptically polarized with linear and circular polarizations as special cases. For a fixed location, the locus of points traced out by the tip of the electric field polarization vector over time is considered the polarization ellipse [87]. The AR is defined as the ratio of the polarization ellipse major axis (OA) to the minor axis (OB) [87]

$$AR = \pm\frac{OA}{OB}, \tag{2.3}$$

where

$$OA = \left[\frac{E_x^2 + E_y^2 + [E_x^4 + E_y^4 + 2E_x^2E_y^2\cos(2\Delta\Phi)]^{1/2}}{2}\right]^{1/2}, \tag{2.4}$$

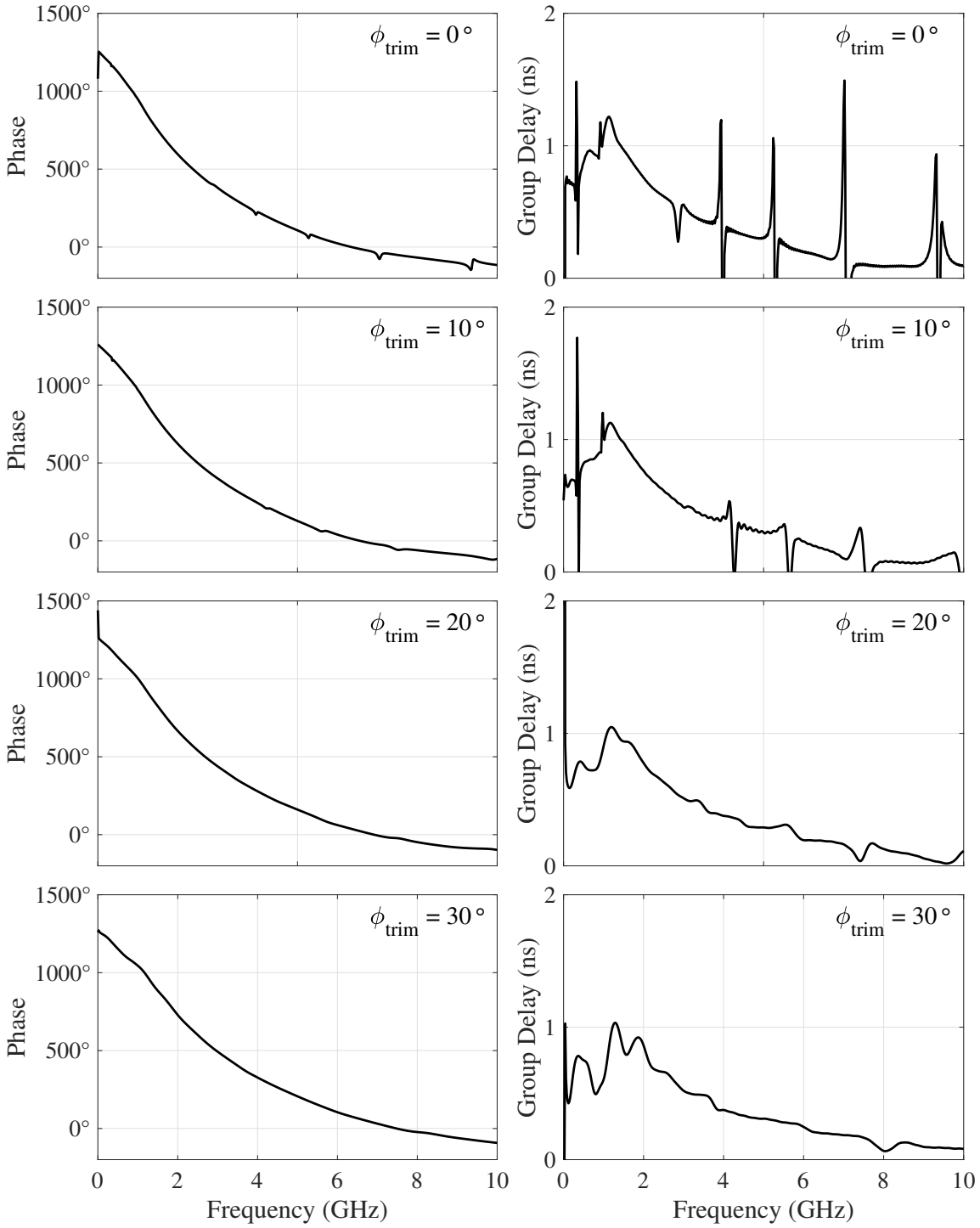

Figure 2.12: Simulated phase (left) and group delay (right) from the trimmed sinuous antennas. The phase is unwrapped starting with the 10 GHz sample.

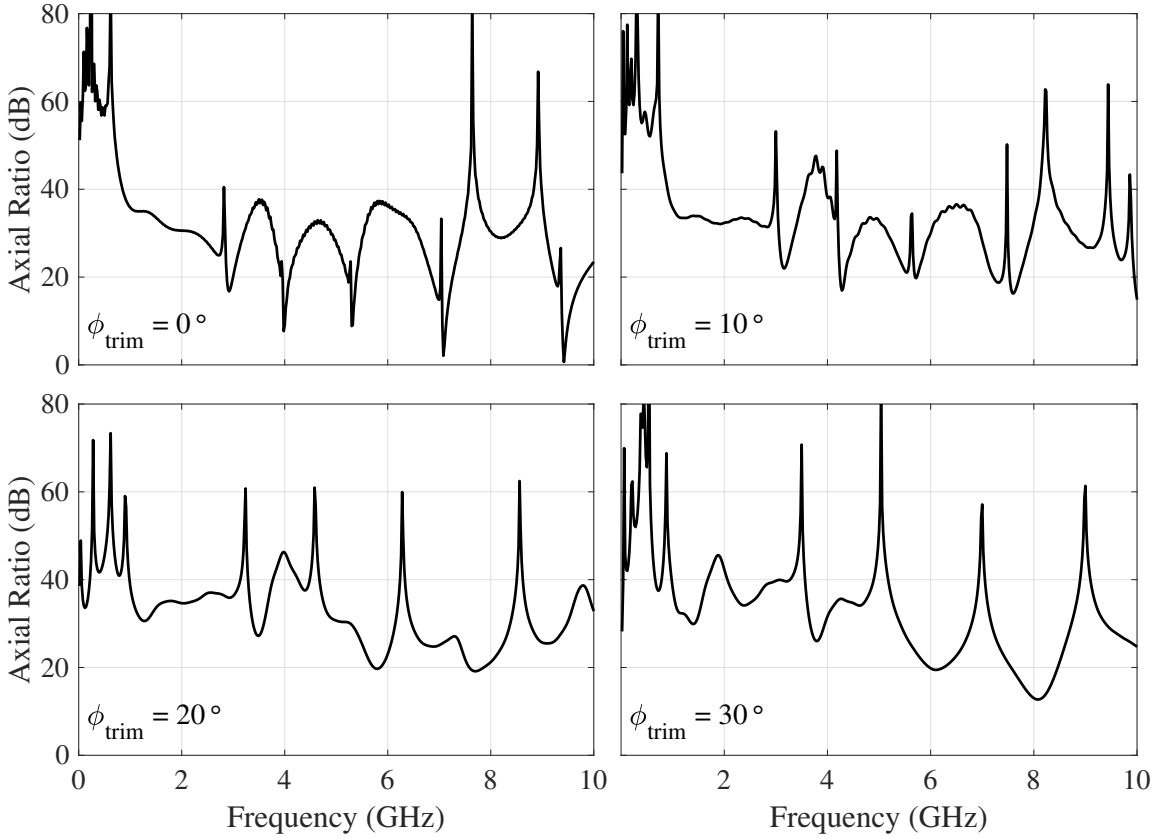

Figure 2.13: Axial Ratio (AR) of the simulated sinuous antennas with various amounts of cell trimming.

and

$$OB = \left[\frac{E_x^2 + E_y^2 - [E_x^4 + E_y^4 + 2E_x^2 E_y^2 \cos(2\Delta\Phi)]^{1/2}}{2} \right]^{1/2} . \tag{2.5}$$

In the above equations, the E_x and E_y terms represent the magnitudes of the two field components, and $\Delta\Phi$ represents their phase difference. Given this definition, an AR of ∞ dB would indicate perfect linear polarization (E_y or E_x) while an AR of 0 dB indicates circular polarization. The results in Figure 2.13 show that AR is improved (radiation is more linear) by cell ends trimming since the radiation becomes increasingly elliptical at the resonance frequencies. For example, at 7.08 GHz, the polarization is almost circular (AR = 2.089 dB) when $\phi = 0$ and is almost lineal (AR =25.62 dB) when $\phi = 20°$. Notice that significant improvement in the AR is obtained with only $10°$ of trimming and the $\phi_{trim} = 20°$ antenna gives the best result.

Figure 2.14: Trimmed sinuous antennas explored in this section: (a) sharp ends removed and cell tips trimmed ($\phi_{trim} = 20°$) on all arms, (b) sharp ends removed and cell tips trimmed ($\phi_{trim} = 20°$) on one pair of arms, and (c) sharp ends removed on all arms and cell tips trimmed ($\phi_{trim} = 20°$) on one pair of arms.

2.2.1 Ends Trimming Technique Applied to Single Pair of Arms

In an effort to better understand the benefits obtained by the sinuous cell trimming described in the previous analysis, an experiment was conducted where only one set of opposite arms were trimmed while the other two arms were not. More specifically, the motivation for this experiment is to understand whether improved performance is obtained by trimming the arms which the port is directly feeding or whether the improvement is due to having the adjacent arms trimmed. Simulated results of the three antennas shown in Figure 2.14 are analyzed in this section. The first antenna is that presented in the previous section which has all arms clipped by $20°$ as well as the sharp ends removed (Figure 2.14a). This antenna will serve as the baseline for the other two experiments. The second antenna (Figure 2.14b) is similar to the first with one pair of arms being unmodified (feed port 1). Finally, the third antenna (Figure 2.14c) is similar to the second antenna except for the sharp ends of the two full arms have also been removed.

The simulated radiated fields of the trimmed antenna and the hybrid designs are shown in Figure 2.15. From the results, it is evident that the benefits of cell trimming are not localized to the trimmed arms. Mitigation of the log-periodic resonances by ends trimming

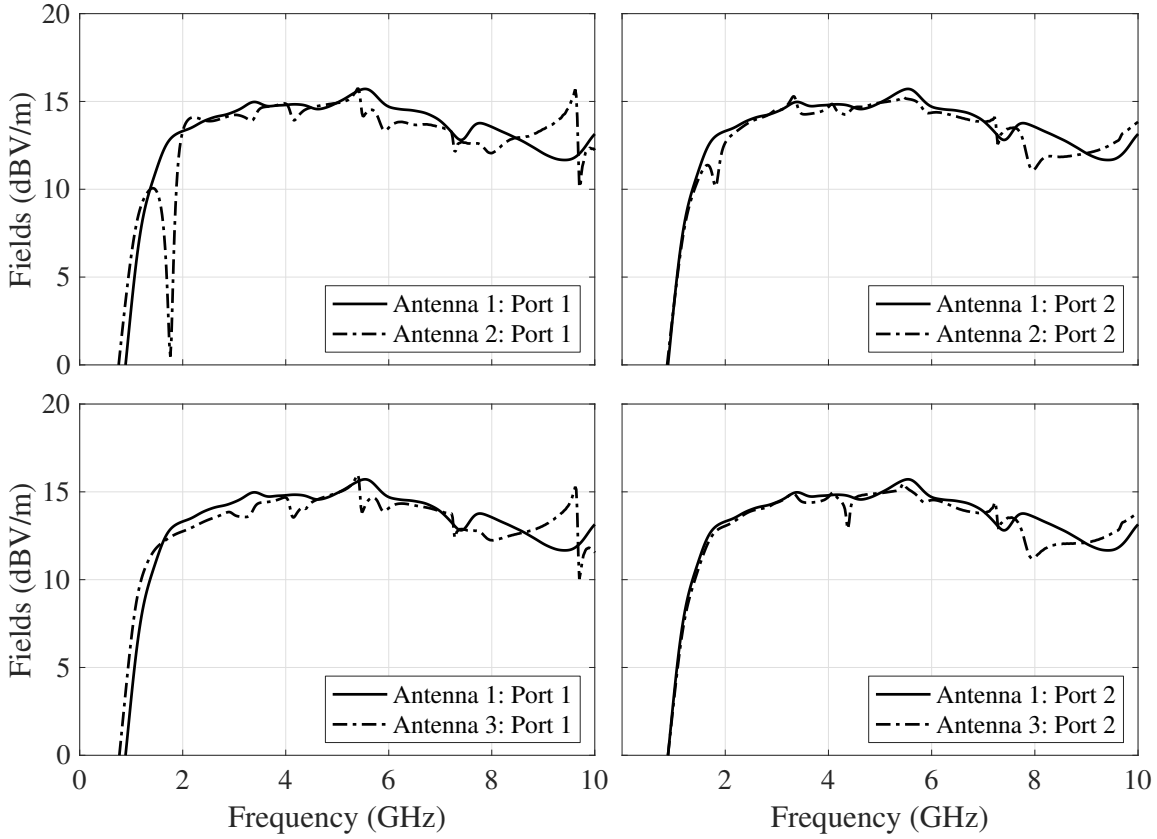

Figure 2.15: Co-polarized radiated fields at 2m (on bore-sight) from the simulated sinuous antennas with different trimming.

indicates reduced interaction of the tips with adjacent arms. Otherwise, the fields radiated from the port connected to the clipped arms should show all the same improvements as the those radiated from any port of the first antenna. Furthermore, trimming the sharp end removes only the low-frequency resonance from that specific arm, i.e., the sharp-end resonance does not seem to be related to interactions with adjacent arms.

2.2.2 Ends Trimming Technique Applied to Sinuous Antennas with Larger Angular Width

The preceding analysis was limited to sinuous antennas with $\alpha = 60°$; however, larger values for α may be desired for specific applications (e.g., lower operating frequencies) and therefore the analysis of the clipping techniques was extended to a sinuous antenna with $\alpha = 90°$. The other design parameters were kept consistent with the previous analysis

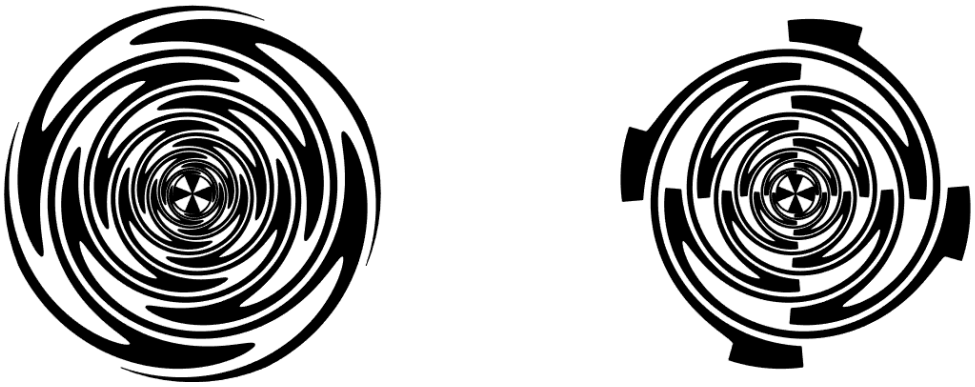

Figure 2.16: Sinuous antennas with $\alpha = 90^\circ$ investigated for the cell ends trimming analysis: (a) no trimming and (b) $\phi_{trim} = 20^\circ$ with sharp ends removed.

($P = 8$, $R_1 = 5$ cm, $\tau = 0.75$, and $\delta = 22.5^\circ$). The cell ends were then trimmed 20° ($\phi_{trim} = 20^\circ$) since the 20° case provided the best results in the previous discussion (see Figure 2.7 and Figure 2.8). The investigated $\alpha = 90^\circ$ antennas are shown in Figure 2.16.

The antenna matches are compared in Figure 2.17. As can be seen, there is a significant degradation of the antenna match when the antenna cell ends are trimmed (see also Figure 2.18). Although some degradation of the antenna match is expected, since the antenna is no longer self-complementary, the amount observed is significantly more than the $\phi_{trim} = 20^\circ$ case of the $\alpha = 60^\circ$ sinuous antenna shown in Figure 2.6. Moreover, as shown in Figure 2.19, the resonances present in the realized gain are still significant and have only been slightly reduced with the cell ends trimming. Subsequently, the radiated pulses of the trimmed antenna exhibit nearly the same amount of ringing as the untrimmed version (Figure 2.20). These results indicate that cell ends trimming does not mitigate the unintended resonances for all sinuous antenna designs.

2.2.3 Summary

While the techniques for mitigating unintended resonant modes in sinuous antennas presented in the literature have been successful to some degree, they destroy the self-complementary nature of the antenna, which reduces both elegance and frequency inde-

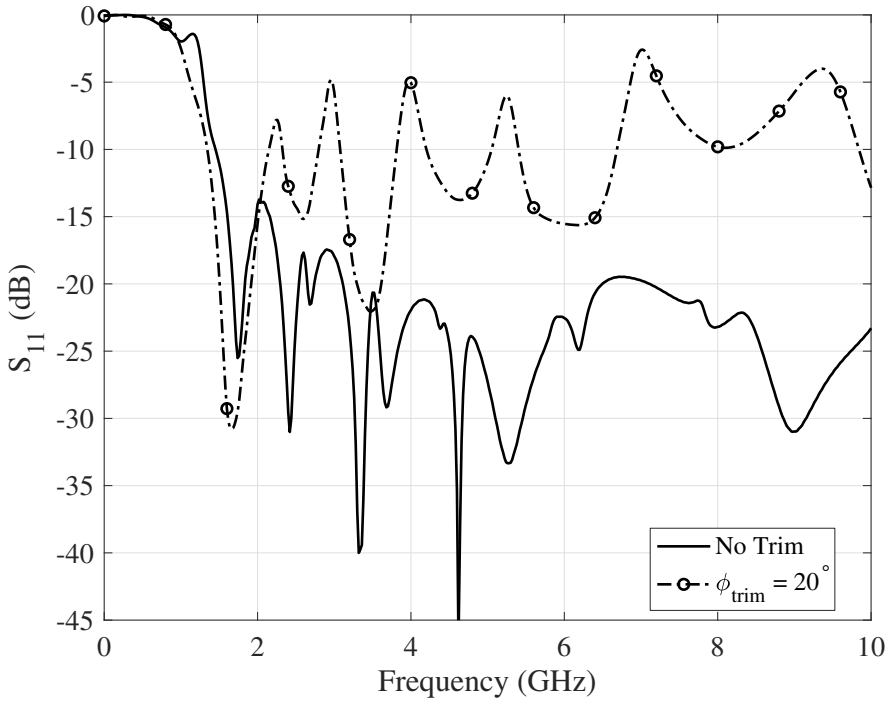

Figure 2.17: Simulated match for the $\alpha = 90°$ sinuous antennas with and without cell trimming. Trimming the cells results in significant degradation in the match.

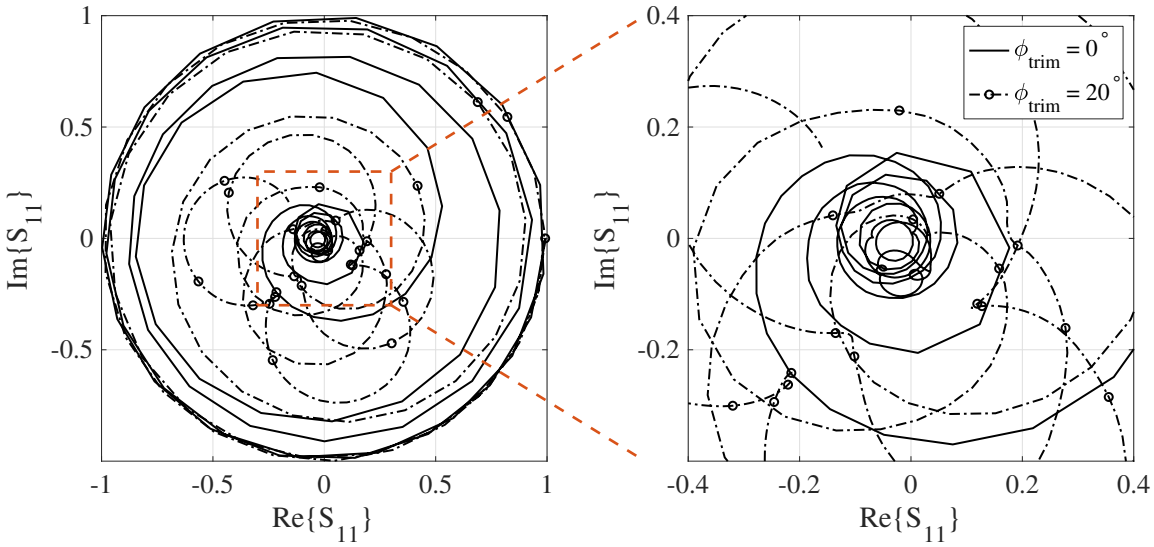

Figure 2.18: Simulated match for the $\alpha = 90°$ sinuous antennas with and without cell trimming plotted on the complex plane.

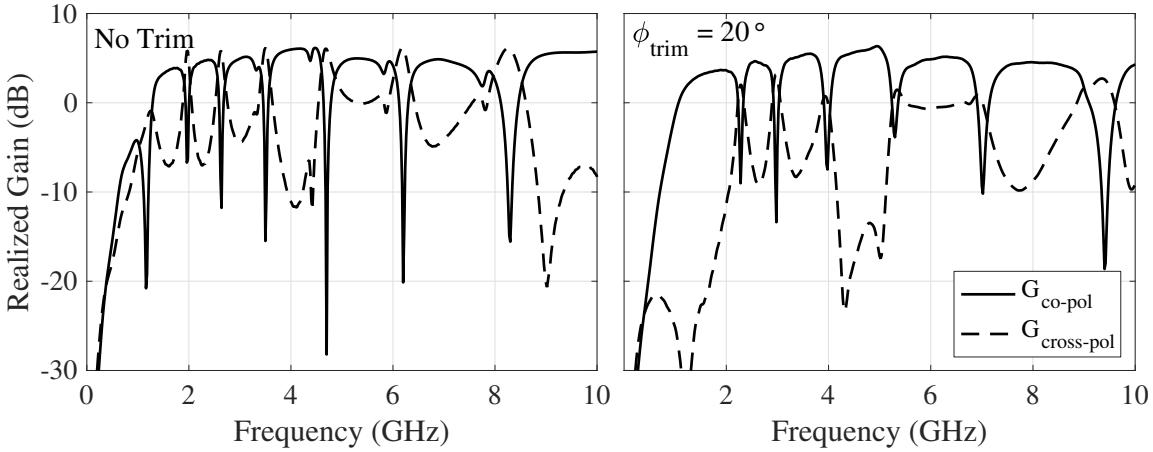

Figure 2.19: Bore-sight realized gain from the simulated sinuous antennas with $\alpha = 90°$.

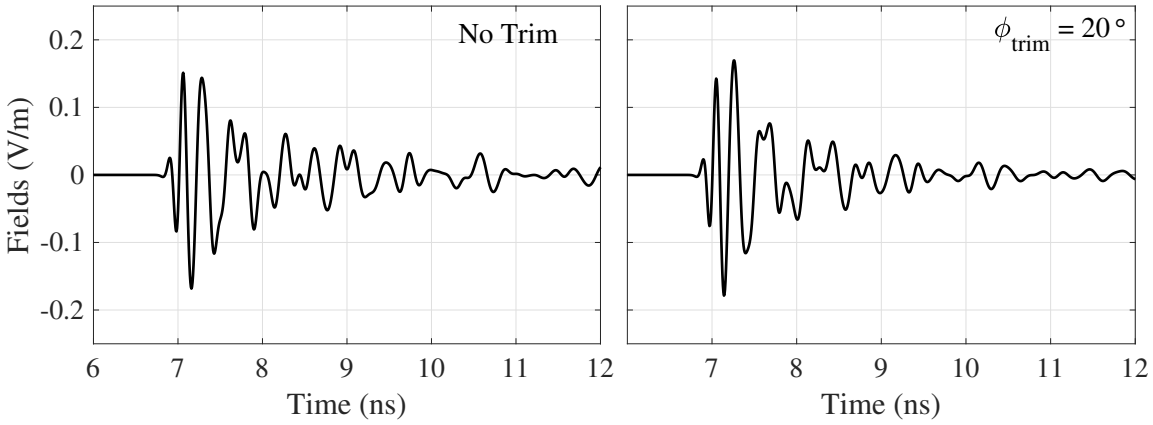

Figure 2.20: Time-domain radiated pulses at 2m (on bore-sight) from the simulated sinuous antennas with $\alpha = 90°$.

pendence. Furthermore, additional experiments indicate that trimming the cell ends is not a direct solution to the log-periodic resonances problem. Rather, as will be discussed in the next section, the cell ends trimming technique presented in [37, 51] is only an approximation for a sinuous antenna with a smaller angular width (α). The evidence points to mutual interaction between adjacent antenna arms as the source of the unintended resonances.

2.3 Parametric Study

In an effort to understand the relationship between the observed log-periodic resonances and the sinuous antenna design parameters, both the expansion ratio (τ) and the angular

width (α) were varied, and the performance of the subsequent sinuous antenna designs examined.

For the log-periodic sinuous antenna, the inner-most radius of the antenna (where the feed must be implemented) may be defined as

$$R_{feed} = R_1 \tau^P. \tag{2.6}$$

From this relationship, it is evident that given a fixed inner and outer antenna radius, the number of cells P is determined entirely by the expansion ratio τ and *vice versa*. Continuing with this set of assumptions, i.e., a log-periodic sinuous antenna with fixed inner and outer radii, the following bounds for τ and P are established:

$$R_{feed}/R_1 \leq \tau < 1 \tag{2.7}$$

and

$$1 \leq P < \infty. \tag{2.8}$$

However, a minimum value of 0.65 is recommended for τ in order to maintain pattern uniformity [12]. While larger τ is attributed to better patterns and increased operating bandwidth [12, 33, 39], keeping τ small provides some advantages such as better power handling and easier fabrication due to thicker traces [48, 39]. For this study, the inner and outer radii were selected to be 0.5 and 5 cm respectively ($R_{feed}/R_1 = 0.1$). The values of τ, and subsequently P, selected for study are listed in Table 2.1 along with the other design parameters. The parameter α was also varied with all other parameters remaining constant.

As shown in Section 1.2, the parameter α controls the angular width of the sinuous antenna arm, i.e., the wrapping of the arms. In Section 2.2, the log-periodic resonances were attributed to mutual coupling between adjacent arms. In this study, the value of α is decreased from 65° to 35° in an effort to reduce interactions between adjacent arms. An

Table 2.1: Sinuous antenna design parameters for parametric study.

Parameter	Value(s)
R_1	5 cm
R_{in}	0.5 cm
P	8, 12, 16
τ	0.75, 0.8254, 0.866
α	35°, 40°, 45°, 50°, 55°, 60°, 65°, 90°
δ	22.5°

additional sample of α at 90° is also analyzed. The parametric sweep of α is repeated for three different values of τ which are summarized in Table 2.1. The sinuous antenna designs produced by the different parameters are summarized graphically in Figure 2.21 through Figure 2.23.

The simulated boresight realized gain of the antennas are presented in Figure 2.24 through Figure 2.26. Inspection of the gains indicates that the log-periodic resonances may be entirely mitigated by reducing α. Note that the sharp end was not removed for the antennas considered and the resulting dip in gain at low frequency (approximately 2 GHz) is present in all the data. Additionally, modifying τ slightly impacts the results as values larger than 0.75 show similar resonance mitigation with slightly larger values of α. Further, improvements in group delay (increased smoothness) and AR (better linear polarization purity) were also observed with decreased α and are shown in Figure 2.27 and Figure 2.28 respectively.

The mutual coupling (S_{21}) for the sinuous antennas considered is displayed in Figure 2.29. From the results, it is evident that spikes in mutual coupling corresponding to the resonances are present in the antennas with larger values of α but decrease as α is decreased. This further indicates a relationship between the unintended resonant modes and mutual coupling effects. A secondary observation, not related to the resonances, is that the mutual coupling for the 12 and 16 cell antennas tends to be slightly larger than the 8 cell case. This is not surprising since increasing τ (more cells) results in smaller gaps between adjacent arms (see Figure 2.21 through Figure 2.23). Note that the S_{21} simulation results

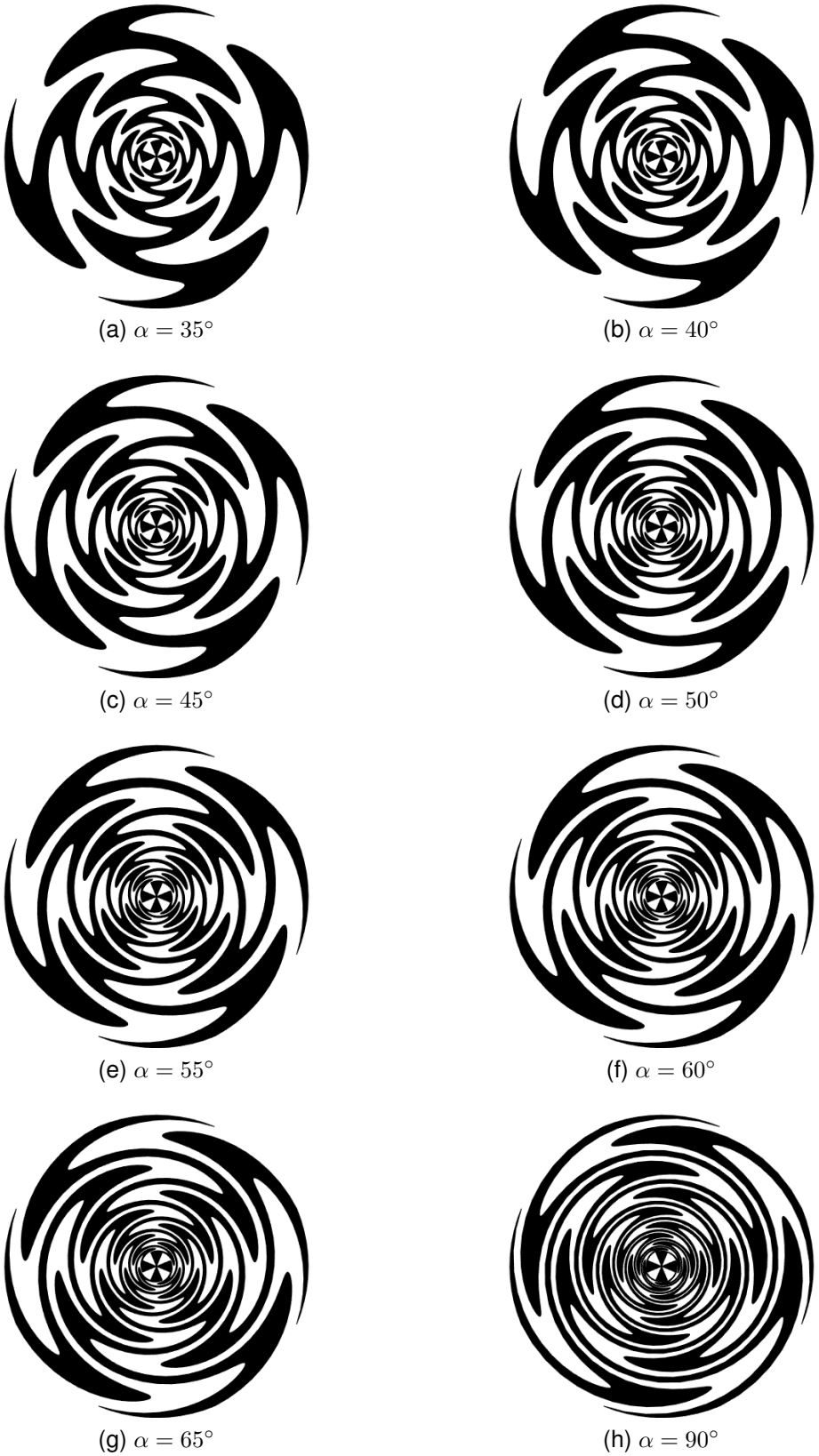

(a) $\alpha = 35°$ (b) $\alpha = 40°$

(c) $\alpha = 45°$ (d) $\alpha = 50°$

(e) $\alpha = 55°$ (f) $\alpha = 60°$

(g) $\alpha = 65°$ (h) $\alpha = 90°$

Figure 2.21: Sinuous antennas simulated for α parameter sweep analysis ($\tau = 0.75$).

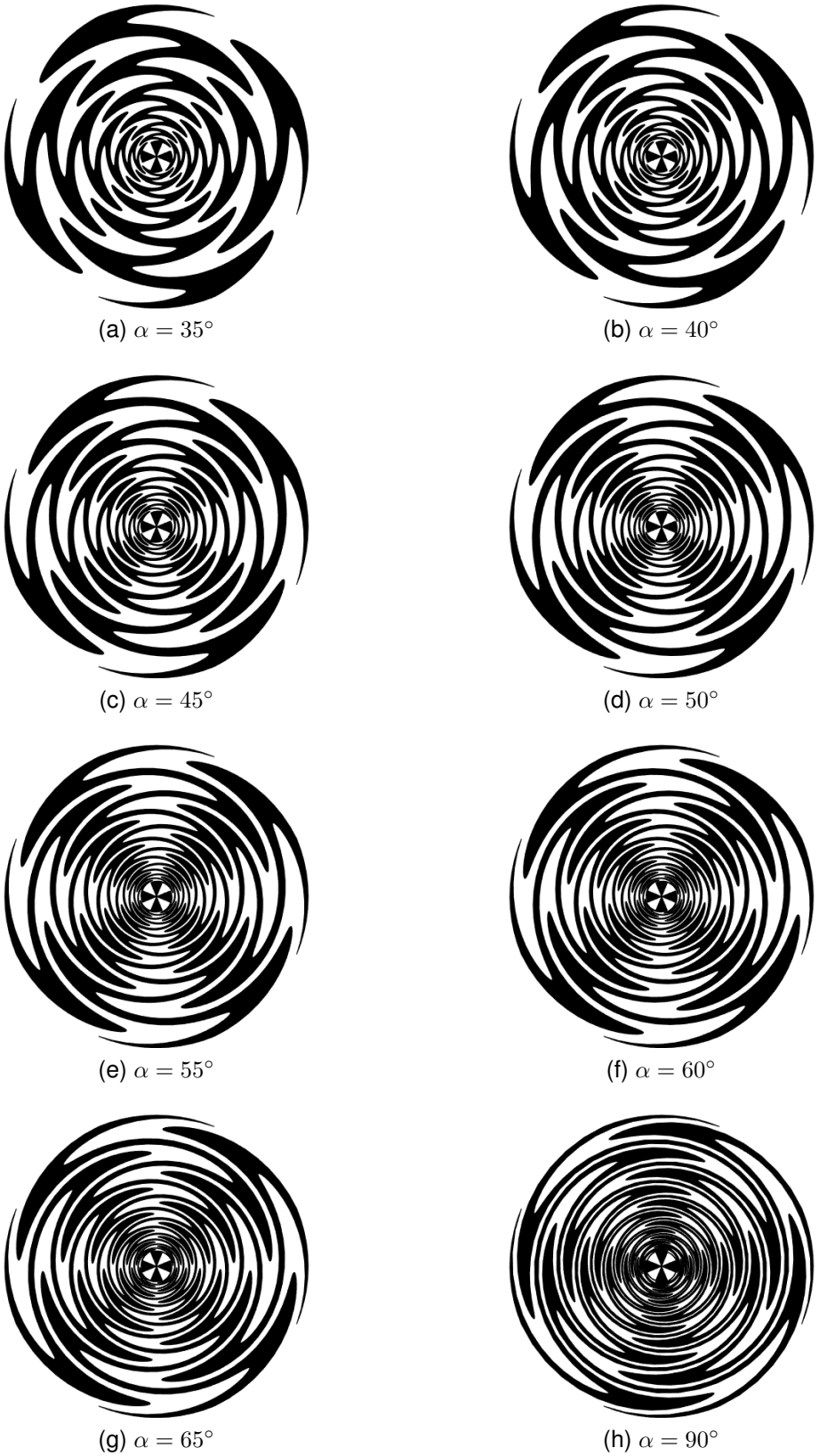

(a) $\alpha = 35°$ (b) $\alpha = 40°$

(c) $\alpha = 45°$ (d) $\alpha = 50°$

(e) $\alpha = 55°$ (f) $\alpha = 60°$

(g) $\alpha = 65°$ (h) $\alpha = 90°$

Figure 2.22: Sinuous antennas simulated for α parameter sweep analysis ($\tau = 0.8254$).

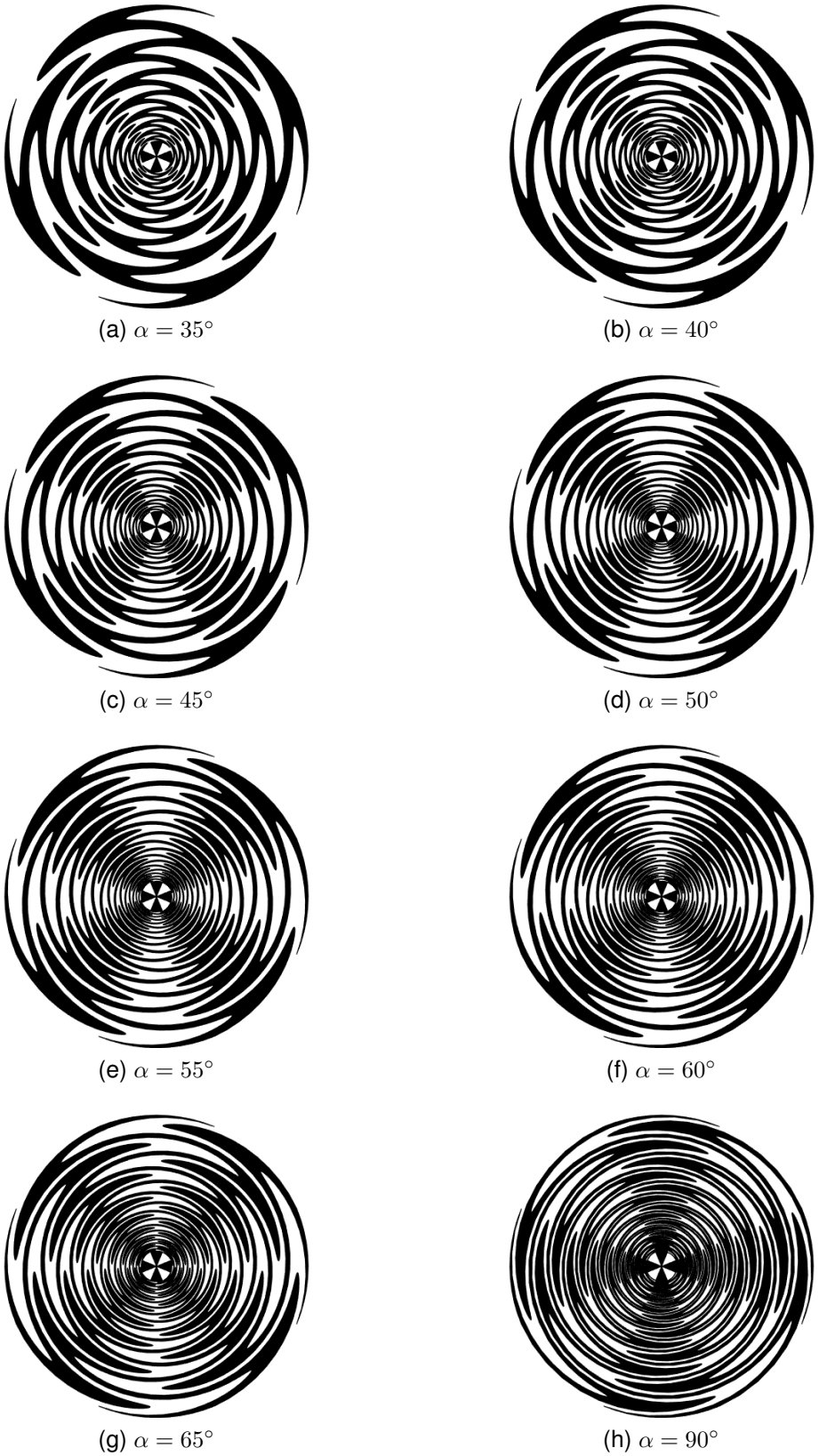

(a) $\alpha = 35°$ (b) $\alpha = 40°$

(c) $\alpha = 45°$ (d) $\alpha = 50°$

(e) $\alpha = 55°$ (f) $\alpha = 60°$

(g) $\alpha = 65°$ (h) $\alpha = 90°$

Figure 2.23: Sinuous antennas simulated for α parameter sweep analysis ($\tau = 0.866$).

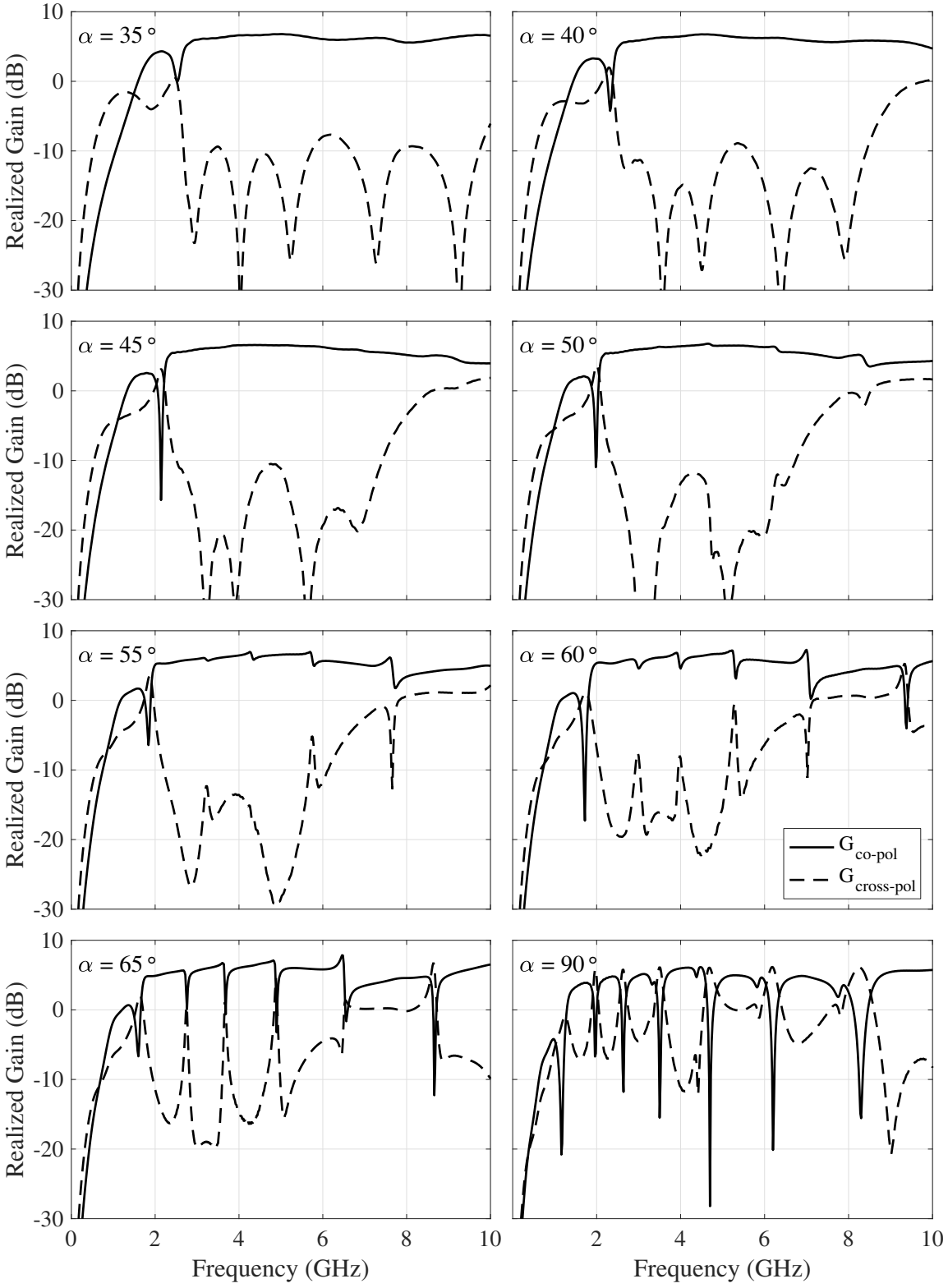

Figure 2.24: Boresight realized gain of the simulated eight-cell ($\tau = 0.75$) sinuous antennas with different α values.

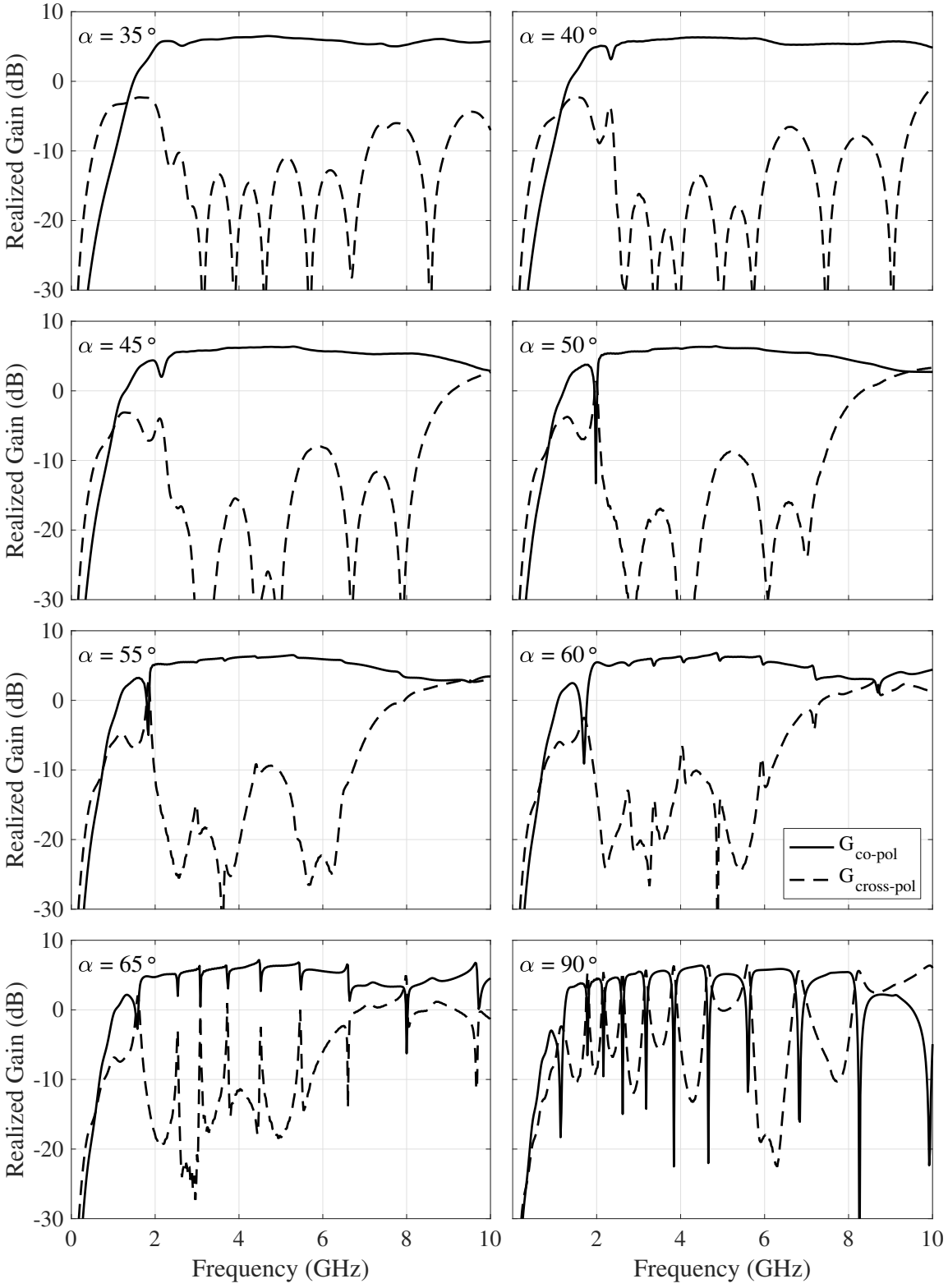

Figure 2.25: Boresight realized gain of the simulated 12-cell ($\tau = 0.8254$) sinuous antennas with different α values.

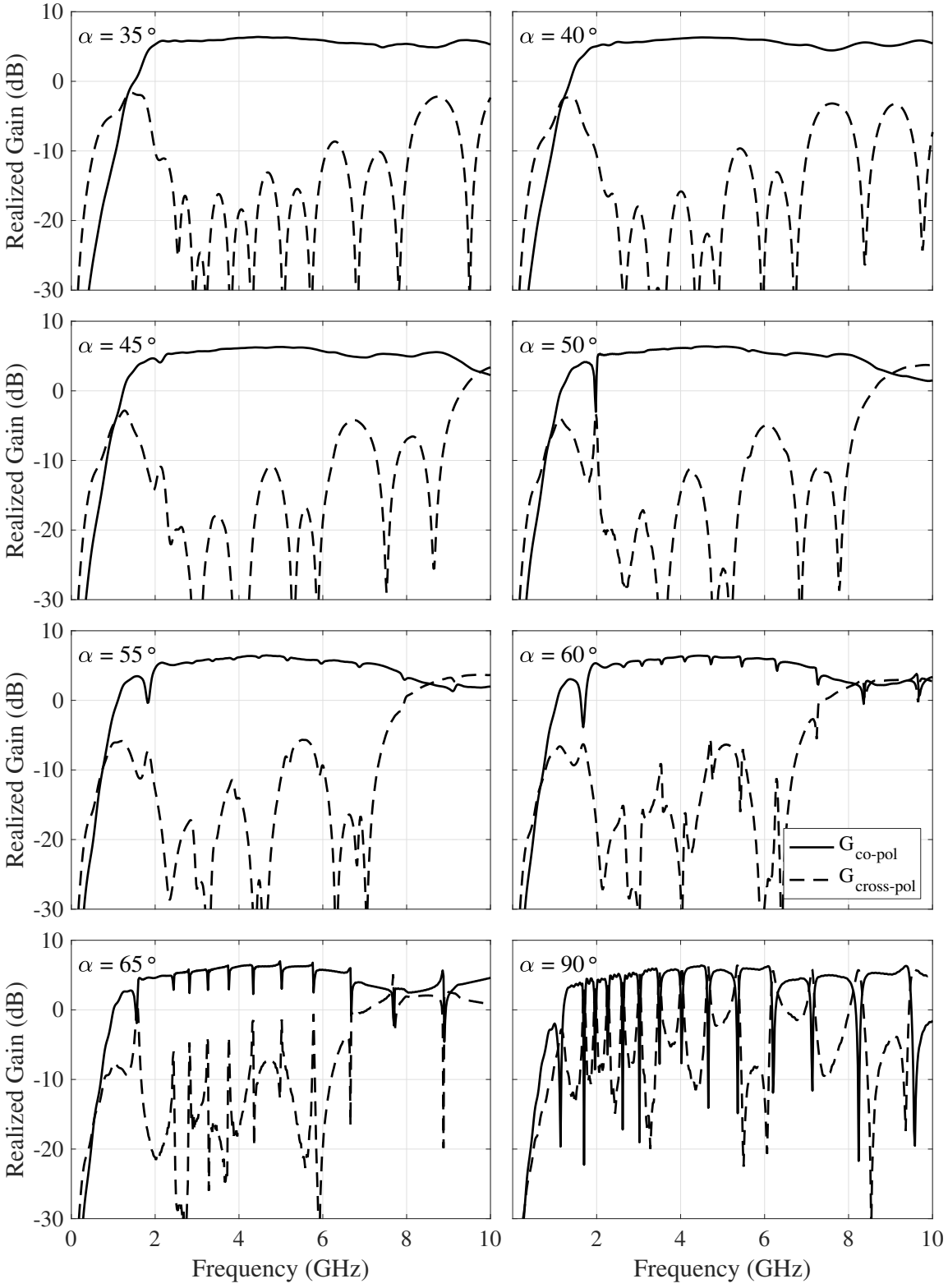

Figure 2.26: Boresight realized gain of the simulated 16-cell ($\tau = 0.866$) sinuous antennas with different α values.

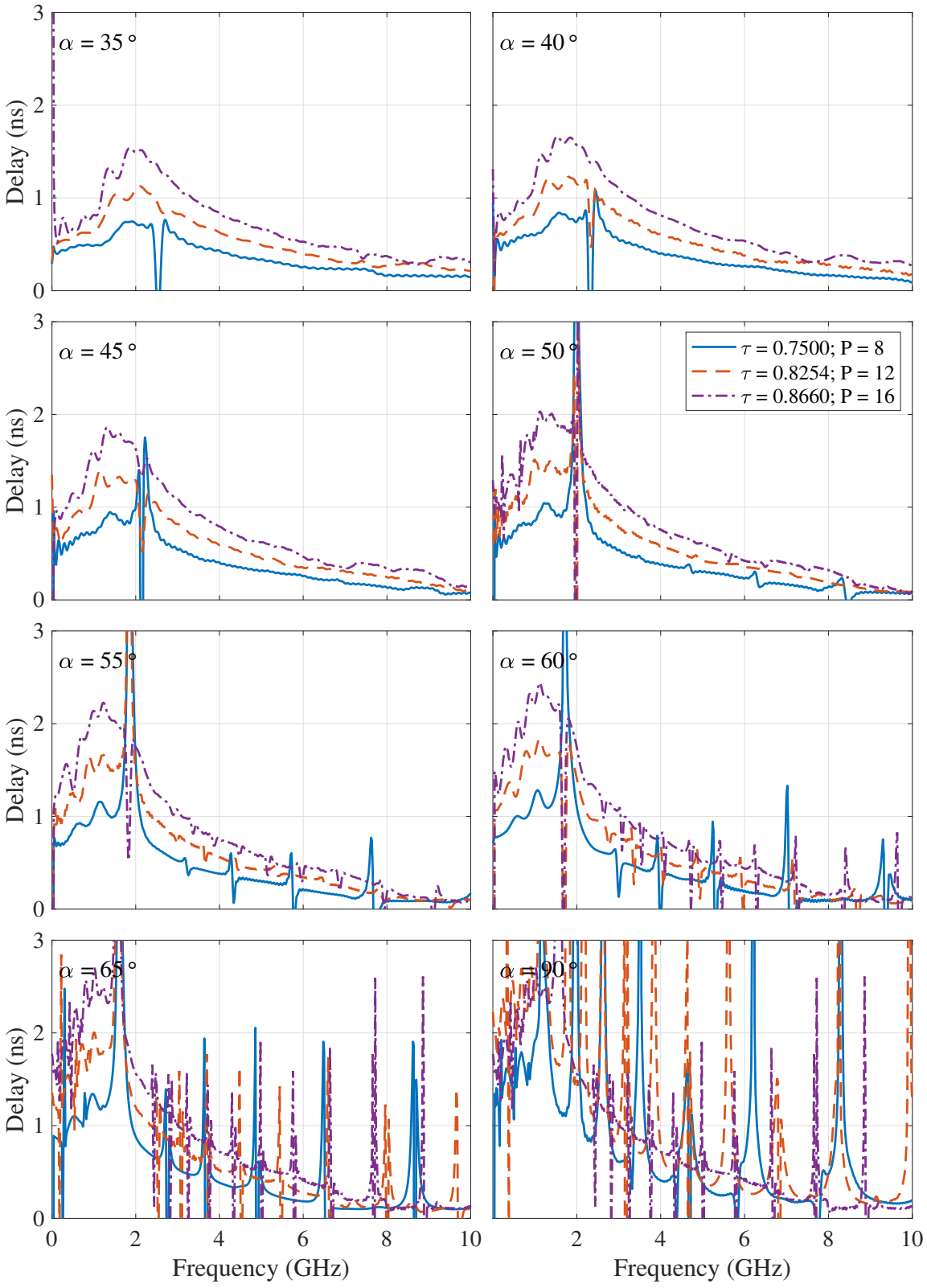

Figure 2.27: Group delay of fields radiated from the sinuous antennas simulated.

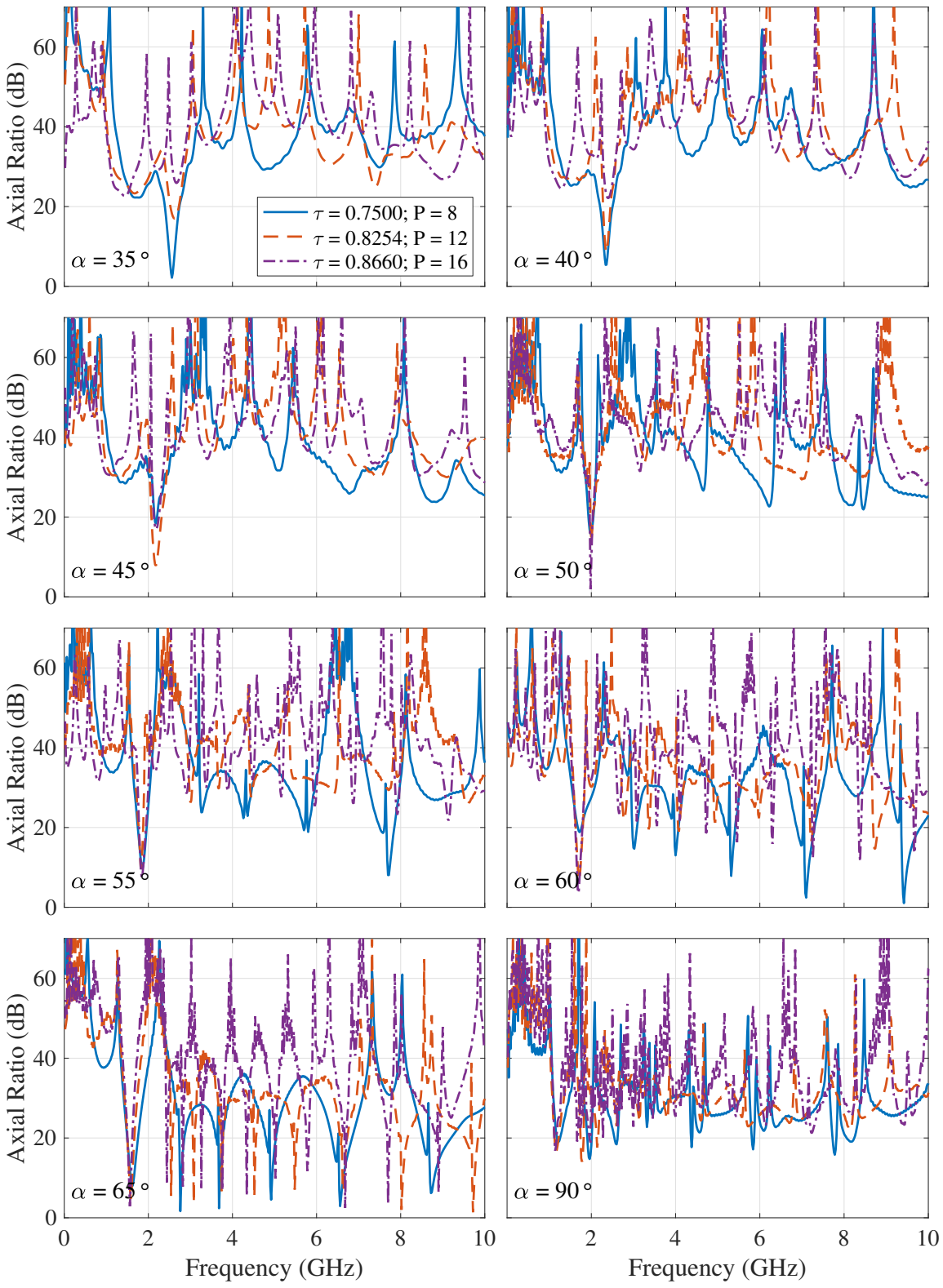

Figure 2.28: AR of fields radiated from the simulated sinuous antennas.

were produced with the CST FEM frequency-domain solver (see Appendix A).

With a large amount of data accumulated for the parametric study, it was desired to develop a *gain-smoothness metric* for quantifying the effectiveness of each parameter combination at mitigating the log-periodic resonances. The metric M is the root-mean-squared error between the co-polarized realized gain and its N-point simple moving average (see Figure 2.30) as

$$M = \sqrt{\frac{1}{N}\sum_{f_n=f_s}^{f_e}\left(|G(f_n)| - \frac{1}{N}\sum_{k=n-N/2}^{n+N/2}|G(f_k)|\right)^2}, \tag{2.9}$$

where in this case $f_{start} \approx 3$ GHz, $f_{stop} = 10$ GHz and $N = 31$ (600 MHz wide). The actual starting frequency was adjusted for each design to ensure all the log-periodic resonances were included and not the resonance due to the sharp end. The results of the metric are shown in Figure 2.31 and indicate that the gain *smoothness* converges at approximately $\alpha = 45^\circ$ for all values of τ.

Decreasing α to $\leq 45^\circ$ may produce smooth radiation over wide bandwidths; however, the overall length of the sinuous antenna arms is decreased, thus negatively impacting the low-frequency operation of the antenna. The lowest frequency of operation is inversely proportional to α by the following approximate relation

$$f_{lo} = \frac{v}{4R_T(\alpha + \delta)}, \tag{2.10}$$

where v is the wave velocity, and α and δ are specified in radians [12]. For applications desiring smooth gain in addition to low-frequency operation, $\alpha = 50^\circ$ may be used with a larger τ. The results in Figure 2.31 indicate $\tau = 0.825$ to be optimal. Although, other performance trade-offs must be considered with larger values of τ such as increased dispersion [88] and conductor losses [33].

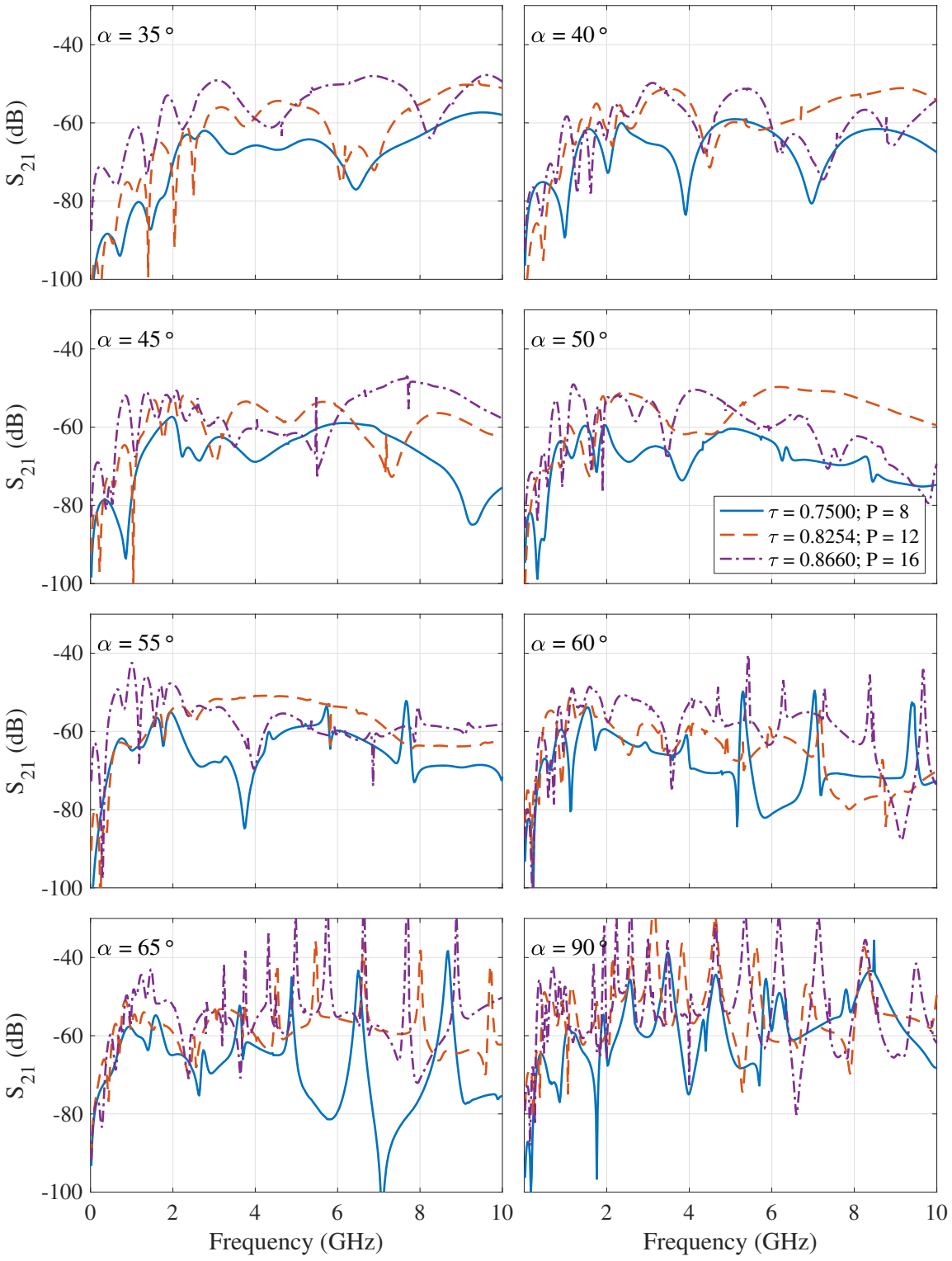

Figure 2.29: Mutual coupling (S_{21}) for the simulated sinuous antennas.

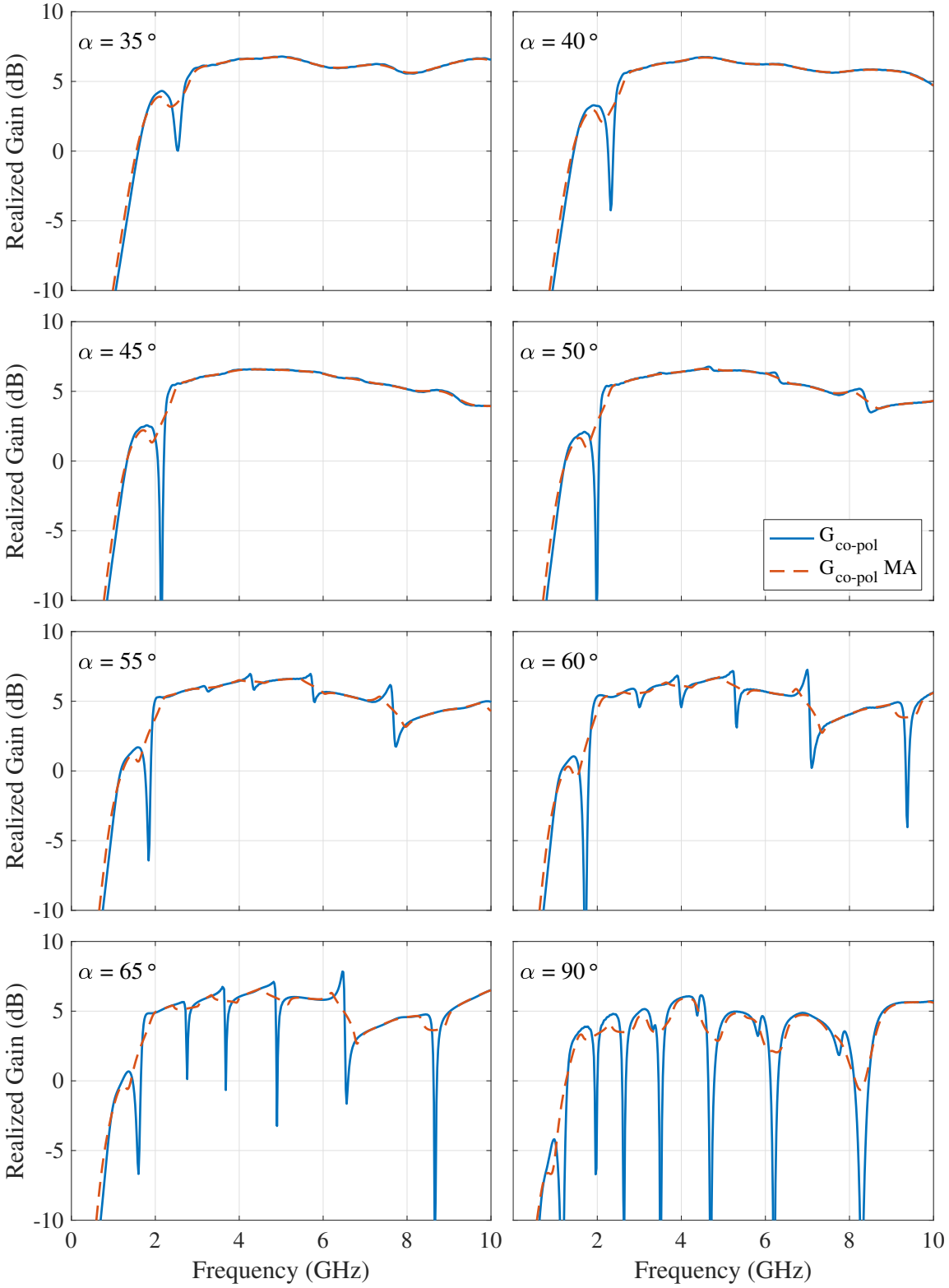

Figure 2.30: Comparison of eight-cell sinuous antenna boresight gain and its simple moving average ($N = 31$ or 600 MHz wide) used for computing the *gain-smoothness metric*.

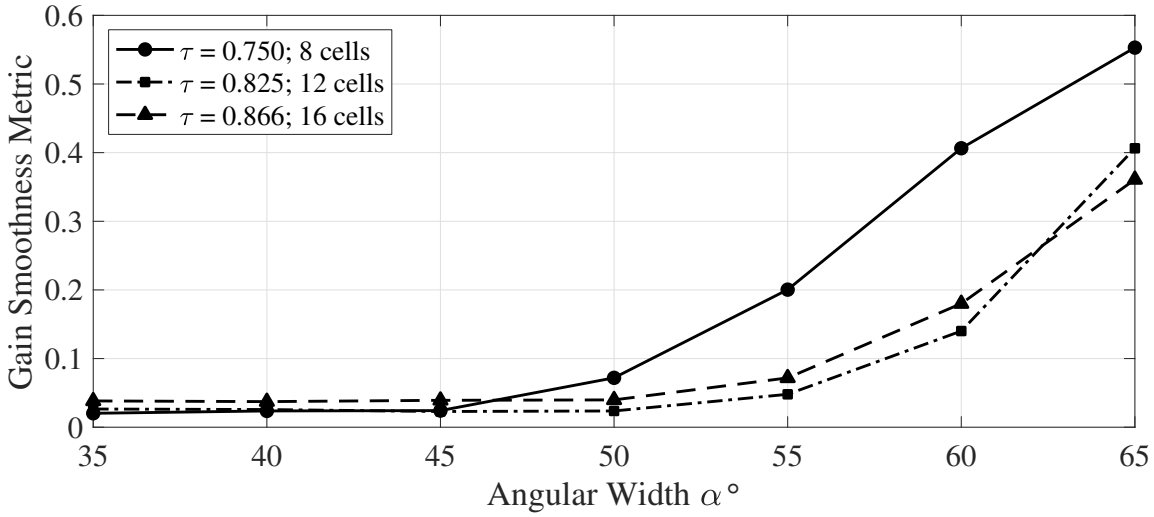

Figure 2.31: Gain-smoothness metric M computed for the parametric study, which shows distortion of gain over frequency increases with α. For this study, the value of α was swept from 35° to 65° in 5° increments for three values of τ (0.75, 0.825, and 0.866) while keeping all other design parameters constant.

2.4 Outer Truncation

Traditionally, sinuous antennas have been truncated in a circle of radius R_T applied at the end of the last cell, i.e., $R_T = R_1$. This truncation method produces "sharp ends" at the outer radius of the antenna, as shown in Figure 2.32a, that resonate when their length is approximately $\lambda/2$ and results in the drop in gain observed at 1.7 GHz in Figure 2.2. While the severity of this resonance is reduced by choosing smaller values of α (see Figure 2.24–2.26), the effects are not removed completely and may be undesirable for some applications. In [64, 58, 53, 62, 69, 37, 22, 51] this resonance is mitigated by clipping off the sharp ends (illustrated in Figure 2.32b); however, a new technique is presented here that simply changes the circular truncation radius R_T to the tip of the outermost cell (i.e., $R_T = \sqrt{\tau}R_1$), as illustrated by the antenna in Figure 2.32c. This technique mitigates the resonance as the sharp ends are no longer produced. Additionally, the self-complementary nature of the antenna is maintained.

Figure 2.32: Sinuous antenna truncation methods: (a) traditional circular truncation which produces sharp ends, (b) sharp ends removed, and (c) circular truncation moved to the outer cell tip.

2.4.1 Clipping Truncation Method

Removal of the sharp ends by clipping has been implemented in various ways, e.g., curved [64] vs. straight [51] clip. The simple straight clipping shown in Figure 2.32b can be described mathematically as follows. The sharp end only occurs on the outermost cell; therefore we can set $p = 1$ in Equation 1.1 which gives

$$\phi = \alpha \sin\left[\frac{\pi \ln(r/R_1)}{\ln \tau}\right] \pm \delta. \tag{2.11}$$

It is desired to trim the part of the arm that occurs after the bend in the outermost cell, i.e., the value of r where it is greater than the value that causes the argument of the $\sin$ function to be equal to $\pi/2$. Setting the argument of the $\sin$ function equal to $\pi/2$ and solving for r gives

$$r = \sqrt{\tau} R_1. \tag{2.12}$$

The sharp end extends from the angle $\alpha - \delta$. Therefore, we can clip the sharp end by removing the points where both the angle ϕ is less than $\alpha - \delta$, and r is larger than $\sqrt{\tau} R_1$.

While this technique has been shown in the literature to be successful at preventing a low-frequency drop in gain, it reduces the self-complementary nature of the sinuous anten-

nas as well as requiring an additional empirical design step.

2.4.2 Novel Truncation Method

An alternative method for the truncation of sinuous antennas that does not produce resonant sharp ends is shown in Figure 2.32c. In this method, the circular truncation is moved to the tip of the outermost cell thereby preventing the sharp end while maintaining self-complementariness after truncation. This is accomplished by setting the truncation radius R_T to $\sqrt{\tau}R_1$ instead of R_1.

Simulated co-pol radiated fields from an eight-cell $\alpha = 60^\circ$ sinuous antenna truncated by the traditional method with sharp ends (Figure 2.32a), traditional with sharp ends clipped (Figure 2.32b), and the novel tip truncation method (Figure 2.32c) are presented in Figure 2.33. The results show both methods for truncating the antenna without sharp ends successfully mitigate the dip in radiation caused by the resonance resulting in an $\sim$ 5 dB improvement. However, the low-frequency fields of the novel tip truncated sinuous antenna is lower. This is due to the reduction in antenna size by moving the truncation inward on the antenna which results in less usable bandwidth at low-frequency. In order to maintain the same outer radius, and thus similar low frequency performance, as a traditionally truncated sinuous antenna, τ and R_1 must be appropriately chosen.

2.5 Improved Design

Utilizing the design guidance developed herein, a sinuous antenna was developed to produce smooth radiation over UWB frequency. The value of α is chosen as 45° in order to prevent the log-periodic resonances while the outer region is truncated by the new method proposed in Section 2.4. Both τ and R_1 have been adjusted, 0.7628 and 5.72 cm respectively, for both the truncation radius and inner feed radius to be equal to that of the reference design[1], i.e., $R_T = R_1^{ref} = 5$ cm and $R_{in} = R_{in}^{ref} = 0.5$ cm. The number of cells P is

[1] The reference was selected to be the sinuous antenna used to illustrate the problem of the resonances at the beginning of the chapter. It has the following design parameters: $R_1 = 5$ cm, $P = 8$, $\tau = 0.75$, $\alpha = 60^\circ$,

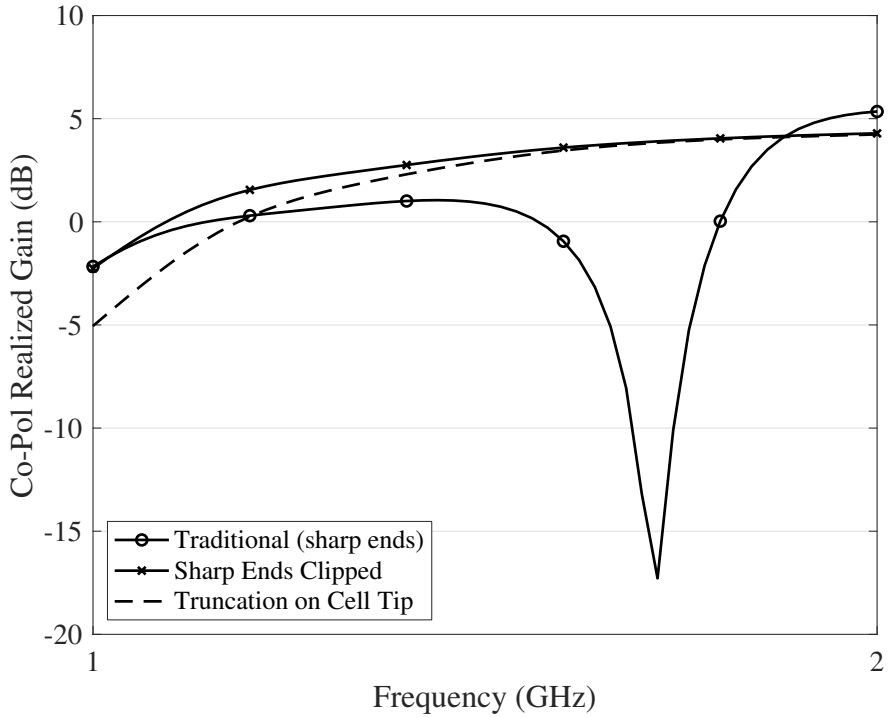

Figure 2.33: Comparison of co-polarized radiation at low frequency for sinuous antennas ($\alpha = 60^\circ$ and $\tau = 0.75$) with different outer truncation methods applied.

increased by one to have the same number of complete cells as the reference antenna when the circular truncation is applied to the outermost cell tip. The modified expansion ratio τ was computed by

$$\tau = \left(\frac{R_{in}}{R_T}\right)^{\left(P-\frac{1}{2}\right)^{-1}}, \tag{2.13}$$

which allowed R_1 to be calculated as $R_T/\sqrt{\tau}$. Although for practical designs such scaling may not be necessary, it was important for comparison to have both radii match. The antenna, referred to as the improved design, is illustrated in Figure 2.34c. It should be noted that a traditionally truncated $\alpha = 45^\circ$ sinuous with the sharp ends removed (see Section 2.4.1) could have also been used to provide similar resonance mitigation; however, a fully self-complementary design was desired. Furthermore, from the results presented in Figure 2.31, one might have based the improved design on the 12-cell ($\tau = 0.825$) antenna with 50° angular width; however, for comparison purposes, particularly in the time-domain,

and $\delta = 22.5^\circ$.

Figure 2.34: Sinuous antenna resonance mitigation methods: (a) traditional circular truncation which produces unintended resonant modes, (b) trimming technique proposed in [37], and (c) improved design developed for this work.

the improved design was kept as close to the reference as possible.

For further comparison, the reference antenna was trimmed according to the methods discussed in Section 2.2 (shown in Figure 2.5c) in order to mitigate the resonances. This required the removal of the sharp ends via clipping as well as a 20° trim of all the sinuous cell tips. This antenna is compared against the reference as well as the improved design in the following analysis. The trimmed antenna is compared visually to the traditional and improved versions in Figure 2.34.

2.5.1 Frequency-Domain Analysis

The simulated boresight co-polarized realized gains of the three antennas are shown in Figure 2.35. The results show that the improved design successfully mitigates both the log-periodic and truncation resonances while producing a similar (sometimes higher) gain. The resonance at 1.7 GHz was mitigated by the new truncation method, while the log-periodic resonances were mitigated by the selection of α. In comparison, the trimmed design is also able to mitigate the resonances, but the realized gain is not as smooth. Similarly, the group delay is significantly smoother with the removal of the resonances as shown in Figure 2.36. The simulated match (S_{11}) of the antennas to an ideal 267 Ω port is shown in Figure 2.37. The different designs all have $S_{11} \leq -10$ dB starting before 2 GHz with

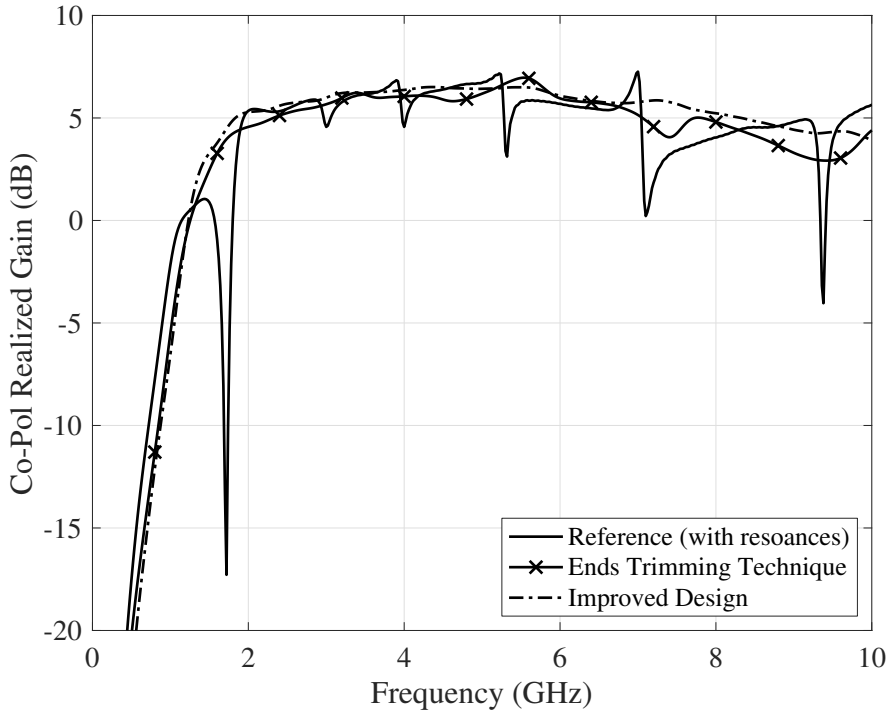

Figure 2.35: Comparison of co-polarized realized gain for traditional sinuous with resonances and modified versions that mitigate the resonances.

the improved design having an overall better match than the trimmed version–which is no longer self-complementary due to the trimming.

2.5.2 Time-Domain Analysis

Distortion in the gain of the sinuous antenna—due to the resonances—ultimately results in ringing when the antenna is used in pulsed type applications. Ringing can be particularly troublesome for close-in sensing applications such as GPR. Examination of the radiated fields in the time domain is necessary to determine the extent of such ringing. Figure 2.38 shows the radiated pulses at 2 m for the sinuous antennas investigated when driven by a UWB pulse. The input pulse used is a differentiated Gaussian with 1 V peak voltage and maximum spectral energy at 3.2 GHz (see Appendix B). The radiated pulses shown in Figure 2.38 do not have the shape of a differentiated Gaussian pulse (see Figure B.2), this is due to dispersion. Compensation of dispersion in sinuous antennas will be discussed in

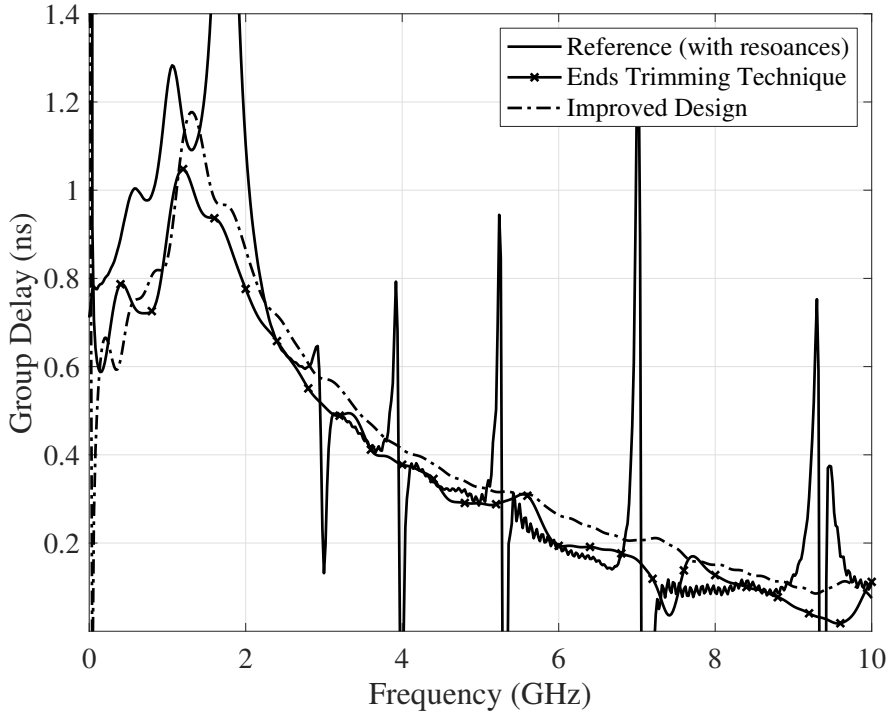

Figure 2.36: Comparison of group delay for traditional sinuous with resonances and modified versions that mitigate the resonances.

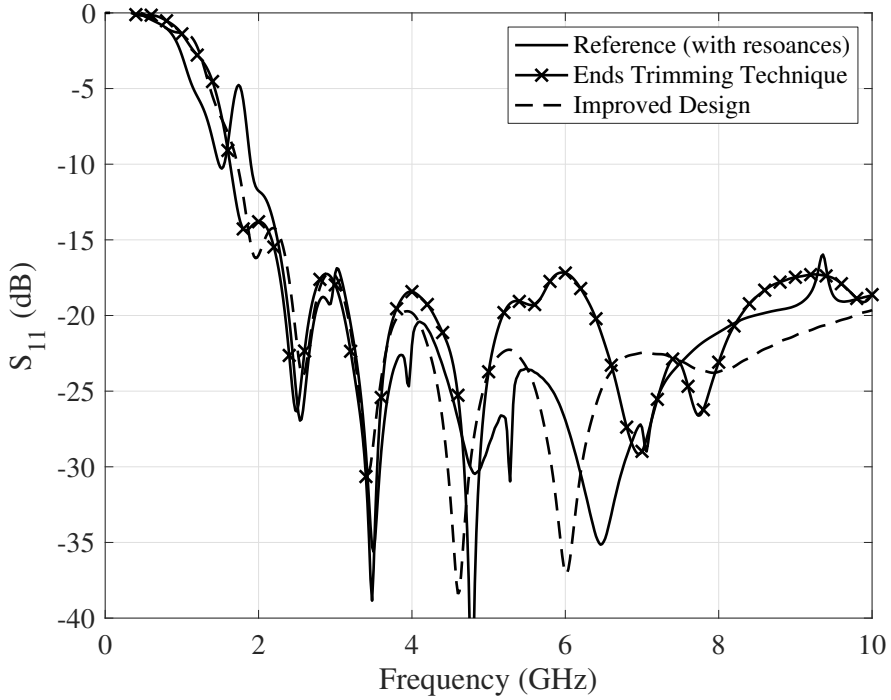

Figure 2.37: Comparison of match (S_{11}) for traditional sinuous with resonances and modified versions that mitigate the resonances.

Chapter 3.

As shown in Figure 2.38, the resonances present in the reference antenna radiation produce high-frequency ringing following the pulse in time. Mitigation of the frequency domain resonances eliminates the time domain ringing, as illustrated by the improved design. Note that the improved design has a slightly different pulse shape, compared to the reference design, due to the change in τ. The improved design is able to produce smooth radiation merely by selecting the appropriate angular width and outer truncation.

2.6 Measurements

In order to provide experimental validation for the previous analysis conducted through simulation, both the reference and improved designs (described above) were fabricated and measured.

2.6.1 Antenna Fabrication

The constructed antennas were produced by an LPKF PCB milling machine [89] out of 0.062" Rogers RT/duroid® 5880 laminate (0.5 oz. copper clad). The 5880 material has a very low loss (tanδ of 0.0009 at 10 GHz) and a relative permittivity ε_r of 2.20 [90]. The fabricated antennas are shown in Figure 2.40. As can be seen, each set of opposing sinuous arms was placed on opposite sides of the substrate, which simplified feeding the antennas. Since linear polarization was desired for the validation measurements, only a single pair of arms was fed by a tapered microstrip balun while the other pair was terminated with a 215 Ω chip resistor [60, 79]. Simulation results showed the presence of the substrate lowered the input impedance to approximately 215 Ω (averaged over the band). The constructed balun started as an unbalanced 50 Ω microstrip which was then tapered over a 90 mm length to a balanced 215 Ω parallel stripline. The top trace was tapered linearly, while an exponential taper was used for the ground plane (pictured in Figure 2.40). A diagram of the balun is presented in Figure 2.39. An SMA edge connector fed the microstrip. Triangular braces

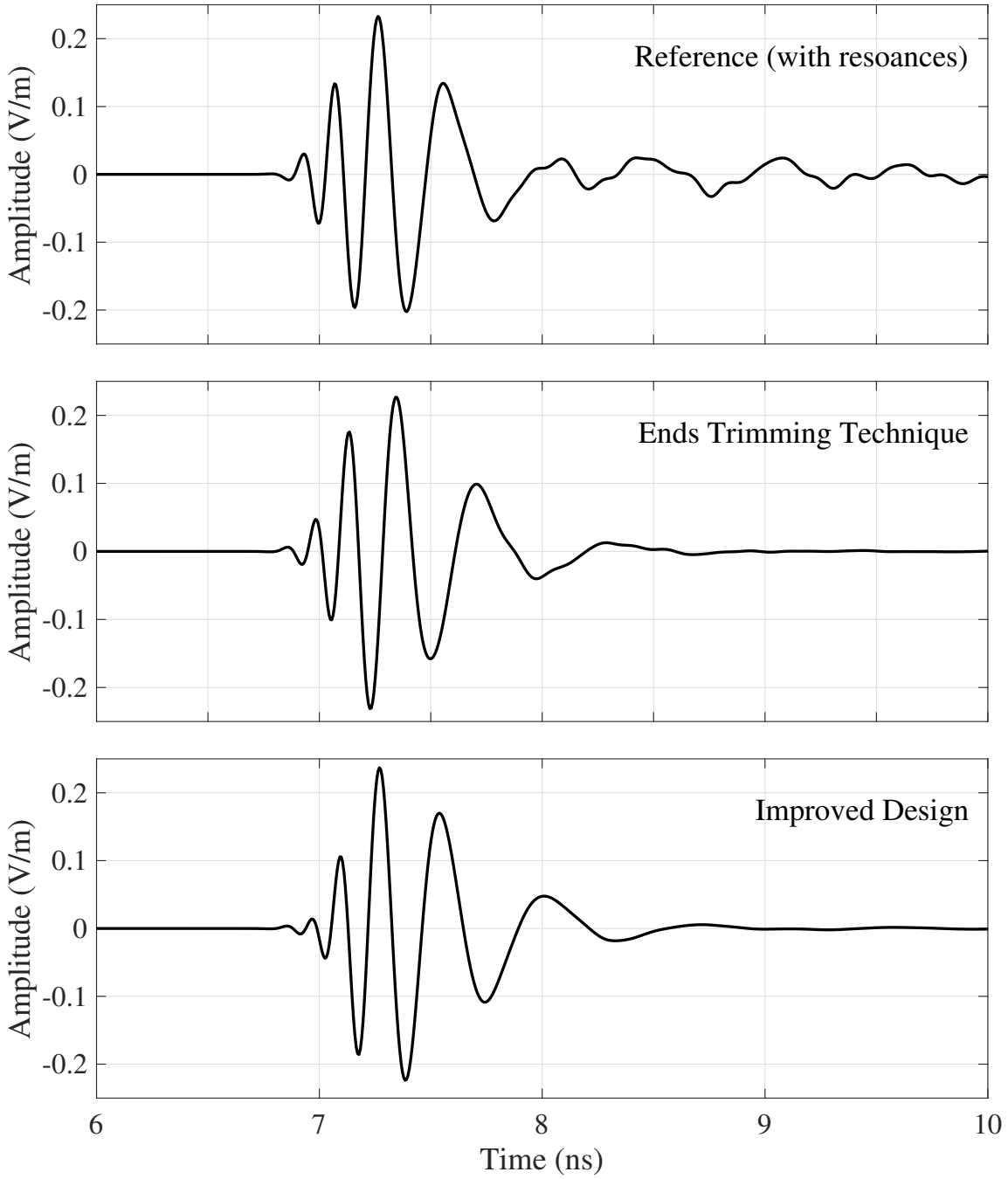

Figure 2.38: Comparison of radiated pulses at 2 m (boresight) for Reference Design (with resonances) and Improved Design (without resonances). Note the significant late time ringing present in the Reference Design.

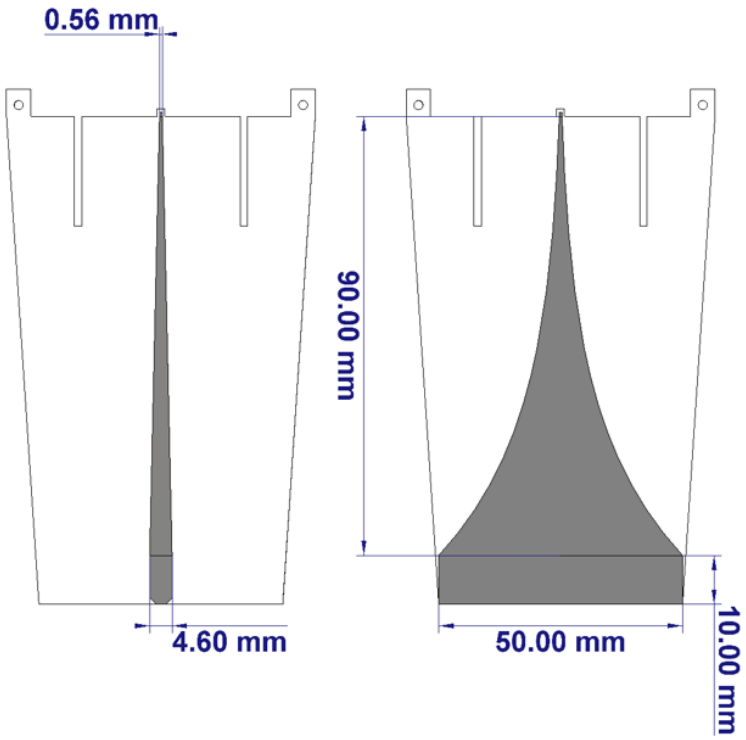

Figure 2.39: Diagram of tapered balun constructed for testing. The top trace (left) is linearly tapered while the bottom trace (right) is exponentially tapered.

(also cut from the 5880 material) provided structural stability, and the balun had tabs that extended through slots cut into the antenna substrate allowing plastic pins to hold the parts together.

2.6.2 Results

The antenna patterns were measured using an MVG StarLab near-field measurement system [91]. Full models of the measured antennas (including the SMA transition and the substrates) were developed in CST and simulated using the time-domain solver. The simulated and measured boresight realized gains of the reference and improved designs are shown in Figure 2.41 (co-polarized) and Figure 2.42 (cross-polarized). As can be seen, the simulated and measured results correlate very well from 2 to 6 GHz. At the lower and higher frequencies, some relatively small discrepancies are observed. Such discrepancies are not surprising since the antenna is not well matched below 2 GHz. Furthermore, at

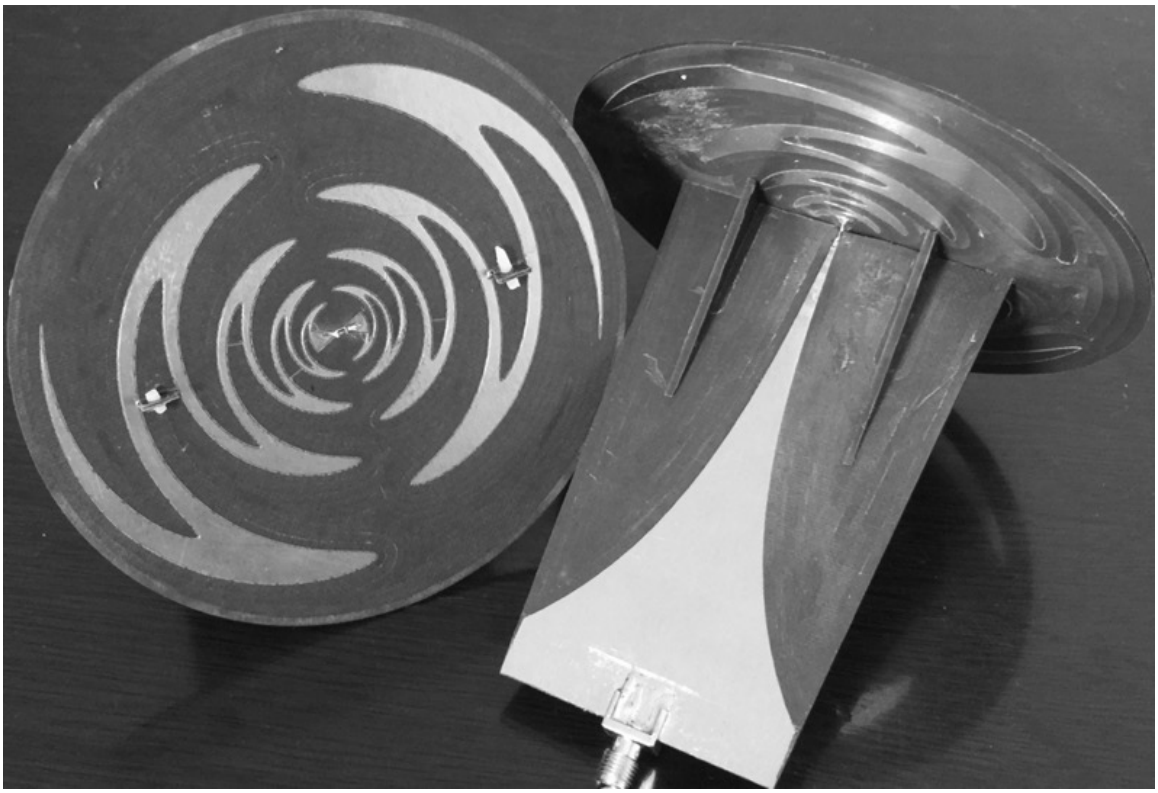

Figure 2.40: Fabricated sinuous antennas: reference (left) and improved design (right).

higher frequencies, the coarseness of the mesh, as well as fabrication imperfections, start to affect the results. However, the presence and mitigation of the resonances in the gain are unmistakably clear. Also, note that the presence of the substrate shifts the resonances observed down in frequency from that shown in Figure 2.2. The measured match (S_{11}) of the antennas is also compared vs. simulation in Figure 2.43. As can be seen the fabricated antennas maintained a good match over the intended frequency band of 2 to 10 GHz.

2.7 Summary

In this chapter, the effects of unintended resonant modes that are known to occur in sinuous antennas were investigated along with potential mitigation techniques. Such resonances produce distortion in the radiation which is undesirable for pulsed radar applications. Common mitigation techniques provided in the literature require trimming parts of the antenna to mitigate the resonances. While these techniques have had some success, they destroy

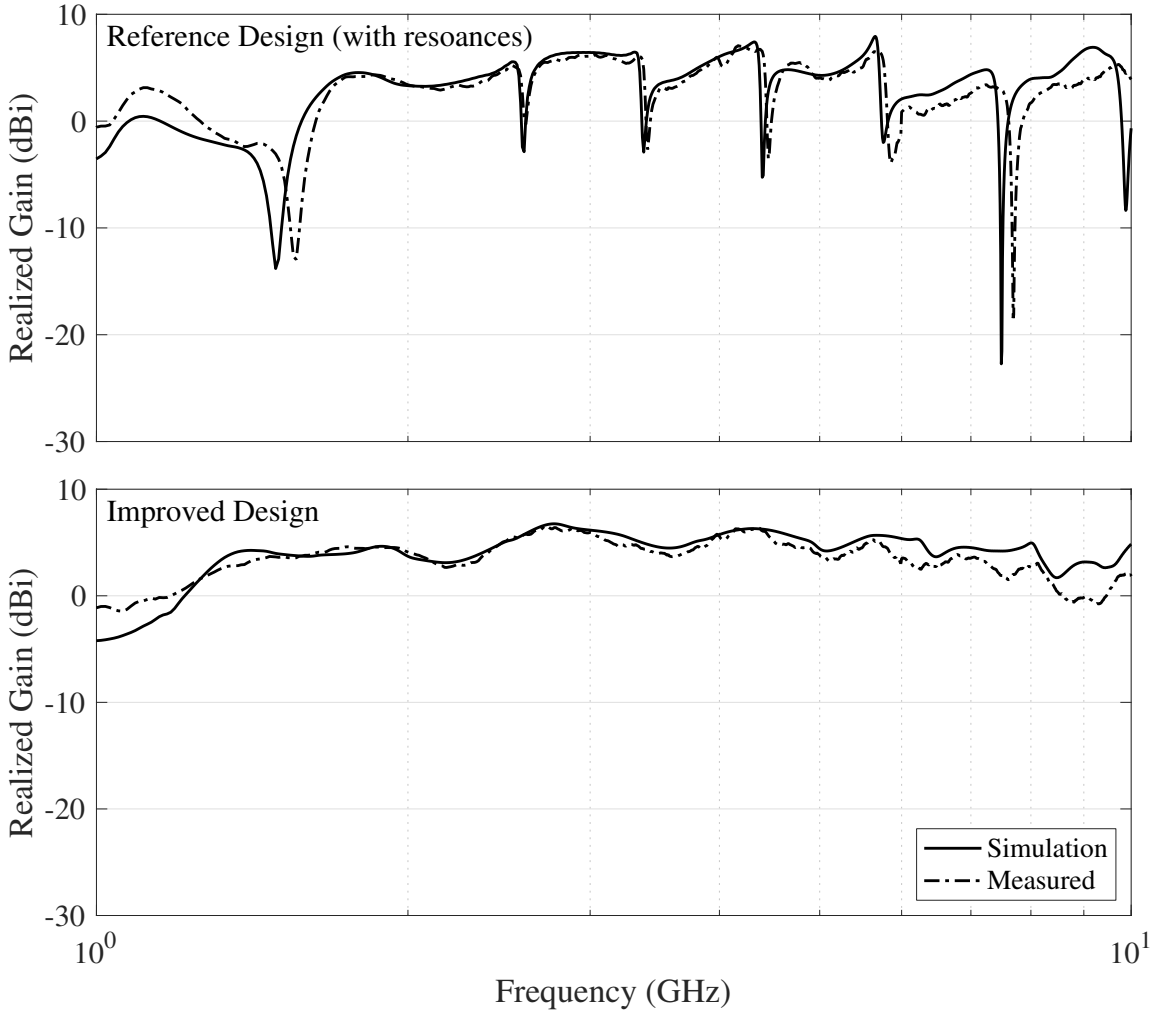

Figure 2.41: Measured and simulated boresight co-polarized realized gain (logarithmic frequency scale) of the fabricated antennas: reference design (top) and improved design (bottom). Simulation results are overlayed as the dashed line.

both the elegance and self-complementariness of the antennas. A thorough analysis of the relationship between the sinuous antenna design parameters and the log-periodic resonances showed that the resonances might be eliminated by proper selection of the arm angular width α. Evidence was presented which indicated a link between the unintended resonances and mutual interactions between adjacent antenna arms. By choosing a value of α that reduces the interleaving of the arms, the log-periodic resonances were subsequently reduced. The optimal value of α was slightly impacted by choice of expansion ration τ but performance converged at approximately $\alpha = 45^\circ$ for all the designs investigated.

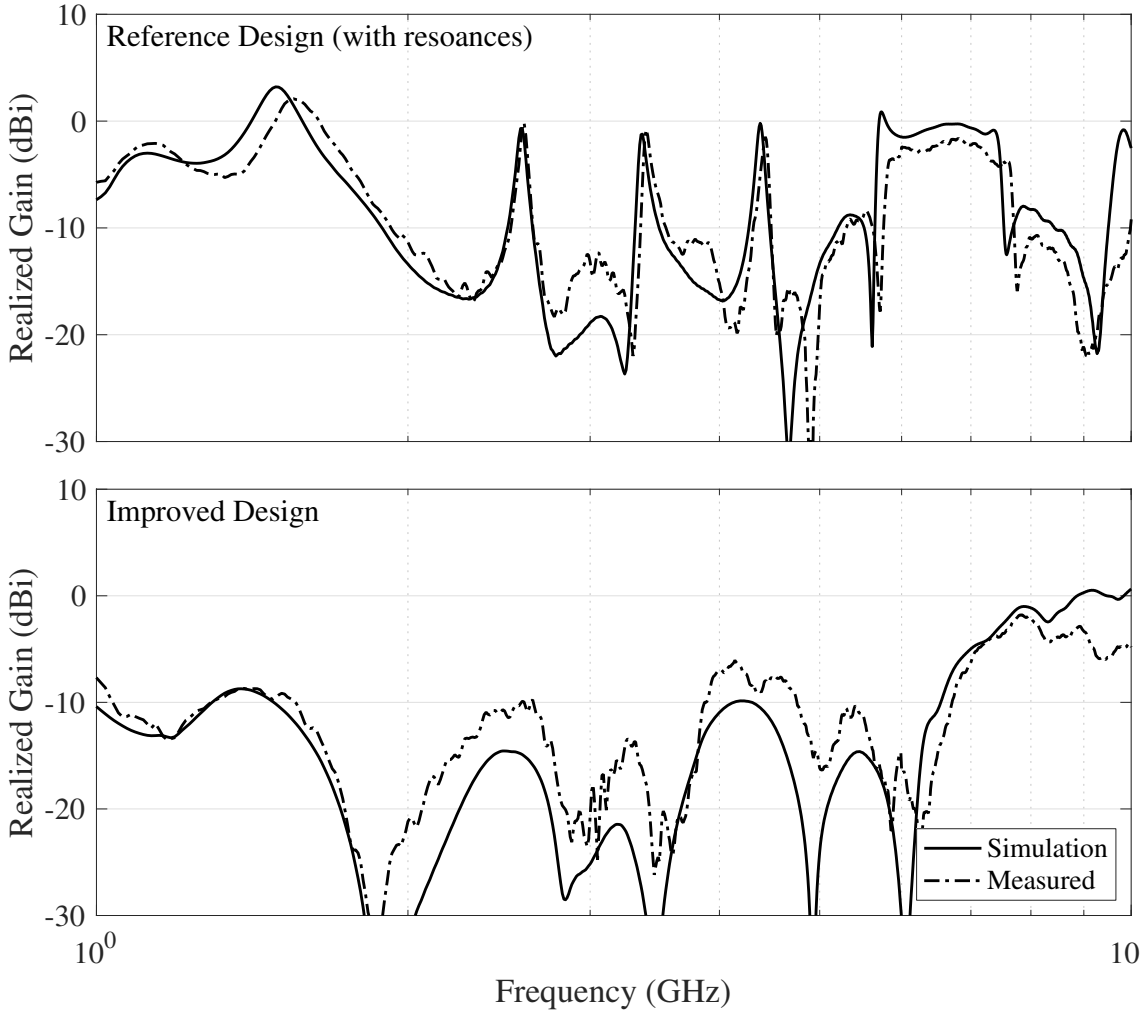

Figure 2.42: Measured and simulated boresight cross-polarized realized gain (logarithmic frequency scale) of the fabricated antennas: reference design (top) and improved design (bottom). Simulation results are overlayed as the dashed line.

These results are corroborated by design guidance provided in [66] which suggests $\alpha + \delta$ be kept $\leq 70^\circ$ "to ensure good efficiency and gain performance without dropouts over the frequency band." Mitigation of the log-periodic resonances by proper choice of design parameters provides advantages over other techniques proposed in the literature since the antenna remains self-complementary and does not require additional, empirical, design steps, i.e., removing sections of the antenna via trimming.

In addition to the log-periodic resonances, a low-frequency resonance occurs due to the sharp end left by the sinuous antenna outer truncation. It was shown that by moving

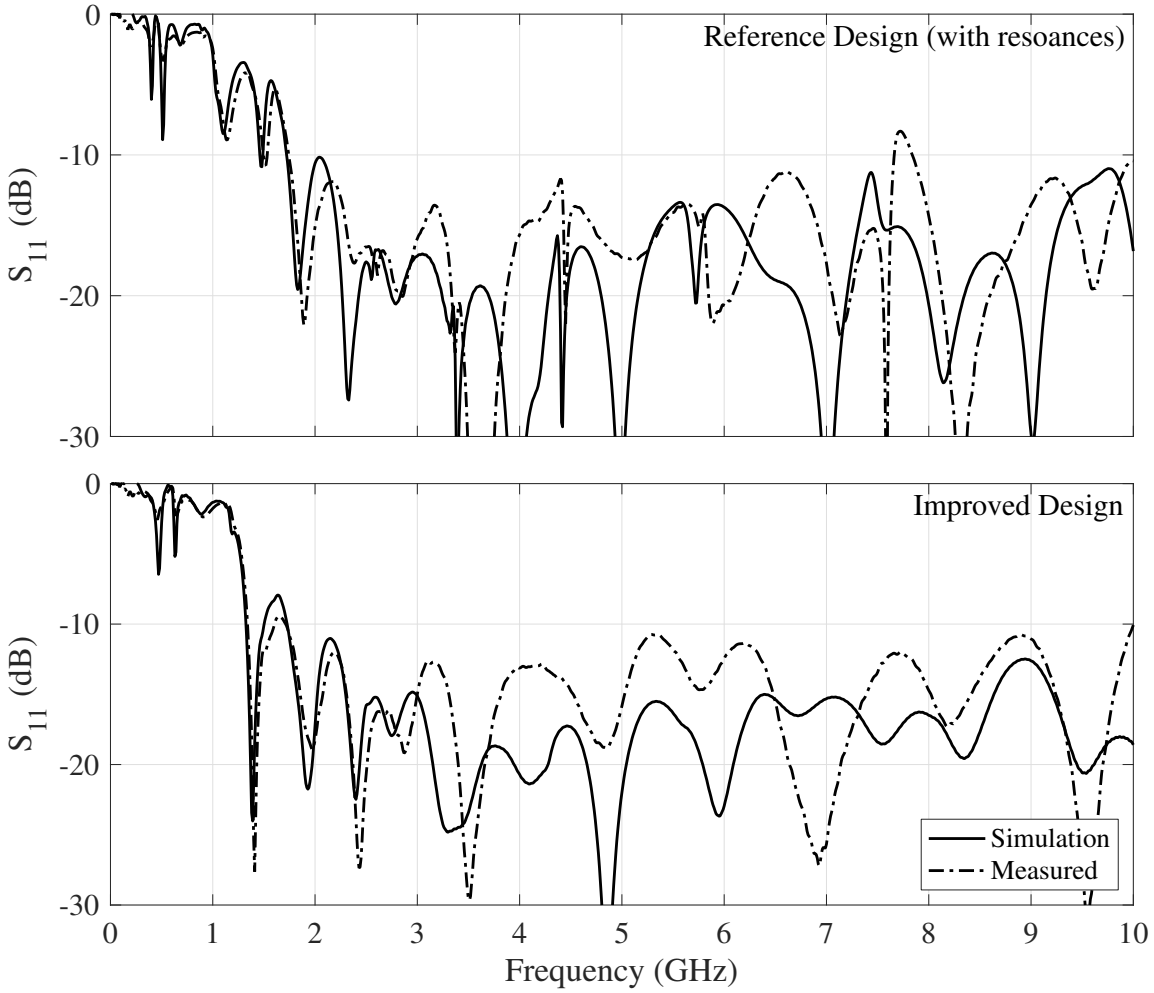

Figure 2.43: Measured and simulated match (S_{11}) of the fabricated antennas: reference design (top) and improved design (bottom). Simulation results are overlayed as the dashed line. Note the frequency scale is linear.

the truncation radius to the tip of the outermost sinuous cell, both the sharp end and the corresponding resonance are eliminated. This novel truncation method has the benefit of maintaining the self-complementary structure of the antenna as opposed to manual removal of the sharp ends via clipping.

Finally, a sinuous antenna was designed using these principles and was shown via simulation and measurement to provide the desired performance in both the frequency and time domain. More specifically, the improved sinuous antenna produced smooth radiation over a wide band while maintaining a good match to the theoretical input impedance.

CHAPTER 3
DISPERSION IN SINUOUS ANTENNAS

Sinuous antennas may be designed to radiate UWB pulses without ringing in the time domain due to unintended resonant modes by implementing the design guidance presented in Chapter 2; however, as shown in Fig 2.38, the radiated pulses are still distorted due to dispersion. Sinuous antennas are dispersive since the active region (see Figure 1.7) moves on the structure with frequency. Dispersive behavior is well documented in other log-periodic antennas such as planar spirals [92], conical spirals [14], log-periodic dipole [93, 94], and planar toothed log-periodic antennas [95]. Dispersive antennas are problematic for pulsed-radar applications since the radiated pulses become distorted in the time domain, thereby reducing range resolution. Dispersed pulses may be corrected via signal processing by applying compensating phase information, which may be obtained through accurate simulation or measurement of the antenna [14]. However, for practical GPR antennas, accurate measurement or simulation may be difficult. Furthermore, environmental effects such as thermal expansion or the dielectric loading of the soil may alter the antenna performance and thereby reduce the accuracy of previously obtained phase information. Alternatively, analytical models based on the antenna design parameters may be used to compensate for the dispersion. Such models may be desirable for GPR applications since they can be adjusted *in-situ* to accommodate environmental effects and have low memory storage requirements. Similar analytical models have been applied successfully to GPR systems with spiral antennas [96, 97]. However, for such models to remain valid when implemented for sinuous antennas, care must be taken when making antenna design decisions to avoid the excitation of unintended resonant modes–see discussion in Chapter 2–which may result in pulse distortion not correctable with simple dispersion models.

The work presented in this chapter seeks to build an understanding of the dispersive

Figure 3.1: Sinuous antennas having parameters: $P = 20$ cells, $\tau = 0.8547$ (left); $P = 16$ cells, $\tau = 0.8228$ (center); and $P = 12$ cells, $\tau = 0.773$ (right). Other parameters constant for all antennas: $N = 4$ arms, $R_T = 10$ cm, $R_{in} = 0.4$ cm, $\alpha = 45°$, and $\delta = 22.5°$.

nature of sinuous antennas and develop a model for its compensation, thereby enabling polarimetric GPR systems to obtain the benefits of sinuous antennas while utilizing them for transmitting/receiving UWB pulses with polarization diversity. It should be noted that such models do not account for dispersion resulting from propagation through dispersive media, e.g., soil, which must be corrected by additional methods [98, 99].

3.1 Sinuous Antenna Dispersion

Radiation from a sinuous antenna, as described in [12], occurs at active regions which are formed when the length of a cell is approximately a multiple of $\lambda/2$. In this case, the current at the start and end of a cell is in phase due to the wrapping of the arm and $\lambda/2$ travel as illustrated by Figure 1.7. These active regions move inward and outward on the antenna as the frequency increases and decreases respectively, resulting in a time delay between frequencies, i.e., dispersion. The dispersion increases with τ since larger values of τ result in more cells, i.e., longer travel times along the arms, which may encourage GPR system designers to choose small values of τ. However, larger values of τ result in better pattern uniformity and increase operating bandwidth [12, 33, 39].

To investigate the dispersion, full-wave electromagnetic analysis of the sinuous antennas illustrated in Figure 3.1 was conducted using CST Microwave Studio's [86] time-

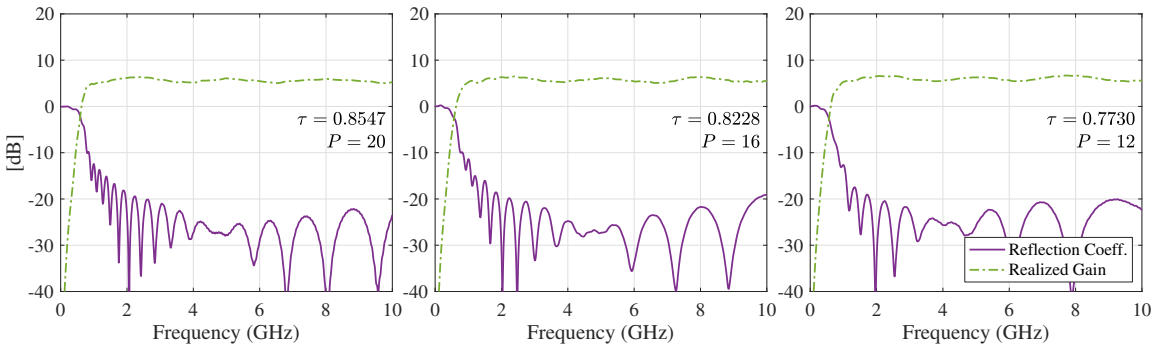

Figure 3.2: Reflection coefficient and boresight realized gain vs. frequency for the sinuous antennas investigated.

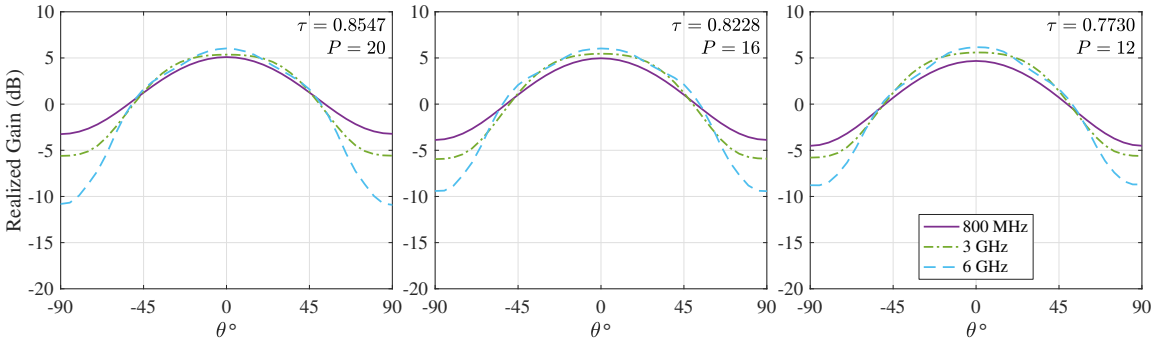

Figure 3.3: Principle E-plane pattern cuts at 800 MHz, 3 GHz, and 5 GHz for the sinuous antennas investigated.

domain solver. The sinuous antennas simulated were designed to operate from 800 MHz to 10 GHz using the following design parameters: $R_T = 10$ cm, $R_{in} = 0.4$ cm (bow-tie radius), $\alpha = 45°$, and $\delta = 22.5°$. Three different values of τ, and subsequently P, were evaluated while maintaining all other parameters constant. Additionally, α was selected as $45°$ in order to prevent unintended resonant modes which distort the radiation [37, 100]. The selection of α will be further discussed in Section 3.4. The antennas were simulated in free-space (no substrate) to simplify the analysis. Both pairs of opposing sinuous arms were terminated by an ideal port set to the theoretical impedance of 267 Ω [39]. A single pair was then driven, with the other pair remaining matched, to produce linearly-polarized radiation. The simulated reflection coefficient and realized gain for each antenna are provided in Figure 3.2 and Figure 3.3, respectively.

The simulated co-polarized radiated fields $E^x_{sim}(z = z_p, \omega)$ were probed at a boresight

distance of $z_p = 2$ m (far-field) and the corresponding phase was then propagated back to the antenna leaving only the phase due to dispersion

$$\Phi^d_{sim}(\omega) = \arg\left[E^x_{sim}(z_p, \omega)\exp(jkz_p)\right]. \tag{3.1}$$

The phase is then unwrapped (starting with the 10 GHz sample) and shown in Figure 3.4. The corresponding group delay [95]

$$\zeta^{gd} = -\frac{d}{d\omega}\Phi^d_{sim}(\omega) \tag{3.2}$$

is also shown in Figure 3.4 (right column). Note that Figure 3.4 also displays the simple dispersion models, which will be discussed in Section 3.2. As expected, lower frequencies exhibit a larger delay since the corresponding active region is farther out on the antenna—where the antenna is larger. Furthermore, the results confirm the relationship between the dispersion and τ, i.e., increasing τ also increases dispersion. These effects are also evident in the time domain as will be discussed next.

The time-domain radiated pulse $E^x_{pulse}(r_p, t)$ for a given excitation $v_{pulse}(t)$ can be computed from the frequency-domain radiated fields by Equation 2.1. The pulse excitation used was a double-differentiated Gaussian, which is described in Appendix B. In the presented analysis, the pulse parameters were set to produce a 1 V peak signal at 0.36 ns with maximum spectral energy at 3 GHz as shown in Figure 3.5. The corresponding radiated pulses for the antennas simulated are shown in Figure 3.6. As expected from the group delay shown in Figure 3.4, the lower-frequency content is delayed in time from the higher-frequency content resulting in a distorted pulse with larger values of τ resulting in greater dispersion. It is important to note that this is only the *radiated* pulse; the dispersive properties will double when the antenna is used for both transmit and receive.

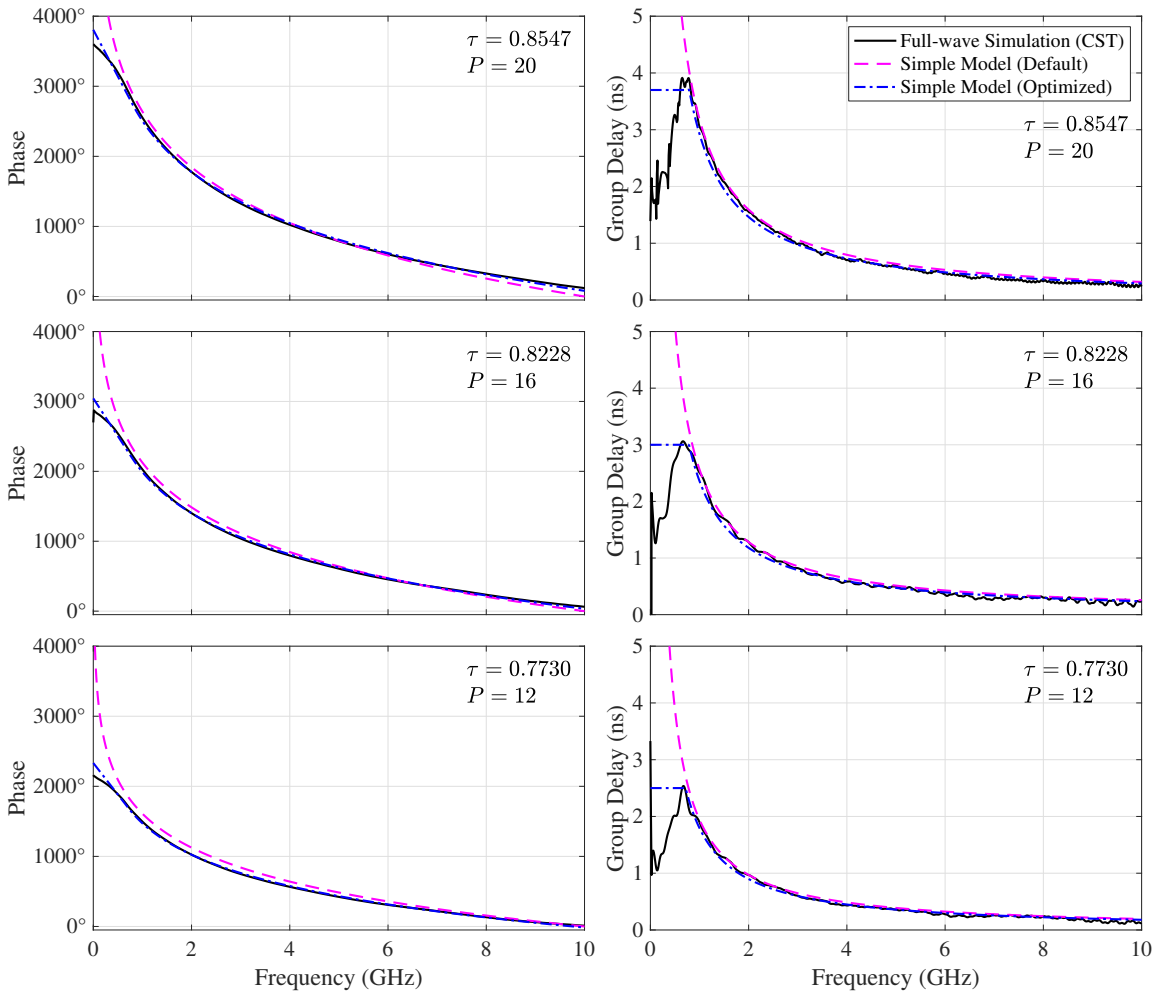

Figure 3.4: Full-wave simulation vs. simple model of both phase (left) and group delay (right) due to dispersion in the 20, 16, and 12 cell sinuous antennas. Note, phase unwrapping starts at 10 GHz.

3.2 Log-Periodic Dispersion Model

Since the values of both α and τ remain constant for each cell in the sinuous antennas analyzed, the antennas are log-periodic structures [12]. Thus, the radiated fields at frequency ω will repeat, since the structure repeats (scaled in size), at frequencies $\tau^n\omega$ where n is an integer [49]. A dispersion model for log-periodic antennas has been presented in the literature [95, 93, 94]. As will be demonstrated, this model may also be successfully applied to log-periodic sinuous antennas.

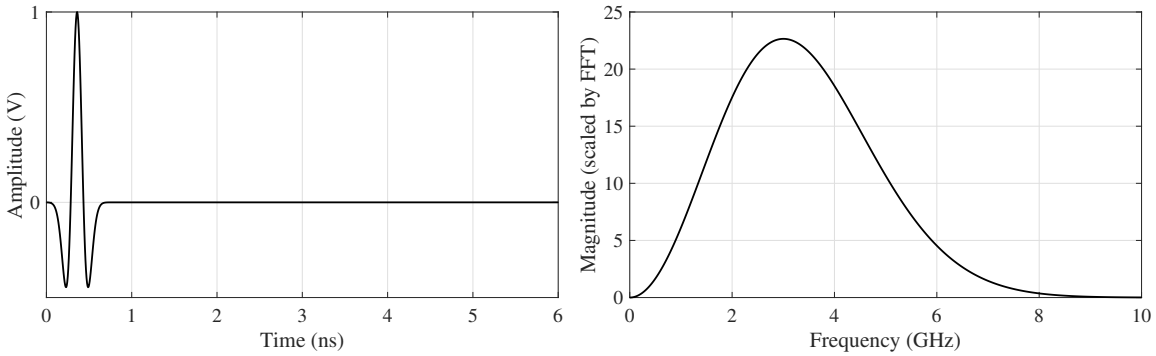

Figure 3.5: Double-differentiated Gaussian pulse used as the voltage excitation $v_{pulse}(t)$ to compute the radiated pulses $E^x_{pulse}(z_p, t)$ from the simulated electric field data using Equation 2.1. The time-domain representation of the signal (left) shows a peak amplitude of 1 V at 0.36 ns, while the frequency-domain (right) shows maximum spectral energy at 3 GHz.

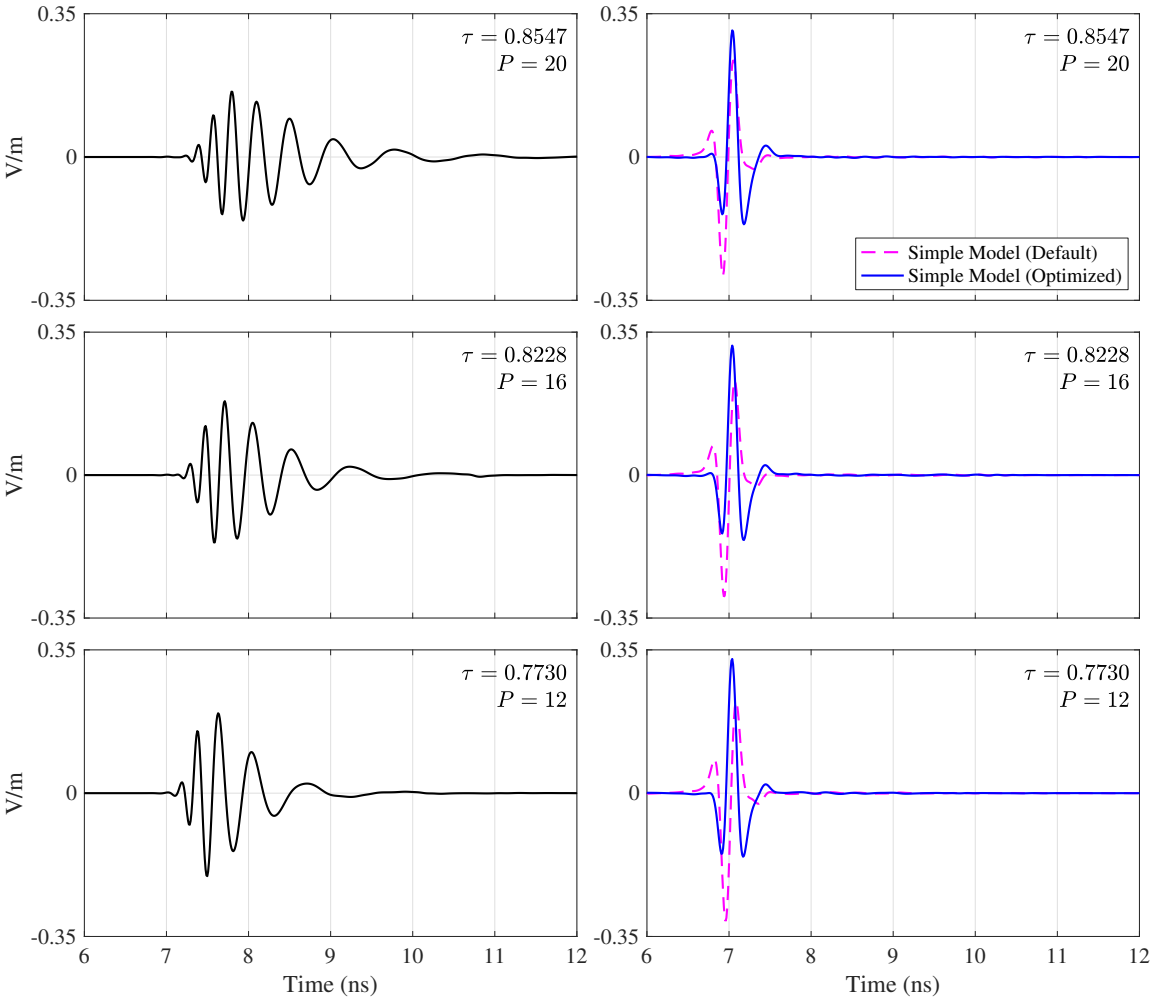

Figure 3.6: Dispersed radiated pulses at 2 m on boresight (left), and the corrected radiated pulse at 2 m on boresight after the simple antenna dispersion model has been applied (right).

Table 3.1: Log-periodic dispersion model parameters from Equation 3.3 and optimized versions for the three different sinuous antennas investigated.

Antenna		Default Model			Optimized Model		
P	τ	ϕ_0 (rad)	$\omega_0/2\pi$ (GHz)	d_c (ns)	ϕ_0 (rad)	$\omega_0/2\pi$ (GHz)	d_c (ns)
20	0.8547	20.01	10.0	N/A	18.38	10.8	3.7
16	0.8228	16.11	10.0	N/A	14.82	10.4	3.0
12	0.7730	12.20	10.0	N/A	11.28	9.77	2.5

The model represents the phase due to dispersion as

$$\Phi^d_{mod}(\omega) = -\phi_0 \ln \frac{\omega}{\omega_0} \tag{3.3}$$

where $\phi_0 = -\pi/\ln\tau$ [94]. The value ω_0 controls the zero crossing of the phase model and is generally set to the highest frequency of operation (where the dispersion is defined to be zero); for this case, $\omega_0/2\pi = 10$ GHz was used. In Figure 3.4, the model with the default parameters fits the stimulation results well, but with some noticeable deviation. An optimization procedure, similar to what was done in [95], may be employed to produce an improved model Φ^d_{opt} as shown in Figure 3.4. The optimization was done using MATLAB's global optimizer [101] to find the best values for ϕ_0 and ω_0 when fitting the simulated phase Φ^d_{sim}, from 800 MHz to 10 GHz, starting with the initial suggested values. The default and optimized model parameters are compared in Table 3.1. The group delay can then be computed from the phase model using Equation 3.2 and is shown in Figure 3.4. As can be seen, the model fits the delay well, with only a slight improvement obtained from the curve fit optimization. However, the model degrades at frequencies below 800 MHz, where the sinuous antenna cells become electrically small and no longer radiates as intended. A similar model developed for spiral antennas implemented a constant delay below the antenna's intended operating frequency [92]. In this work, Φ^d_{opt} has a constant delay d_c imposed for frequencies below 800 MHz (see Table 3.1) as illustrated in Figure 3.4.

The optimized dispersion model was then used to correct the dispersed radiated pulse

$E^x_{sim}(z_p, t)$ via

$$E^x_{comp}(z_p, t) = \mathcal{F}^{-1}\left\{\mathcal{F}[v_{pulse}(t)]\frac{E^x_{sim}(z_p, \omega)\exp[-j\Phi^d_{opt}(\omega)]}{V_{sim}(\omega)}\right\}. \tag{3.4}$$

The radiated pulse with applied dispersion compensation $E^x_{comp}(z_p, t)$ is shown for each antenna in Figure 3.6. For comparison, Figure 3.6 also shows the corrected pulse computed with the default dispersion model. The applied correction causes the radiated pulse to closely match the shape of the input voltage with the optimized model giving the best result.

3.2.1 Off-Boresight Angles

For close-in sensing applications like GPR, it is important to understand the performance of the dispersion model at off-boresight angles. To investigate this, simulated co-polarized radiated fields were sampled along the x-axis running parallel to the face of the 16 cell ($\tau = 0.8228$) antenna 20 cm away on boresight ($z = 20$ cm). The x-axis samples are 0, 10, and 20 cm corresponding to the off-boresight angles 0°, 26°, and 45° respectively. The dispersed radiated pulses were computed at each sample location similarly to those computed in Section 3.1. Both the dispersed and corrected pulses are shown in Figure 3.7. The parameters for the dispersion model used are from Table 3.1, which are optimized for $z = 2$ m. The results show the model can successfully correct the dispersed pulses at the off-boresight angles. Should increased accuracy be desired for imaging algorithms, separate model parameters may be stored in a look-up table corresponding to the different angles and used when the relative antenna and image pixel locations are known. The benefit of a simple model in such a case would be significantly less computer memory required compared to full phase datasets.

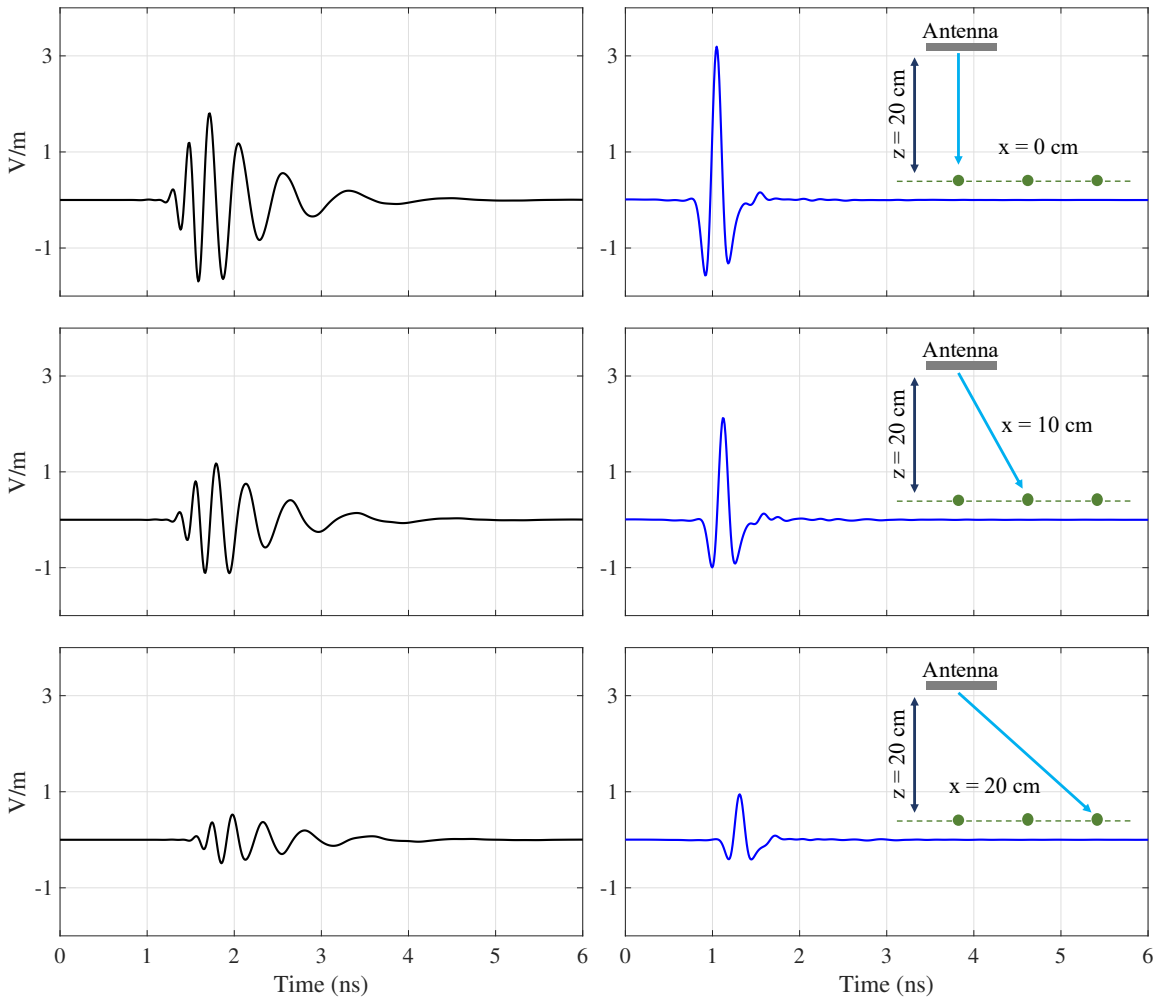

Figure 3.7: Radiated pulses from the 16 cell antenna at 20 cm boresight depth and three perpendicular scan locations: 0, 10, 20 cm. The pulses are shown both before (left) and after (right) application of the optimized simple antenna dispersion model listed in Table 3.1.

3.2.2 Effectiveness for Different Soil Environments

The effectiveness of the dispersion model in the presence of different soils was investigated by simulating the 16 cell antenna over both dry and wet sandy soil. The simulations were done using CST Microwave Studio's [86] built-in dispersive models for dry and wet sandy soil. The wet sandy-soil model ($\varepsilon_r = 15.73 - 3.48j$ at 3 GHz) represented 18.8% moisture content and was significantly more lossy and dispersive than the dry sandy-soil model ($\varepsilon_r = 2.54 - 0.0084j$ at 3 GHz). The antenna was placed 2.5 cm above a soil half-space,

and the radiated electric field was probed at a boresight depth of 5 cm below the surface. The soil was replaced with air ($\varepsilon_r = 1$) for comparison as well. The phase of the simulated radiated fields was propagated backward through the soil (5 cm) and free-space (2.5 cm) layers to the antenna, using the appropriate propagation constant per frequency, leaving approximately only the phase due to dispersion. The dispersion model was then fit to this phase–similar to what was done in Section 3.1. The optimized dispersion model parameters show little difference between materials: ϕ_0 equal to 14.80, 14.80, 14.74 for the air, dry sand, and wet sand, respectively. These similarities indicate the presence of the soil had a negligible effect on the antenna's dispersion.

The results, shown in Figure 3.8, indicate the dispersion model is effective at removing the dispersion from the antenna; however, it does not remove dispersion due to propagation through the soil. The effects of the slight soil dispersion in the dry sand case and the moderate soil dispersion in the wet sand case is evident in the graphs. Such effects of the soil must be compensated by additional methods [98, 99]. Additionally, both pulses simulated with the soil show a late-time pulse, which is attributed to multiple reflections between the soil surface and the antenna. The large reflected wave is received and re-transmitted again from the antenna showing up delayed in time and further dispersed by the antenna. Although it cannot compensate for all non-ideal effects, the results indicate that the simple model is accurate enough to correct the antenna dispersion in multiple environments.

3.3 GPR Simulations

The dispersion model was applied to a simulated GPR scenario where the 16-cell ($\tau = 0.8228$) sinuous antenna was simulated over a dry sandy-soil half-space (CST Microwave Studio) as depicted by Figure 3.9. Each pair of antenna arms were excited individually in order to produce orthogonal senses of linear polarization, i.e., $E^x_{sim}(x, z, \omega)$ and $E^y_{sim}(x, z, \omega)$. The radiated electric field was probed at a 20 cm depth along the x-axis

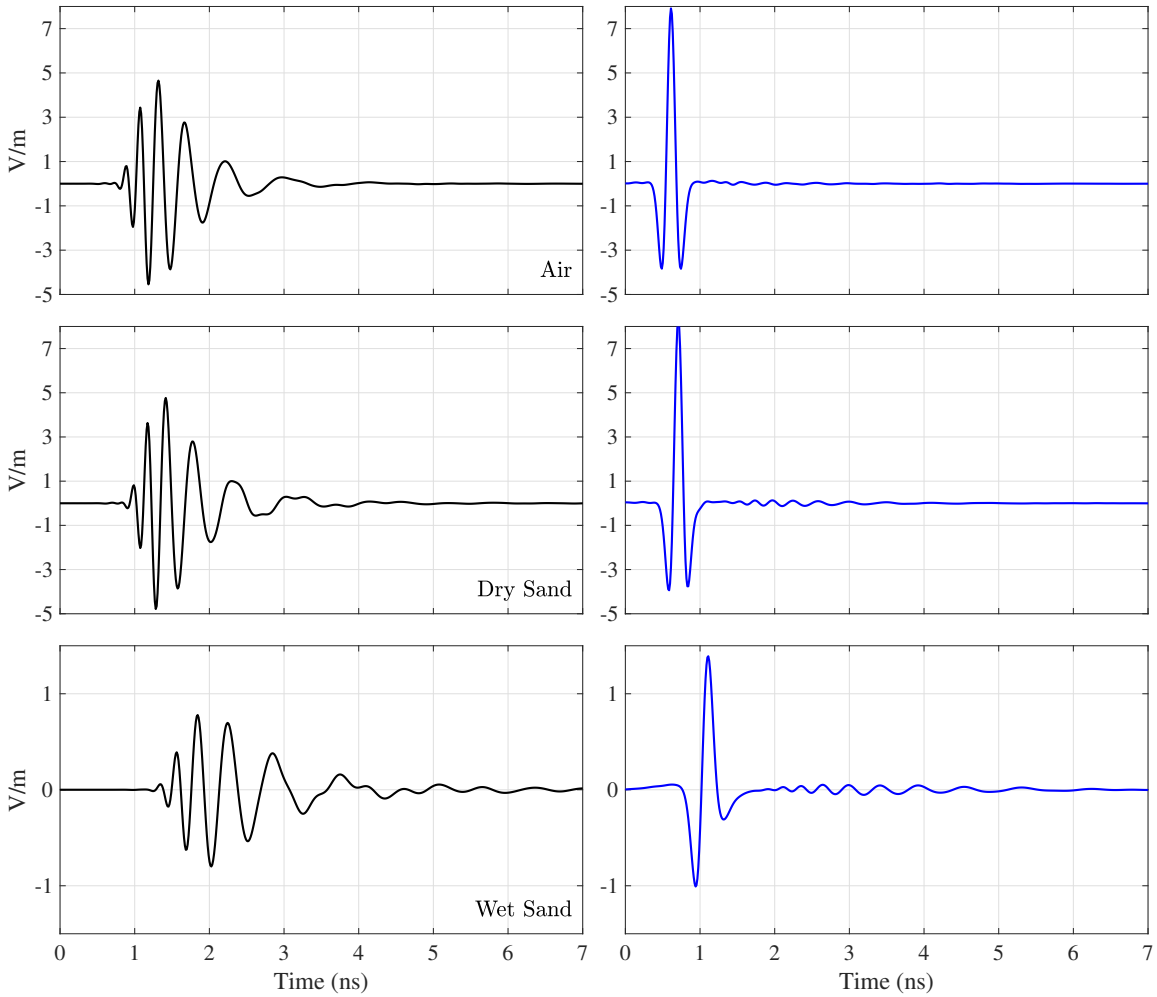

Figure 3.8: Boresight radiated pulses at 5 cm depth in three different materials: air, dry sand, and wet sand. The pulses are shown both before (left) and after (right) application of the dispersion model. The wet sand was highly lossy and dispersive resulting in significantly smaller pulses and less effective pulse correction when using only the simple dispersion model for the antenna.

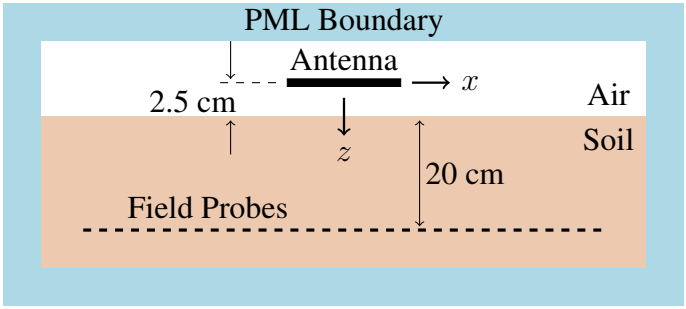

Figure 3.9: Illustration of the GPR simulation: the sinuous antenna is simulated over a lossy soil half-space containing field probes at a depth of 20 cm. The target response at each field-probe location was determined with a reciprocity model.

and used to compute the returned signal from a small linear scatter (3 cm long wire with a 1 mm radius) via the reciprocity model and polarizability tensor developed in [92]. Two orientations of the target were considered: first, the target was aligned at a 45° angle in the x-y plane to produce equal co-polarized and cross-polarized returns, and second, the target was aligned at a 0° to produce only a co-polarized response. The resulting time-domain B-scans, both with and without dispersion compensation, for the cross-polarized and co-polarized targets, are displayed in Figure 3.10 and Figure 3.11 respectively. The returns were normalized to the peak voltage for display purposes.

The optimized dispersion model from Table 3.1 was applied twice to the received voltage to compensate for the dispersion produced during both transmit and receive. Results presented in Section 3.2.2 indicated the applicability of this dispersion model since the proximity of the dry sandy-soil produced only negligible effects on the antenna's dispersion. As can be seen, the model can successfully correct the dispersed pulses both on and off-boresight, thereby significantly increasing the GPR's range resolution. Furthermore, the dispersion model behaves as expected for both co-polarized and cross-polarized targets. The results confirm the applicability of the model to sinuous antennas employed in polarimetric systems.

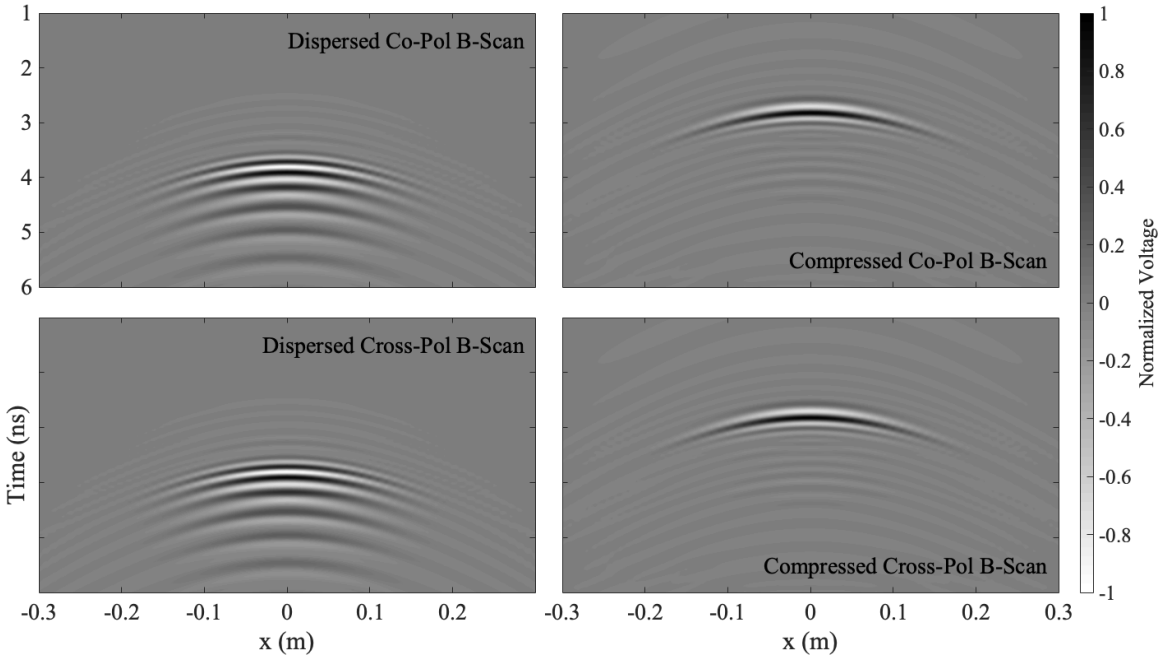

Figure 3.10: GPR simulation results: dispersed co-pol and cross-pol B-scans (left) and corrected B-scans using an optimized dispersion model (right) for a small linear target aligned at a 45° angle to the incident wave polarization.

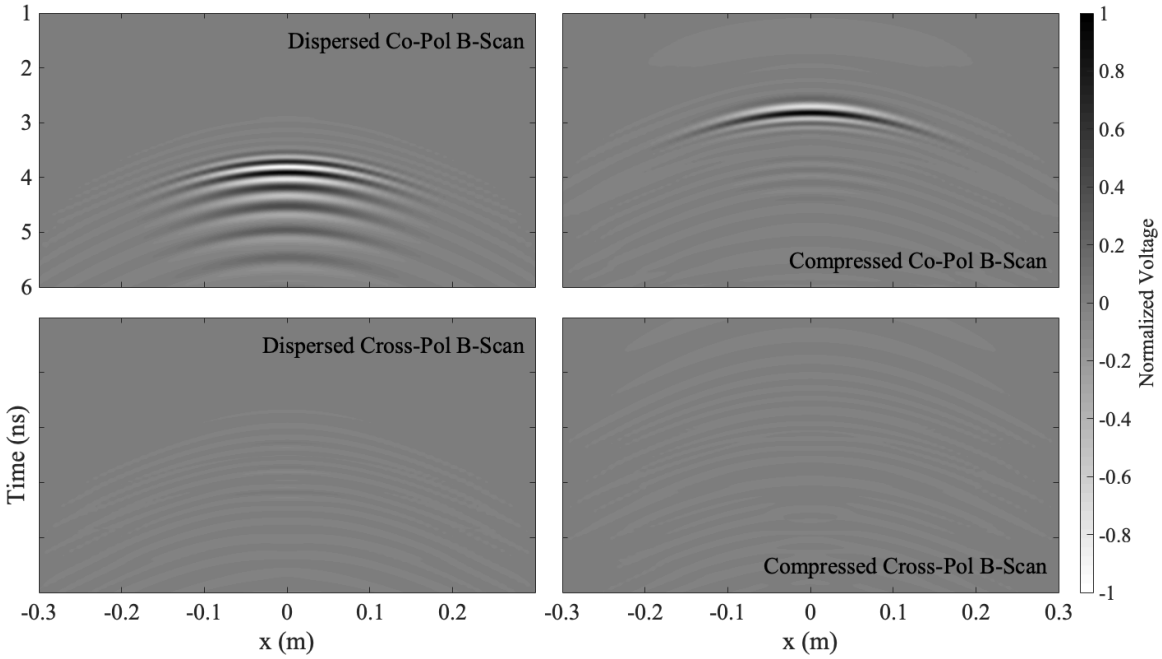

Figure 3.11: GPR simulation results: dispersed co-pol and cross-pol B-scans (left) and corrected B-scans using an optimized dispersion model (right) for a small linear target aligned with the incident wave polarization.

3.4 Limitations of the Log-Periodic Dispersion Model

The presented dispersion model assumes the antenna radiation is log-periodic, i.e., the radiated fields at frequency f will repeat at frequencies $\tau^n f$ where n is an integer [49]. When the actual radiation from the antenna breaks this assumption, the dispersion model becomes invalid. Such behavior was evident for frequencies below the operating range of the antenna, where the constant delay was applied to the dispersion model (see Figure 3.4). Another factor that reduces the effectiveness of the dispersion model is radiation from the bow-tie feed. A good guideline is to keep $R_{in} < \lambda/8$, for the highest frequency desired, to prevent such radiation. Reducing R_{in} also results in small trace widths at the feed, which may be difficult to manufacture reliably. For this reason, some have proposed breaking the log-periodic nature of the sinuous by letting τ vary with the radius [47, 48]. In this case, the model would need to be altered since the antenna is now quasi-log-periodic [12].

Another potential pitfall is the unintended excitation of resonant modes that produce sharp discontinuities in gain and phase of the antenna over frequency, as shown in Chapter 2. Such discontinuities may occur if the sinuous antenna design parameters and outer truncation method are not properly selected [100]. The lower bound on the sinuous antenna operating frequency ω_L may be approximated as

$$\omega_L = \frac{2\pi v}{4R_1(\alpha + \delta)}, \tag{3.5}$$

where v is the wave velocity, and α and δ are specified in radians [12]. Such a relationship may encourage GPR antenna designers to choose larger values of α for lower operating frequencies. However, large values of α have been shown to result in undesired resonate modes excited between adjacent antenna arms; furthermore, the traditional truncation of sinuous antennas produces a sharp end that resonates at low frequencies [37, 100]. These unintended resonate modes reduce the ability of simple dispersion models to compensate for dispersion in radiated pulses accurately.

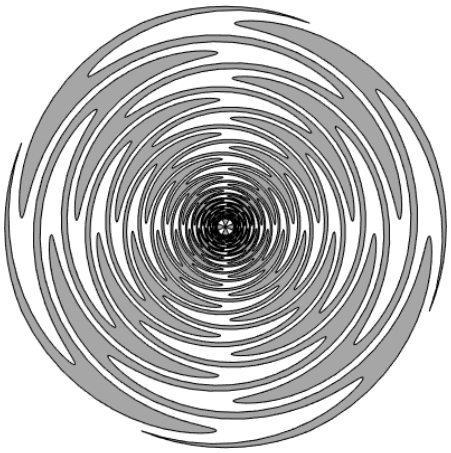

Figure 3.12: Traditional sinuous antenna having parameters: $N = 4$ arms, $P = 20$ cells, $R_1 = 10$ cm, $\tau = 0.8547$, $\alpha = 65^\circ$, and $\delta = 22.5^\circ$. This antenna exhibits sharp discontinuities in the gain due to unintended resonate modes.

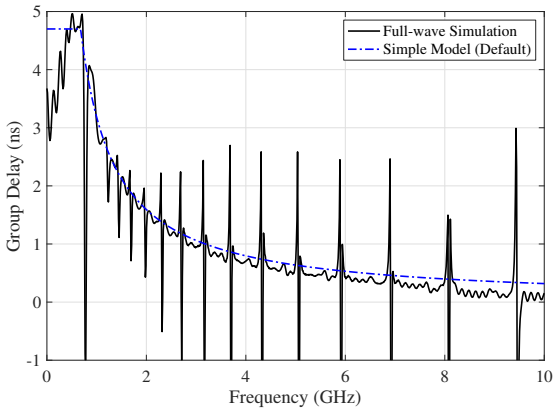

Figure 3.13: Full-wave simulation vs. simple model (default parameters with fixed delay cap d_c) of the group delay due to dispersion in the traditional sinuous antenna with resonances.

To illustrate the deficiencies of the dispersion model in the presence of unintended resonate modes, a traditionally truncated sinuous antenna with $\alpha = 65^\circ$ (see Figure 3.12) was simulated similarly to the antennas presented in Section 3.1. The group delay is shown in Figure 3.13 and displays sharp discontinuities resulting from the excitation of unintended resonant modes. The group delay computed from the corresponding dispersion model is also shown in Figure 3.13. The default model with a fixed delay cap d_c of 4.7 ns at low frequencies is used here since the sharp discontinuities complicate improving the model with an optimized curve fit. The dispersion model is used to correct the radiated pulse, as shown in Figure 3.14; it is not able to correct the ringing resulting from the unintended resonant modes since it no longer fully represents the group delay of the antenna. Thus, the sinuous antenna must be designed to mitigate such ringing, as outlined in [100], before the application of the simple log-periodic dispersion model.

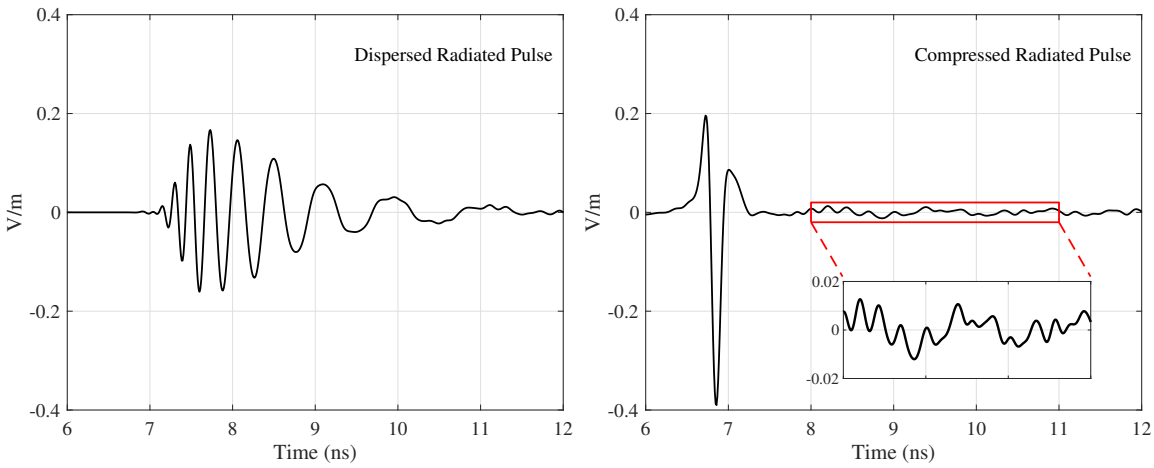

Figure 3.14: Dispersed radiated pulse at 2 m (left), and the corrected radiated pulse at 2 m after the dispersion model has been applied (right) for the traditional sinuous antenna with resonances. Note, the dispersion model does not compensate for the late-time ringing due to the unintended resonant modes.

3.5 Experimental Validation

In order to validate the analysis presented above, the 16 cell antenna defined in Section 3.1 was fabricated and measured. The dispersive nature of the antenna was investigated by measuring the response from a 5.08 cm diameter sphere. The sphere was placed 15.24 cm from the antenna on boresight and then scanned perpendicular to the antenna another 15.24 cm in 1.27 cm increments. The fabricated antenna in the measurement setup is shown in Figure 3.15.

The antenna was manufactured using an LPKF PCB milling machine [89] out of 0.031" Rogers RT/duroid® 5880 laminate (1 oz. copper clad). The 5880 material has a very low loss (tanδ of 0.0009 at 10 GHz) and a relative permittivity ε_r of 2.20 [90]. Simulations showed the effect of the substrate on the antenna's dispersion to be small (see Figure 3.16). As can be seen from Figure 3.15, each set of opposing sinuous arms were placed on opposite sides of the substrate. Separation of the arm pairs simplified feeding the antenna. A tapered microstrip balun fed a single pair of arms while the other pair of arms were terminated with a 221 Ω chip resistor resulting in the antenna producing linear (horizontal)

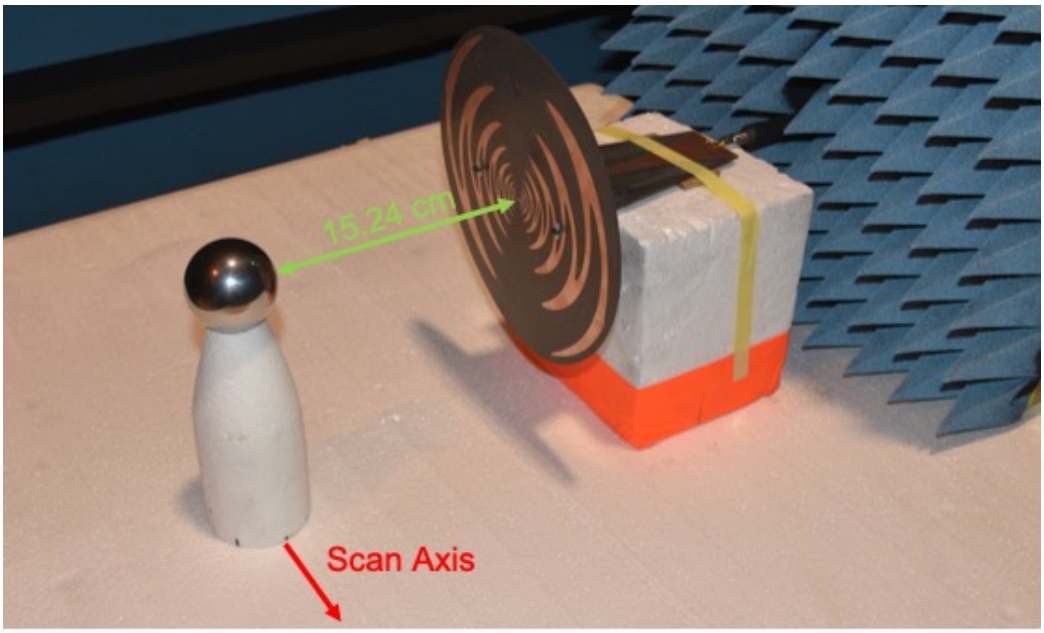

Figure 3.15: Setup of the validation measurement showing the fabricated 16 cell sinuous antenna and the 5.08 cm spherical target at the boresight scan location.

polarization [60, 79, 100]. Simulation results showed the presence of the substrate lowered the input impedance to approximately 230 Ω (averaged over the band). The constructed balun was milled from 0.062" Rogers RT/duroid® 5880 laminate (0.5 oz. copper clad) and started as an unbalanced 50 Ω microstrip which was then tapered over a 150 mm length to a balanced parallel stripline. The top trace was tapered linearly while an exponential taper was used for the ground plane. An SMA edge connector fed the microstrip end of the balun. For structural stability, triangular braces were included (also cut from the 5880 material), and the balun had tabs that extended through slots cut into the antenna substrate allowing plastic pins to hold the parts together [100]. A detailed model of the measured antenna—including the substrate, the balun, and the SMA transition—was developed in CST Microwave Studio and simulated using the time-domain solver. The simulated and measured reflection coefficient vs. frequency is compared in Figure 3.17. As can be seen, the simulated and measured results correlate quite well.

The target returns (S_{11}) were measured in the frequency domain from 10 MHz to 10 GHz with a vector network analyzer. The background, including the foam mast, was also

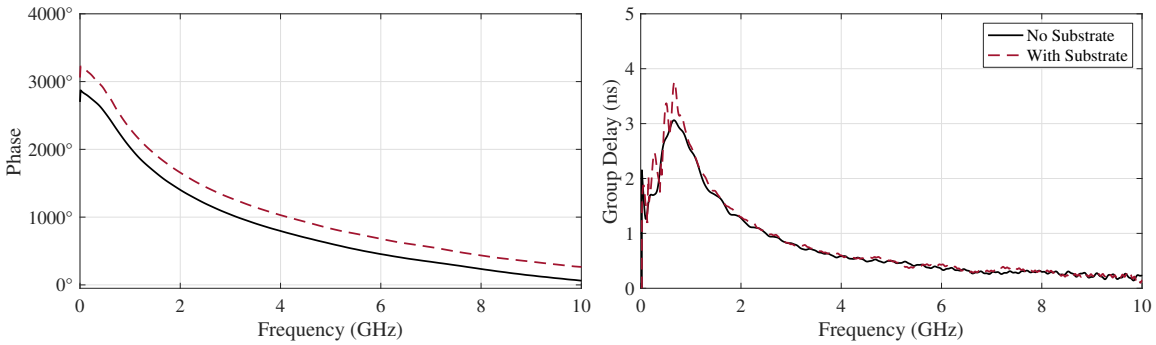

Figure 3.16: Full-wave simulations of the 16 cell antenna's phase (left) and group delay (right) due to dispersion both with and without the inclusion of a substrate. Note, phase unwrapping starts at 10 GHz.

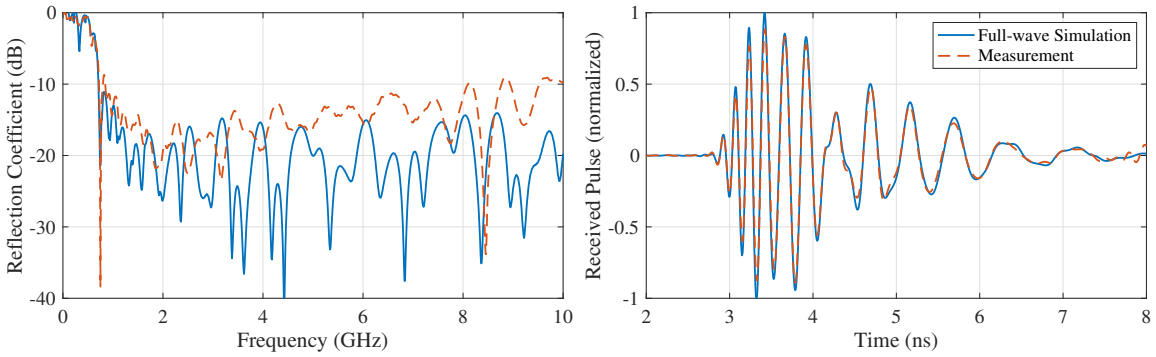

Figure 3.17: Full-wave simulation vs. measurement of the 16 cell antenna with tapered balun feed. Reflection coefficient comparison (left) and 2" sphere target return pulse (right).

measured at each scan location and subsequently removed from the target results by coherent subtraction. Note that the calibration plane is located at the SMA connection to the antenna; therefore, the results include the time delay due to the balun. The sans background target returns were then weighted by a Taylor window ($\bar{n} = 15$ and $PSR = -80$) [102] and transformed to the time domain via inverse fast Fourier transform (IFFT). The measurement setup, i.e., antenna and 2" sphere on boresight, were also simulated, and the resulting received (dispersed) pulses are compared in Figure 3.17. The waterfall diagram in Figure 3.18 shows the processed time-domain responses for each scan location both with and without dispersion compensation. The dispersion model parameters were determined by an optimization process that maximized the cross-correlation of the boresight return with that of the time-domain window function, i.e., the IFFT of the Taylor window. The

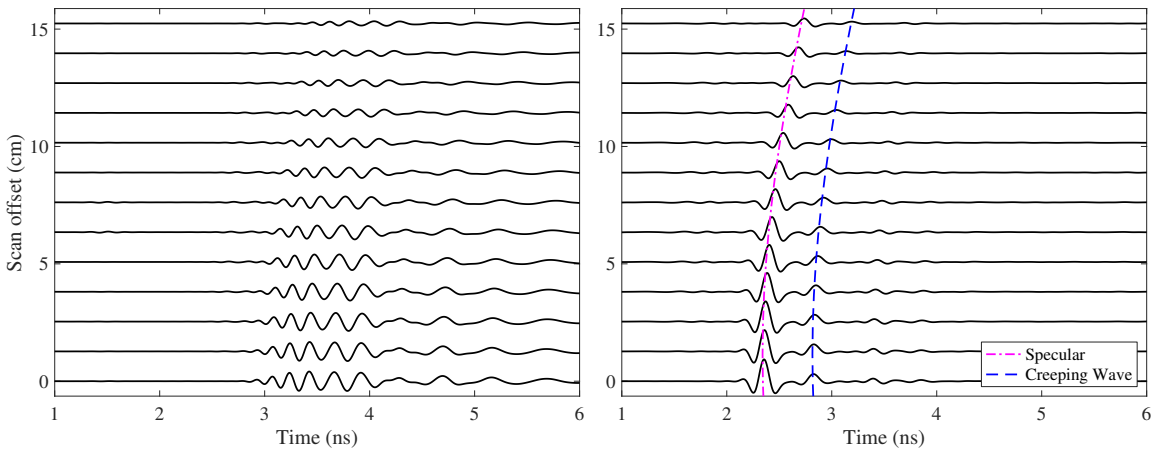

Figure 3.18: Waterfall plot of measured B-scan showing the dispersed (left) and corrected (right) time-domain responses from the measured 5.08 cm sphere. Both the specular and creeping wave reflections (denoted by the hyperbolic curves) are evident in the corrected results. Note that the results also contain the time delay due to the balun.

optimization was done to adjust the model for the presence of the substrate and feed. The optimized parameters were $\phi_0 = 16.23$ and $f_0 = 14.7$ GHz. As can be seen, identifying aspects of the target are indistinguishable before dispersion compensation. With the dispersion model applied, the specular and creeping wave returns from the sphere become clearly visible. The model is also able to remove the dispersion for the off-boresight scan locations successfully.

3.6 Summary

Sinuous antennas embody many characteristics that are advantageous to GPR applications, e.g., ultra-wideband (UWB) radiation and polarization diversity. However, they are dispersive which reduces effectiveness when radiating UWB pulses. In this chapter, a model was presented for the compensation of dispersion in log-periodic sinuous antennas, which is based on antenna design parameters and can be optimized for a better fit. The model was shown to have application for different sinuous antenna designs as well as in the vicinity of different soils. Additionally, it was shown that care must be taken when designing sinuous antennas to ensure the applicability of such dispersion models, i.e., preventing unin-

tended resonant modes. Both numerical and experimental scenarios were investigated with the model successfully used to compensate sinuous antenna dispersion thereby improving range resolution for polarimetric GPR applications. Such a model may have advantages over applying simulated or measured phase information since the model is simplistic and can be adjusted in the field to accommodate any changes in antenna performance due to the environment.

CHAPTER 4

OTHER SINUOUS ANTENNA DESIGN CONSIDERATIONS

While the previous chapters have laid the groundwork for the successful utilization of sinuous antennas in pulsed-radar systems, additional practical issues remain. In this chapter, the theoretical input impedance of self-complementary sinuous antennas will be derived and discussed. The input impedance of practical sinuous antennas will deviate from the theoretical due to the finite size of the antenna and the use of dielectric substrates. Simulated results of the sinuous antenna input impedance on some common substrates will be provided. Finally, the effects of an absorber loaded cavity backing, included to absorb the back radiation lobe, will be investigated.

4.1 Sinuous Antenna Input Impedance

In [103], it is shown that the voltages and currents at each port of an infinite, self-complementary, N-port structure—like that shown in Figure 4.1a—are related, independent of frequency, by

$$\begin{bmatrix} I_1 \\ I_2 \\ \vdots \\ I_N \end{bmatrix} = \begin{bmatrix} Y_0 & Y_1 & \dots & Y_{N-1} \\ Y_{N-1} & Y_0 & \dots & Y_{N-2} \\ \vdots & \vdots & \ddots & \vdots \\ Y_1 & Y_2 & \dots & Y_0 \end{bmatrix} \begin{bmatrix} V_1 \\ V_2 \\ \vdots \\ V_N \end{bmatrix} \tag{4.1}$$

where

$$Y_m = \frac{4}{N\eta} \left(\frac{\sin(\pi/N)}{\cos(2m\pi/N) - \cos(\pi/N)} \right). \tag{4.2}$$

In Equation 4.2, η represents the intrinsic impedance of the medium, and N is the number of rotationally symmetric conducting sections, e.g., sinuous antenna arms. Note that Y_m is

real valued when the medium is lossless. In the four-arm ($N = 4$) sinuous antenna case, Equation 4.2 becomes

$$Y_m = \frac{1}{\eta}\left(\frac{1}{\frac{2}{\sqrt{2}}\cos(m\pi/2) - 1}\right). \tag{4.3}$$

If the antenna is fed in the standard mode-1 configuration [104], where opposite arms are driven in a balanced manner as depicted in Figure 4.1b, the input voltage and current may be described as [39]

$$V_1 = -V_3 = \frac{V_{in}}{2} \tag{4.4}$$

and

$$I_1 = -I_3 = I_{in} \tag{4.5}$$

where the voltage and current are related through the admittance vector as

$$I_1 = V_1Y_0 + V_2Y_1 + V_3Y_2 + V_4Y_3. \tag{4.6}$$

Given that $Y_1 = Y_3$, Equation 4.6 may be simplified (V_2 and V_4 will cancel) such that we can solve for the input impedance [39]

$$Z_{ant} = \frac{V_{in}}{I_{in}} = \frac{2}{(Y_0 - Y_2)}. \tag{4.7}$$

Plugging Equation 4.3 into Equation 4.7 and simplifying gives

$$Z_{ant} = \frac{\eta}{\sqrt{2}}. \tag{4.8}$$

Assuming η represents the intrinsic impedance of free space ($\approx$ 377 Ω), Equation 4.8 results in 267 Ω as the theoretical input impedance of the four-arm ($N = 4$) sinuous antenna when driven in mode-1.

For practical sinuous antennas, the input impedance will deviate from the theoretical since the antenna is truncated to some finite size (see Chapter 2 for a discussion on sinuous

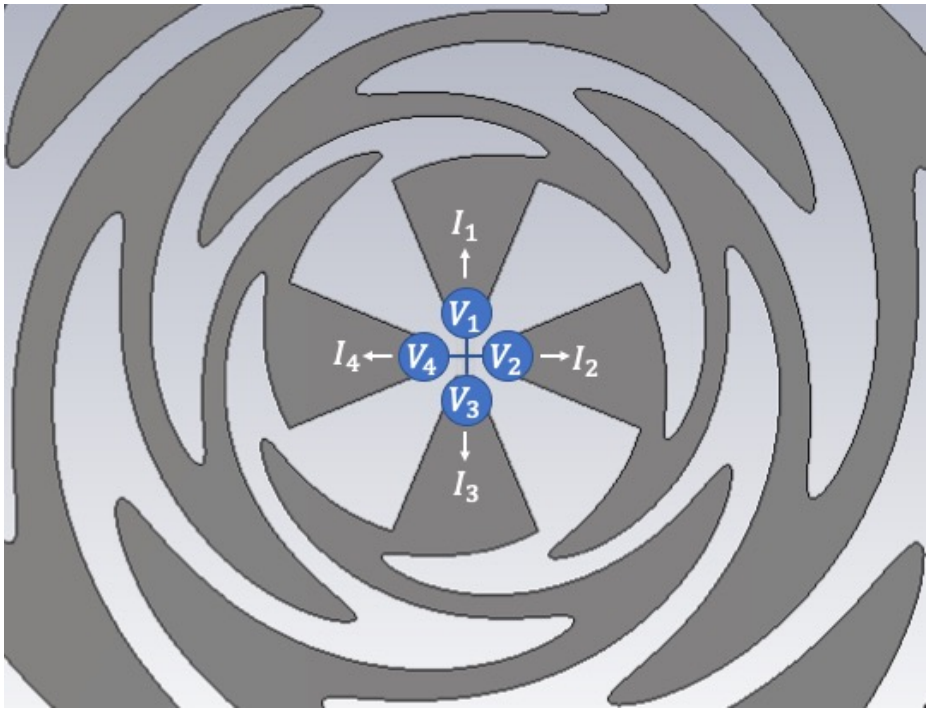

(a) Port voltages and currents from Equation 4.1.

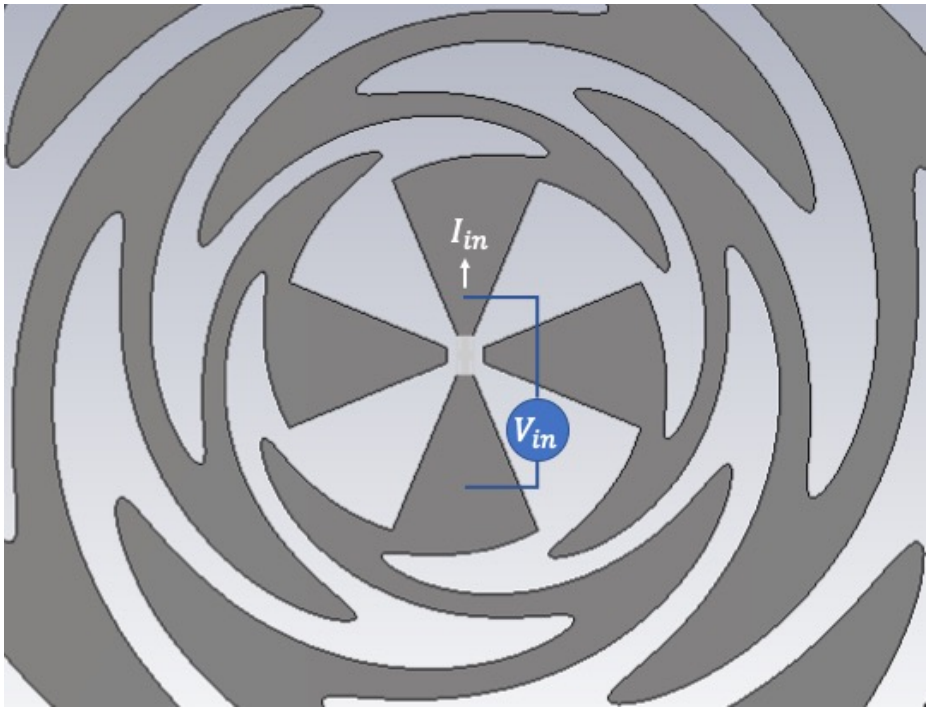

(b) Mode-1 port configuration i.e., balanced driving of opposite ports.

Figure 4.1: Illustration of sinuous antenna ports.

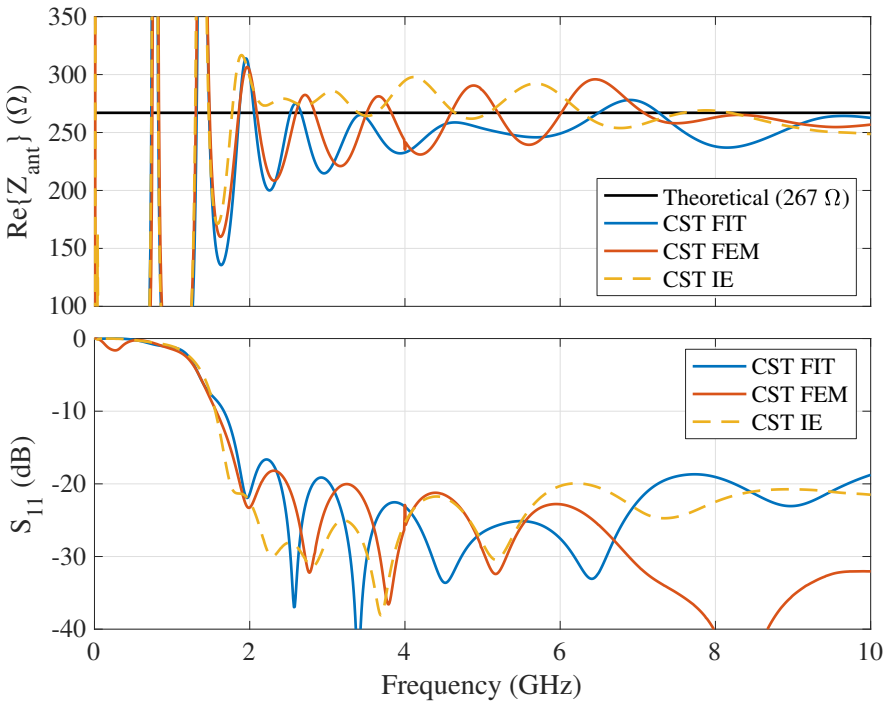

Figure 4.2: Comparison of input impedance Z_{ant} and match S_{11} to 267 Ω for the improved sinuous design when simulated with different CST solvers: time domain (FIT), frequency domain (FEM), and integral equation (IE) [86].

antenna truncation). The truncation results in reflections that disrupt the input impedance—particularly at the lower frequencies where the reflections from the truncation are strong. Figure 4.2 shows the input impedance of a sinuous antenna computed with the time-domain (FIT), frequency-domain (FEM), and integral-equation (IE) solvers provided by CST [86]. The antenna simulated was the improved design, discussed in Section 2.5 and illustrated in Figure 2.34c, having parameters $P = 8$, $R_T = 5$ cm, $\alpha = 45°$, and $\tau = 0.7628$. In the simulation, ports 1 and 3 were driven in a balanced fashion (see Figure 4.1b) while ports 2 and 4 remained open. Since $Y_1 = Y_3$ in Equation 4.6, the open circuit state of ports 2 and 4 in the simulation will not affect the input impedance. The results show the input impedance to vary largely from the theoretical below 2 GHz, where the reflections from the truncation are a problem, then converge close to 267 Ω above 2 GHz with some variation between solvers. The input impedance will vary more from the theoretical when the antenna is placed on a dielectric substrate, as will be discussed in the following section.

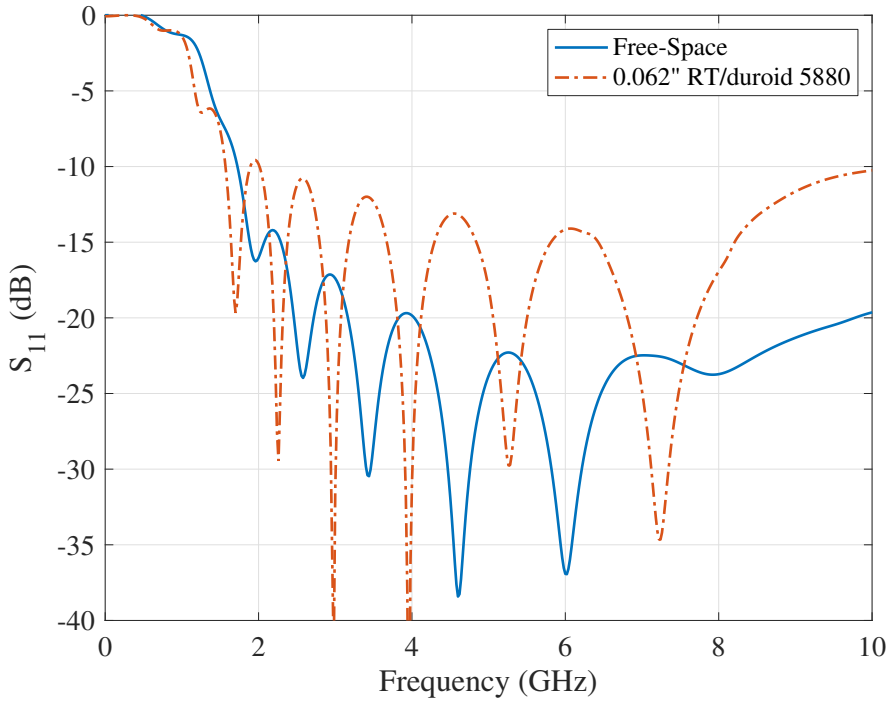

Figure 4.3: Comparison of simulated S_{11} (matched to 267 Ω) for the improved sinuous design ($P = 8$, $R_T = 5$ cm, $\alpha = 45°$, $\tau = 0.7628$) in free-space and on 1.5748 mm (62 mil) thick Rogers RT/duroid® 5880 substrate.

4.2 Substrate Effects

Practical implementation of the sinuous antenna requires the arms to be etched or milled on a printed circuit board (PCB). The PCB substrate a some relative permittivity $\varepsilon_r > 1$ that will affect the antenna's performance. In order to investigate this, the improved sinuous antenna design, discussed in Section 2.5 and illustrated in Figure 2.34c, was simulated on different substrates of various thicknesses and ε_r values. The simulations were done with the CST Microwave Studio [86] time-domain solver and used CST's built-in models (complex permittivity) for the materials.

Figure 4.3 shows the inclusion of a substrate reduces the antenna match (S_{11}) to the theoretical free-space impedance of 267 Ω. The material simulated was 1.57 mm (62 mil) thick Rogers RT/duroid® 5880 laminate which has a very low loss (tanδ of 0.0009 at 10 GHz) and a relative permittivity ε_r of 2.20 [90]. The reduction in the match is due to the

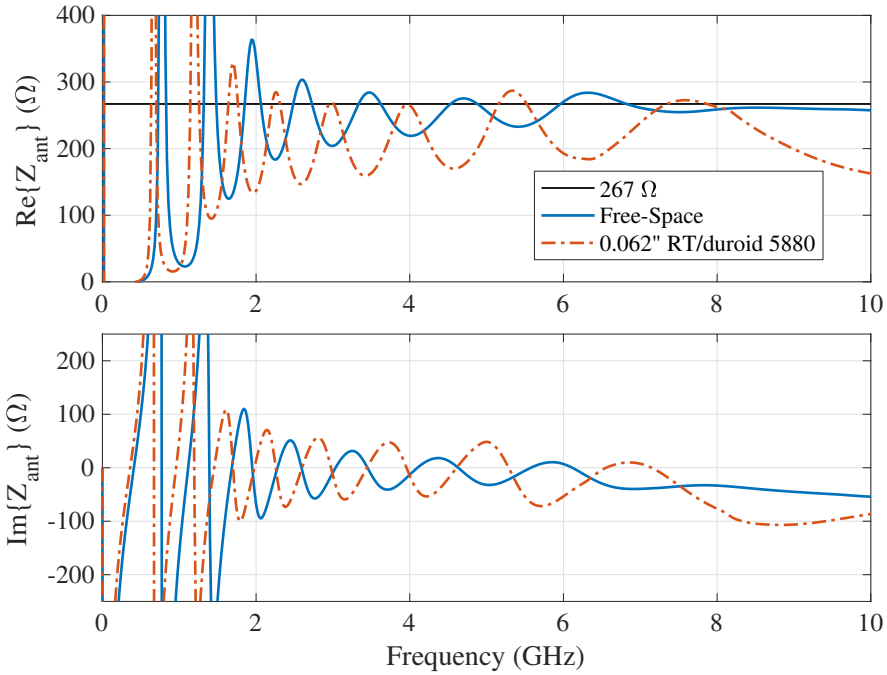

Figure 4.4: Comparison of simulated input impedance Z_{ant} for the improved sinuous design ($P = 8$, $R_T = 5$ cm, $\alpha = 45^\circ$, $\tau = 0.7628$) in free-space and on 1.5748 mm (62 mil) thick Rogers RT/duroid® 5880 substrate.

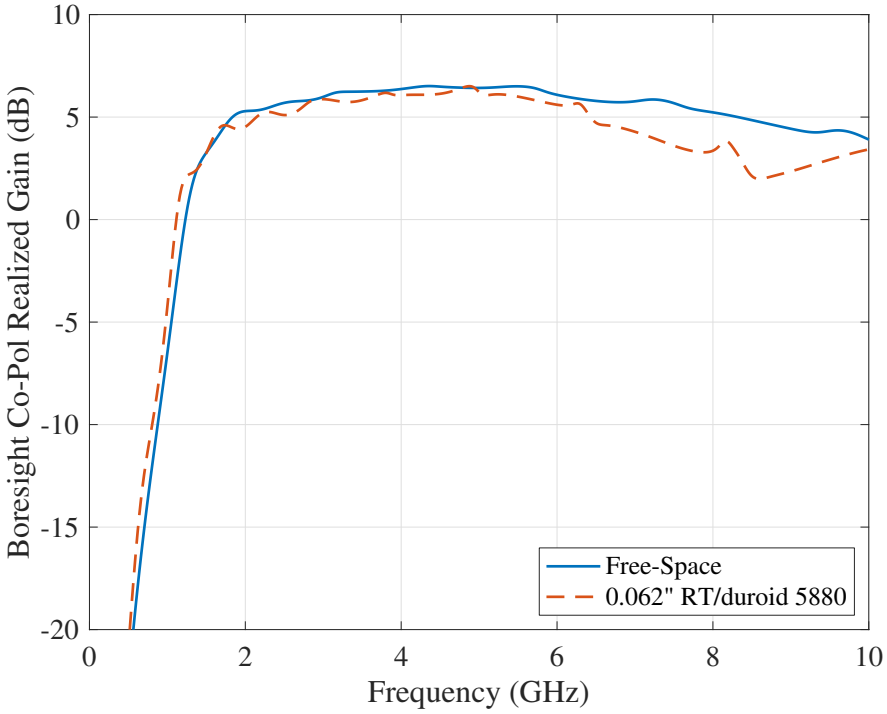

Figure 4.5: Comparison of simulated realized gain for the improved sinuous design ($P = 8$, $R_T = 5$ cm, $\alpha = 45^\circ$, $\tau = 0.7628$) in free-space and on 1.5748 mm (62 mil) thick Rogers RT/duroid® 5880 substrate.

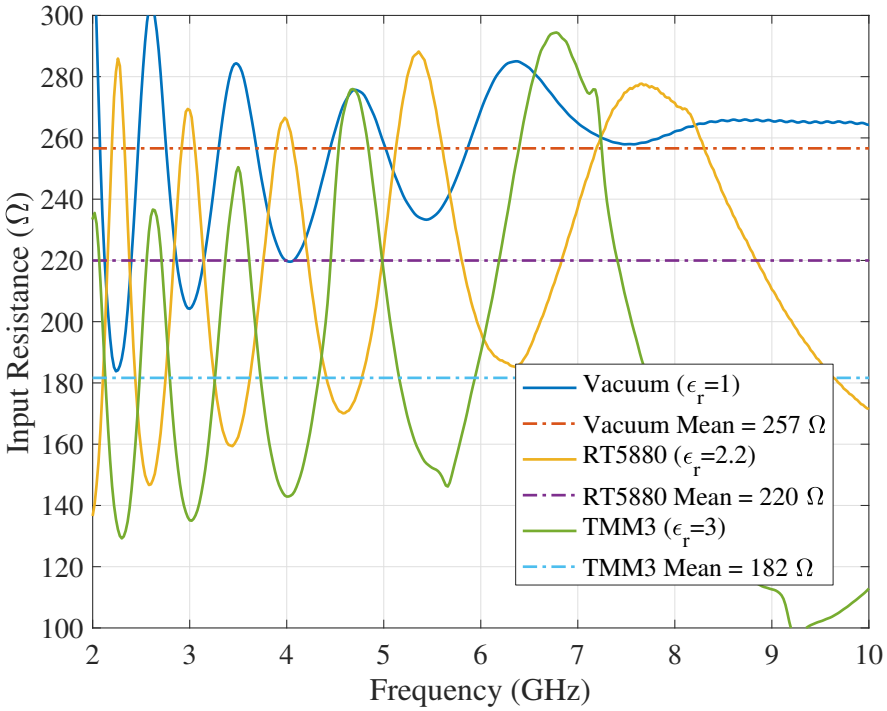

Figure 4.6: Comparison of simulated input resistance for the improved sinuous design ($P = 8$, $R_T = 5$ cm, $\alpha = 45°$, $\tau = 0.7628$) on various 1.524 mm (60 mil) thick substrates.

substrate changing the input impedance of the antenna Z_{ant} as shown by Figure 4.4. The effect of the substrate material lowers the average input resistance and produces a larger variation in input resistance over frequency since the concentration of the fields in and out of the substrate will vary with frequency [105]. Another effect of the substrate is increased ripple in the boresight gain vs. frequency, as shown in Figure 4.5.

Additional simulation results with the antenna on various thicknesses of some common substrate materials are presented in Figures 4.6 through 4.9. The results consistently show that increasing either the material thickness or dielectric constant ε_r decreases the average input resistance $\text{Re}\{Z_{ant}\}$ while also increasing the variation of input resistance over frequency. The substrate's presence also shifts the operating frequency down slightly since the antenna appears electrically larger due to the higher effective permittivity. The results for 62 mils thick RT/duriod 5880 [90] in Figure 4.7 were used as design guidance for the fabricated baluns described in Section 2.6 and Section 3.5.

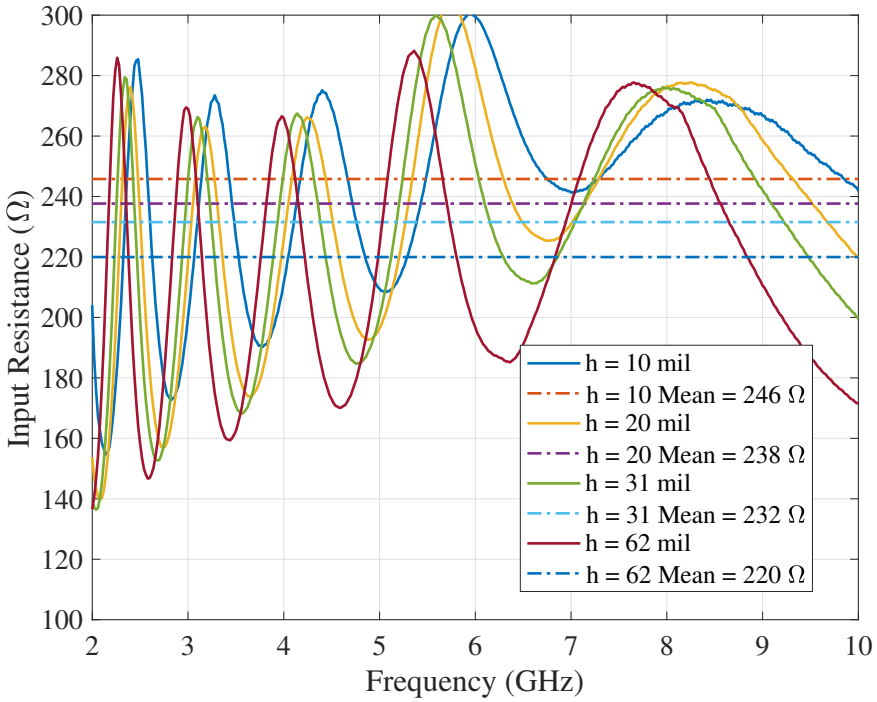

Figure 4.7: Comparison of simulated input resistance for the improved sinuous design ($P = 8$, $R_T = 5$ cm, $\alpha = 45°$, $\tau = 0.7628$) on Rogers RT/duroid® 5880 substrate ($\varepsilon_r = 2.2$) of varying thicknesses vs. free-space.

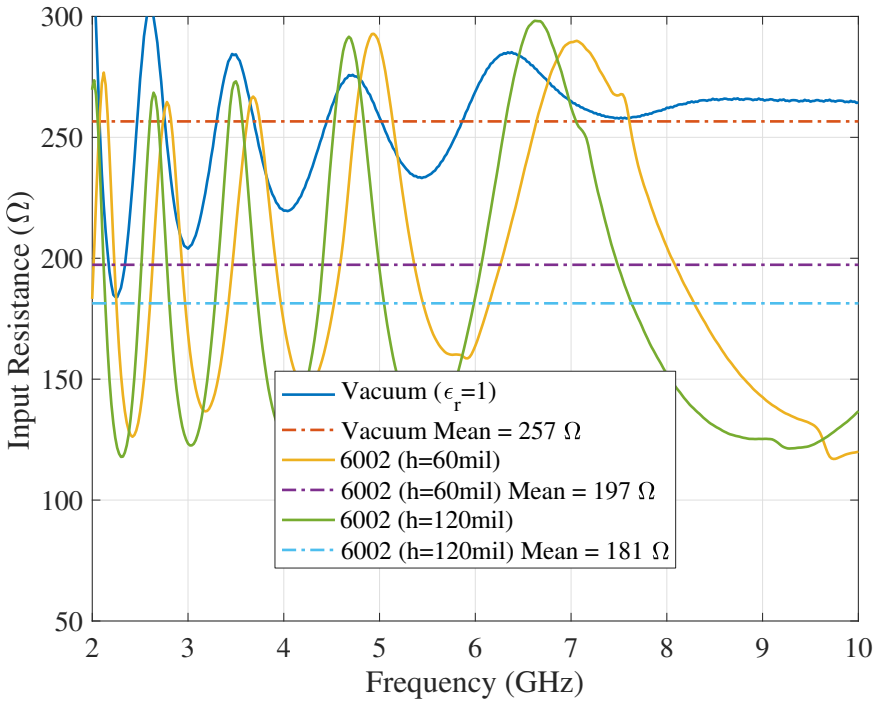

Figure 4.8: Comparison of simulated input resistance for the improved sinuous design ($P = 8$, $R_T = 5$ cm, $\alpha = 45°$, $\tau = 0.7628$) on Rogers RT/duroid® 6002 [106] substrate ($\varepsilon_r = 2.94$) of varying thicknesses vs. free-space.

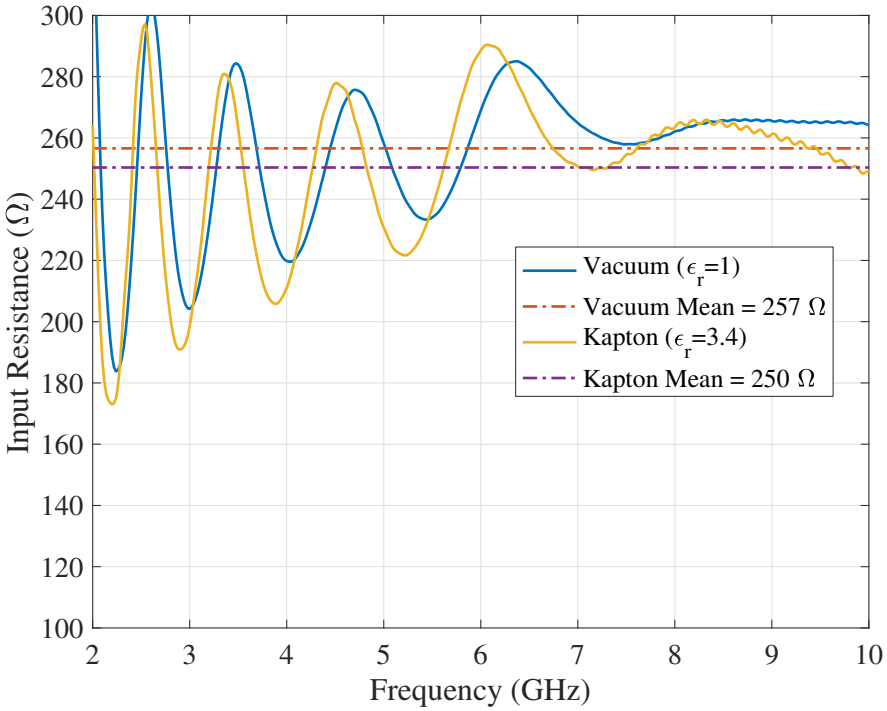

Figure 4.9: Comparison of simulated input resistance for the improved sinuous design ($P = 8$, $R_T = 5$ cm, $\alpha = 45°$, $\tau = 0.7628$) on two mil Kapton™ film vs. free-space.

4.3 Absorber Loaded Cavity

As shown in Figure 1.7, the sinuous antenna radiates bidirectionally, which is often an undesirable characteristic. The antennas constructed in Section 2.6 and Section 3.5 had a block of RF absorber placed behind the antenna to isolate it from the measurement equipment. In practical radar systems, the back lobe must be absorbed to prevent interference with the rest of the system. Absorber loaded cavities are often employed to remove the back lobe [70, 92, 52, 69, 41] although this decreases the efficiency[1] by 50% [42]. In this section, analysis is presented on sinuous antenna performance with an absorber loaded cavity backing.

A model of the sinuous antenna on 1.575 mm (62 mils) Roger's RT/duroid 5880 [90] and backed by an absorber loaded cavity was developed in CST Microwave Studio [86]. The antenna simulated was based on the improved design presented in Section 2.5 and had

[1]For GPR applications, this loss in efficiency is immaterial when the targets are very close to the antennas.

parameters $P = 16$, $R_T = 10$ cm, $\alpha = 50^\circ$, and $\tau = 0.83$. Figure 4.10 shows a cross-section of the CST model. The absorber was modeled using 19 mm layers of ECCOSORB® LS series absorbers [107] in order to replicate the performance of ECCOSORB® AN-79 free-space absorber [108]. Material properties of the LS absorbers are included in CST's built-in library of materials. An air gap h_{gap} was left between the antenna and absorber in order to minimize the impact of the absorber on the antenna performance. The absorber transitions its impedance, and subsequently, the loss, to decrease reflections from the surface and maximize absorption. The AN-79 material was extensively evaluated in [92] which influenced the choice of LS absorbers used for each layer (see Figure 4.10).

The model was simulated in CST Microwave Studio using the time-domain solver with GPU acceleration. The mesh size (≈177M mesh cells) and corresponding memory requirements were quite large which required the GPU acceleration for decent simulation times. Field maps produced by the simulations are shown for 1 GHz, 3 GHz, and 6 GHz in Figures 4.11, 4.12, and 4.13 respectively. Note that for the simulation results shown, h_{gap} was set to 1 cm. The electric-field plots indicate that the back lobes are absorbed effectively since the wavefront propagates well into the absorber. There is a slight improvement in the match (S_{11} shown in Figure 4.14) which may be attributed to higher loss at the low frequencies as shown by the boresight gain plot in Figure 4.15. The increased loss at the low frequencies is expected since the lower frequencies travel further out the antenna arms being attenuated along the way, and the absorber is closer in wavelengths at the lower frequencies.

Far-field antenna pattern cuts, both with and without the absorber loaded cavity backing are presented in Figure 4.16a through Figure 4.19. The far-field patterns show good performance as the main lobe generally matches that of the antenna without the cavity back. At the higher frequencies, a small but noticeable back lobe is evident, which may be attributed to the diffraction of waves on the outside of the metal can. Additionally, as previously discussed, the gain at 1 GHz is lower; however, this may be helped by increasing the spacing

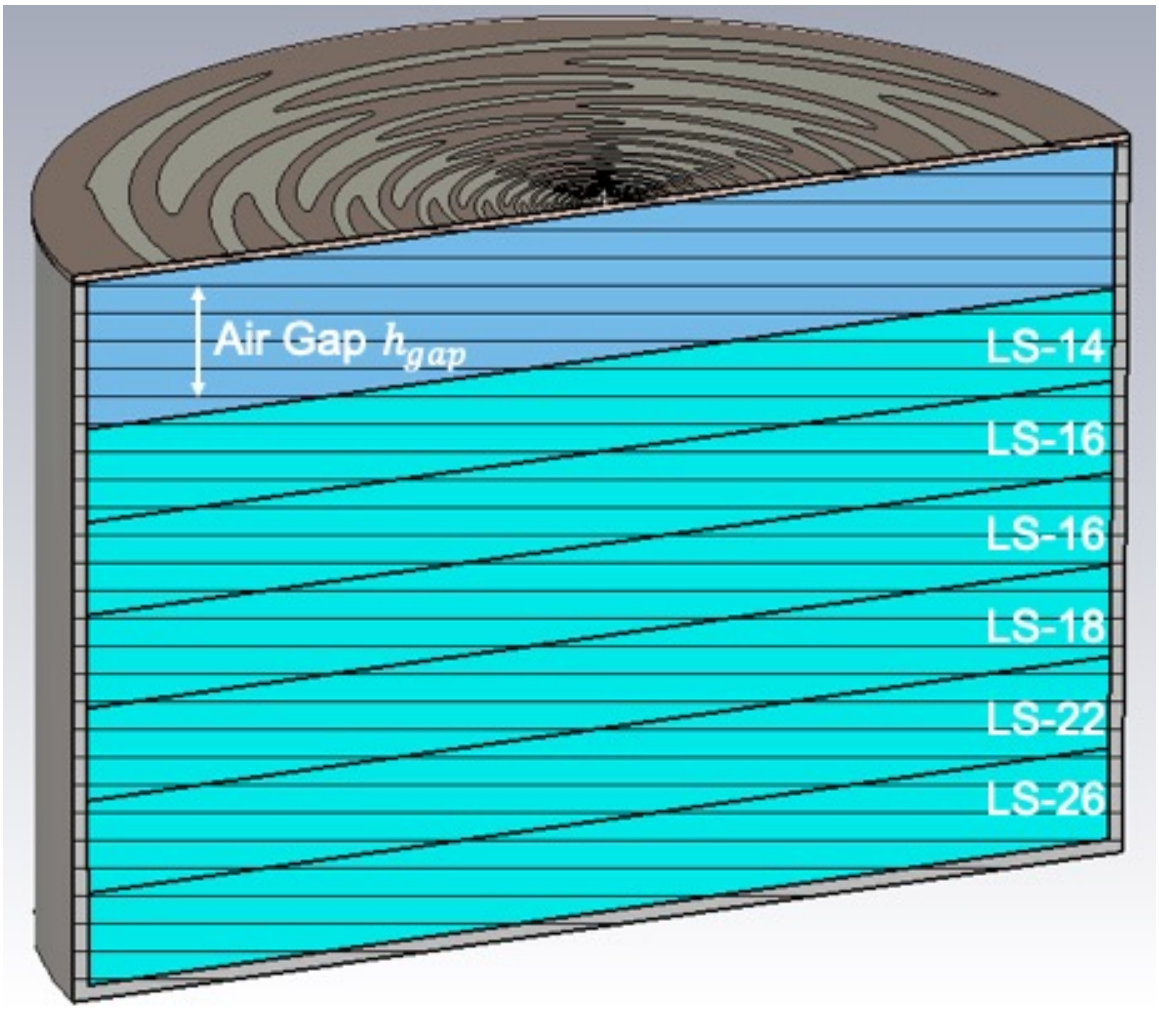

Figure 4.10: Cross-section view of the antenna with absorber loaded cavity ($h_{gap} = 3$ cm pictured) modeled in CST Microwave Studio. The antenna diameter is 20 cm and the overall height of the structure is 14.86 cm.

between the antenna and the absorber h_{gap}.

The spacing between the antenna and the absorber was varied to determine the optimum value of h_{gap}. The S_{11} and boresight gain of the antenna and cavity with varying values of h_{gap} are shown in Figure 4.20 and Figure 4.21 respectively. The 2 cm and 3 cm spacing both correlate well with the results without the absorber loaded cavity, while the 1 cm and 5 mm gaps result in increased attenuation of the lower frequencies. The larger gaps may be selected when minimizing the impact of the absorber on the radiation is desirable. However, the loss in gain may be acceptable when reducing the antenna's height is needed.

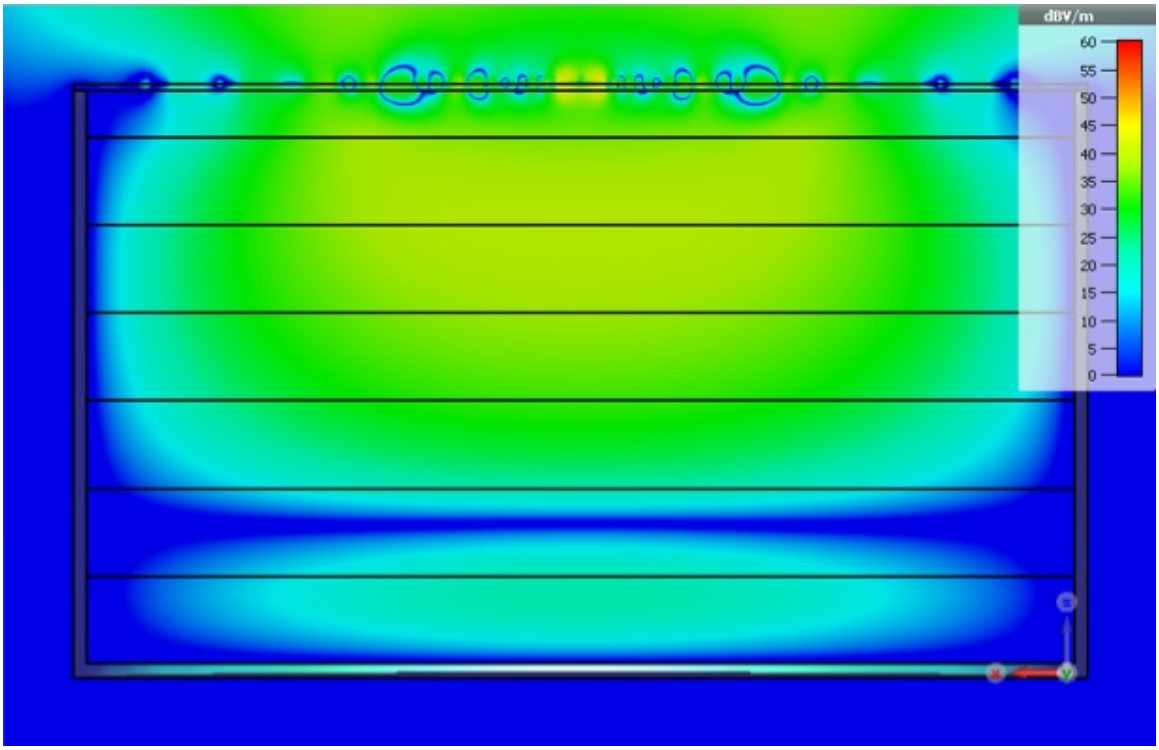

Figure 4.11: Cross-section view ($\hat{x}$-$\hat{z}$ plane) of the antenna and absorber loaded cavity showing the electric field Re$\{E_y\}$ at 1 GHz when excited to produce $\hat{y}$ polarized radiation.

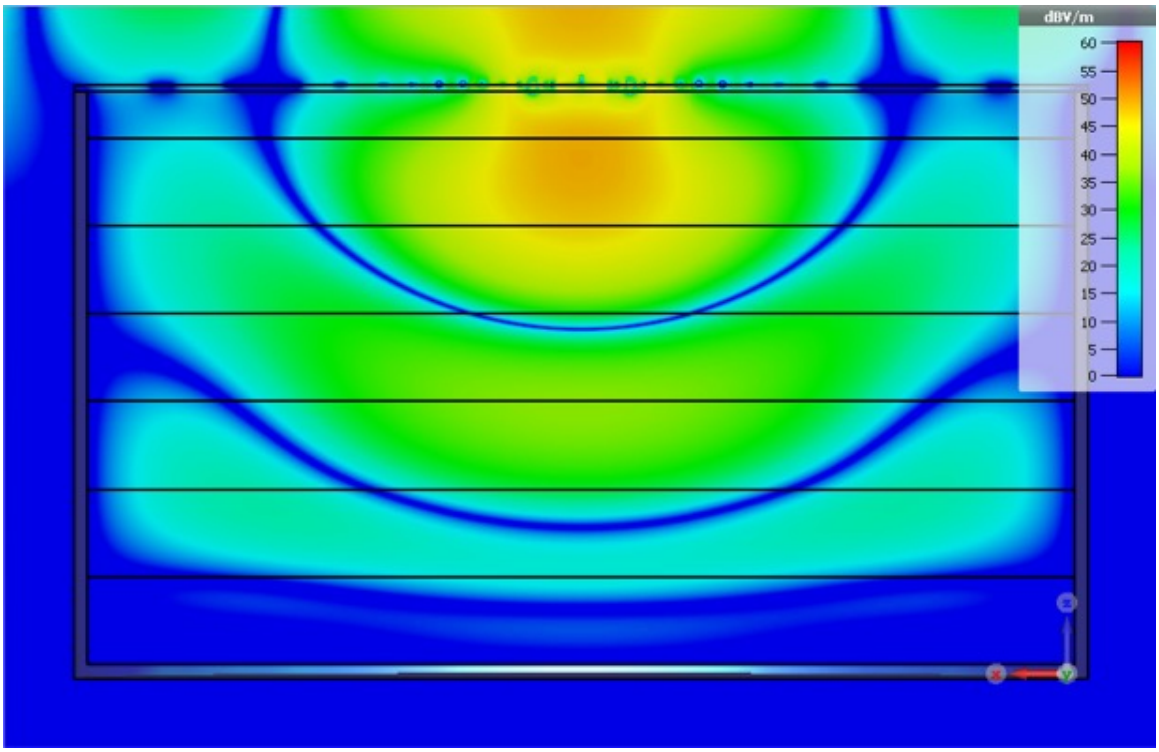

Figure 4.12: Cross-section view ($\hat{x}$-$\hat{z}$ plane) of the antenna and absorber loaded cavity showing the electric field Re$\{E_y\}$ at 3 GHz when excited to produce $\hat{y}$ polarized radiation.

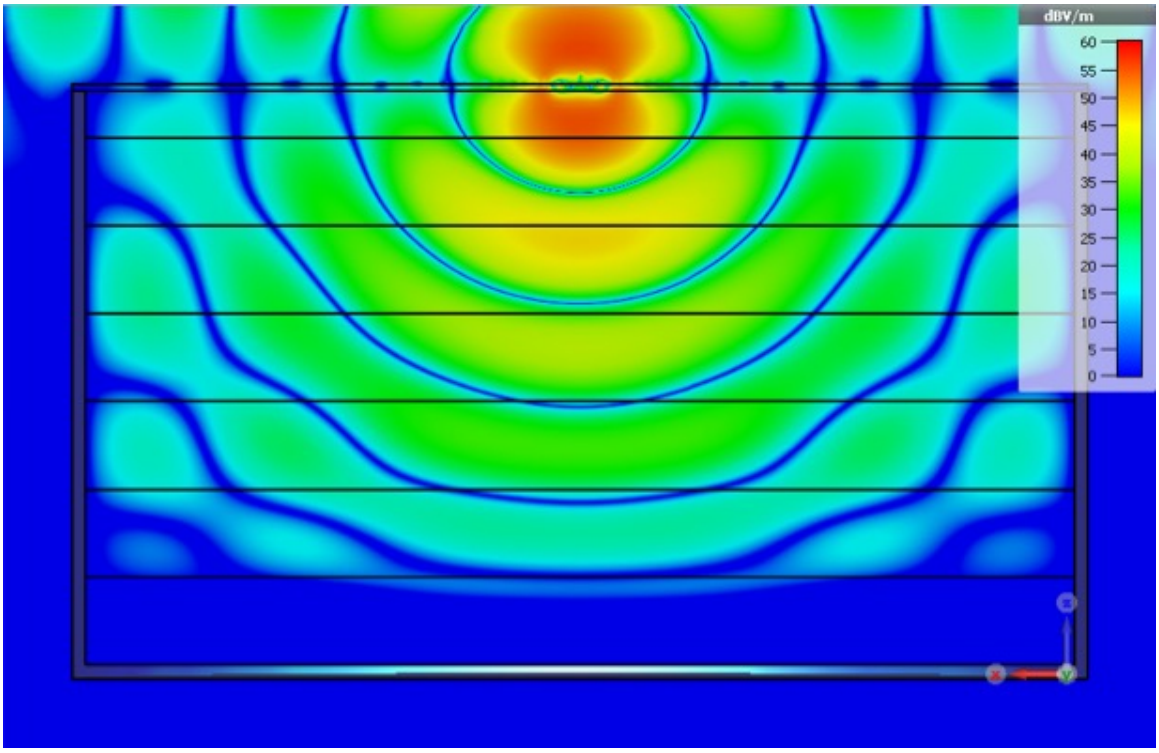

Figure 4.13: Cross-section view ($\hat{x}$-$\hat{z}$ plane) of the antenna and absorber loaded cavity showing the electric field Re$\{E_y\}$ at 6 GHz when excited to produce $\hat{y}$ polarized radiation.

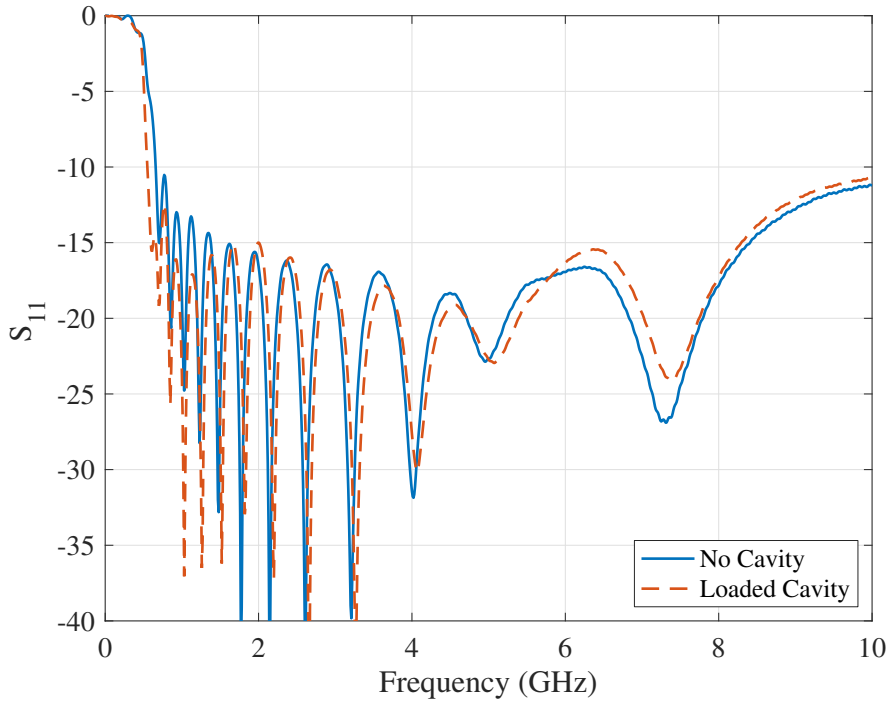

Figure 4.14: S_{11} with and without the absorber loaded cavity. Simulation ports are set to $Z_o = 267\ \Omega$.

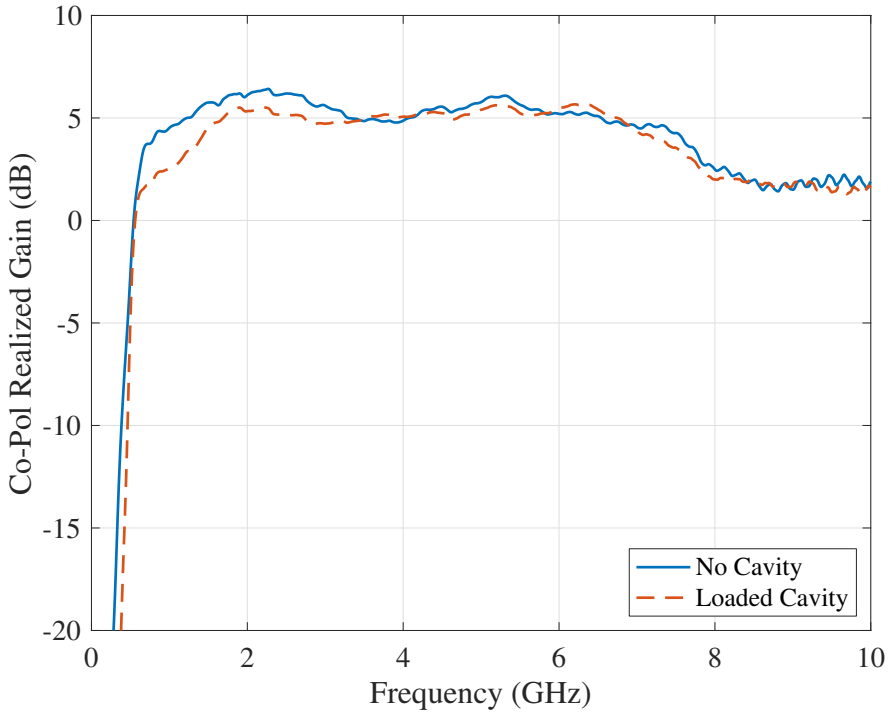

Figure 4.15: Boresight realized gain with and without absorber cavity.

4.3.1 Reducing the Profile of the Antenna with Cavity

For many applications, particularly hand-held GPR systems, low-profile antennas are desired. While the sinuous antenna is itself low-profile in nature, the addition of an absorber loaded cavity may significantly increase the antenna's height. In an effort to reduce the height of the antenna, the absorber layer thickness was reduced by half (9.5 mm per layer) and h_{gap} was kept at 1 cm as illustrated by Figure 4.22. The simulated far-field patterns are shown in Figure 4.23 and indicate the performance closely matches that of the antenna with the taller cavity. This change in absorber height resulted in the antenna structure being 20 cm wide and only 7.2 cm tall without significantly altering the antenna's radiation. Further reduction in absorber thickness will eventually reduce performance more noticeably. System designers will need to evaluate the trade-off between performance and antenna height/weight when selecting the thickness of the absorber.

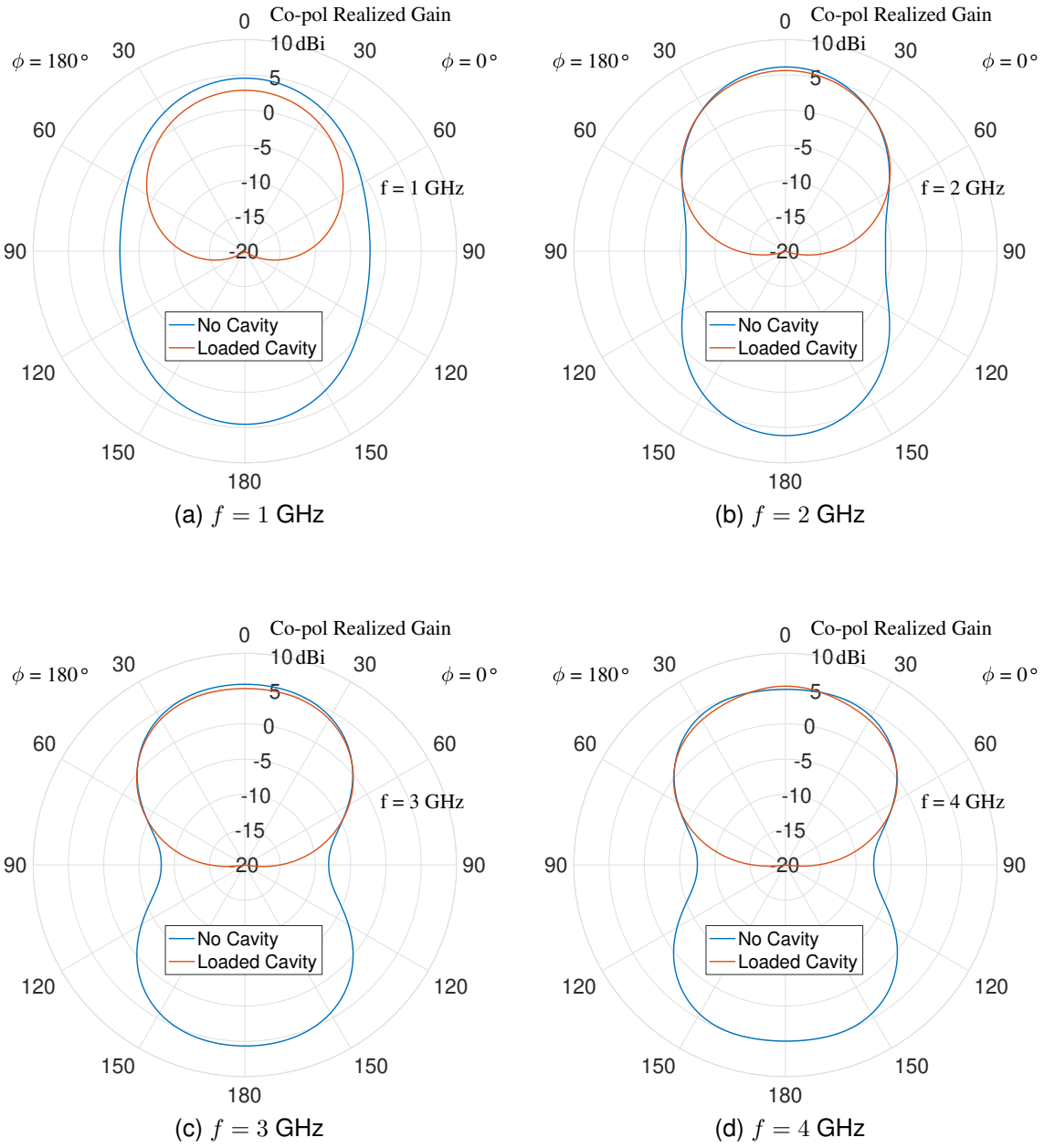

(a) $f = 1$ GHz (b) $f = 2$ GHz

(c) $f = 3$ GHz (d) $f = 4$ GHz

Figure 4.16: Sinuous antenna E-plane pattern cuts with and without the absorber loaded cavity.

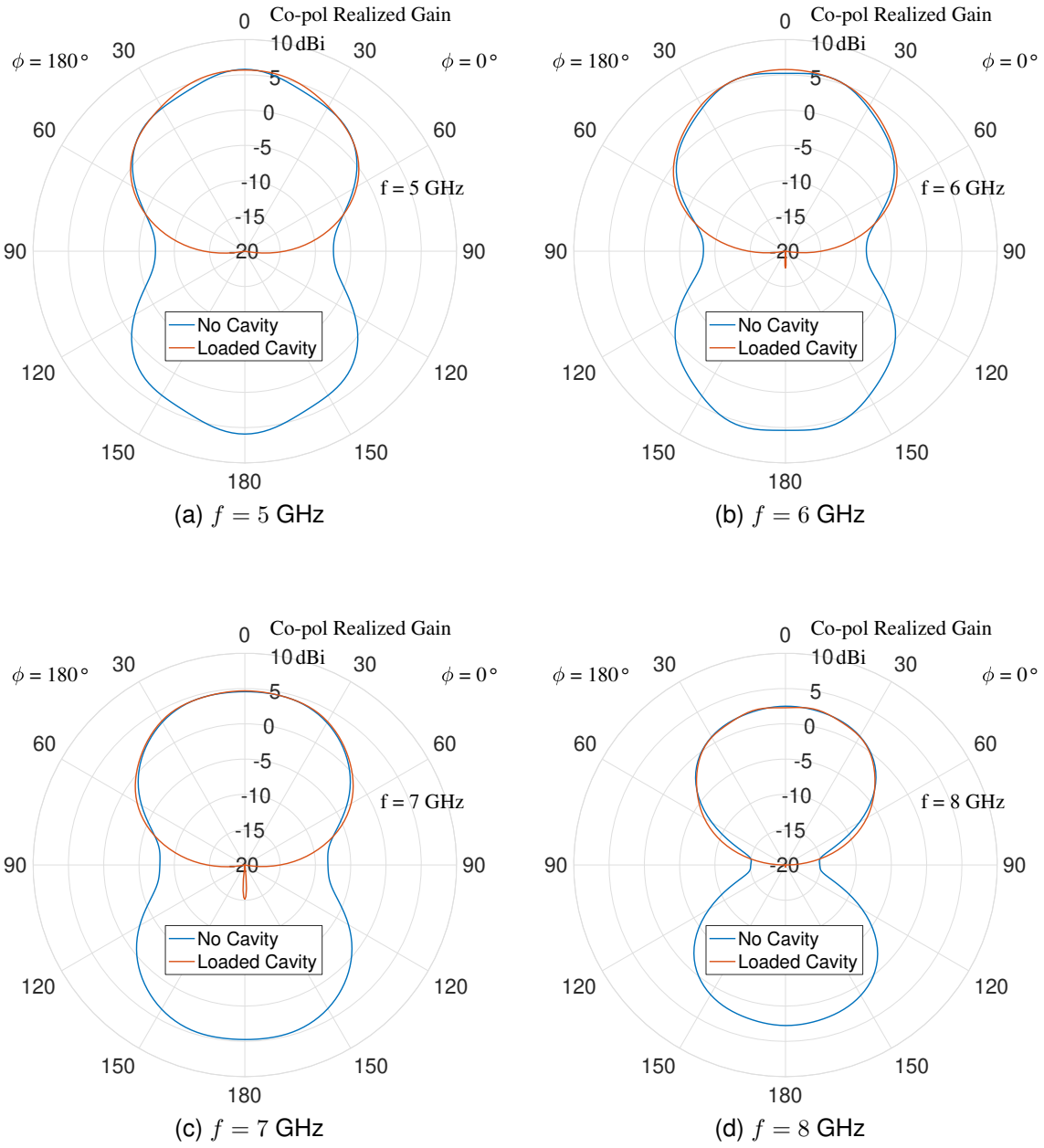

(a) $f = 5$ GHz (b) $f = 6$ GHz

(c) $f = 7$ GHz (d) $f = 8$ GHz

Figure 4.17: Sinuous antenna E-plane pattern cuts with and without the absorber loaded cavity.

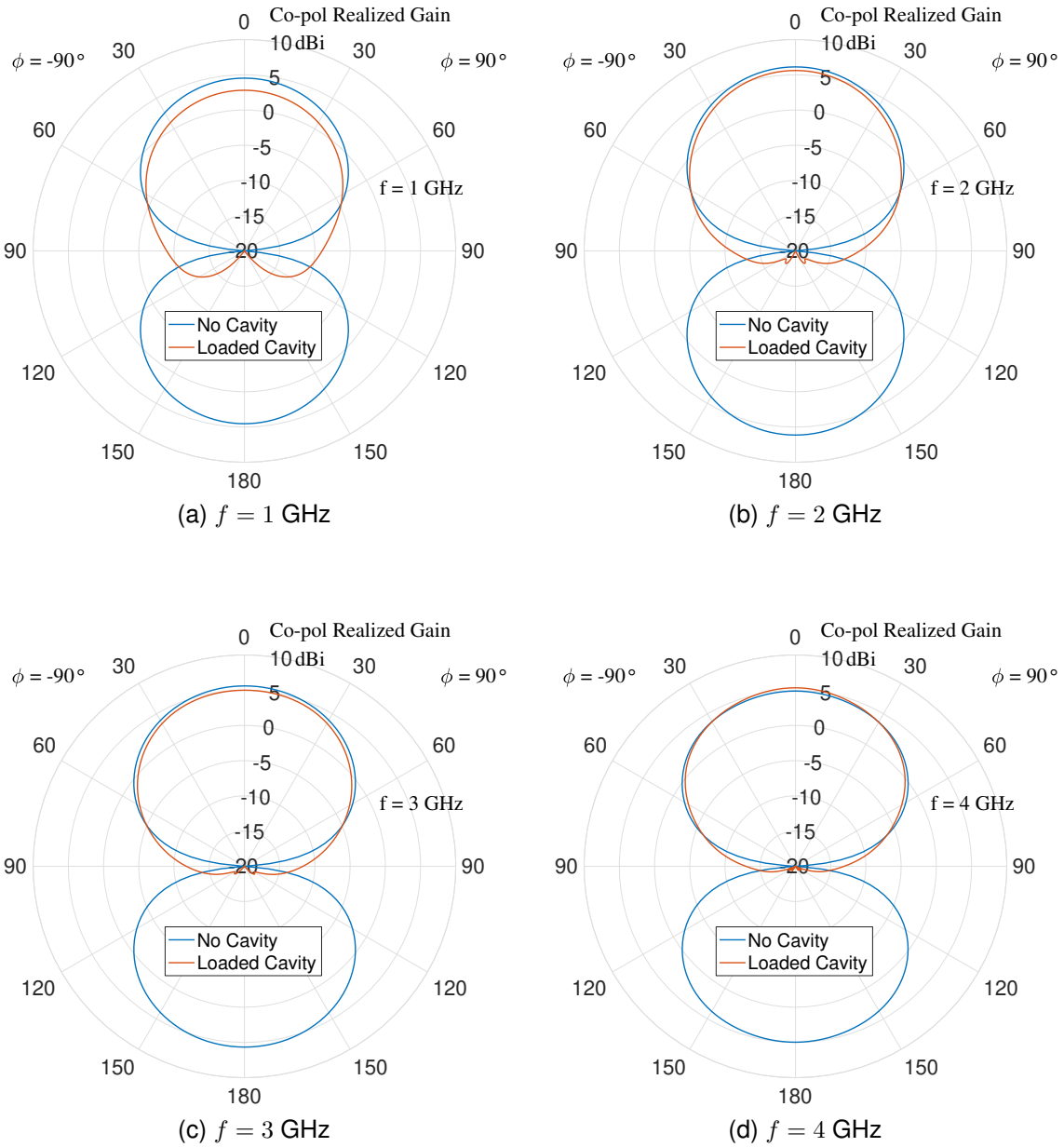

(a) $f = 1$ GHz

(b) $f = 2$ GHz

(c) $f = 3$ GHz

(d) $f = 4$ GHz

Figure 4.18: Sinuous antenna H-plane pattern cuts with and without the absorber loaded cavity.

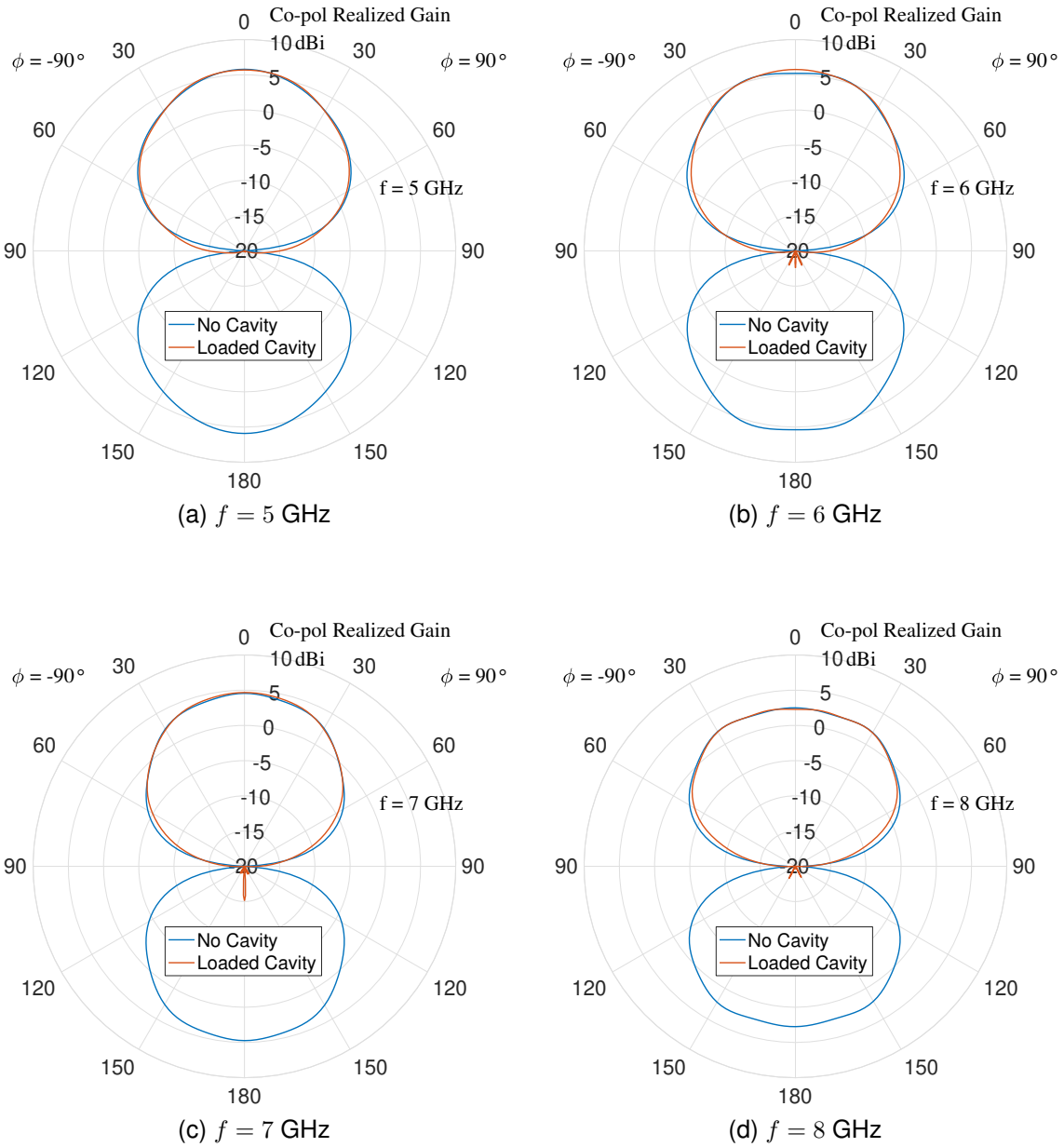

(a) $f = 5$ GHz

(b) $f = 6$ GHz

(c) $f = 7$ GHz

(d) $f = 8$ GHz

Figure 4.19: Sinuous antenna H-plane pattern cuts with and without the absorber loaded cavity.

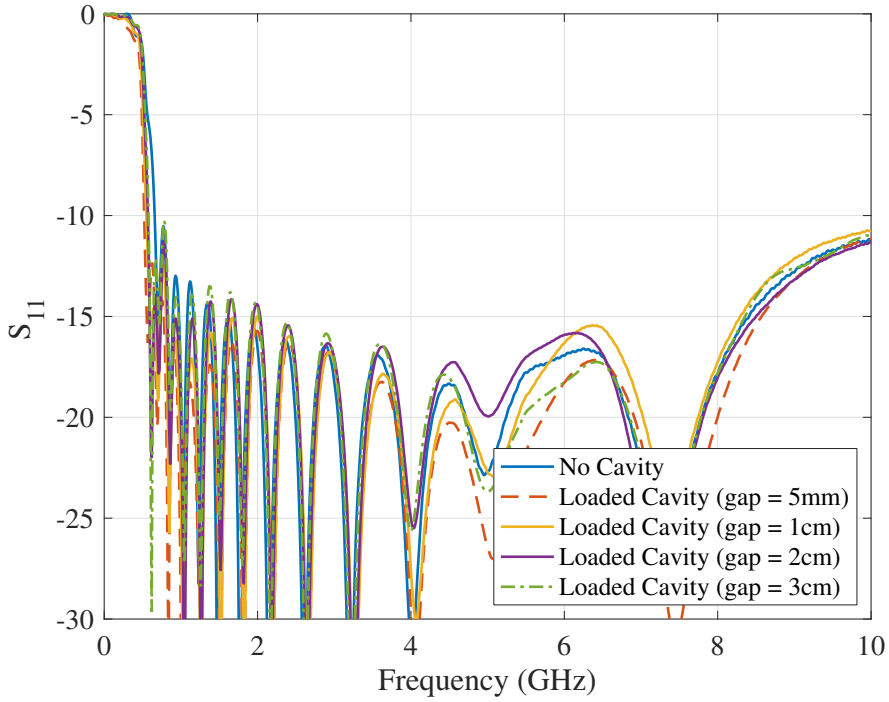

Figure 4.20: S_{11} with varied spacing between the antenna and absorber in the cavity.

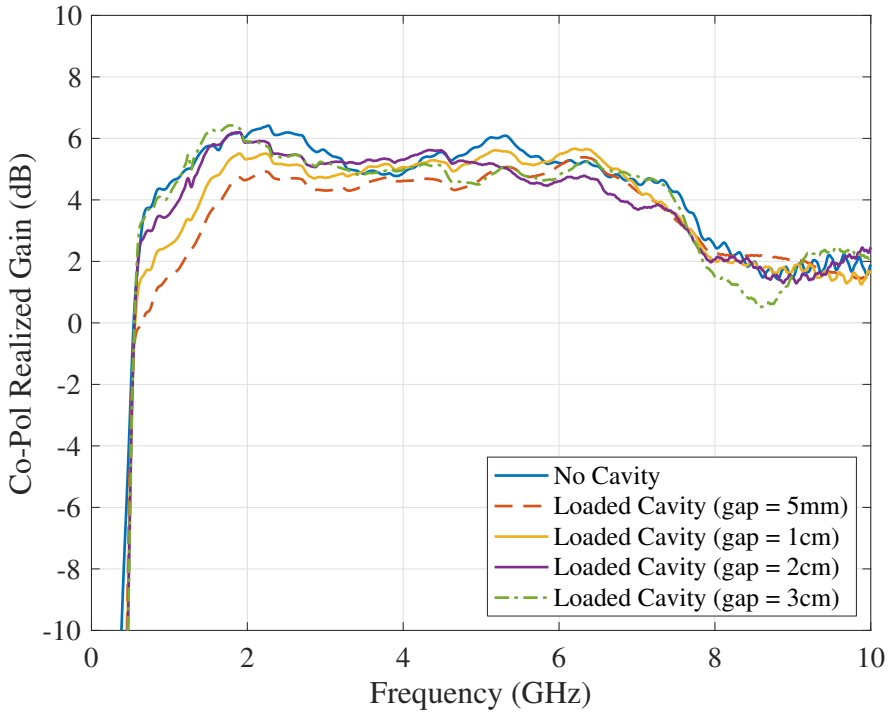

Figure 4.21: Boresight realized gain with varied spacing between the antenna and absorber in the cavity.

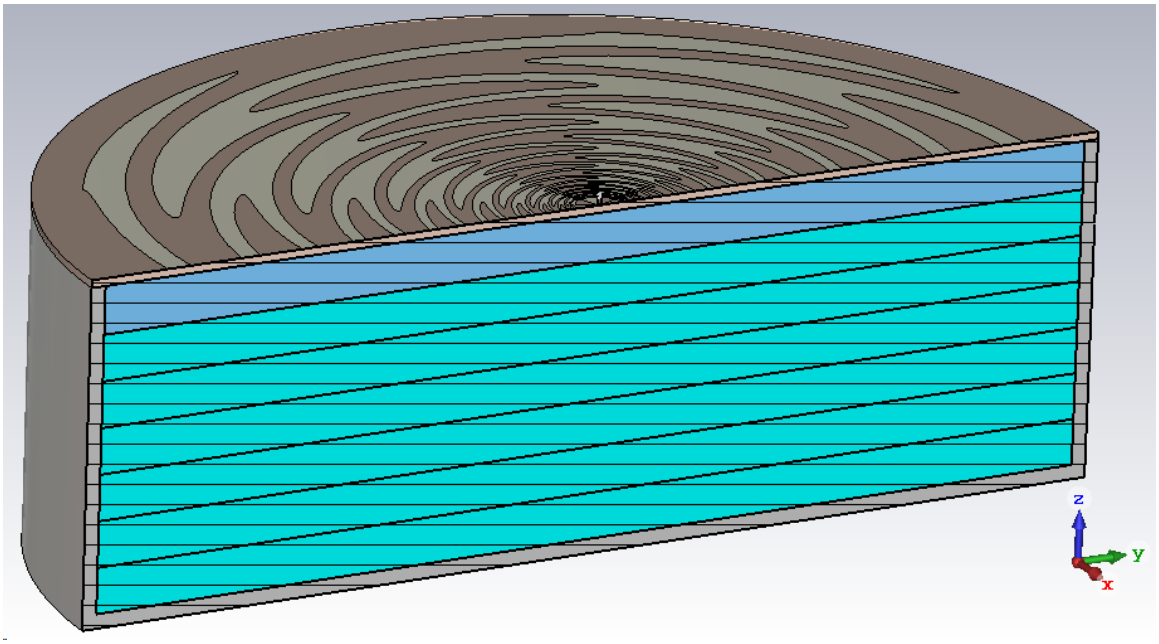

Figure 4.22: Cross-section view of the antenna with low-profile absorber loaded cavity modeled in CST Microwave Studio ($h_{gap} = 1$ cm). The antenna diameter is 20 cm, while the height of the structure is only 7.2 cm.

4.4 Summary

In this section, the theoretical input impedance of the four-arm sinuous antenna when driven in a balanced manner, i.e., mode-1, was derived analytically from Deschamp's equations [103, 39]. The theoretical calculations were shown to correlate well with full-wave simulation results from CST. The effects of adding a PCB substrate to the antenna were also evaluated. It was shown that the presence of the substrate results in a lower and more frequency-dependent input impedance Z_{ant}. Next, the addition of an absorber loaded cavity was investigated for the purpose of absorbing the back lobe radiation. The analysis showed that the addition of the cavity did not significantly alter the radiation characteristics of the front lobe. Furthermore, the absorber loaded cavity may be implemented while maintaining a relatively low antenna profile.

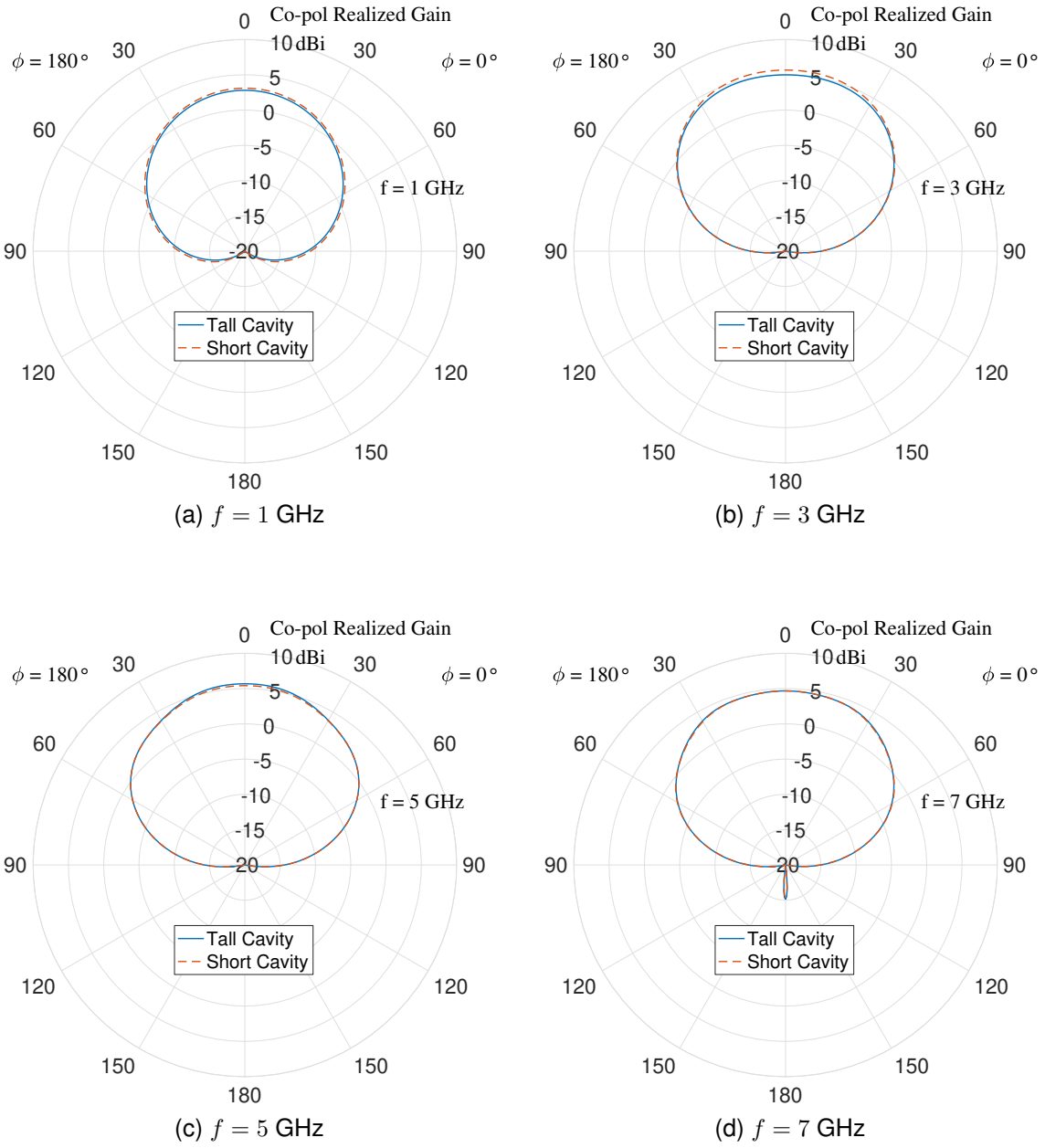

(a) $f = 1$ GHz

(b) $f = 3$ GHz

(c) $f = 5$ GHz

(d) $f = 7$ GHz

Figure 4.23: Sinuous antenna E-plane pattern cuts with the tall and reduced profile absorber loaded cavities.

CHAPTER 5
UNBALANCED SINUOUS ANTENNAS

In Section 1.1, it was shown that the common bi-static configuration of GPR antennas might result in extreme bi-static angles when attempting to sense targets close to the antenna, e.g., landmines. In an effort to reduce these angles and provide dual-polarized radiation, a resistive-vee dipole (RVD) antenna design was proposed in [7, 8] (pictured in Figure 1.3). The design interleaved four RVD elements in order to achieve isolation between transmit and receive channels while reducing bi-static angles. However, the RVD antenna has some limitations, including variable gain with frequency and the dependence on height for low-frequency performance. The sinuous antenna, on the other hand, provides relatively flat gain over frequency and requires increasing diameter only (not height) to achieve lower operating frequencies. Even when incorporating an absorber-loaded cavity, the sinuous antenna can maintain a relatively low profile as shown in Section 4.3.1.

In this chapter, a different method of driving the sinuous antenna for close-in sensing applications is proposed, which operates each arm independently, thereby isolating transmit and receive channels while still providing dual-polarized radiation in a quasi-monostatic configuration, i.e., small bistatic angles.

5.1 Unbalanced Four-Arm Sinuous Antenna

In this section, the performance of a four-arm sinuous antenna, based on the improved design developed in Section 2.5, is evaluated when each arm is driven independently, as illustrated in Figure 5.1. In the configuration shown, ports 1 and 3 will produce radiation polarized predominately in the $\hat{x}$ direction while ports 2 and 4 will in the $\hat{y}$ direction. When transmit and receive are separated to individual ports, co-polarized transmit/receive pairs will be ports 1 & 3 and ports 2 & 4 and their reciprocals. The corresponding cross-polarized

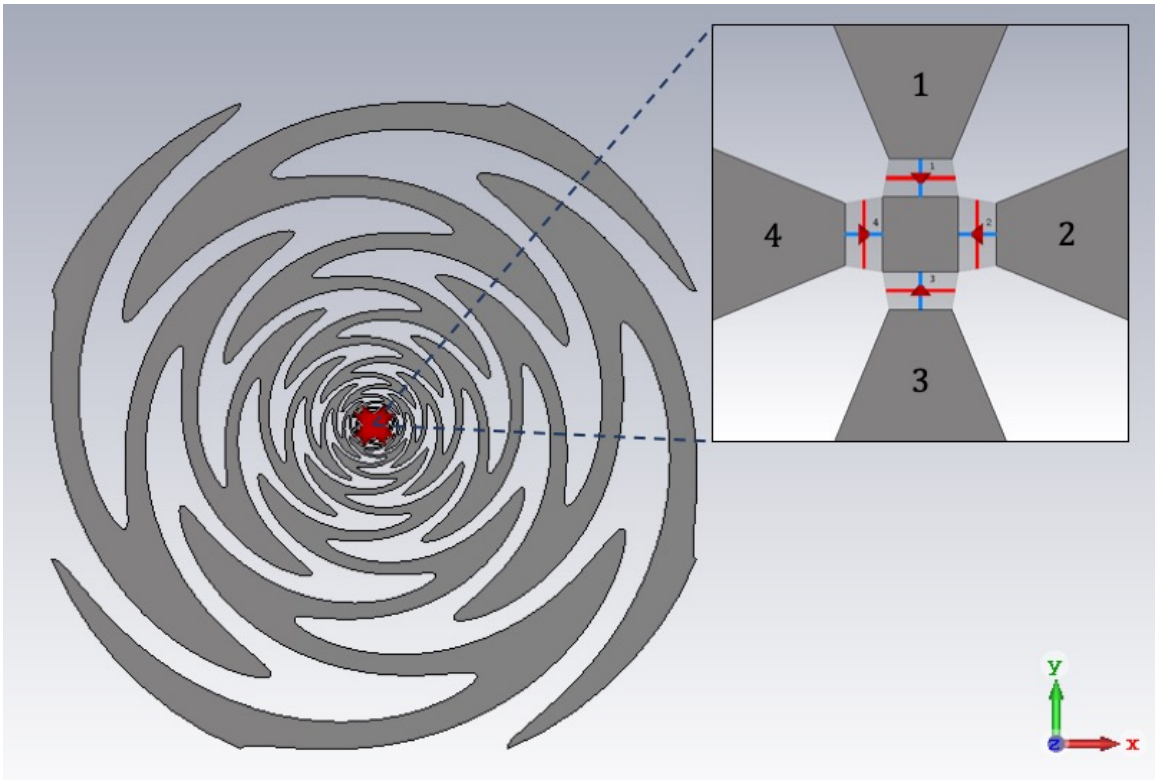

Figure 5.1: CST model of unbalanced four-arm sinuous antenna. The antenna pictured is based on the improved design from Section 2.5 and has parameters: $N = 4$ arms, $P = 12$ cells, $R_T = 9.5$ cm, $\tau = 0.773$, $\alpha = 45°$, and $\delta = 22.5°$.

transmit/receive pairs will be ports 1 & 2, 1 & 4, 2 & 3, and 4 & 3 with their reciprocals. Circular polarization can then be achieved by driving two orthogonal ports, e.g., ports 1 and 2, with a $\pm 90°$ phase progression.

5.1.1 Driving Port Impedance

As presented in Section 4.1, the admittance matrix $[\,Y\,]$ for an infinite, N-port (N-arm), self-complementary, sinuous antenna may be determined using Equation 4.2 [103].

However, independently driving the arms of the sinuous antenna invalidates the simplification used for Equation 4.7 since the loading of the other ports will have a direct impact on the input impedance Z_{ant}.

However, since the arms of the sinuous antenna are being driven independently, the simplification used for Equation 4.7 is no longer valid. In fact, the loading of the other

ports will have a direct impact on the input impedance Z_{ant}.

We can compute Z_{ant} in the unbalanced case by starting with the admittance matrix and then computing the four-port scattering parameter matrix (S-parameters) [109]. The derivation of the S-parameters from the admittance matrix is straight forward; however, it is often neglected in the literature in favor of the impedance matrix $[\,Z\,]$. The use of the admittance matrix to compute the S-parameter matrix $[\,S\,]$ here is a necessary step because the admittance matrix is non-invertible for the self-complementary structure, i.e., one cannot simply compute $[\,Z\,] = [\,Y\,]^{-1}$. The derivation of $[\,S\,]$ from $[\,Y\,]$ is provided here for reference.

Given the relationships between voltage and current at port n with characteristic admittance Y_C,

$$V_n = V_n^+ + V_n^- \tag{5.1}$$

and

$$I_n = I_n^+ - I_n^- = Y_C(V_n^+ - V_n^-), \tag{5.2}$$

the following equalities may be derived in matrix form [109]

$$[\,Y\,][\,V\,] = [\,I\,] = [\,Y\,][\,V^+\,] + [\,Y\,][\,V^-\,] = Y_c([\,V^+\,] - [\,V^-\,]) \tag{5.3}$$

where $[\,Y\,]$, for the sinuous antenna, is defined by Equation 4.2. Rearranging terms gives

$$([\,Y\,] + Y_C[\,U\,])[\,V^-\,] = (Y_C[\,U\,] - [\,Y\,])[\,V^+\,] \tag{5.4}$$

where $[\,U\,]$ is the identity matrix. The S-parameter matrix is then defined as

$$[\,S\,] = ([\,Y\,] + Y_C[\,U\,])^{-1}(Y_C[\,U\,] - [\,Y\,]). \tag{5.5}$$

The driving port impedance Z_{ant} is equivalent for all ports and may be computed from S_{11},

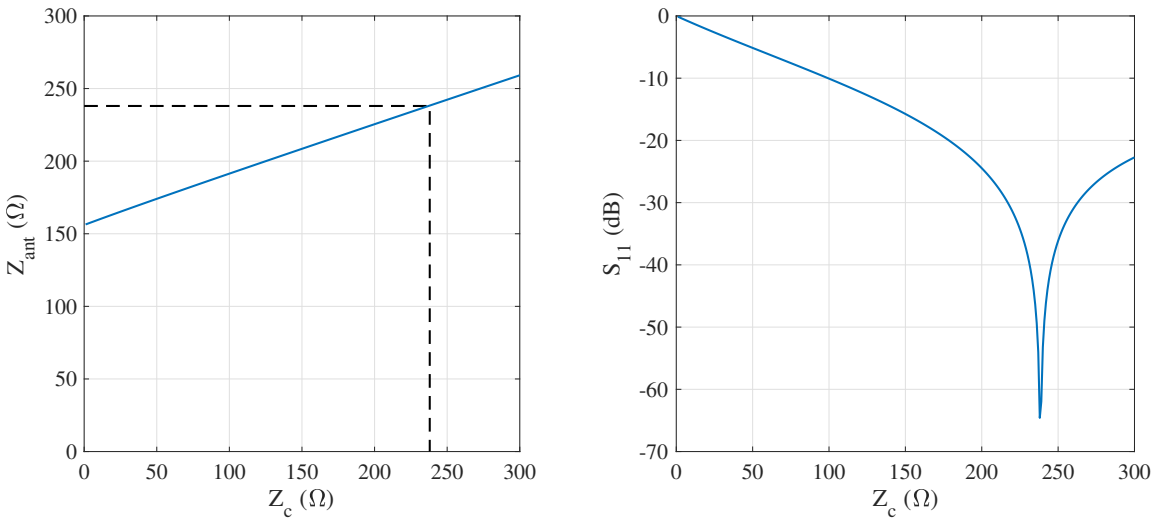

Figure 5.2: Graph of Z_{ant} and S_{11} for an infinite, four-port, unbalanced, sinuous antenna vs. feed port characteristic impedance. Notice $Z_{ant} = Z_C$ when $Z_C = 238\ \Omega$.

S_{22}, S_{33}, or S_{44} as

$$Z_{ant} = \frac{1}{Y_C}\frac{1+S_{jj}}{1-S_{jj}} \ : \ j \in \{1,2,3,4\}. \tag{5.6}$$

Graphs of Z_{ant} and S_{11} as a function of feed port characteristic impedance $Z_c = 1/Y_c$ are shown in Figure 5.2 for the four-arm sinuous antenna. The optimal characteristic impedance of the driving port is 238 Ω.

The four-port antenna shown in Figure 5.1 was simulated in CST (time-domain solver) for multiple values of Z_C and the resulting S_{11} is plotted in Figure 5.3 vs. frequency. Above 1 GHz, the reflections from the end of the antenna are minimal and the simulated S_{11} correlates well with the theoretical results for the infinite antenna provided in Figure 5.2. The S-Parameters calculated in this manner can also be used to analyze the mutual coupling between ports, which will be discussed further in Section 5.1.5.

The effects of changing the driving port's characteristic impedance may be analyzed without requiring multiple full-wave simulations since the results of a single simulation may be re-normalized for different port impedances. The N-port network impedance matrix $[Z]$, for ports with the characteristic impedance Z_C^{old}, can be calculated from the S-

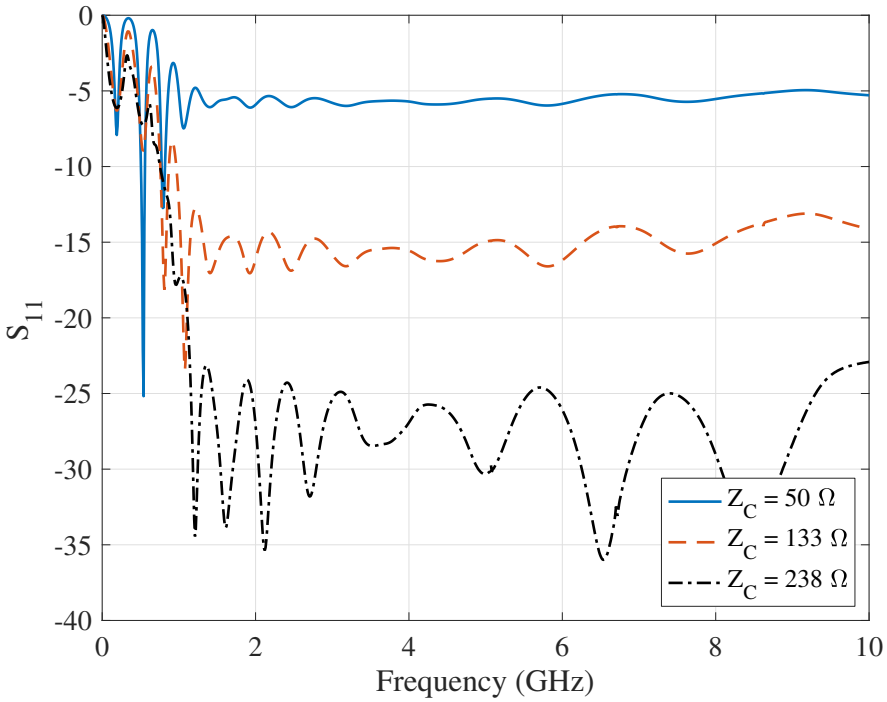

Figure 5.3: Graph of the full-wave simulated S_{11} for the four-port sinuous antenna with different driving-port characteristic impedances Z_C.

Parameters, $[S^{old}]$, as [109]

$$\frac{1}{Z_C^{old}}[\,Z\,] = ([\,U\,] + [\,S^{old}\,])([\,U\,] - [\,S^{old}\,])^{-1} \tag{5.7}$$

We can normalize the impedance matrix to a different port characteristic impedance Z_C^{new} and then compute the new S-parameters as

$$[\,S^{new}\,] = \left(\frac{1}{Z_C^{new}}[\,Z\,] + [\,U\,]\right)^{-1}\left(\frac{1}{Z_C^{new}}[\,Z\,] - [\,U\,]\right). \tag{5.8}$$

An example S-parameter re-normalization is shown in Figure 5.4 which shows S_{11} vs. frequency for the antenna simulated with $Z_C = 50\ \Omega$ and then re-normalized to $Z_C = 133\ \Omega$ and $Z_C = 238\ \Omega$. As can be seen, the re-normalized results match those from the full-wave simulations presented in Figure 5.3.

The addition of a PCB substrate to the 4-port sinuous antenna produces similar effects

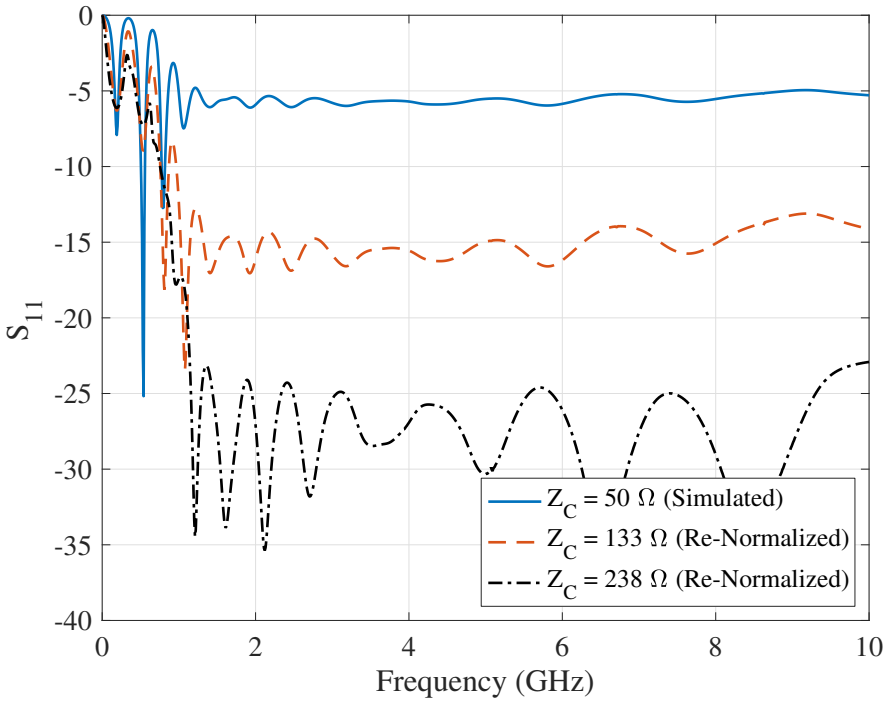

Figure 5.4: Graph of the full-wave simulated S_{11} for the four-port sinuous antenna with driving-port characteristic impedances $Z_C = 50\ \Omega$ and re-normalized to $Z_C = 133\ \Omega$ and $Z_C = 238\ \Omega$.

as those presented in Section 4.2. More specifically, the addition of a substrate resulted in a lower and more frequency-dependent input impedance Z_{ant}. Simulation results are presented in Figure 5.5 which indicates the addition of a 0.60" substrate with $\varepsilon_r = 2.94$ lowers the average input impedance by approximately 30 Ω over the 1–10 GHz band.

5.1.2 Far-Field Radiation

Driving a single arm of the sinuous antenna results in changes to the far-field radiation pattern compared to the balanced mode. The far-field patterns for the antenna in Figure 5.1 were generated in CST and are shown in Figure 5.6 which displays the magnitude of the realized gain when arm 1 is driven by an ideal port with a characteristic impedance of 238 Ω. The antenna had no substrate or absorber backing—hence the bi-directional radiation pattern. The pattern is no longer symmetric about boresight but rather tilts away from the driven arm below the $\hat{x} - \hat{z}$ plane. The peak realized gain is 2 to 3 dB lower than the

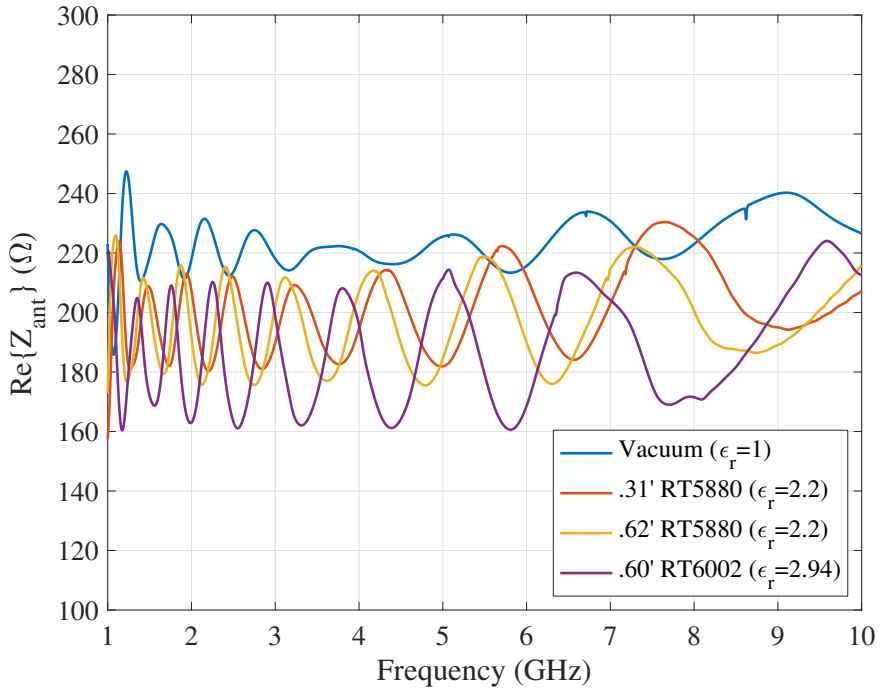

Figure 5.5: Comparison of simulated input resistance $Re\{Z_{ant}\}$ for the 4-port sinuous antenna on different substrates vs. free-space.

balanced antenna as shown by the comparison in Table 5.1. Furthermore, the peak gain moves from side to side with frequency due to the active region moving on the structure. In the balanced mode, this is counteracted by the opposite arm which combines to create a symmetric pattern. Both E-plane ($\hat{x} - \hat{z}$) and H-plane ($\hat{y} - \hat{z}$) pattern cuts of the 4-port antenna (driven on arm 1) are compared with those from the balanced mode in Figures 5.7—5.11. Notice how the E-plane pattern is more symmetric than the H-plane since the asymmetry in the excitation is in the H-plane. The balanced antenna was simulated with an ideal port ($Z_C = 267\ \Omega$) driving arm 1 against arm 3.

While the far-field patterns are degraded for the unbalanced mode compared to the balanced, the near-field radiation (discussed in the following section) will dictate the performance when the antenna is used for close-in sensing.

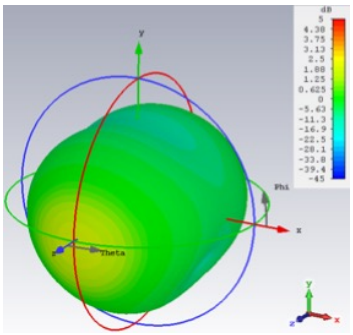

(a) $f = 1$ GHz

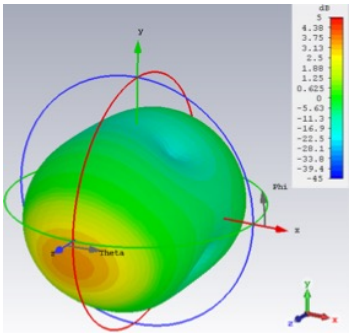

(b) $f = 2$ GHz

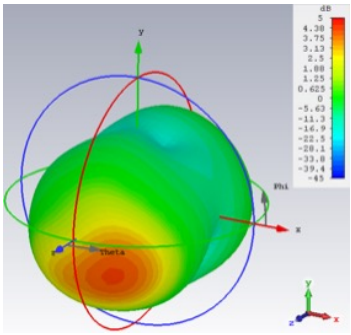

(c) $f = 3$ GHz

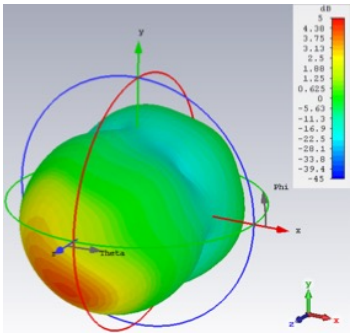

(d) $f = 4$ GHz

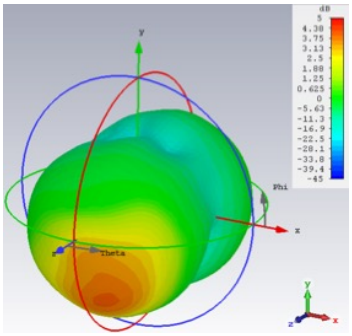

(e) $f = 5$ GHz

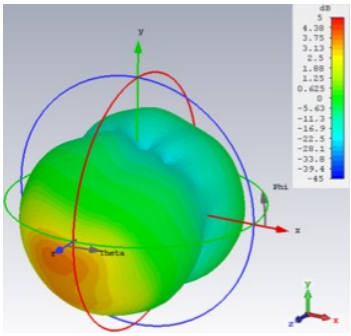

(f) $f = 6$ GHz

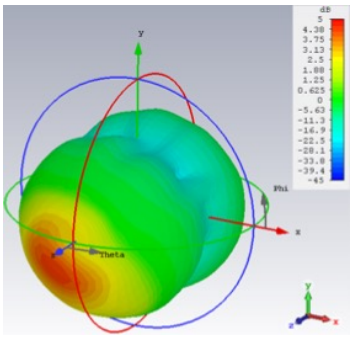

(g) $f = 7$ GHz

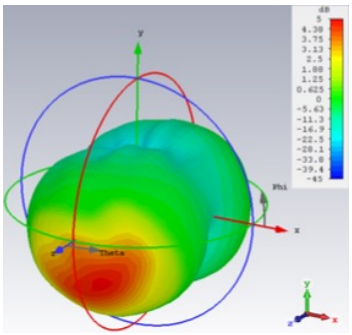

(h) $f = 8$ GHz

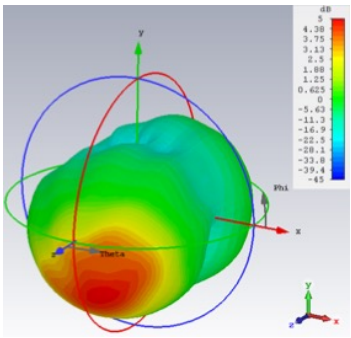

(i) $f = 9$ GHz

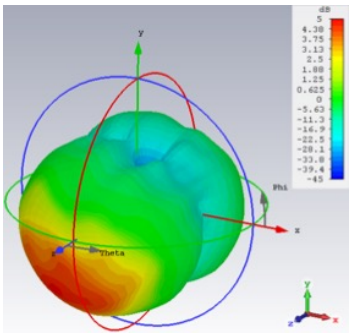

(j) $f = 10$ GHz

Figure 5.6: Far-field radiation patterns $|\vec{G}_{rlzd}|$ generated by CST of the 4-port sinuous antenna driven on arm 1 by an ideal port with characteristic impedance of 238 Ω.

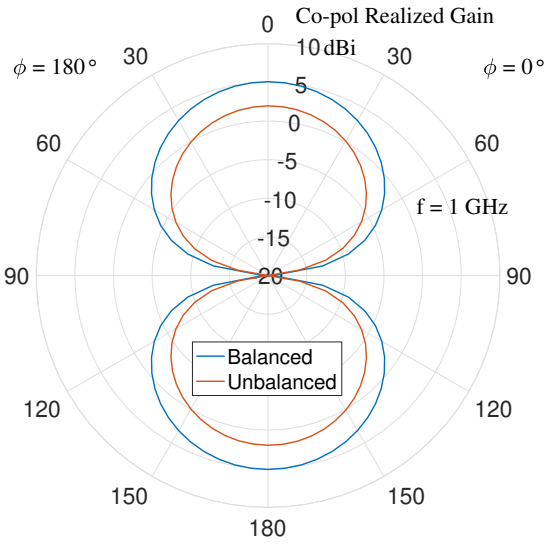

(a) E-plane; $f = 1$ GHz

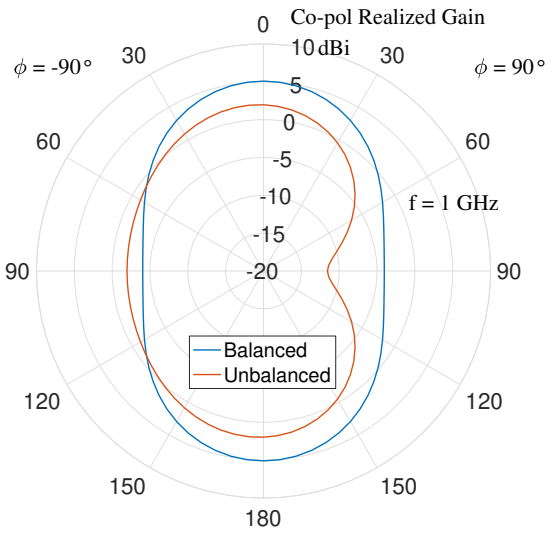

(b) H-plane; $f = 1$ GHz

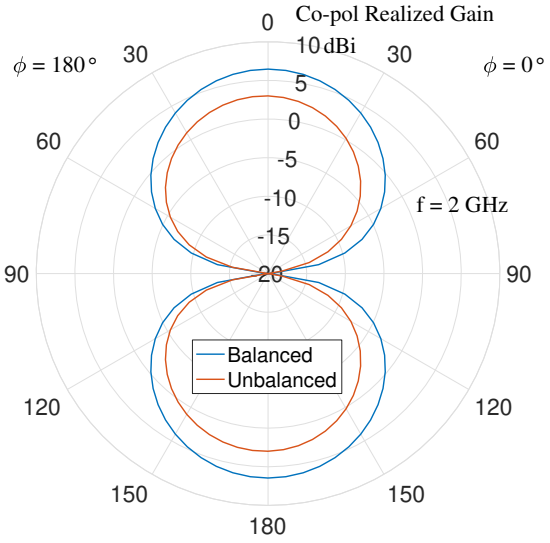

(c) E-plane; $f = 2$ GHz

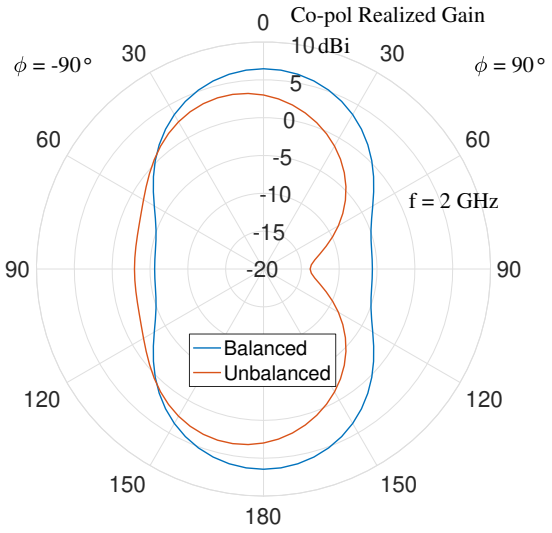

(d) H-plane; $f = 2$ GHz

Figure 5.7: Sinuous antenna pattern cuts when driven balanced (arm 1 vs. arm 3, $Z_C = 267\Omega$) and unblanaced (arm 1, $Z_C = 238\Omega$) at 1 GHz and 2 GHz.

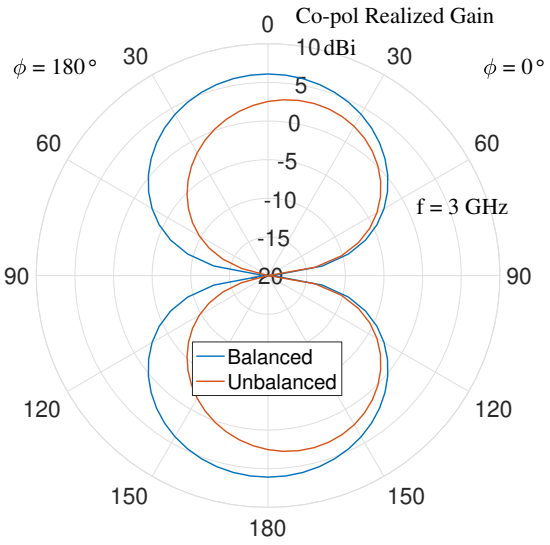

(a) E-plane; $f = 3$ GHz

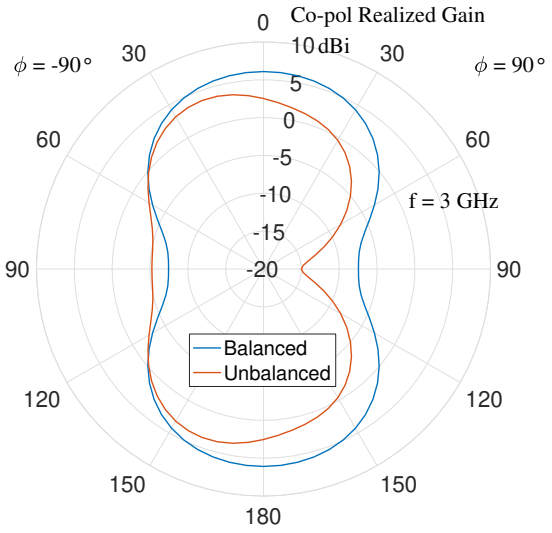

(b) H-plane; $f = 3$ GHz

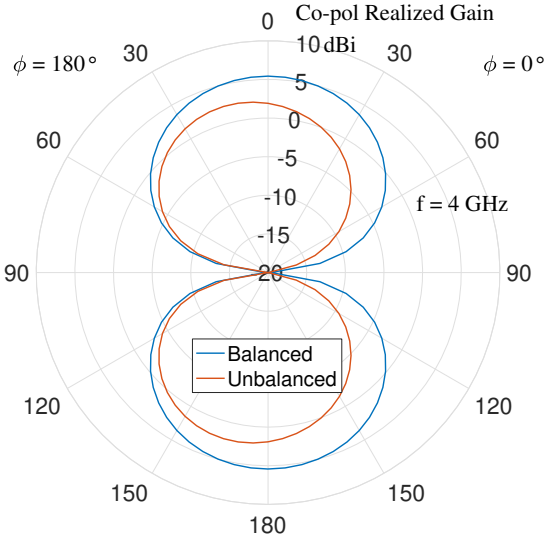

(c) E-plane; $f = 4$ GHz

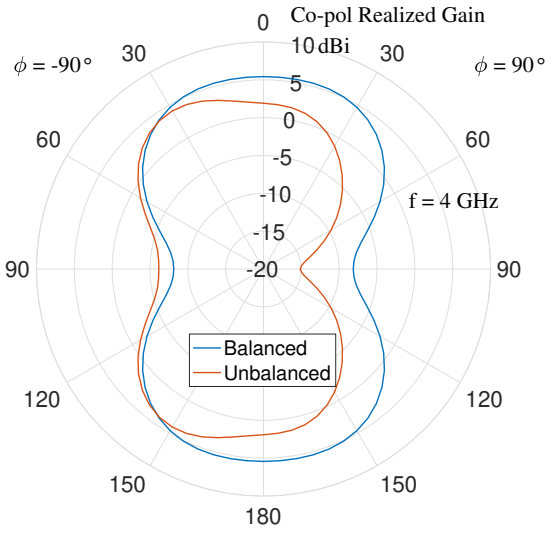

(d) H-plane; $f = 4$ GHz

Figure 5.8: Sinuous antenna pattern cuts when driven balanced (arm 1 vs. arm 3, $Z_C = 267\Omega$) and unblanaced (arm 1, $Z_C = 238\Omega$) at 3 GHz and 4 GHz.

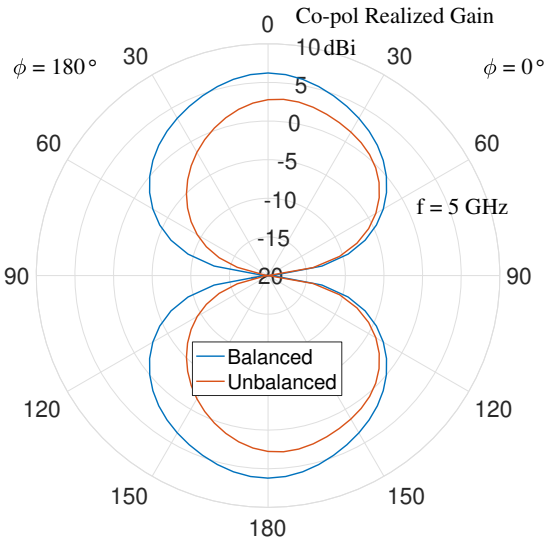

(a) E-plane; $f = 5$ GHz

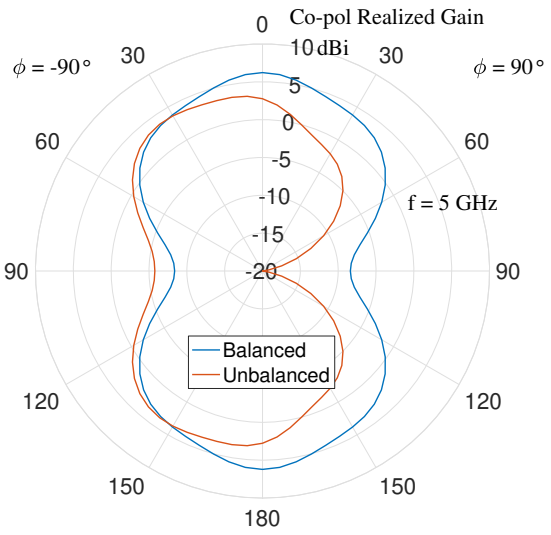

(b) H-plane; $f = 5$ GHz

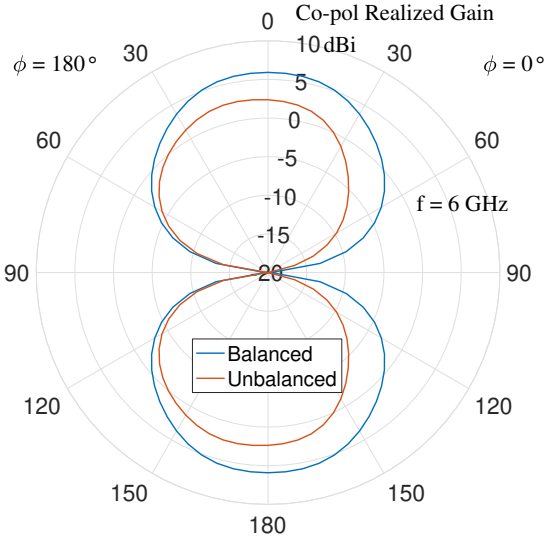

(c) E-plane; $f = 6$ GHz

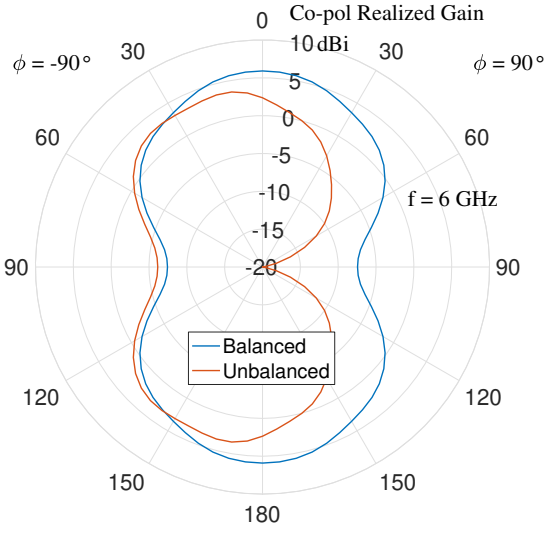

(d) H-plane; $f = 6$ GHz

Figure 5.9: Sinuous antenna pattern cuts when driven balanced (arm 1 vs. arm 3, $Z_C = 267\Omega$) and unblanaced (arm 1, $Z_C = 238\Omega$) at 5 GHz and 6 GHz.

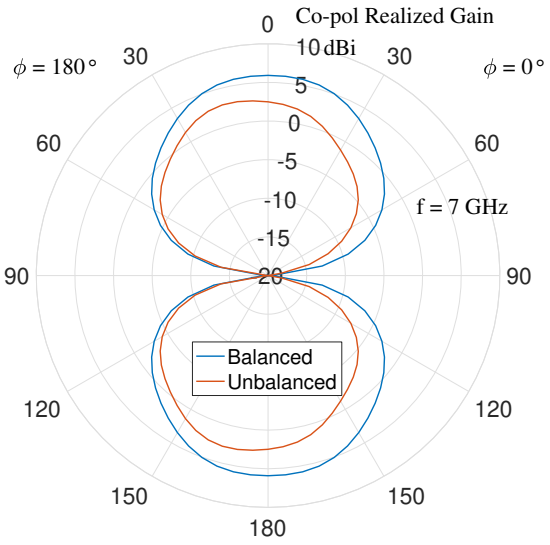

(a) E-plane; $f = 7$ GHz

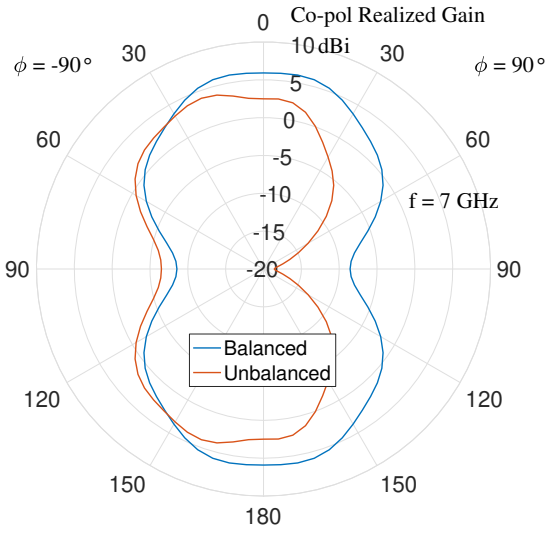

(b) H-plane; $f = 7$ GHz

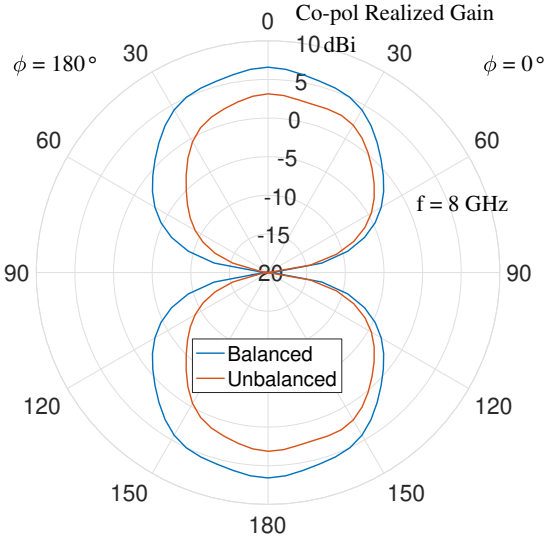

(c) E-plane; $f = 8$ GHz

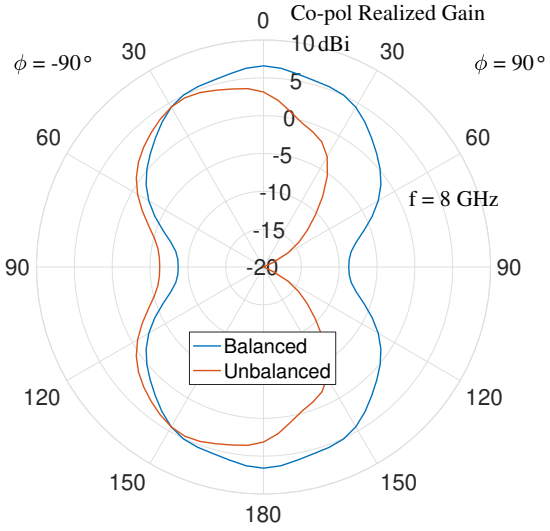

(d) H-plane; $f = 8$ GHz

Figure 5.10: Sinuous antenna pattern cuts when driven balanced (arm 1 vs. arm 3, $Z_C = 267\Omega$) and unblanaced (arm 1, $Z_C = 238\Omega$) at 7 GHz and 8 GHz.

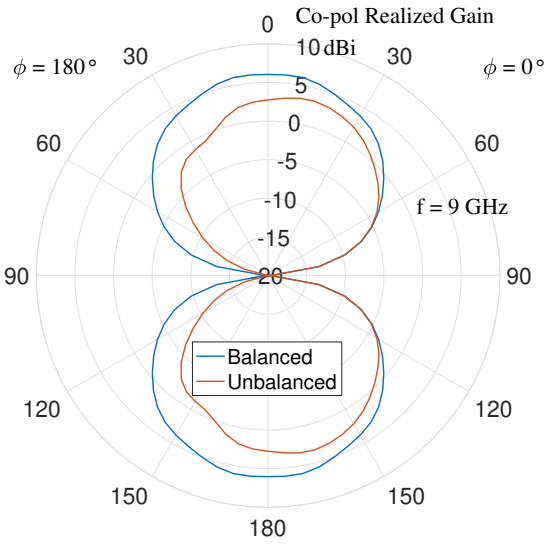

(a) E-plane; $f = 9$ GHz

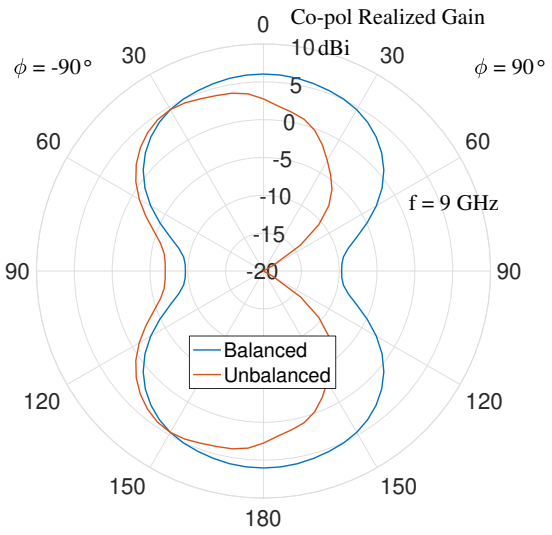

(b) H-plane; $f = 9$ GHz

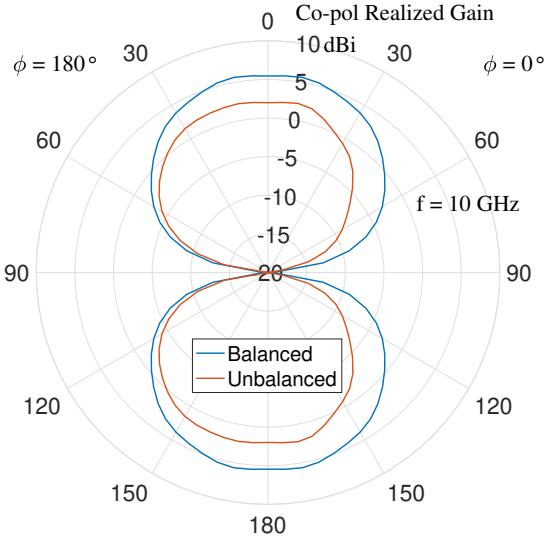

(c) E-plane; $f = 10$ GHz

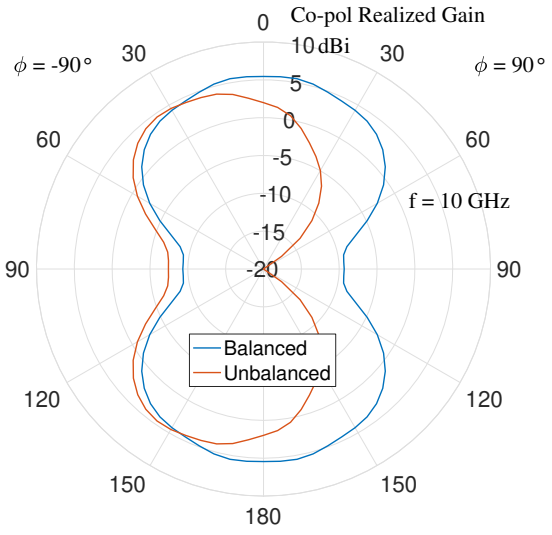

(d) H-plane; $f = 10$ GHz

Figure 5.11: Sinuous antenna pattern cuts when driven balanced (arm 1 vs. arm 3, $Z_C = 267\Omega$) and unblanaced (arm 1, $Z_C = 238\Omega$) at 9 GHz and 10 GHz.

Table 5.1: Comparison of peak realized gain (simulated) for the sinuous antenna when driven balanced (arms 1 vs. 3, $Z_C = 267\ \Omega$) and unblanaced (arm 1, $Z_C = 238\ \Omega$). For the balanced case, the peak gain is on the z-axis where $G_\theta = G_x$ and $G_\phi = G_y$ for this table.

	Balanced		Unbalanced	
f (GHz)	G_θ (dB)	G_ϕ (dB)	G_θ (dB)	G_ϕ (dB)
1	5.09	5.09	1.96	1.98
2	6.46	6.46	2.99	3.43
3	6.09	6.09	3.70	3.83
4	5.44	5.45	3.13	4.25
5	6.21	6.21	3.06	3.89
6	5.91	5.91	3.30	3.53
7	5.95	6.05	4.00	4.11
8	6.58	6.58	4.10	4.70
9	6.07	6.03	4.19	4.88
10	5.82	5.53	3.83	4.52

5.1.3 Near-Field Sensitivity

It is desired to compute the unbalanced antenna's response to targets in the near-field to understand the antenna's performance for close-in targets. However, this requires the target to be included in the full-wave simulation, and the simulation must be repeated many times with the target in different locations. Such an analysis would require a prohibitively large amount of computation time with currently available equipment. However, for small targets, the response may be computed with a single forward simulation using reciprocity.

In [92] it was shown that the calibrated response from a target, as measured by port j of the antenna when transmitting on port k, may be computed from the incident fields via reciprocity [105] as

$$V_{j,k}(\omega) = -\frac{j\omega\varepsilon Z}{2V_{in}(\omega)}\left(\vec{\mathbf{E}}^{inc,j}(\omega,\vec{\mathbf{r}})\cdot\alpha_e\cdot\vec{\mathbf{E}}^{inc,k}(\omega,\vec{\mathbf{r}})\right) \tag{5.9}$$

where Z represents the characteristic impedance of the ports, V_{in} is the incident voltage at the antenna driving port, ε is the permittivity of the medium, α_e is the polarizability tensor which relates the field values to the current induced on the target, and $\vec{\mathbf{r}}$ is the spacial

vector that locates the target. Note that Equation 5.9 assumes no magnetic current loops are induced on the target [92]. Additionally, if the target is small and linear, the response simplifies to [92]

$$V_{j,k}(\omega) = -\frac{j\omega 4\pi h^3 \varepsilon Z}{6V_{in}(\omega)[\ln(2h/a) - 1]} \left(\vec{\mathbf{E}}^{inc,j}(\omega, \vec{\mathbf{r}}) \cdot \hat{\mathbf{n}}\right)\left(\vec{\mathbf{E}}^{inc,k}(\omega, \vec{\mathbf{r}}) \cdot \hat{\mathbf{n}}\right) \tag{5.10}$$

where $\hat{\mathbf{n}}$ is a vector parallel to the scatterer. This result may be generalized away from target specifics by normalization which results in the following sensitivity metric

$$M_s^{j,k}(\omega) = \frac{\left(\vec{\mathbf{E}}^{inc,j}(\omega, \vec{\mathbf{r}}) \cdot \hat{\mathbf{n}}\right)\left(\vec{\mathbf{E}}^{inc,k}(\omega, \vec{\mathbf{r}}) \cdot \hat{\mathbf{n}}\right)}{\max\limits_{\vec{\mathbf{r}}} \left[\left(\vec{\mathbf{E}}^{inc,k}(\omega, \vec{\mathbf{r}}) \cdot \hat{\mathbf{n}}_{co-pol}\right)\left(\vec{\mathbf{E}}^{inc,k}(\omega, \vec{\mathbf{r}}) \cdot \hat{\mathbf{n}}_{co-pol}\right)\right]}. \tag{5.11}$$

Here the normalization was chosen as the peak monostatic response from a co-polarized target. Due to the rotational symmetry of the antenna, the sensitivity M_s will be presented for $k = 1$ (transmit port) over the range $j = 1$, 2, and 3 (receive ports). Three linear target orientations will be considered: a co-polarized target $\hat{\mathbf{n}} = \hat{x}$, a cross-polarized target $\hat{\mathbf{n}} = \hat{y}$ which should produce only a small response due to polarization mismatch, and an equally co- and cross-polarized target $\hat{\mathbf{n}} = (\hat{x} + \hat{y})/\sqrt{2}$.

The sensitivity metric, computed from the forward-modeled fields in air, is plotted on the $x = 0$, $y = 0$, and $z = 100$ mm planes at 4 GHz in Figures 5.12, 5.13, and 5.14, respectively. In these figures, only M_{11}, M_{21}, and M_{31} are graphed since all the other cases are simply related to these. For the $\hat{\mathbf{n}} = \hat{x}$ case, the response is seen to be strongest for the ($j = 1$,$k = 1$) and ($j = 3$,$k = 1$) pairs since the target is co-polarized with both the transmit and receive antenna arms. Similar to the far-field patterns, driving only a single arm of the antenna produces asymmetric radiation; however, the area directly beneath the antenna is well illuminated. Furthermore, when transmitting on arm 1 and receiving on arm 3, the co-polarized sensitivity becomes more symmetric since the arms are mirrored versions of each other. For the $\hat{\mathbf{n}} = \hat{y}$ case, the response is seen to be weakest for the ($j = 1$,$k = 1$) and ($j = 3$,$k = 1$) pairs since the target is cross-polarized with both the transmit and receive

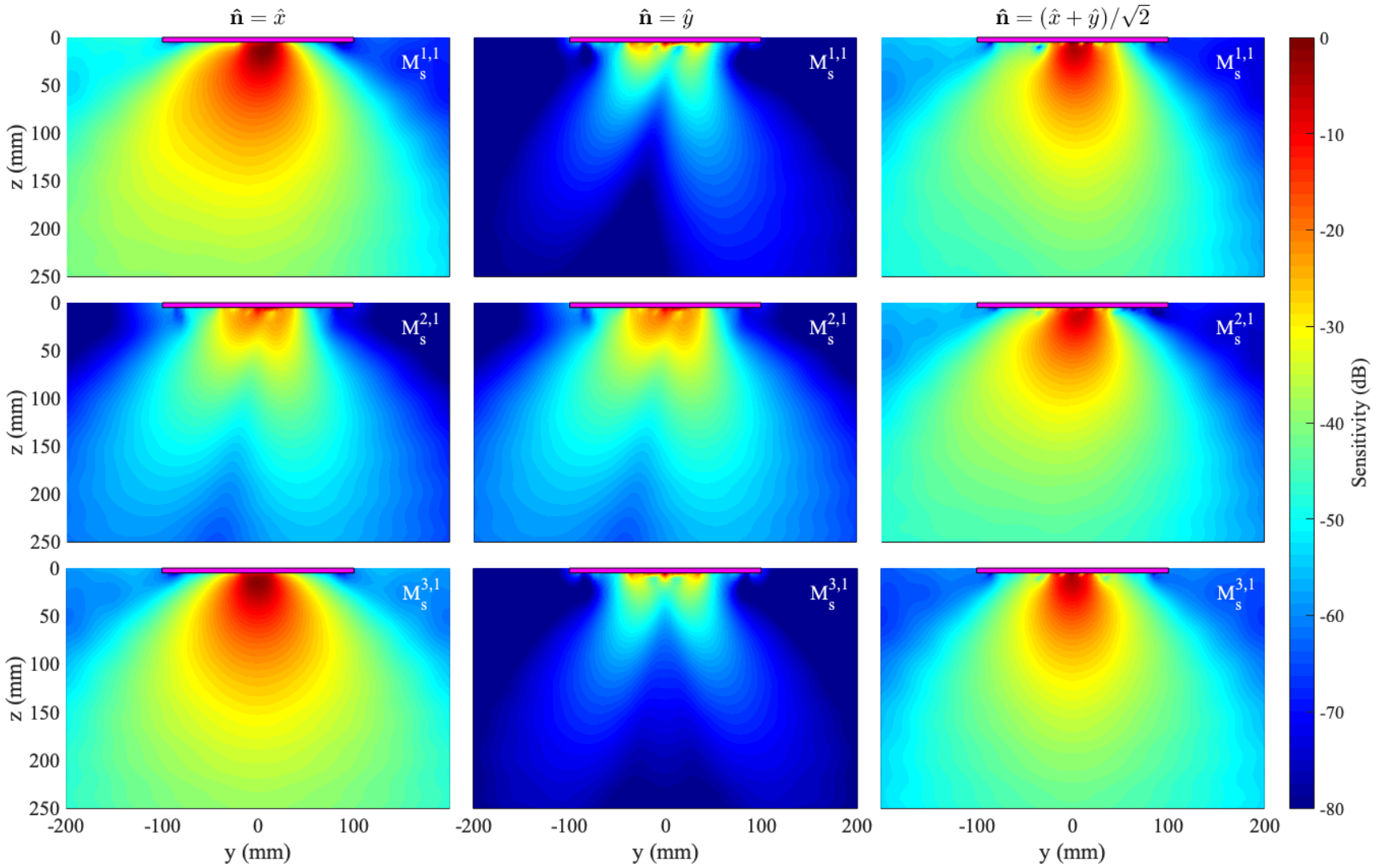

Figure 5.12: Pseudo-color plot of the sensitivity metric $M_s^{j,k}$ on the $x = 0$ plane at 4 GHz. The metric shows co- and cross-polarized performance of the four-port antenna for linear targets at multiple orientations defined by $\hat{\mathbf{n}}$.

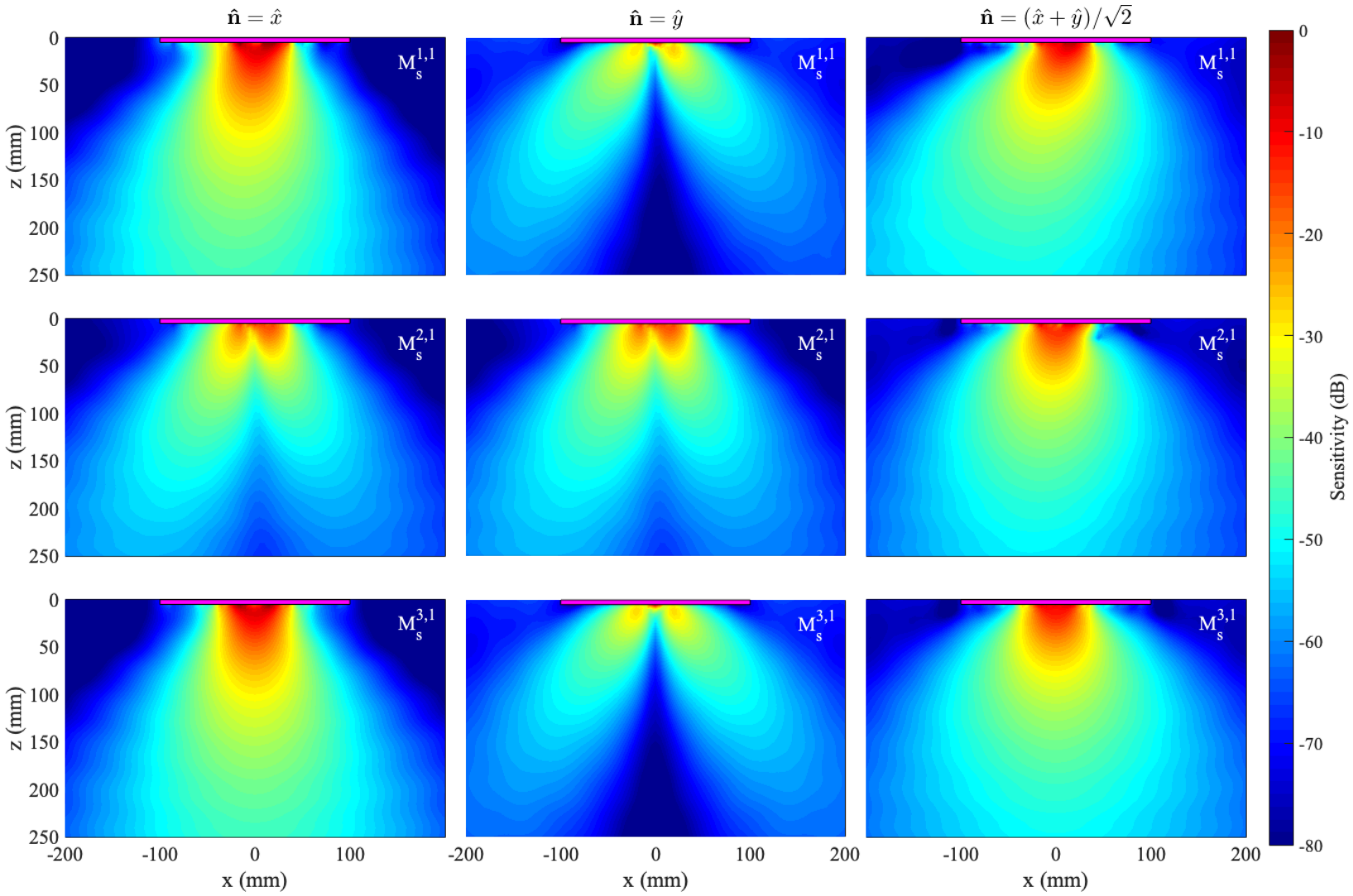

Figure 5.13: Pseudo-color plot of the sensitivity metric $M_s^{j,k}$ on the $y = 0$ plane at 4 GHz. The metric shows co- and cross-polarized performance of the four-port antenna for linear targets at multiple orientations defined by $\hat{\mathbf{n}}$.

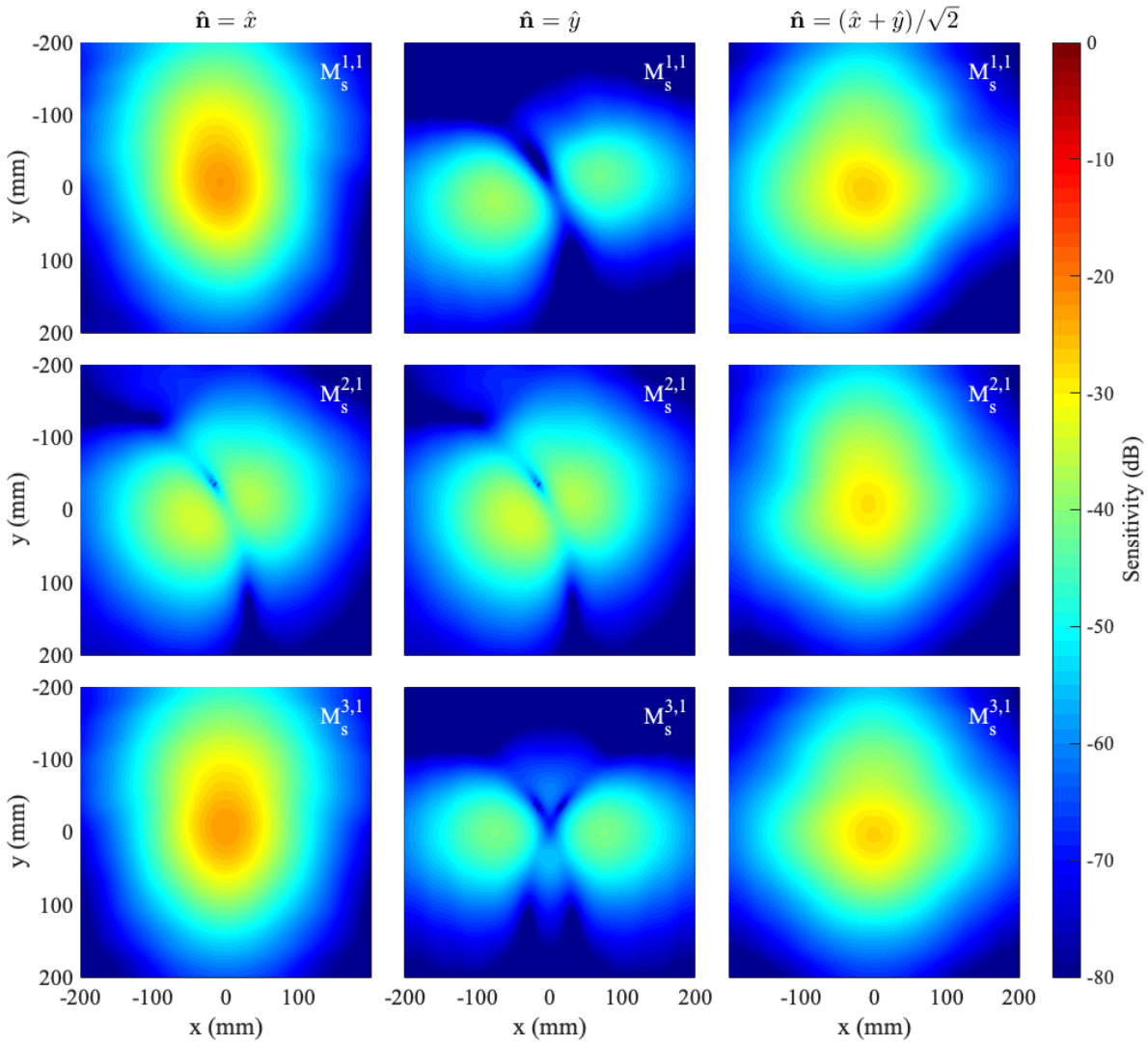

Figure 5.14: Pseudo-color plot of the sensitivity metric $M_s^{j,k}$ on the $z = 100$ mm plane at 4 GHz. The metric shows co- and cross-polarized performance of the four-port antenna for linear targets at multiple orientations defined by $\hat{\mathbf{n}}$.

antenna arms. Additionally, the response is also weak in the $\hat{\mathbf{n}} = \hat{x}$ and $\hat{\mathbf{n}} = \hat{y}$ cases for ($j = 2$,$k = 1$), since the target is cross-polarized with one arm and co-polarized with the other. Ideally, the cross-polarized sensitivity would be null with a perfectly polarized antenna. The observed cross-polarized response is due to the degradation of the linear polarization off-boresight which will be discussed further in Section 5.1.4. Finally, for the $\hat{\mathbf{n}} = (\hat{x} + \hat{y})/\sqrt{2}$ case, the response is seen to be relatively strong for all the port pairs since the target is somewhat co-polarized with both the transmit and receive arms. Additional plots of the sensitivity, on the $z = 100$ mm plane, are provided for frequencies 1, 2, 3, and 5 GHz in Figures 5.15–5.18. From these figures, one can observe how the sensitivity–especially the undesired cross-polarized sensitivity–varies with frequency due to the movement of the antenna active region.

It is instructive to compare the sensitivity plots for the above four-port sinuous antenna to a more conventional antenna arrangement. In most conventional GPRs, the transmit and receive antennas are separate, as in Figure 1.1 (see Section 1.1). Consider two sinuous antennas identical to that pictured in Figure 5.1 driven in a balanced manner and separated by 24 cm (center to center). Pseudo-color graphs of the radiated fields are shown in Figures 5.19a and 5.19b. The graphs show that the radiated fields of the transmit and receive antennas overlap minimally. The sensitivity metric for this antenna configuration is shown in Figure 5.19c and is normalized to the same value as the four-port antenna sensitivity plots provided in Figures 5.12–5.18. As can be seen, the lack of direct overlap of the two antenna's radiation results in much lower sensitivity. The result is particularly troublesome for detecting close-in targets, such as landmines buried close to the surface.

5.1.4 Polarization Performance

In the previous section, it was observed that the four-port antenna exhibited undesirable degradation in polarization isolation, particularly at off-boresight angles. The axial ratio (AR), defined in Equation 2.3, is shown for the four-port antenna (driven on arm 1) at a

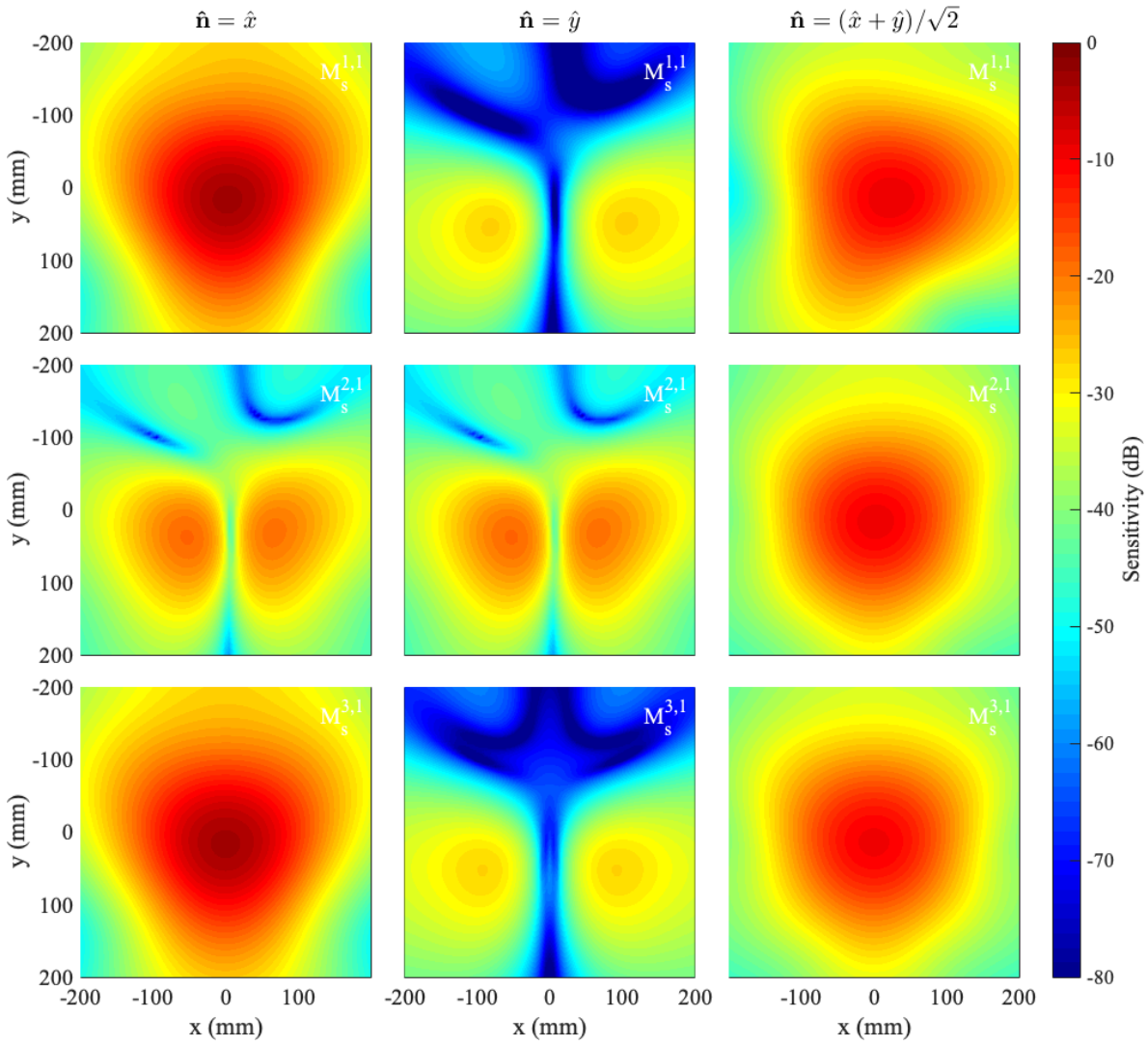

Figure 5.15: Pseudo-color plot of the sensitivity metric $M_s^{j,k}$ on the $z = 100$ mm plane at 1 GHz. The metric shows co- and cross-polarized performance of the four-port antenna for linear targets at multiple orientations defined by $\hat{\mathbf{n}}$.

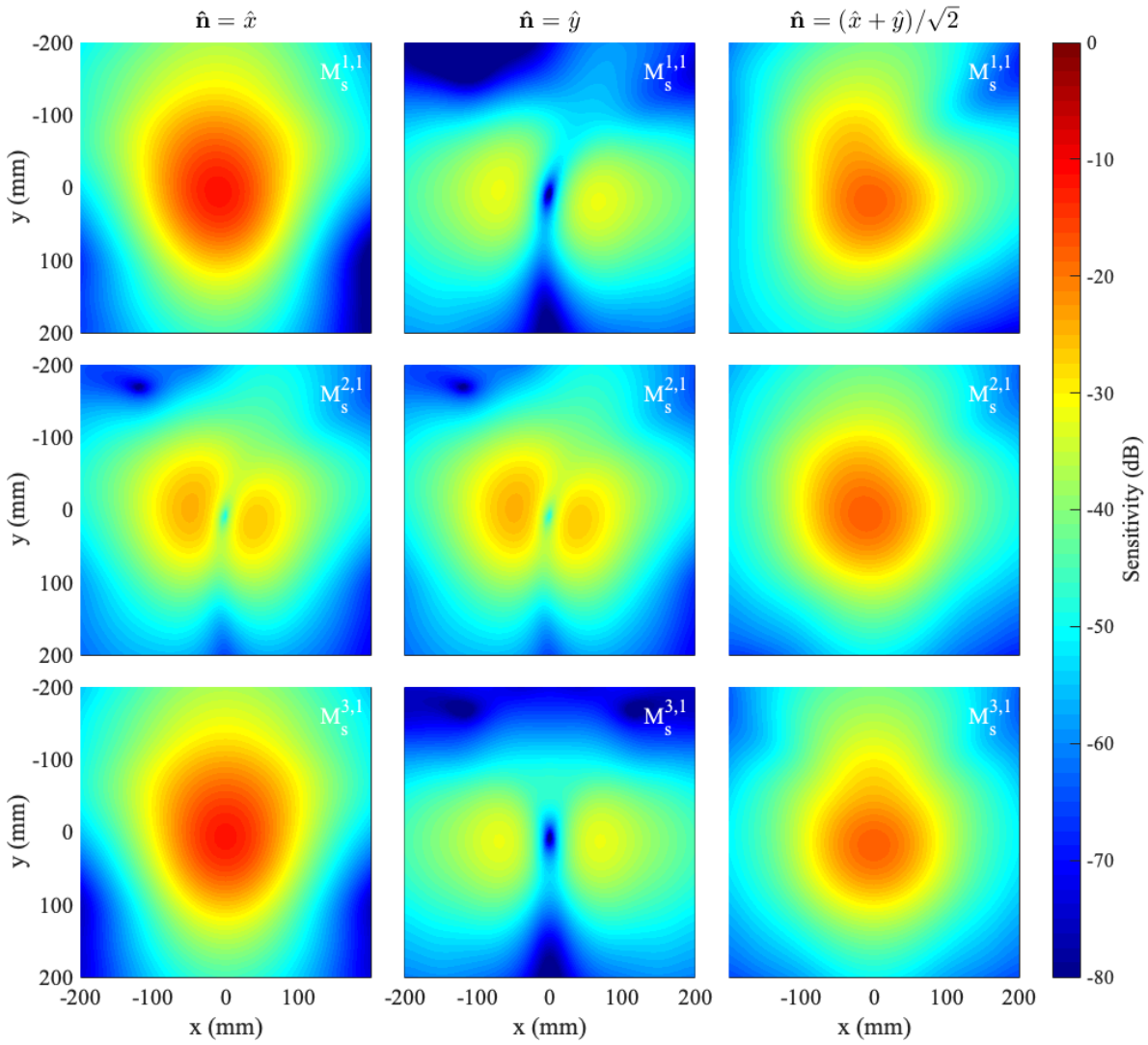

Figure 5.16: Pseudo-color plot of the sensitivity metric $M_s^{j,k}$ on the $z = 100$ mm plane at 2 GHz. The metric shows co- and cross-polarized performance of the four-port antenna for linear targets at multiple orientations defined by $\hat{\mathbf{n}}$.

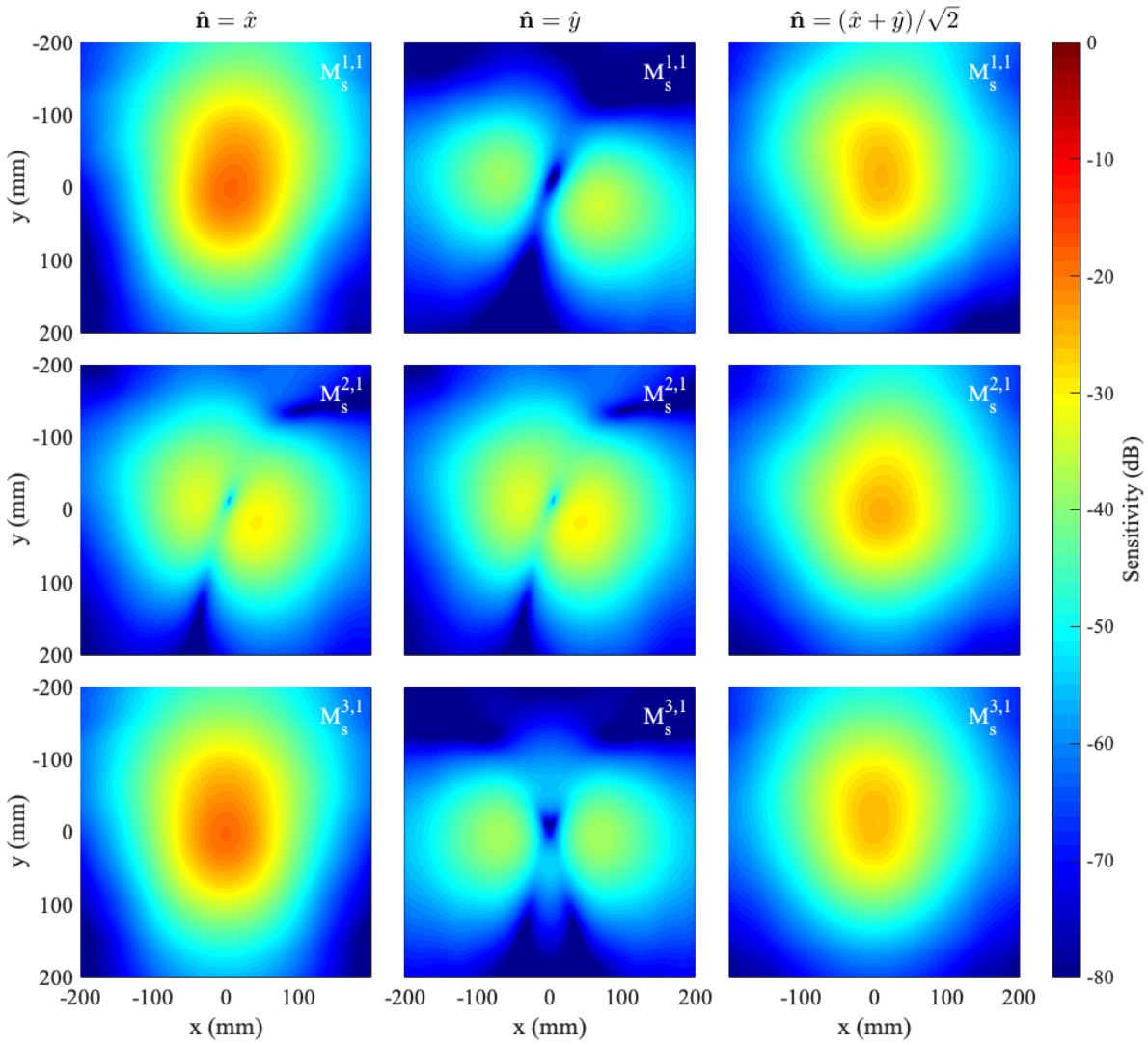

Figure 5.17: Pseudo-color plot of the sensitivity metric $M_s^{j,k}$ on the $z = 100$ mm plane at 3 GHz. The metric shows co- and cross-polarized performance of the four-port antenna for linear targets at multiple orientations defined by $\hat{\mathbf{n}}$.

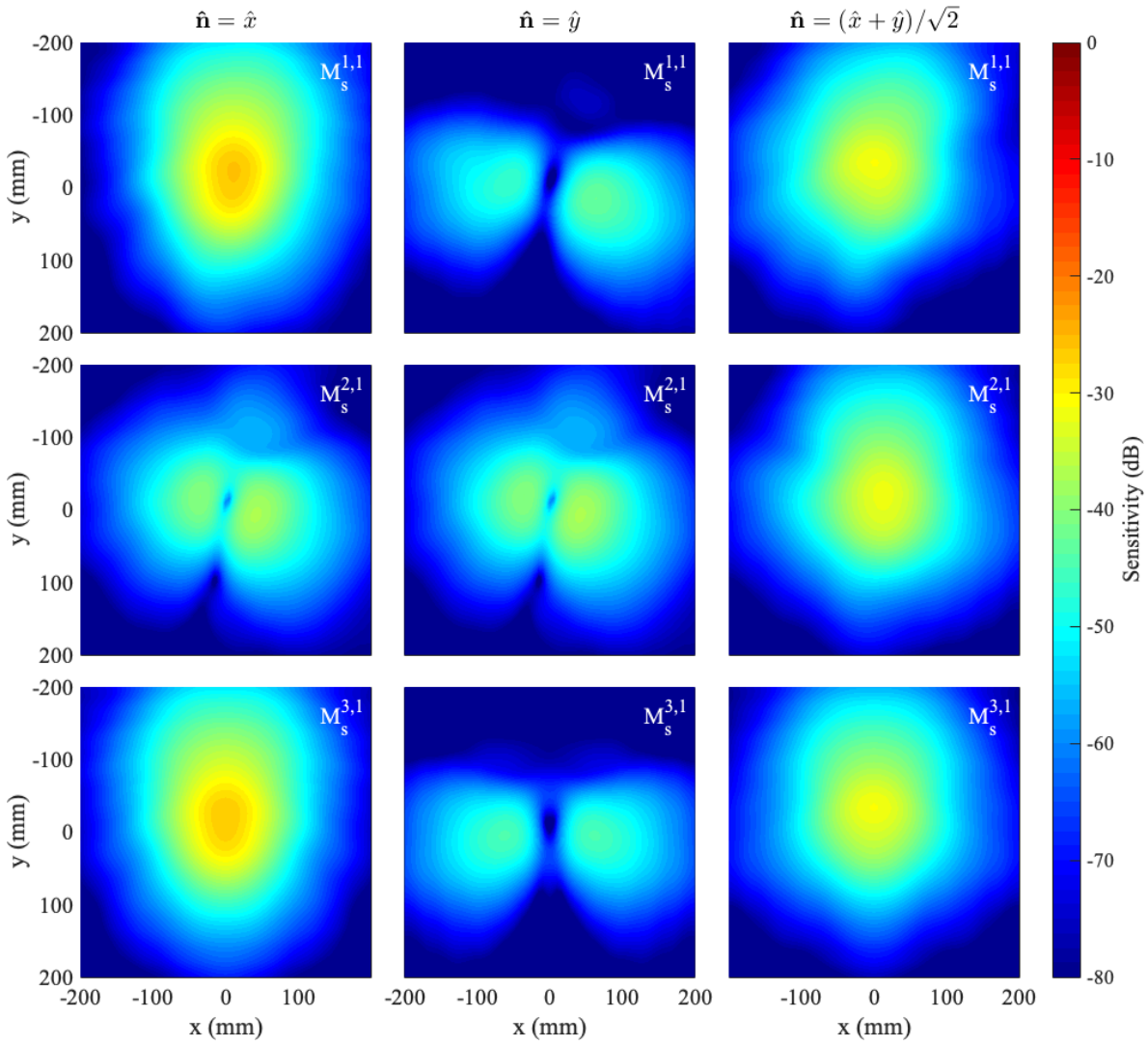

Figure 5.18: Pseudo-color plot of the sensitivity metric $M_s^{j,k}$ on the $z = 100$ mm plane at 5 GHz. The metric shows co- and cross-polarized performance of the four-port antenna for linear targets at multiple orientations defined by $\hat{\mathbf{n}}$.

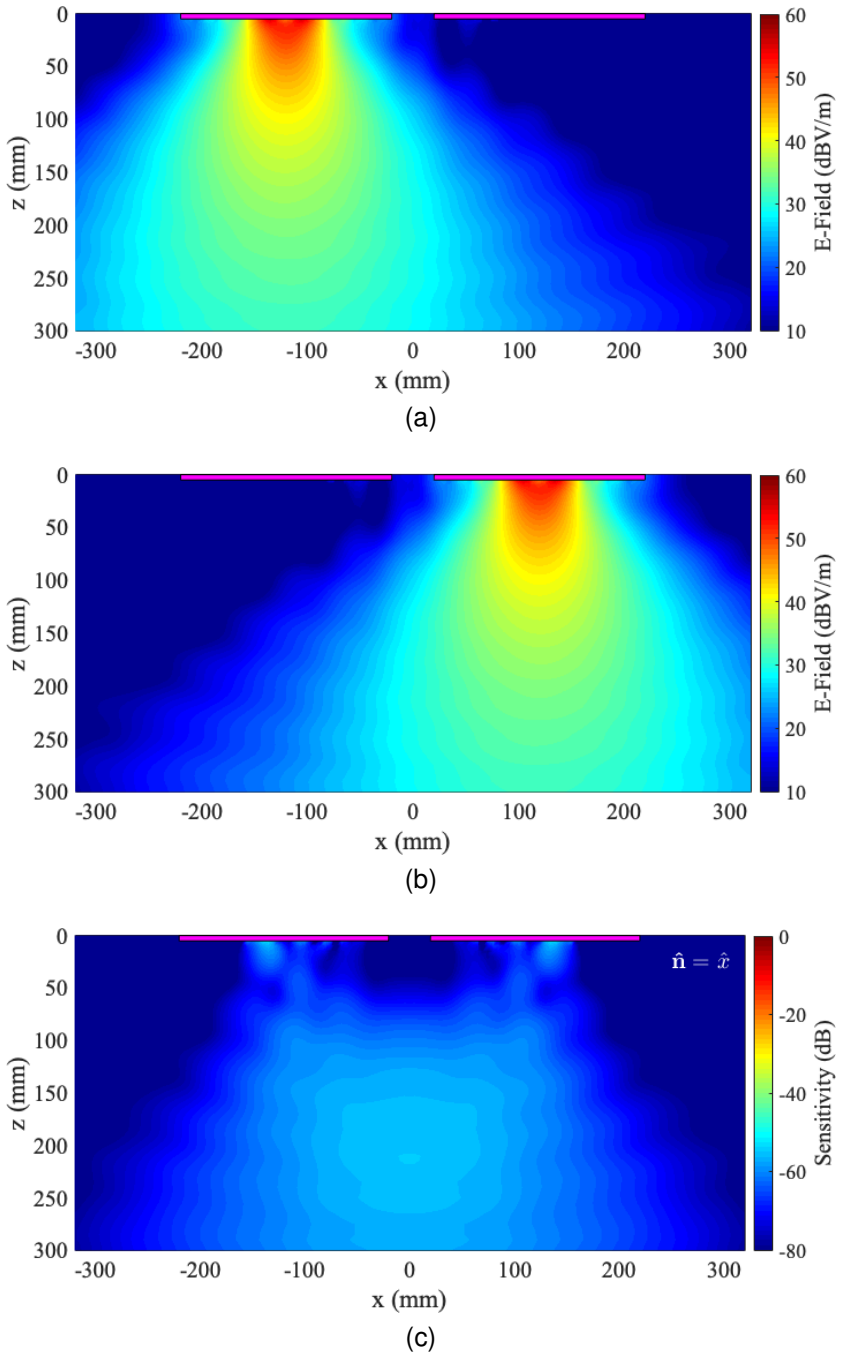

Figure 5.19: Two balanced (driven in mode-1) sinuous antennas operated bistaticly: (a) radiated field for the left antenna, (b) radiated field for the right antenna, and (c) sensitivity metric M_S for a co-polarized scatterer ($\hat{\mathbf{n}} = \hat{x}$) normalized to the same value as the four-port antenna sensitivity plots. All cuts are in the $y = 0$ plane.

distance of 100 mm in Figures 5.20 and 5.21 for various frequencies. As can be seen, the AR reduces at angles off of boresight indicating the polarization changes from linear to elliptical. It is further observed that these areas move with frequency, again due to the non-stationary active region, which corresponds with that observed in the sensitivity metric plots in Figures 5.14–5.18.

5.1.5 Mutual Coupling

The desire to separate transmit and receive channels in a GPR system is motivated by the fact that, for close-in sensing, transmit pulses may still be in the processes of leaving the antenna when target echoes arrive. It is therefore desired to increase isolation between channels, i.e., decrease mutual coupling. The resulting coupling between ports of the antenna when driving port 1 is shown in Figures 5.22, 5.23, and 5.24 for a driving port impedance of 248 Ω, 133 Ω, and 50 Ω, respectively. Here S_{21} represents the coupling between cross-polarized channels ($S_{41} = S_{21}$) and S_{31} is the coupling between the co-polarized channels. Notice that the isolation between ports increases with a reduced match. While a reduced match may be undesirable, the values observed did not have a significant effect on the antenna's realized gain, as shown in Figure 5.25. The relationship between driving port impedance and isolation may be evaluated without full-wave simulation as Equation 5.5 can be used to compute the S-parameters for an infinite version of the antenna. Figure 5.26 shows the S-parameters of the infinite four-port antenna computed with Equation 5.5 vs. the characteristic impedance connected to the antenna ports. The analytical results correlate well with those from the full-wave simulation.

The S-parameters for the $Z_C = 133\ \Omega$ case are transformed into the time domain and shown in Figure 5.27. A Taylor window, with parameters $\bar{n} = 15$ and $PSR = -80$ as defined in [102], weighted the frequency-domain S-parameters before transformation to the time domain via MATLAB's implementation of the inverse fast Fourier transform (IFFT). The time-domain results indicate the primary location of the coupling to be at the

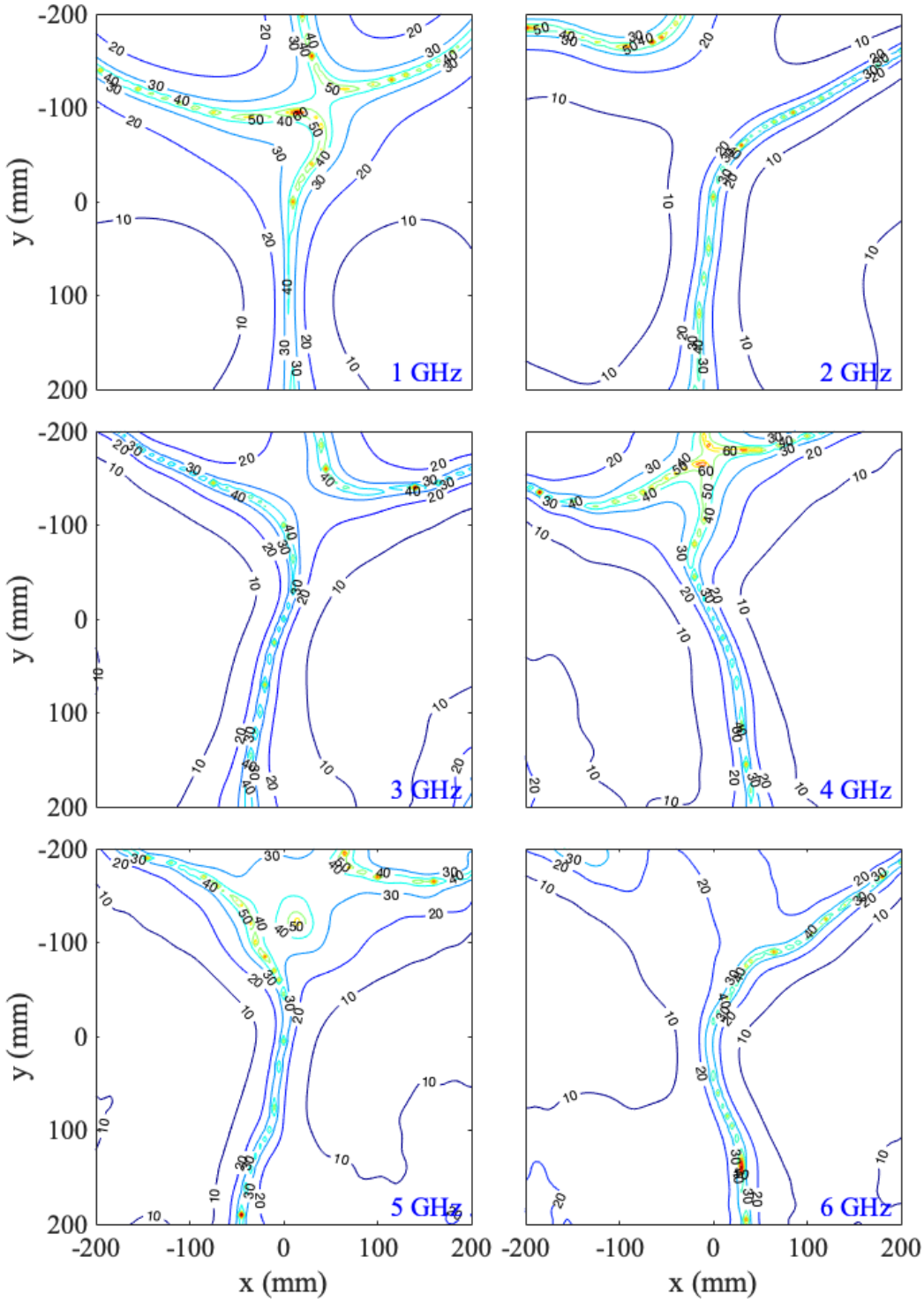

Figure 5.20: Axial ratio (dB) of the four-port antenna, when driven on arm 1, computed from the radiated fields on the $z = 100$ mm plane (frequency samples: 1–6 GHz).

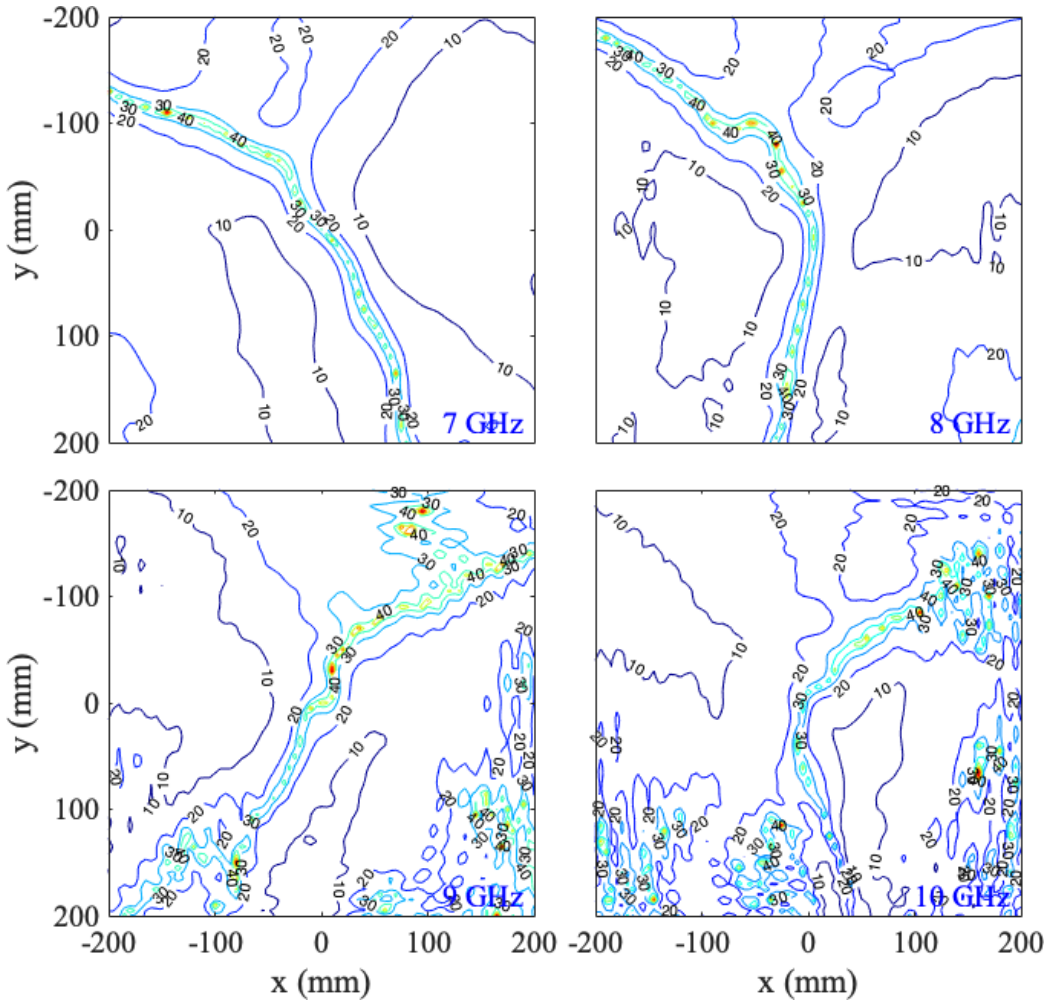

Figure 5.21: Axial ratio (dB) of the four-port antenna, when driven on arm 1, computed from the radiated fields on the $z = 100$ mm plane (frequency samples: 7–10 GHz).

feed ports (at time 0 nanoseconds). A smaller (≈25 dB down) and slightly delayed (≈0.25 ns) response is also observed, which is attributed to distributed coupling in the antenna. The time-domain results, post dispersion correction (detailed in Chapter 3) are also displayed in Figure 5.27. Notice how the application of the dispersion correction disperses and moves into negative time the pulse due to coupling resulting in a 30 to 40 dB reduction of noise at time $t = 0$ nanoseconds. Application of the dispersion correction may assist with the separation of the signals due to mutual coupling and those from a target.

A calibration procedure may be able to remove much of the undesired port coupling. Coherent background subtraction will be used for this purpose in Chapter 6. Furthermore,

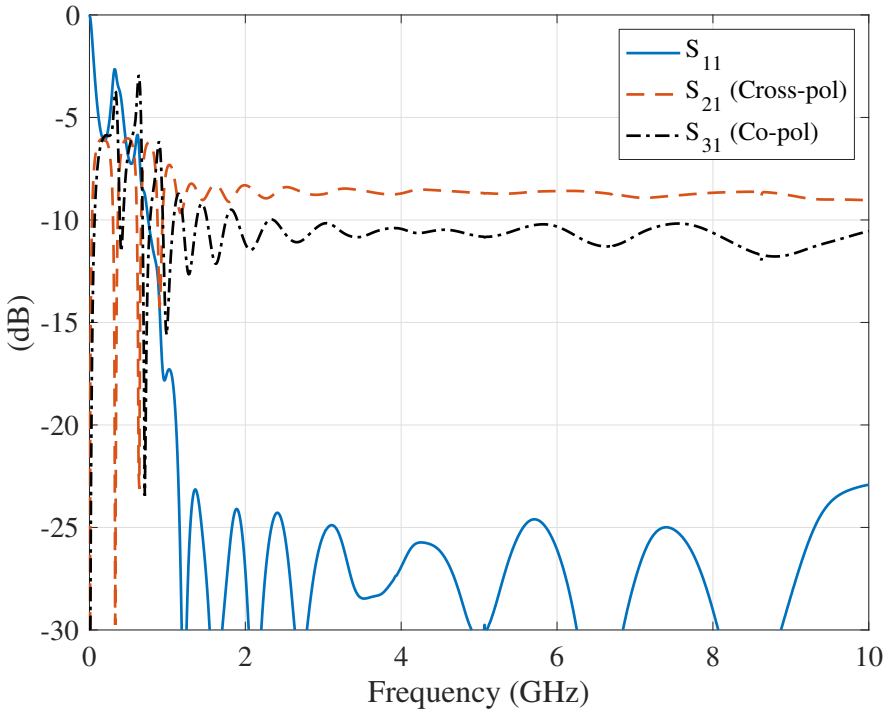

Figure 5.22: S-parameters for the four-port antenna when driving port 1 with an ideal 238 Ω port. Note that S_{21} represents the coupling between cross-polarized channels ($S_{41} = S_{21}$) and S_{31} is the coupling between the co-polarized channels.

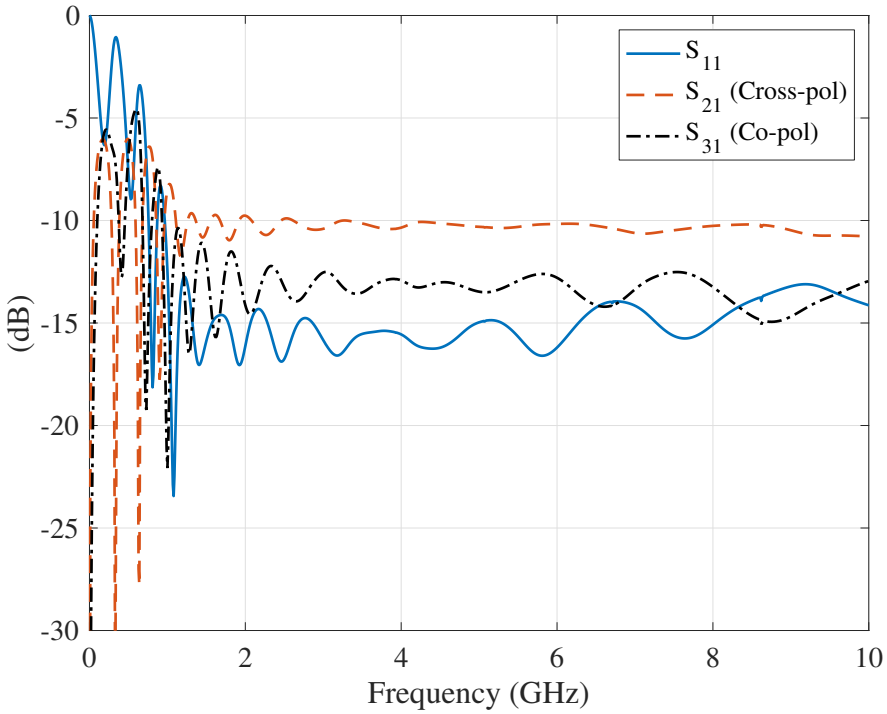

Figure 5.23: S-parameters for the four-port antenna when driving port 1 with an ideal 133 Ω port.

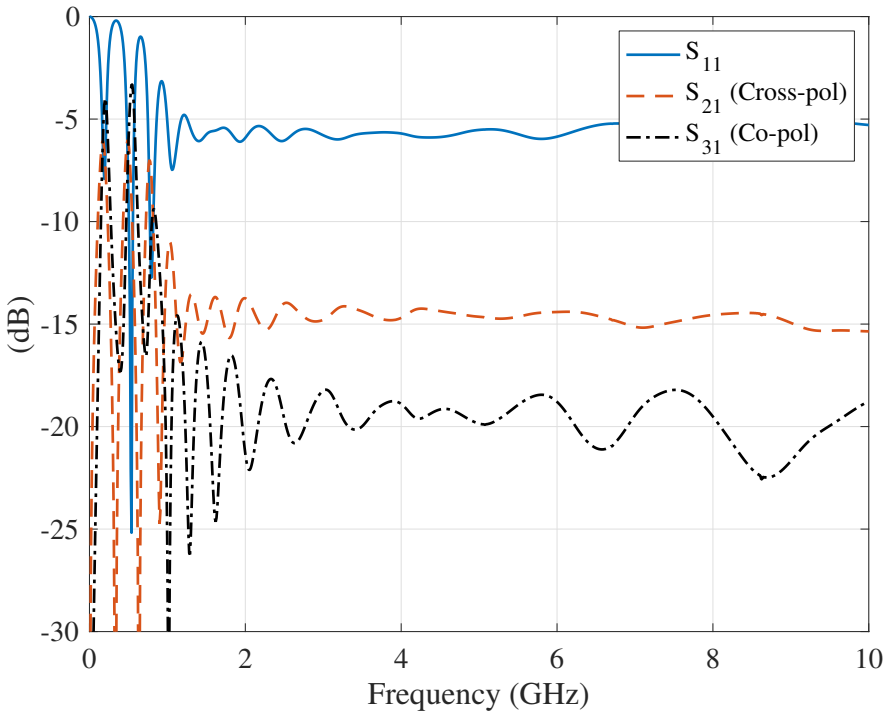

Figure 5.24: S-parameters for the four-port antenna when driving port 1 with an ideal 50 Ω port.

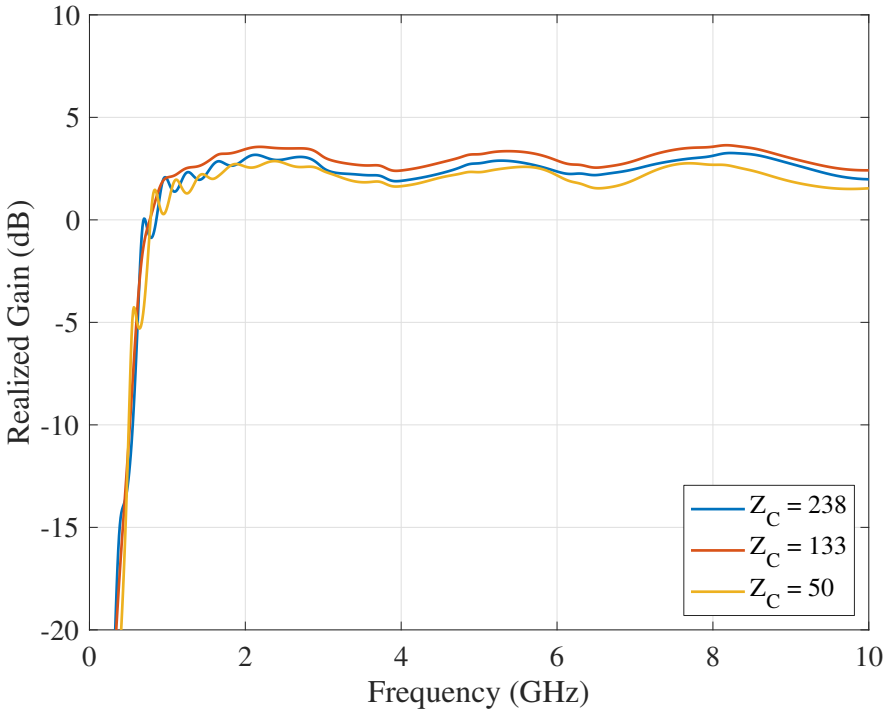

Figure 5.25: Graph of the realized gain as a function of frequency for $Z_c =$ 238 Ω, 133 Ω, and 50 Ω.

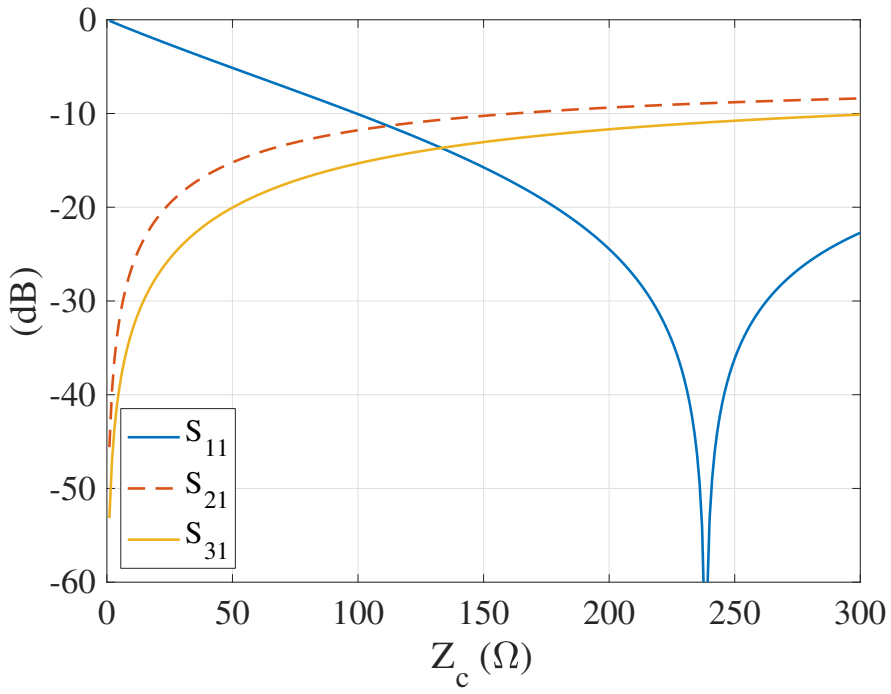

Figure 5.26: Four-port antenna S-parameters vs. port characteristic impedance Z_C (same for all ports) computed analytically with Equation 5.5.

any remaining artifacts from the coupling will be pushed into negative time once dispersion compensation has been applied. While it is possible to reduce the effects of the port coupling, it is still desirable to reduce it as much as possible. Another technique for reducing port coupling will be investigated in the following section.

5.2 Unbalanced Eight-Arm Sinuous Antenna

The unbalanced four-port antenna presented in the previous section shows good promise for use as a quasi-monostatic polarimetric antenna in close-in sensing applications. However, the port-to-port coupling, i.e., transmit and receive channel mutual coupling, is higher than desired. In this section an eight-arm sinuous antenna, illustrated in Figure 5.28, is investigated which achieves increased channel isolation. An eight-arm sinuous antenna was recently proposed in for angle-of-arrival applications that operated each arm connected to a 100 Ω coaxial cable [110]. For this application, the odd-numbered ports will be connected to the measurement system and driven independently like those of the four-port antenna

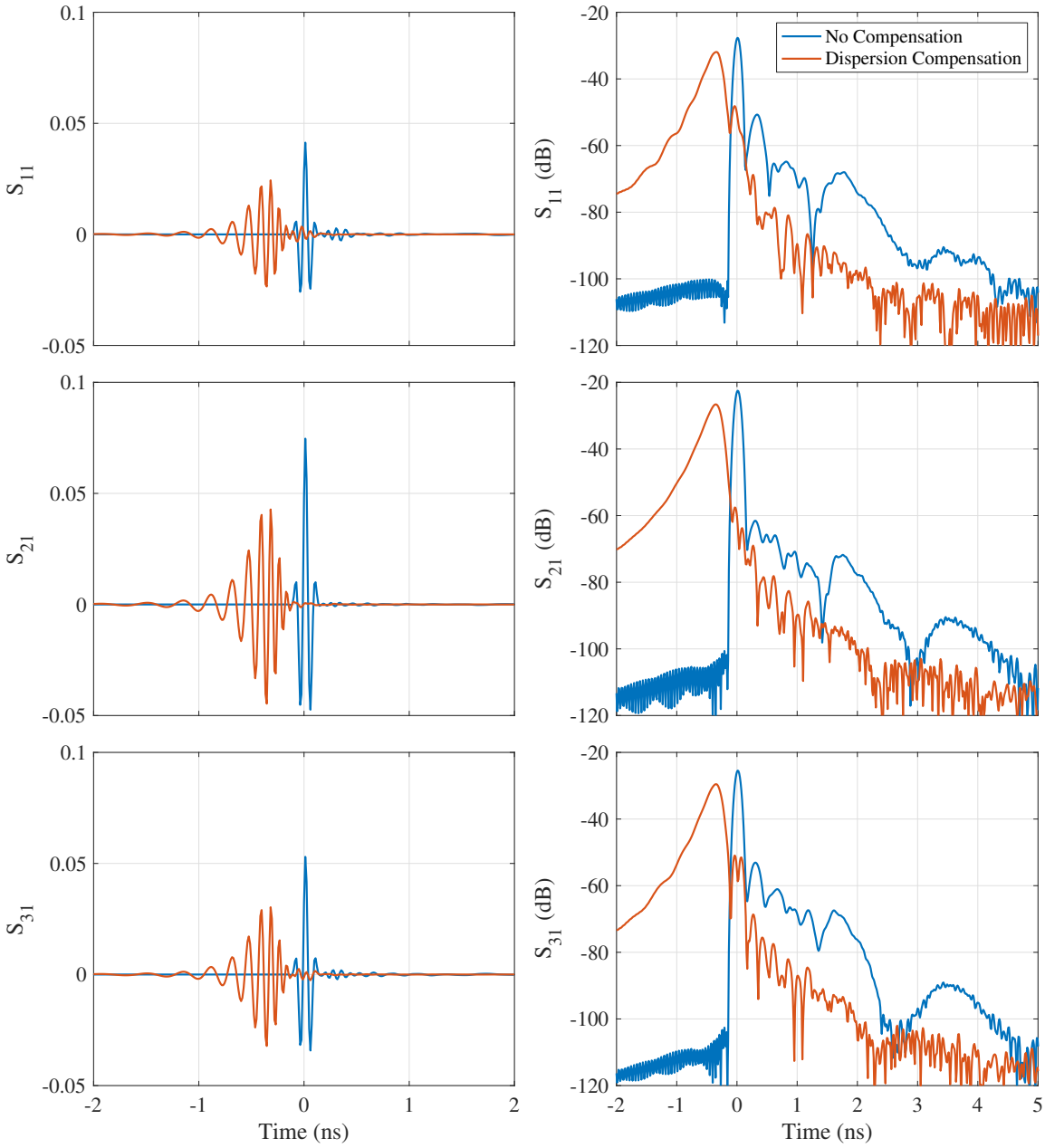

Figure 5.27: S-parameters in the time domain with and without dispersion compensation for the four-port antenna analyzed. The analytic amplitude is plotted (dB scale) on the right. Note that S_{21} represents the coupling between cross-polarized channels ($S_{41} = S_{21}$) and S_{31} is the coupling between the co-polarized channels.

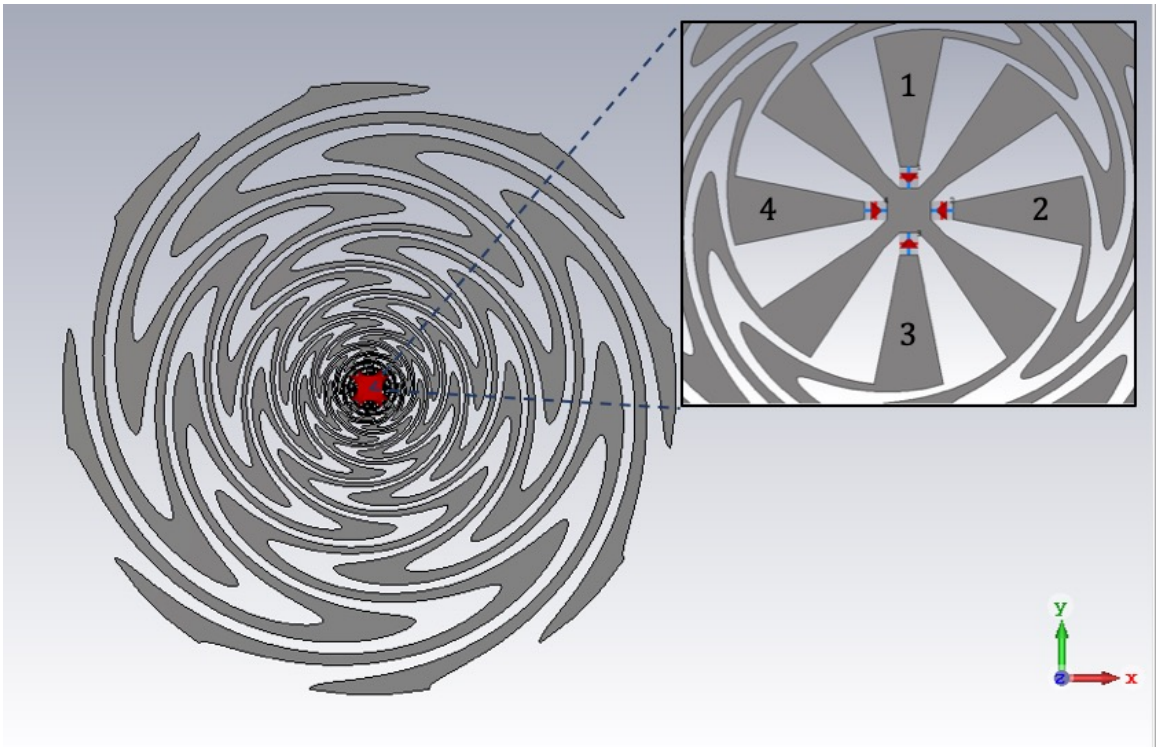

Figure 5.28: CST model of unbalanced eight-arm sinuous antenna. The antenna pictured is based on the improved design from Section 2.5 and has parameters: $N = 8$ arms, $P = 12$ cells, $R_T = 9.5$ cm, $\tau = 0.773$, $\alpha = 45°$, and $\delta = 11.25°$. Arms are driven with a port or shorted in an alternating fashion.

while the remaining even-numbered ports are shorted.

5.2.1 Driving Port Impedance and Mutual Coupling

The input impedance and mutual coupling for an infinite version of the antenna can be computed analytically since the structure is self-complementary with a method similar to that proposed in Section 5.1.1. However, some modification to the method is required to accommodate the fact that not all ports are equally loaded. Generalized scattering parameters may be used when not all ports are terminated by the same load [109, 111].

The generalized scattering parameters S^P define ratios of power transfer or "power waves" instead of voltages like normal S-parameters [111]. The power waves are defined in matrix form as [109]

$$[\,a\,] = [\,F\,]([\,V\,] + [\,Z_R\,][\,I\,]) \tag{5.12}$$

and

$$[\,b\,] = [\,F\,]([\,V\,] - [\,Z_R\,]^*[\,I\,]). \tag{5.13}$$

In the above, $[\,Z_R\,]$ is a diagonal matrix of each port's reference impedance $Z_{R,i}$ and $[\,F\,]$ is also a diagonal matrix defined as

$$[\,F\,] = [\,U\,] \begin{bmatrix} \text{Re}\{Z_{R,1}\}^{-\frac{1}{2}} \\ \text{Re}\{Z_{R,2}\}^{-\frac{1}{2}} \\ \vdots \\ \text{Re}\{Z_{R,N}\}^{-\frac{1}{2}} \end{bmatrix}, \tag{5.14}$$

where $[U]$ is the identity matrix. After some simplification, the generalized scattering matrix can be derived as [109]

$$[\,S^P\,] = [\,b\,][\,a\,]^{-1} = [\,F\,]([\,Z\,] - [\,Z_R\,]^*)([\,Z\,] + [\,Z_R\,])^{-1}[\,F\,]^{-1}. \tag{5.15}$$

However, similar to Section 5.1.1, the definition must be given in terms of $[\,Y\,]$—defined by Equation 4.2—instead of $[\,Z\,]$. If the port terminations are real valued i.e., $[\,Z_R\,]^* = [\,Z_R\,]$, then the generalized scattering parameter matrix may be defined, after some algebraic simplification, as

$$[\,S^P\,] = [\,F\,]([\,Y_R\,] - [\,Y\,])([\,Y\,] + [\,Y_R\,])^{-1}[\,F\,]^{-1} \tag{5.16}$$

where $[\,Y_R\,] = [\,Z_R\,]^{-1}$. The driving port impedance of any port j may then be computed by

$$Z_{in,j} = Z_{R,j}\frac{1 + S^P_{jj}}{1 - S^P_{jj}} \;:\; j \in \{1, 2, \ldots, 8\}. \tag{5.17}$$

Graphs of Z_{ant} and S_{11} as a function of feed port characteristic impedance $Z_c = 1/Y_c$ are shown in Figure 5.29 for the infinite eight-arm sinuous antenna with even number ports shorted. The optimal characteristic impedance of the driving port is 150 Ω and is approximately constant with Z_C since the neighbor arms are shorted. The optimal input impedance

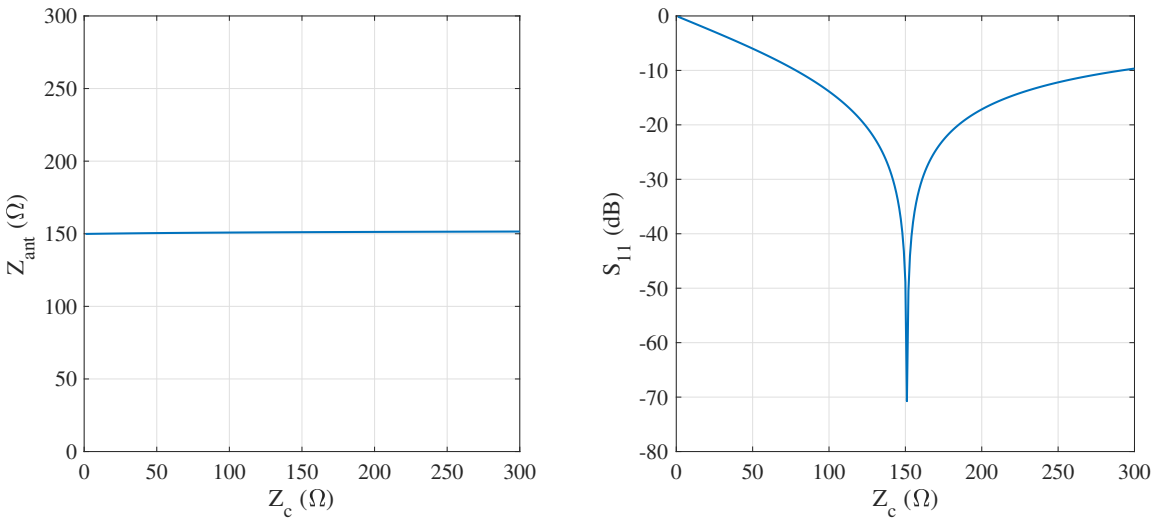

Figure 5.29: Computation of Z_{ant} for the 8-arm unbalanced sinuous antenna with even arms shorted vs. feed port characteristic impedance. Notice Z_{ant} is approximately constant (150 Ω) due to the constant load (short) of the neighbor arms.

is lower than the 4-arm antenna making it easier to feed and match to more common system impedances, e.g., 75 Ohms.

Full-wave simulations of the antenna described in Figure 5.30 were used to compute the match to multiple driving port impedances. The results are given in Figure 5.29. Once the frequency is high enough that the reflections from the antenna truncation are no longer an issue, the S_{11} values correlate well with those computed theoretically for an infinite antenna in Figure 5.29. Notice that the antenna's lowest operating frequency has increased due to the smaller δ. More specifically, the total electrical length of the antenna arms has decreased since they no longer wrap around as far. The lowest frequency of operation is inversely proportional to δ, as shown in Equation 2.10. This means the eight-arm antenna will need to be made larger to achieve the same lowest frequency of operation as the four-port version.

The port mutual coupling, for the $Z_c = 50\ \Omega$ full-wave simulation, is shown in Figure 5.31. The results show a significant improvement in port isolation of 15–20 dB when compared to the four-arm antenna (see Figure 5.24). These results show the eight-arm antenna has promise for polarimetric GPR applications; however, as will be shown, the

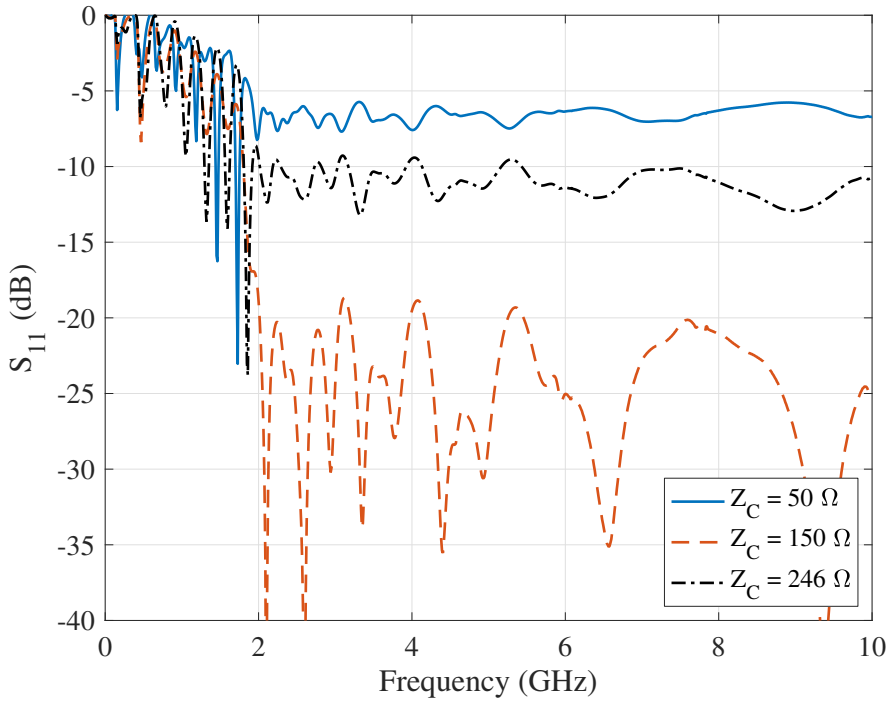

Figure 5.30: Comparison of simulated S_{11} for the eight-arm sinuous antenna with different driving-port characteristic impedances Z_C on odd-numbered arms and even-numbered arms shorted.

radiation characteristics are not as desirable as those of the four-arm antenna.

5.2.2 Radiated Fields

The boresight gain of the eight-arm antenna, simulated with the CST time-domain solver, is shown in Figure 5.32. The gain displays discontinuities similar to those investigated in Chapter 2. The angular width α must be decreased to 22.5° to maintain the same amount of interleaving in the eight-arm antenna as the four-arm antenna, t. This is the same value used for the eight-arm sinuous presented in [110]. A second eight-arm antenna was simulated with the smaller angular width, and the realized gain is plotted in Figure 5.33. For this second antenna, the number of cells was also increased to help the performance. The results show the second antenna does not suffer from the sharp discontinuities above 2 GHz; however, some discontinuities are still present at the lower frequencies where the antenna is resonant but no longer operating as intended.

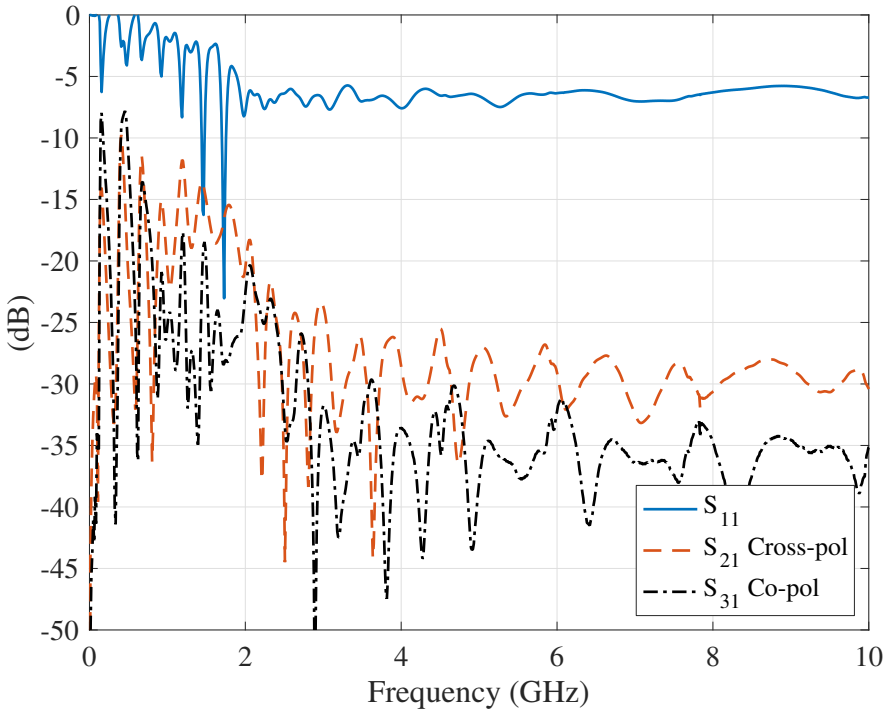

Figure 5.31: S-parameters for the eight-port antenna when driving port 1 with an ideal 50 Ω port.

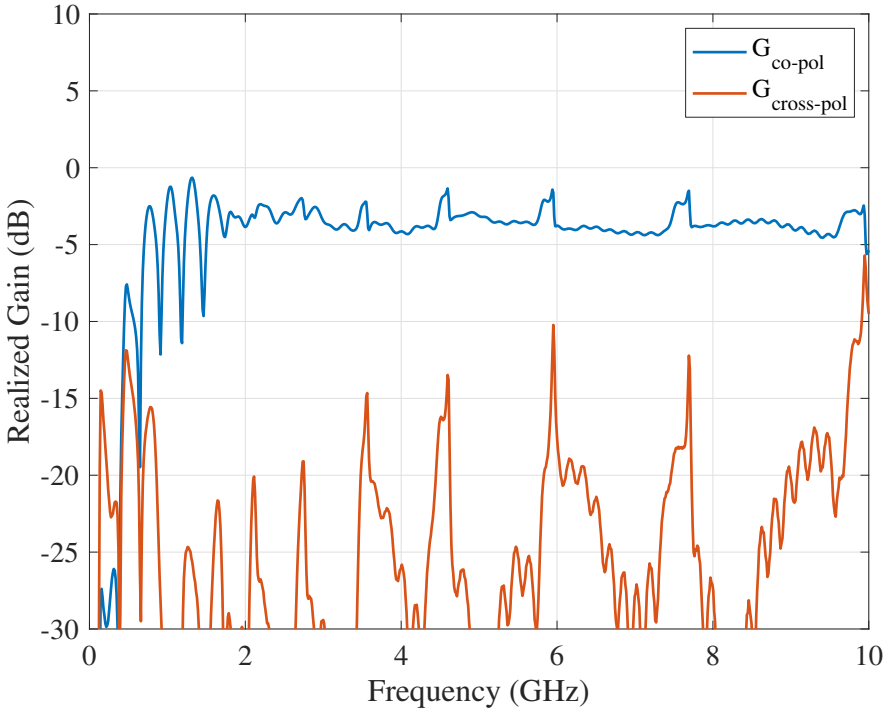

Figure 5.32: Simulated realized gain when driving port 1 of the eight-arm sinuous antenna having parameters: $N = 8$ arms, $P = 12$ cells, $R_T = 9.5$ cm, $\tau = 0.773$, $\alpha = 45°$, and $\delta = 11.25°$. Even-numbered arms are shorted.

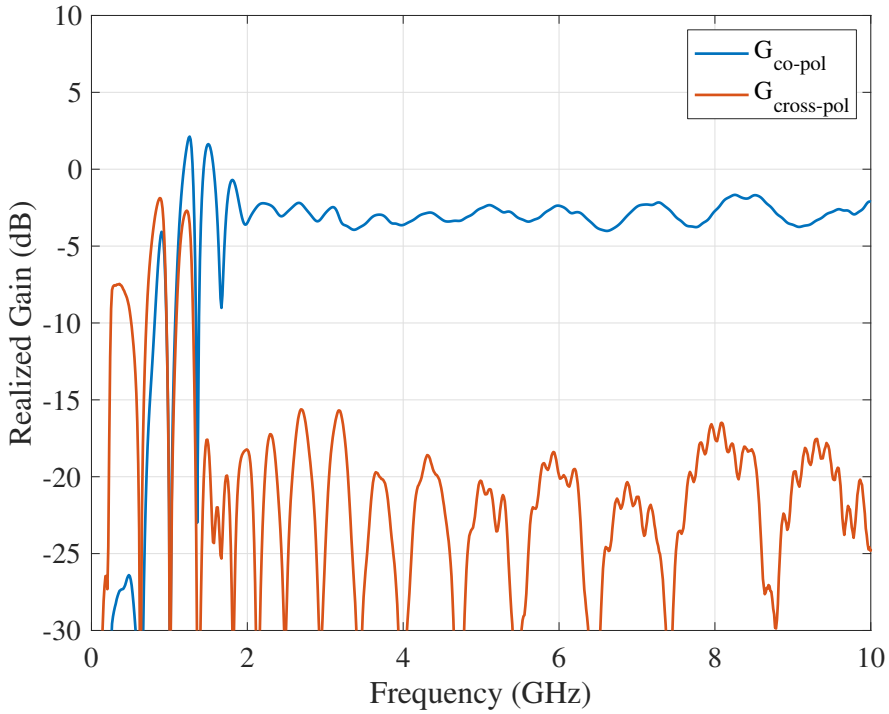

Figure 5.33: Simulated realized gain when driving port 1 of the eight-arm sinuous antenna having parameters: $N = 8$ arms, $P = 20$ cells, $R_T = 9.5$ cm, $\tau = 0.8547$, $\alpha = 22.5°$, and $\delta = 11.25°$. Even-numbered arms are shorted.

The simulations show the eight-arm antenna to have quite low realized gain on boresight. The reduced gain is due to the beam being split and directed off-axis as shown by the plots of the 20 cell ($\alpha = 22.5°$) antenna's far-field radiation in Figure 5.34. The same antenna's near-field sensitivity exhibits similar behavior, as shown in Figure 5.35, which displays sensitivity at 4 GHz on the $z = 100$ cm plane. Notice that this plot is normalized to the same value as the four-port antenna sensitivity plots shown in Figures 5.12–5.18. The overall sensitivity is lower for the eight-arm antenna compared to the four-arm version; however, a larger area is covered. The eight-arm antenna also still improves over the bistatic configuration shown in Figure 5.19. It is also interesting to notice the larger cross-polarized responses off of boresight. Further exploration of this antenna and its potential applications are a topic of future research.

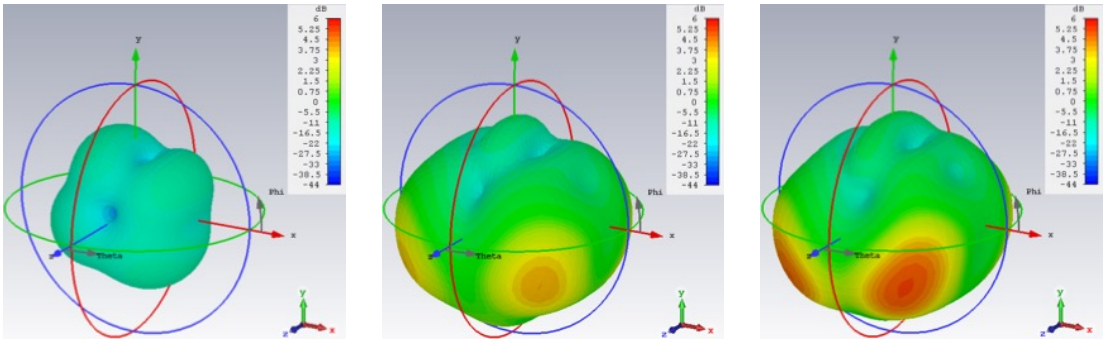

(a) $f = 1$ GHz (b) $f = 2$ GHz (c) $f = 3$ GHz

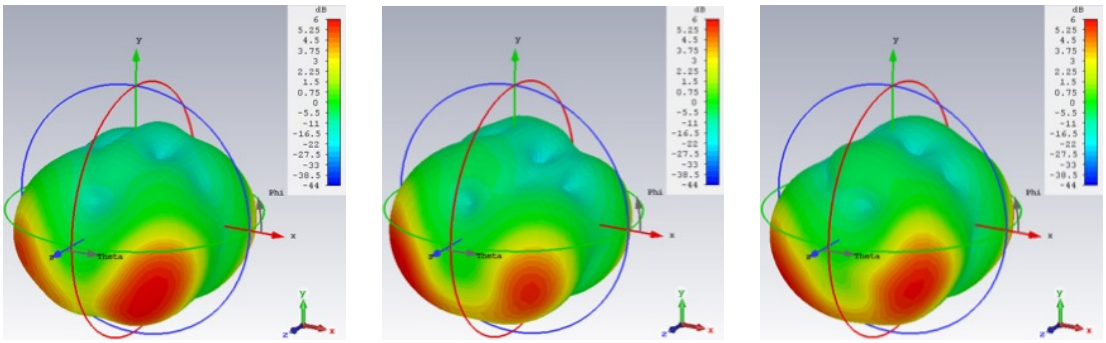

(d) $f = 4$ GHz (e) $f = 5$ GHz (f) $f = 6$ GHz

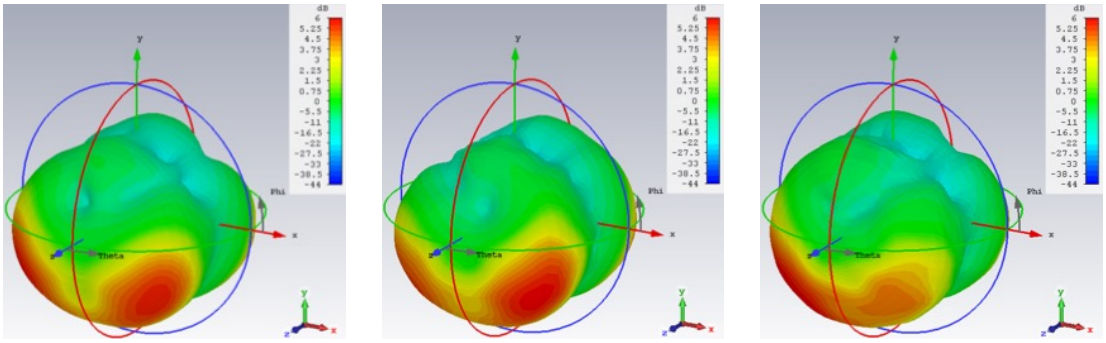

(g) $f = 7$ GHz (h) $f = 8$ GHz (i) $f = 9$ GHz

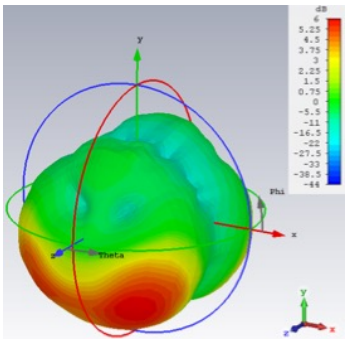

(j) $f = 10$ GHz

Figure 5.34: Far-field radiation patterns $|\vec{G}_{rlzd}|$ generated by CST of the eight-arm antenna ($\alpha = 22.5°$) driven on arm 1 by an ideal port with characteristic impedance of 150 Ω.

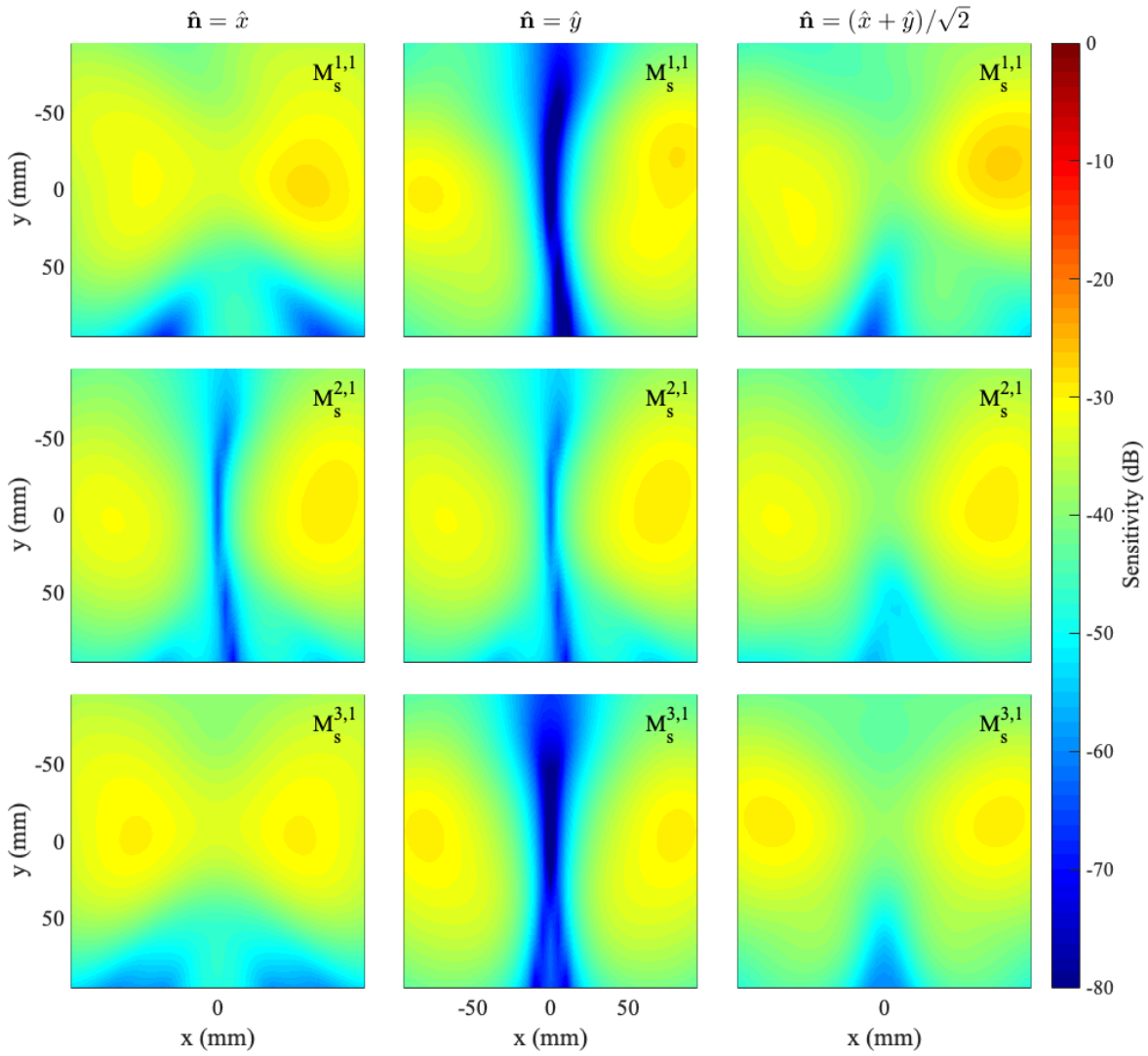

Figure 5.35: Pseudo-color plot of the sensitivity metric $M_s^{j,k}$ on the $z = 100$ mm plane at 4 GHz for the eight-arm antenna ($P = 20$ cells, $\tau = 0.8547$, and $\alpha = 22.5°$). The metric is normalized to the same value as the four-port antenna sensitivity plots.

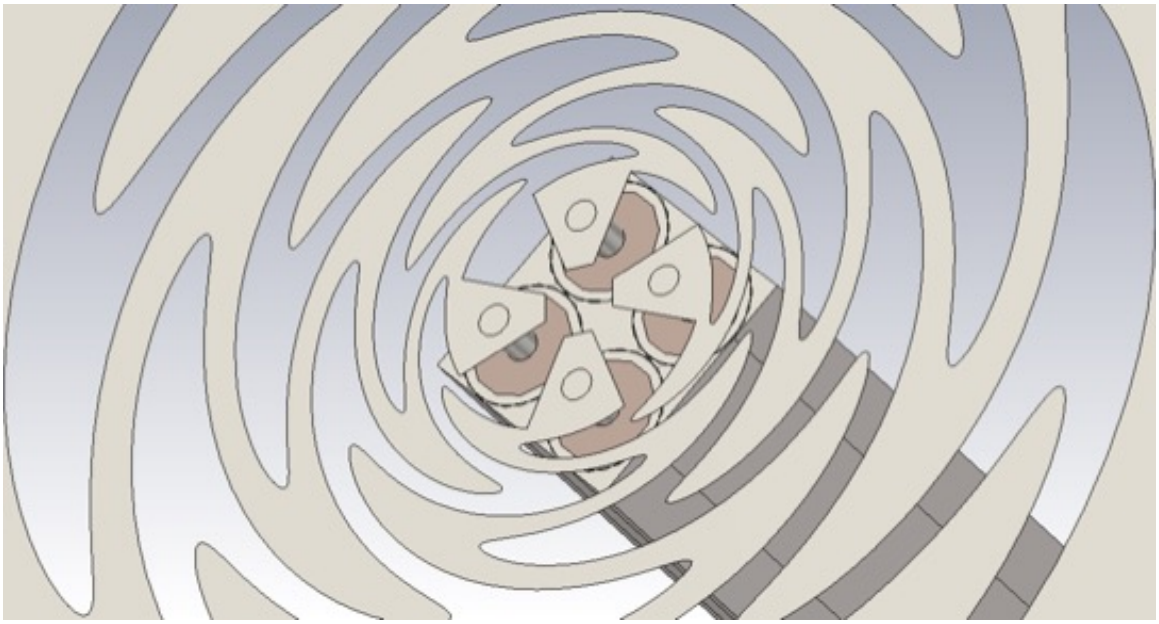

Figure 5.36: Model of the simulated coaxial cable feed with the substrate hidden to show how the cables connect to the antenna. Model of RG-402 cables pictured.

5.3 Constructed Antenna

The four-port antenna analyzed in Section 5.1 was further investigated through fabricated and measurement. Design considerations and initial measurement results will be discussed below. The integration of the antenna into a GPR testbed will be described in Chapter 6.

5.3.1 Coaxial Cable Feed

The antenna was manufactured using an LPKF PCB milling machine [89] out of 1.575 mm (0.062") thick Rogers RT/duroid® 5880 laminate (1 oz. copper clad)—similar to the fabricated antennas detailed in Chapters 2 and 3. The results in Figure 5.5 indicate the addition of the substrate lowers the average input impedance to approximately 197 Ω over the 1–10GHz band. It was decided to feed the antenna with a simple direct connection of coaxial cables, as shown in Figure 5.36. This connection is similar to that in [58], but each cable is operated as an independent channel.

Four different coaxial cable sizes were investigated through simulation in CST (see

Table 5.2: Dimensions of coaxial cables simulated for the four-port antenna feed.

		Shield Dia.		Dielectric Dia.		Center Conductor Dia.	
Z_0	Dielectric	in	mm	in	mm	in	mm
50	PTFE	0.141	3.58	0.117	2.97	0.036	0.91
50	PTFE	0.086	2.21	0.066	1.68	0.02	0.51
75	PTFE	0.141	3.58	0.118	3.00	0.02	0.51
100	PTFE	0.141	3.58	0.118	3.00	0.01	0.254

Figure 5.36). Two 50 Ω, a 75 Ω, and a 100 Ω cable were each evaluated. The cable dimensions are summarized in Table 5.2. Simulated S-parameters of the antenna for each cable type are plotted in Figure 5.37. The results show little variation between the two 50 Ω cables with the 75 Ω and 100 Ω cables giving the best match. Consistent with the results resented in Section 5.1.5, the 50 Ω cables perform best for port isolation. Use of the 50 Ω cables provides the additional advantage of being able to connect directly with the measurement equipment i.e., a network analyzer. Due to these benefits, the larger 50 Ω cable was selected for the constructed antenna feed. The larger diameter center conductor was desired for easier soldering.

5.3.2 Absorber-Loaded Cavity

An absorber-loaded cavity was implemented for the constructed antenna, which served to absorb the back lobe of the radiation as well as provide a mounting structure. The implemented cavity is shown in Figure 5.38. The cavity is filled with AN-79 absorber [108] and is approximately 14.5 cm tall when including the lid and antenna substrate. As discussed in Section 4.3.1, the height of the cavity could be reduced without sacrificing performance; however, the cavity and absorber were selected based on availability from another project [92]. The diameter of the cavity also set the antenna radius, which was chosen to be 9.5 cm to prevent the direct overlap of the antenna arms and cavity wall.

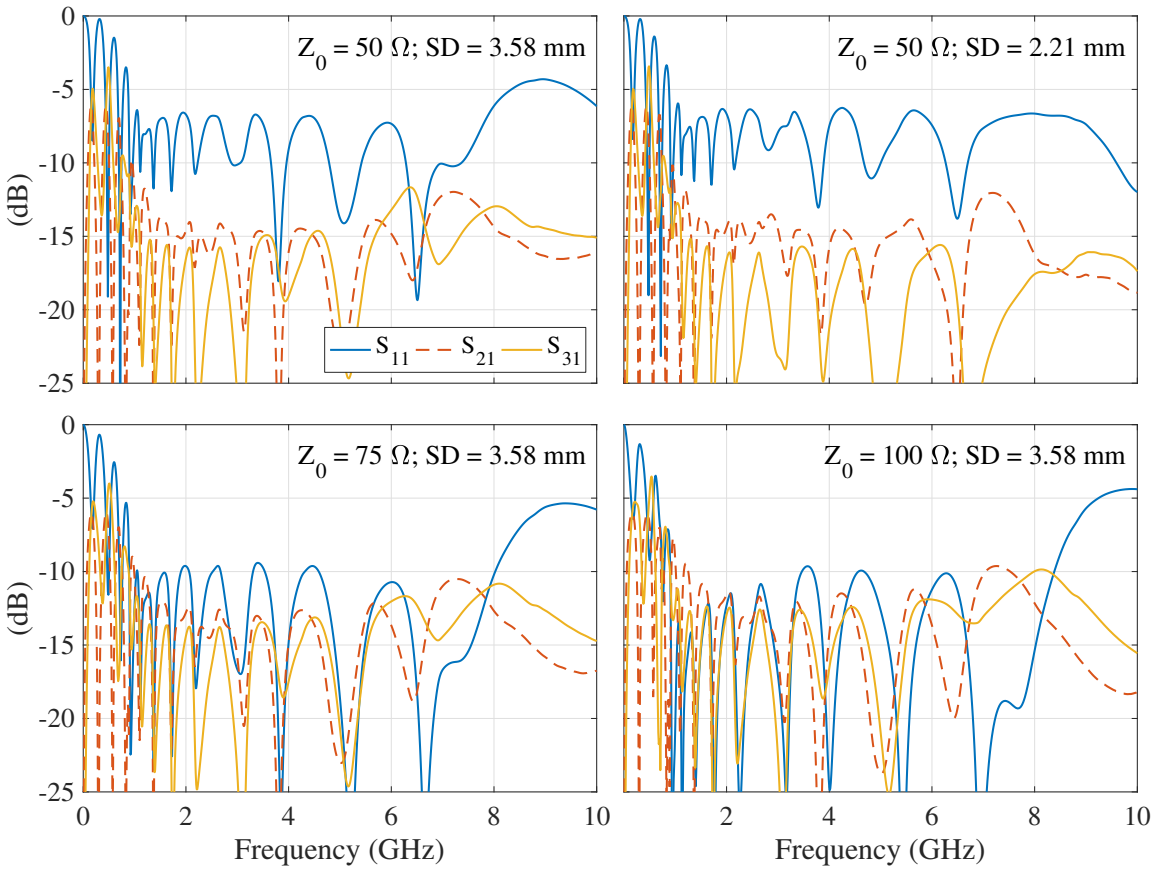

Figure 5.37: Simulated S-parameters for each cable feed configuration of the four-port antenna. Note that S_{21} represents the coupling between cross-polarized channels ($S_{41} = S_{21}$) and S_{31} is the coupling between the co-polarized channels.

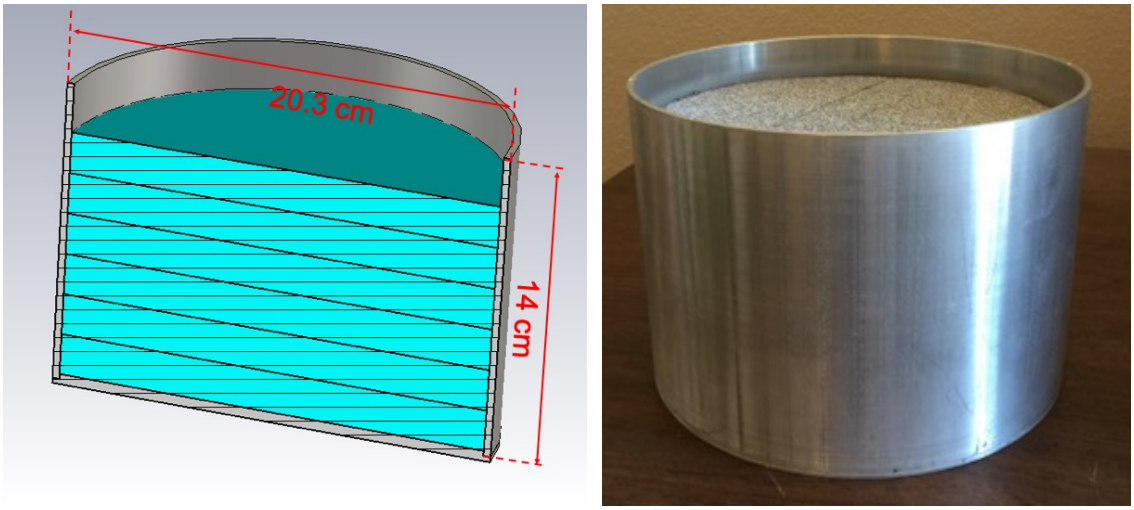

(a) CAD Model (b) Actual

Figure 5.38: Absorber loaded cavity used for the constructed four-port antenna.

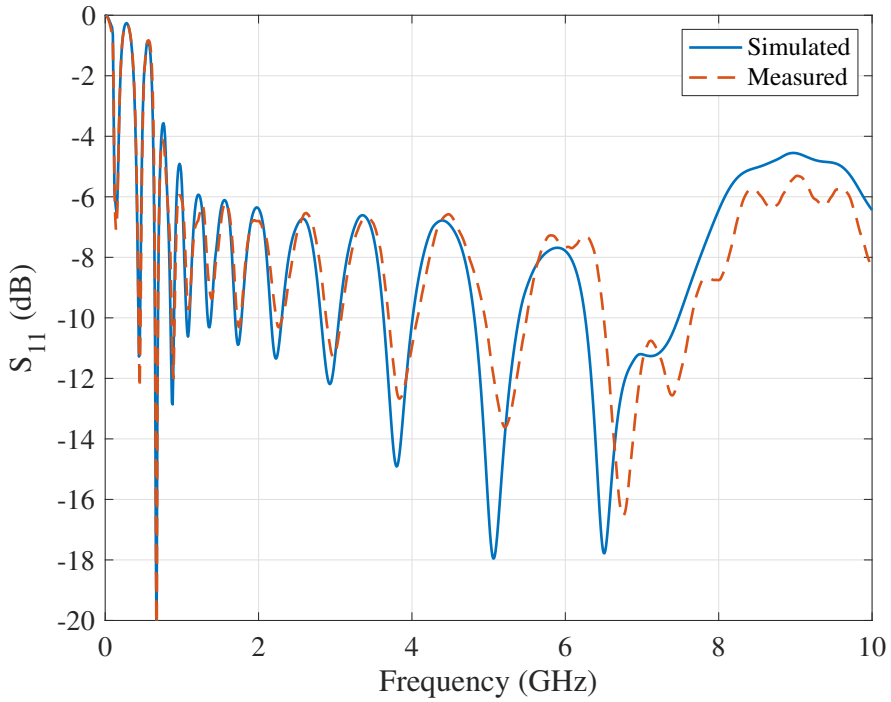

Figure 5.39: Comparison of measured and simulated S_{11} for the constructed four-port antenna. The comparison shows very good agreement.

5.3.3 Measurements

In order to verify the operation of the constructed antenna, it was measured in an anechoic chamber with a 4-port vector network analyzer. A detailed model of the antenna—including the substrate, absorber-loaded cavity, and the coaxial cables—was developed in CST Microwave Studio and simulated using the time-domain solver. The simulated and measured reflection coefficients vs. frequency are compared in Figure 5.39 which shows good agreement.

Scanned measurements of two targets were also performed similarly to what was done for the antenna in Chapter 3. Both targets were placed 15.24 cm from the antenna and then scanned perpendicular to the antenna 15.24 cm in 1.27 cm increments. The first target was a 5.08 cm diameter metal sphere (pictured in Figure 5.40), and the second was a metal rod with length and diameter of 51.24 mm and 1.96 mm respectively. The sphere should only produce a cross-polarized response while the rod was rotated 45° relative to

the antenna to produce equal amounts of co- and cross-polarized returns. The four-port S-parameters were measured, with and without the target, in the frequency domain from 10 MHz to 10 GHz with a vector network analyzer. The background, including the foam mast, was removed from the target results by coherent subtraction. A Taylor window ($\bar{n} = 15$ and $PSR = -80$) [102] weighted the sans background target returns before transformation to the time domain via inverse fast Fourier transform (IFFT). The waterfall diagram in Figure 5.41 shows the processed time-domain co-polarized responses of the sphere for each scan location, both with and without dispersion compensation. The dispersion model parameters were determined by an optimization process similar to that done in Section 3.5. The resulting dispersion model parameters were $\phi_0 = 12.495$ and $f_0 = 11.277$ GHz. With the dispersion model applied, the specular and creeping wave returns from the sphere become clearly visible. The cross-polarized sphere responses show no response on boresight; however, the target begins to appear at off-boresight angles. The appearance of the target is because the antenna polarization degrades to elliptical off of boresight, as shown in Section 5.1.4. The rod measurements (Figure 5.43 and Figure 5.44) show equal co- and cross-polarized responses as expected.

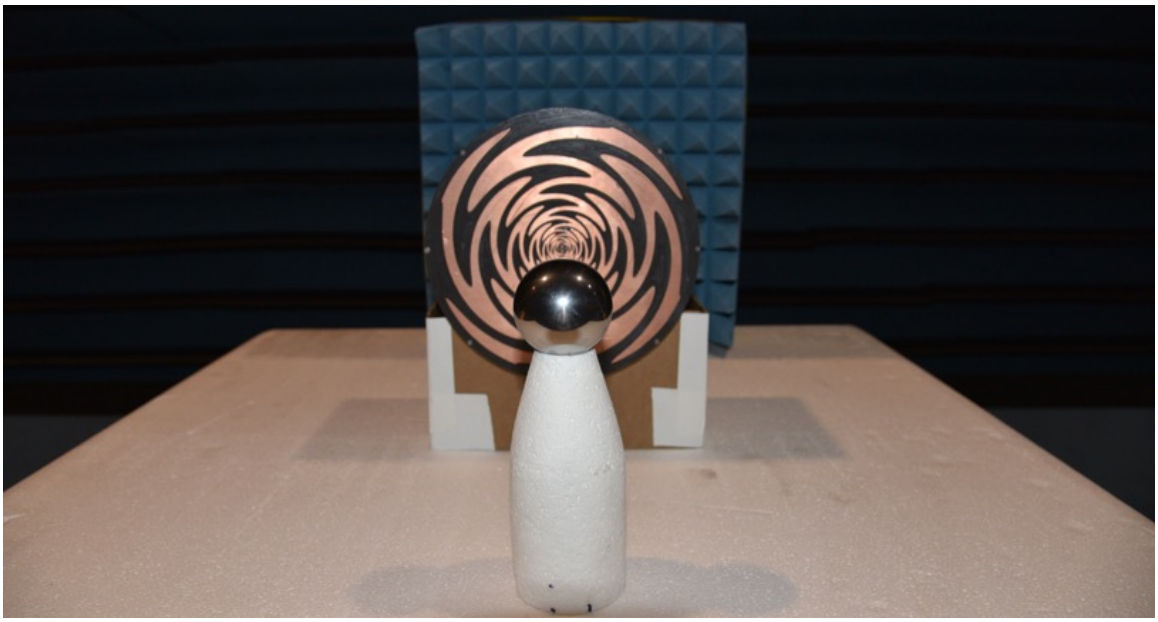

Figure 5.40: Setup of the four-port sinuous antenna and 5.08 cm diameter sphere target placed 15.24 cm from the antenna. The target was then scanned to the right 15.24 cm.

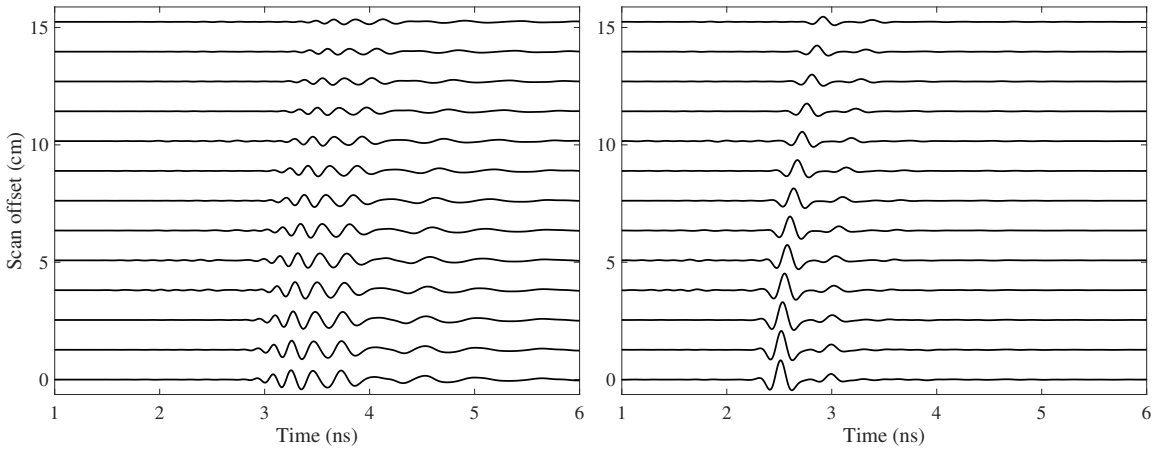

Figure 5.41: Waterfall plot of measured Co-Polarized B-scan showing the dispersed (left) and corrected (right) time-domain responses from the measured 5.08 cm sphere. Both the specular and creeping wave reflections are evident in the corrected results. Note that the results also contain the time delay due to the cables.

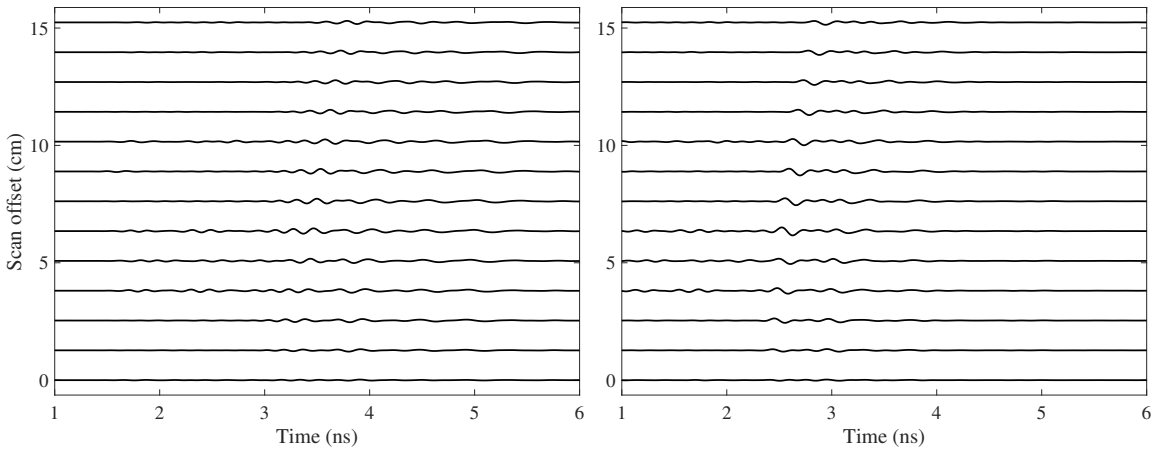

Figure 5.42: Waterfall plot of measured Cross-Polarized B-scan showing the dispersed (left) and corrected (right) time-domain responses from the measured 5.08 cm sphere. Target returns become evident off of boresight due to reduced isolation between channels. Note that the results also contain the time delay due to the cables.

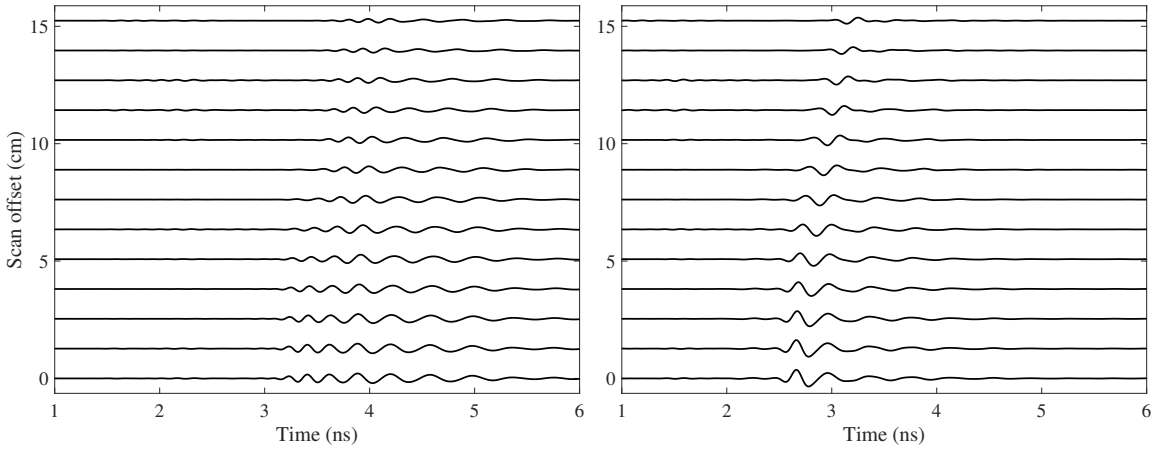

Figure 5.43: Waterfall plot of measured Co-Polarized B-scan showing the dispersed (left) and corrected (right) time-domain responses from the measured 5.08 cm sphere. Both the specular and creeping wave reflections are evident in the corrected results. Note that the results also contain the time delay due to the cables.

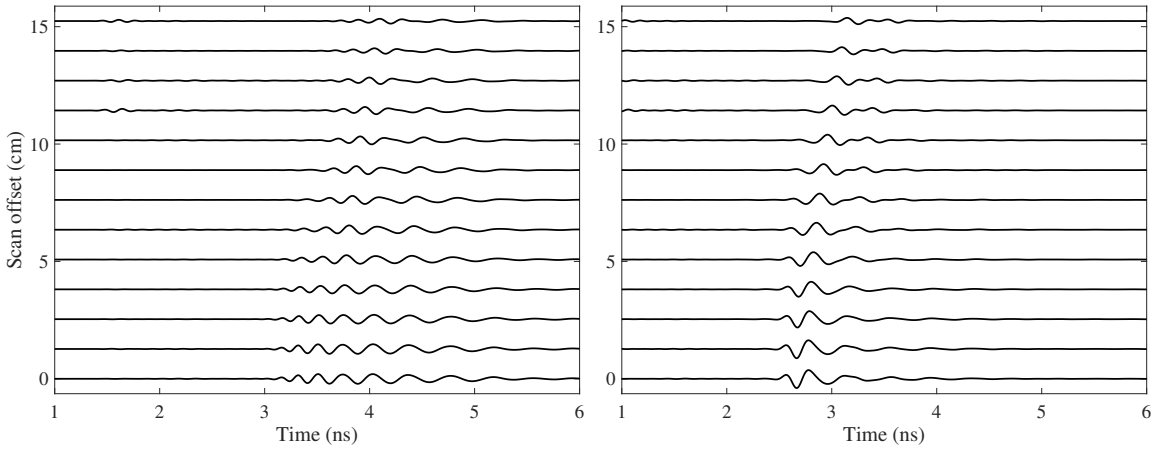

Figure 5.44: Waterfall plot of measured Cross-Polarized B-scan showing the dispersed (left) and corrected (right) time-domain responses from the measured 5.08 cm sphere. Target returns become evident off of boresight due to reduced isolation between channels. Note that the results also contain the time delay due to the cables.

5.4 Summary

In this chapter, it was proposed to operate each arm of a four-port sinuous antenna independently to achieve a quasi-monostatic antenna system capable of polarimetry while separating transmit and receive channels as is common in GPR systems. The quasi-monostatic configuration of the antenna reduces the size as well as prevents extreme bistatic angles, which may significantly reduce sensitivity when attempting to detect close-in targets. A similar antenna system was proposed in [8], which operated four resistive-vee antennas. However, the sinuous antenna has advantages over the resistive-vee such as constant gain over frequency and a lower height profile. A prototype four-port antenna was fabricated and measured. The following chapter details the integration of the prototype antenna into a GPR testbed for further measurements.

CHAPTER 6
EXPERIMENTAL EVALUATION OF THE UNBALANCED SINUOUS ANTENNA IN A GPR TESTBED

In this chapter, the four-arm sinuous antenna, designed and fabricated as described in Chapter 5, is integrated with a GPR testbed for measurements. The antenna is used to acquire polarimetric measured data from multiple targets. The polarimetric data is then used to discriminate between symmetric and asymmetric targets.

6.1 GPR Testbed

The GPR testbed consists of a three-axis positioner and vector network analyzer (VNA), both of which are connected to a controlling desktop computer. A sand-filled pit, in which targets may be buried, is located directly under the measurement apparatus. The positioner can scan the antenna over a two-dimensional area of approximately 1.5 by 1.8 m at different heights. Figure 6.1 shows the antenna mounted to the positioner and lowered to approximately 5 cm above the leveled sand. The measurement data is collected with the VNA in the frequency domain as 4-port S-parameters from 10 MHz to 8 GHz in 10 MHz steps. The data may then be transformed to the time domain via an IFFT after being weighted with window function. The time-domain result of a single measurement is called an A-scan [112]. An ensemble set of A-scans produced by the positioner movement is referred to as a B-scan or a C-scan for 1-D and 2-D positioner scans, respectively [112]. When the positioner is moved, it is allowed to settle mechanically before the VNA records data. This procedure is referred to as the "stop-and-stare" method, which is slower than performing data acquisition during continuous movement but provides increased accuracy. Targets can be measured in the air as well as buried since the positioner can be configured to raise the antenna up to 1 m above the sand.

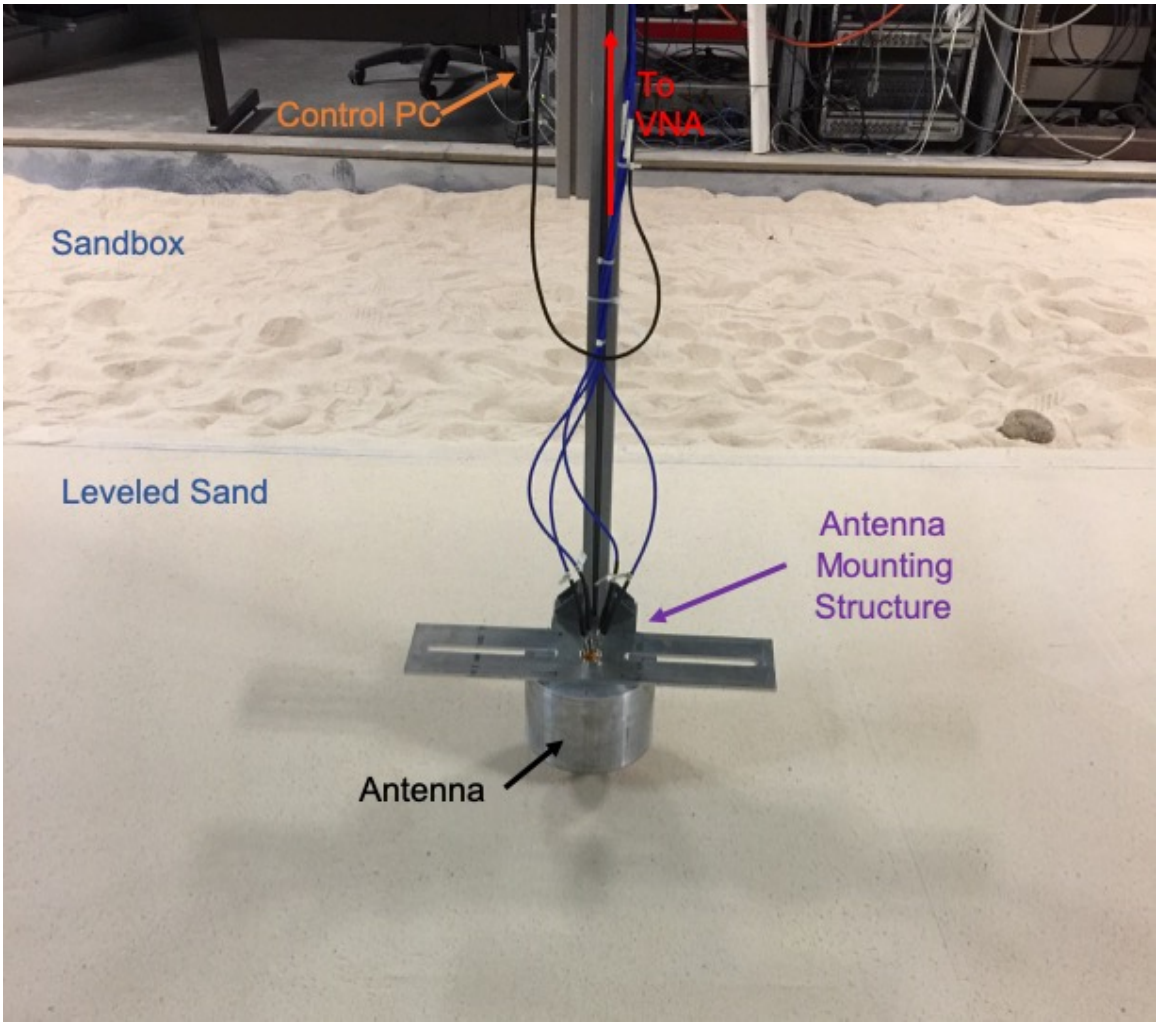

Figure 6.1: GPR Measurement Setup.

6.2 Targets in the Air

The system performance was evaluated with targets positioned in the air before measuring buried targets since the ground represents additional ambiguity. The target-in-air measurements produce cleaner experiments where all parameters may be understood and explained. Furthermore, the measurements are not plagued by issues present in a real GPR, e.g., ground bounce, which allows us to focus solely on the antenna's performance. Figure 6.2 shows an example of the test setup. The response from the ground was minimized by the inclusion of RF absorbing foam underneath the target. Additionally, the scans were repeated without the targets in order to remove the static background via coherent subtrac-

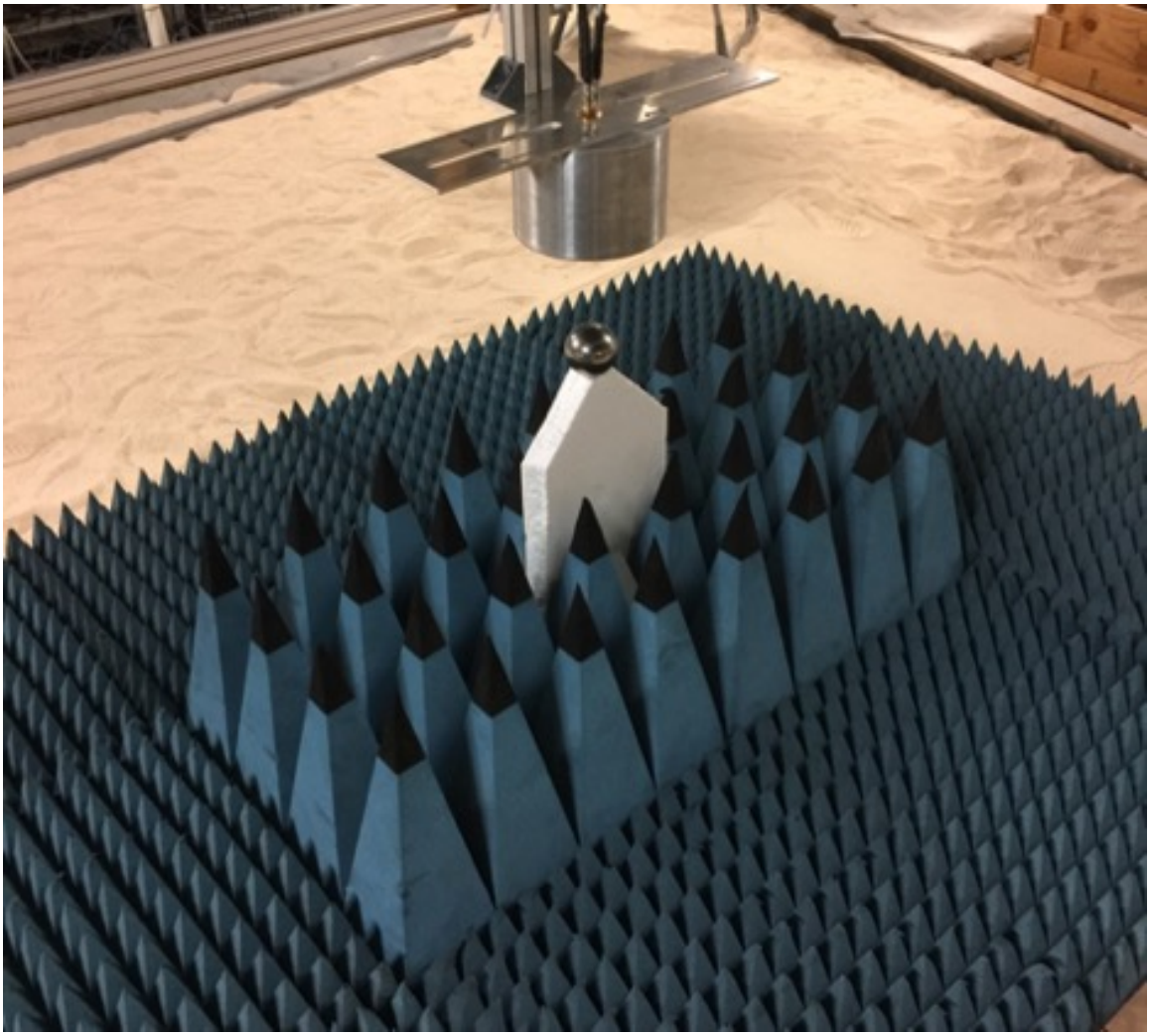

Figure 6.2: Measurement of a 7.62 mm sphere in the air using the GPR testbed. Notice that RF absorber has been placed beneath the target to minimize the response from the sand.

tion.

6.2.1 Background Subtraction

The raw measured data is not ideal as it contains many reflections from sources other than the target. These reflections include: reflection from the measurement setup (e.g., foam support), mismatch between the coaxial cables feeding the sinuous antenna structure (this only applies to the monostatic terms, see Section 5.3), mutual coupling between the antenna ports (see Section 5.1.5), mismatch at the SMA connection between the cables from the

VNA and the antenna, as well as phase drift in the measurement cables and electronics. These unwanted reflections are usually addressed by a coherent background subtraction process where the complex values of the measurement with the target present are subtracted from the complex values of the measurement without the target.

Figure 6.3 shows monostatic measurement results from a B-scan of a sphere (7.62 cm in diameter) placed 15 cm below the antenna before and after coherent background subtraction. Note that the frequency domain data has been transformed to the time domain via an IFFT after weighting with a Taylor window with parameters $\bar{n} = 15$ and $PSR = -80$ as defined in [102]. Without removing the static background, the close-in target response is masked by the much larger reflection at the antenna terminals, as demonstrated by the A-scan with the target on boresight (Figure 6.3c). Notice the difference in the amplitude scale between the before and after figures. Once the background is subtracted, the response from the target can be easily seen. Although a remnant of the background, with amplitude similar to that of the target, is still visible. This remainder of the background is due to small temporal misalignment between background and target measurements. The misalignment can have multiple sources such as instrument phase drift, positioner inconsistencies, as well as changes in the antenna and cables due to temperature. A phase alignment procedure may be used to improve the background subtraction.

The background subtraction algorithm developed for these measurements incorporates a phase alignment procedure based on a divide and conquer algorithm [113] (see Algorithm 6.1). The algorithm searches for a small temporal offset t_{err} that, when applied as a frequency-dependent phase offset $\phi_{err}(\omega)$ to the background, reduces the sans background time-domain response in the 1–3 ns window for each scan location. Essentially the time offset represents drift in the measured data between the background and with-target measurements. We assume here that the offset is quite small and the phase is relatively stable over the acquisition of each individual A-scan. Figure 6.4 shows the optimal time offset between the background and target measurements found by the algorithm for the mono-

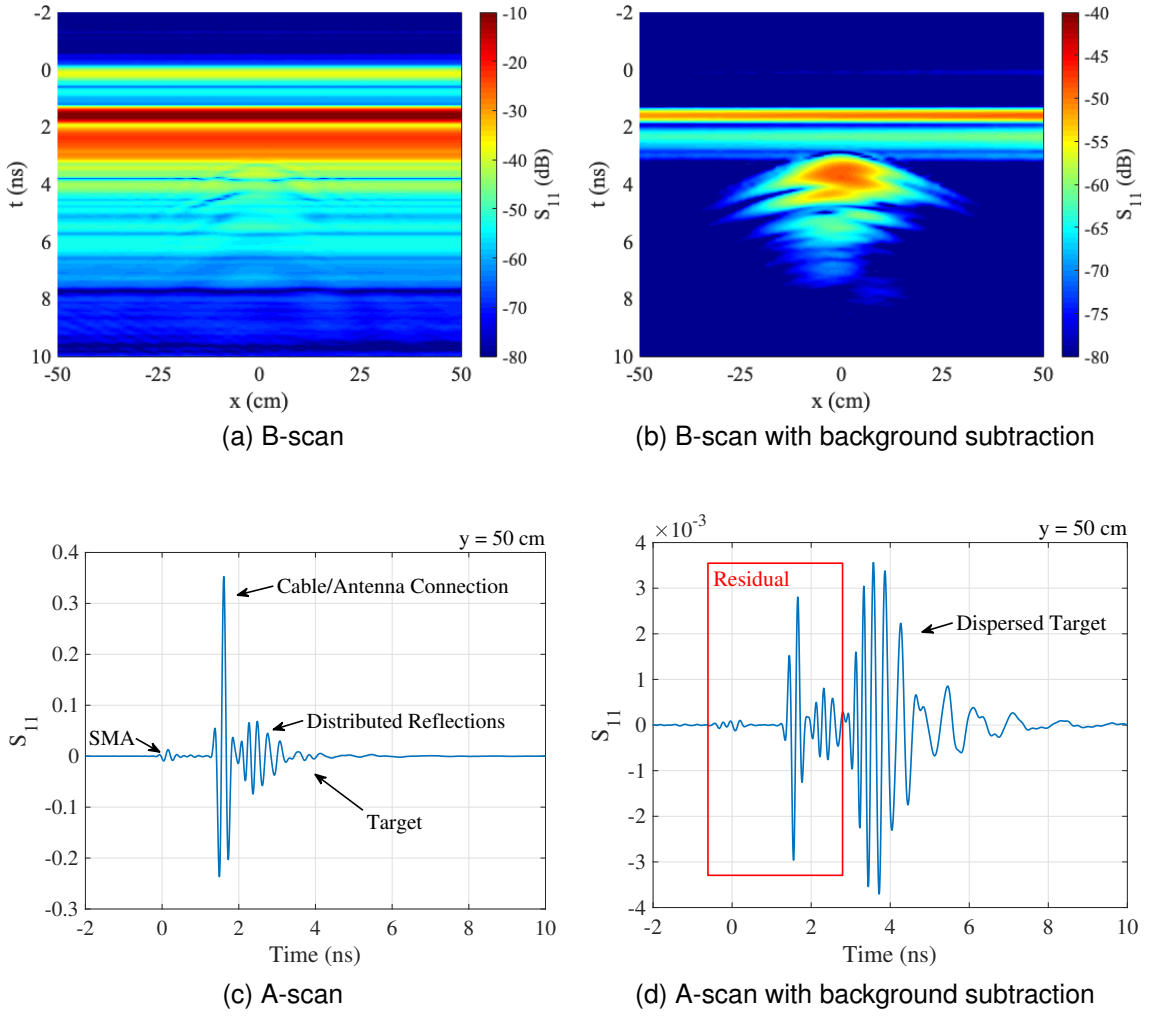

Figure 6.3: Measured response (S_{11}) from the 7.62 cm sphere in the air prior to background subtraction (left) and after initial background subtraction (right). Pseudo-color graphs of the analytic amplitude of the B-scans (top) and line graphs of the A-scan over the target (bottom).

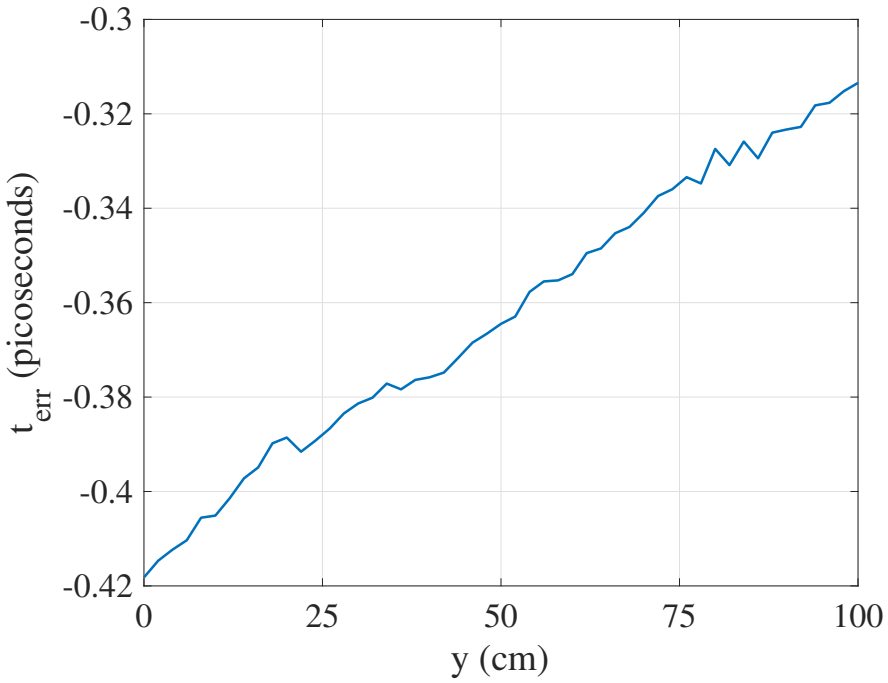

Figure 6.4: Optimal time offset between the background and target measurements found by using Algorithm 6.1 for the monostatic S_{11} measurement of the 7.62 cm sphere in the air at each scan location.

static (S_{11}) measurement of the 7.62 cm sphere at each scan location. These time offsets best align the background and target measurements to produce the optimal subtraction. The resulting improvement in the B-scan background subtraction is shown in Figure 6.5, which shows the remnant of the background is now indistinguishable compared to the target.

The examples presented in this section demonstrate the background subtraction for S_{11} data. However, the same procedure is applied to all the S-parameter measurements, e.g., the S_{ij} background data is also subtracted from the S_{ij} target data. The time offset is only computed for a single measurement (S_{11}) since the error is relatively stable during the acquisition of one measurement.

6.2.2 Dispersion Correction

With the removal of the background, the target returns become clearly distinguishable; however, they are smeared in time due to the dispersive properties of the antenna. The

Data: Y y-axis sample vector
Data: ω Frequency sample vector
Data: M Frequency domain measurement data
Data: B Frequency domain measurement data of backgound only
Result: C Frequency domain measurement data sans background

$N_t \leftarrow$ an even number of time samples to test
$T \leftarrow$ time samples between 1 and 3 ns
foreach *y* **in** *Y* **do**
    `/* Search for time offset between ±10 picoseconds */`
    $t_{start} \leftarrow -10^{-12}$
    $t_{end} \leftarrow 10^{-12}$
    $t_{err}^{old} \leftarrow t_{start}$
    $t_{err} \leftarrow t_{end}$
    while $|t_{err}^{old} - t_{err}| > 0.1^{-15}$ **do**
        `/* Break the time offset range into some discrete samples to test. */`
        $\vec{t}_{samples} \leftarrow$ `linspace` $(t_{start}, t_{end}, N_t)$
        for $n \leftarrow 1$ **to** N_t **do**
            $S \leftarrow M[y] - B[y] * \exp(j\omega\vec{t}_{samples}[n])$
            $s \leftarrow$ `IFFT` S
            residual$[n] = \sqrt{\sum_k |s[k]|^2} : k \in T$
        end
        `/* Find the best phase error sample and then try discrete samples nearby. */`
        $t_{err}^{old} \leftarrow t_{err}$
        $m \leftarrow$ index of smallest residual error
        $t_{err} \leftarrow \vec{t}_{samples}[m]$
        $\Delta_t = t_{end} - t_{start}$
        $t_{start} \leftarrow t_{err} - \Delta_t/4$
        $t_{end} \leftarrow t_{err} + \Delta_t/4$
    end
    $C[y] \leftarrow M[y] - B[y] * \exp(j\omega t_{err})$
end

Algorithm 6.1: Background subtraction with phase drift correction.

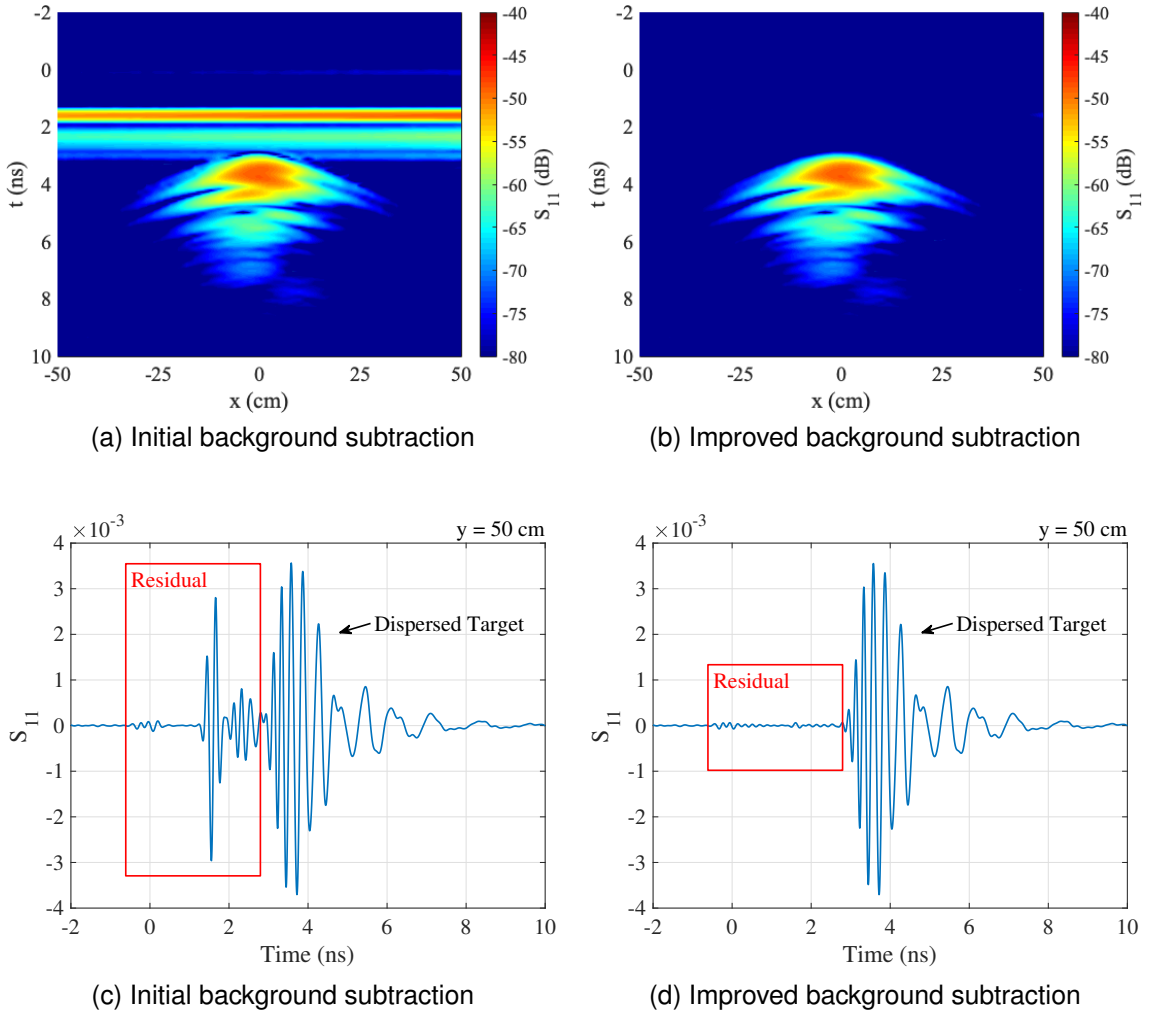

Figure 6.5: Measured response (S_{11}) from 7.62 cm sphere in air with initial background subtraction (left) and after background subtraction with phase alignment (right).

dispersion model, described in Chapter 3, was applied with the parameters determined by the method shown in Section 5.3.3. The B-scan of the 7.62 cm sphere is shown before and after the application of the dispersion correction model in Figure 6.6. The application of the dispersion model allows target attributes to be more clearly distinguished, i.e., the specular and creeping wave returns. The signal-to-noise ratio (SNR) is also increased since the dispersion correction compresses the target return, resulting in a larger amplitude, and any response remaining from the reflection or mutual coupling at the antenna terminals is dispersed toward negative time.

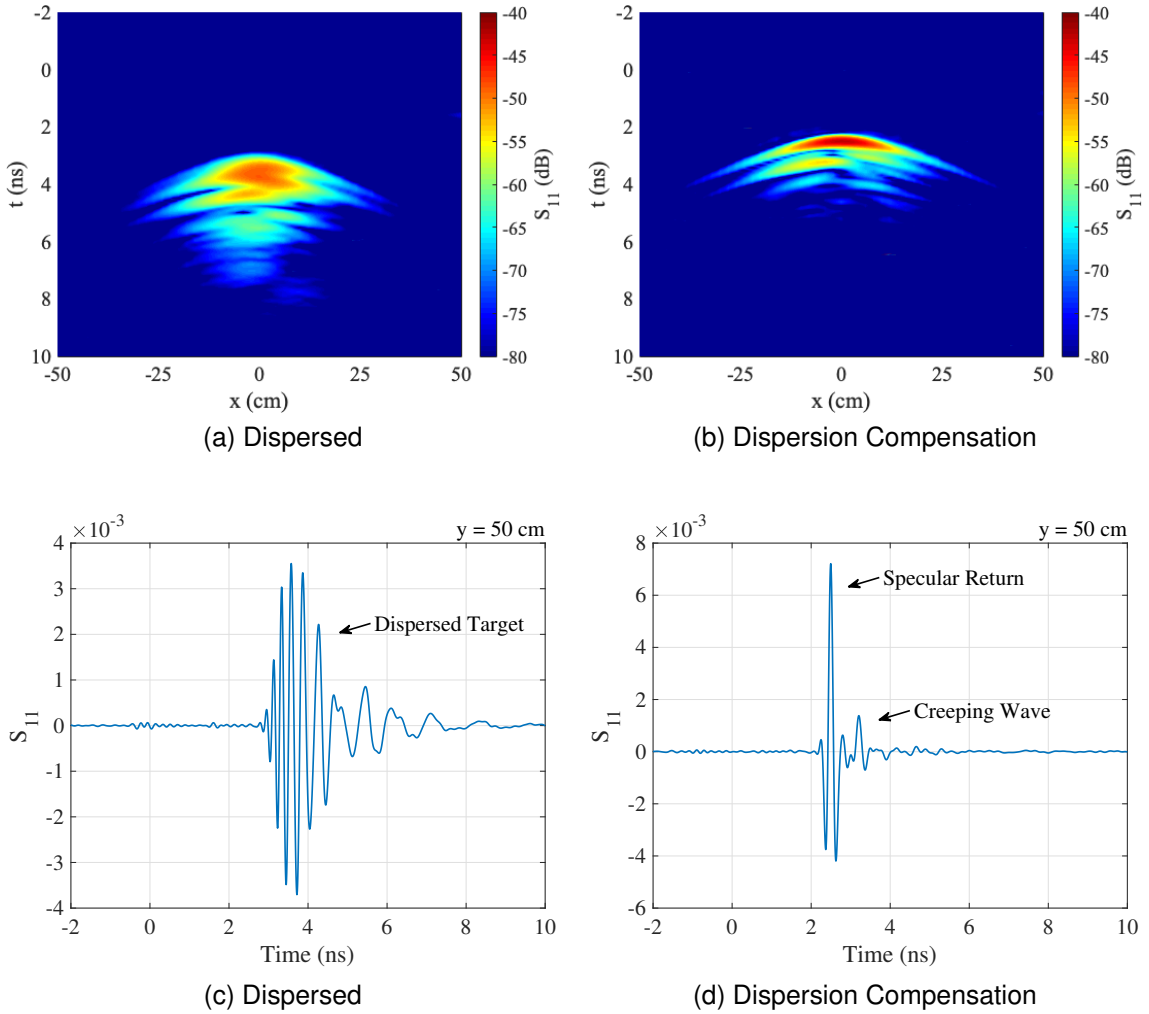

Figure 6.6: Measured response (S_{11}) from 3" sphere in air with background subtraction (left) and after dispersion compensation (right).

6.2.3 Circular Polarization

The sinuous antenna may be used to generate circular polarization (CP) [87] by combining two orthogonal linear polarizations in phase quadrature. GPR systems sometimes utilize CP since it can be used to discriminate between symmetric and asymmetric targets [92, 114]. Dual-linear data was acquired during the measurements since each arm of the antenna was operated independently. However, the CP responses may be synthesized from the dual-

linear responses by the following basis transform [102]

$$\begin{bmatrix} S_{LL} & S_{LR} \\ S_{RL} & S_{RR} \end{bmatrix} = \frac{1}{2} \begin{bmatrix} 1 & -j \\ 1 & +j \end{bmatrix} \begin{bmatrix} S_{HH} & S_{HV} \\ S_{VH} & S_{VV} \end{bmatrix} \begin{bmatrix} 1 & 1 \\ -j & +j \end{bmatrix}. \tag{6.1}$$

With the coordinate system defined in Figure 5.1, the horizontally polarized ($\hat{x}$) channels become antenna ports 1 and 3, and the vertically polarized ($\hat{y}$) channels are ports 2 and 4. If ports 1 and 2 transmit while 3 and 4 receive, the co-polarized terms become

$$S_{HH} = S_{31} \tag{6.2}$$

and

$$S_{VV} = S_{42}. \tag{6.3}$$

Similarly, the cross-polarized terms are

$$S_{HV} = S_{32} \tag{6.4}$$

and

$$S_{VH} = S_{41}. \tag{6.5}$$

Usually, the corresponding cross-polarized terms are equal, but they are not for this antenna since the transmit and receive pairs are not symmetrical. This asymmetry may be observed in the sensitivity plots of Section 5.1.3. The cross-polarized symmetry may be improved by averaging the two cross-polarized terms together as

$$S_{HV} = S_{VH} = \frac{1}{2}(S_{32} + S_{12}). \tag{6.6}$$

Figure 6.7 shows the synthesized cross-polarized CP term S_{RL}, computed from the dual-linear components by Equation 6.1, when defining the linear cross-polarized terms individ-

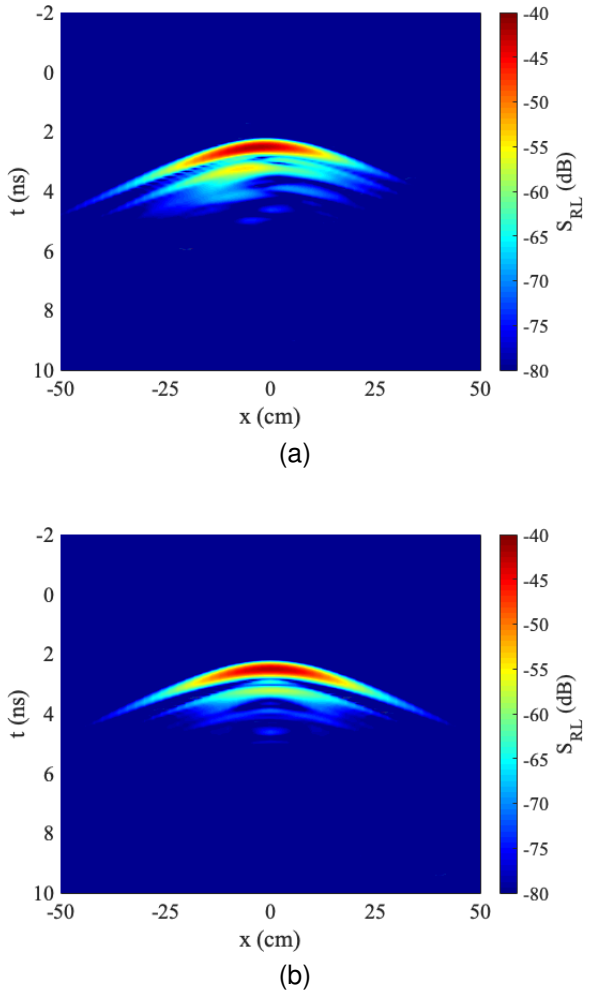

Figure 6.7: Measured cross-polarized CP response (S_{RL}) from the 7.62 cm sphere in the air. The CP was computed from the dual-linear responses with Equation 6.1 using (a) the linear cross-polarized terms individually, and (b) by taking the average. Using the average produces a more symmetric response.

ually (Equations 6.4 and 6.5) and by taking the average (Equation 6.6). Using the average produces a more symmetric response, which may be useful when utilizing the CP components for target discrimination. Thus, the average is used when computing the linear cross-polarized terms for all the remaining data presented in this chapter.

6.2.4 Target Discrimination

The returns from symmetric targets (e.g., spheres) may be distinguished from those from asymmetric targets (e.g., wires) by comparing the co- and cross-polarized components

[114]. Symmetric targets will produce primarily a co-polarized CP response while asymmetric targets will produce both co- and cross-polarized CP responses. False-color maps were created from the CP responses, similar to those developed in [113], which allow for visual discrimination between symmetric and asymmetric targets. The false-color maps are created from the measured B-scan data by setting all pixels 12 dB below the peak response of the target to white while setting the red, green, and blue components of the remaining pixels to

$$\begin{bmatrix} R \\ G \\ B \end{bmatrix} = \begin{bmatrix} \frac{|S_{RL}|}{|S_{LL}|} \\ 0 \\ \frac{|S_{RL}|-|S_{LL}|}{|S_{RL|}}. \end{bmatrix} \tag{6.7}$$

With this color mapping, symmetric targets will appear blue, and asymmetrical targets will appear red in the image. An example false-color map, along with the co- and cross-polarized CP responses, is provided in Figure 6.8 for the 7.62 cm sphere in the air measurement.

6.2.5 Other Targets

In addition to the 7.62 cm sphere, the following targets were also measured in the air: a 5.08 cm sphere, a 4.9 cm diameter loop made from 1.3 mm thick wire, and a straight piece of 1.3 mm diameter wire 10.1 cm long. The straight segment of wire was measured at multiple orientations. Figure 6.9 shows the targets in their specific measurement setups. Circularly-polarized B-scans, both co- and cross-polarized results, along with corresponding false-color maps are provided for each target in Figures 6.10–6.12.

Results for the 5.08 cm sphere and wire loop are given in Figure 6.10. These two targets are symmetric and ideally do not produce a co-polarized CP response; however, a co-polarized response is seen for both targets off of boresight. The off-boresight co-polarized response is not null because the polarization purity degrades off of boresight, as discussed in Section 5.1.4. However, the polarization is sufficiently good that the false-

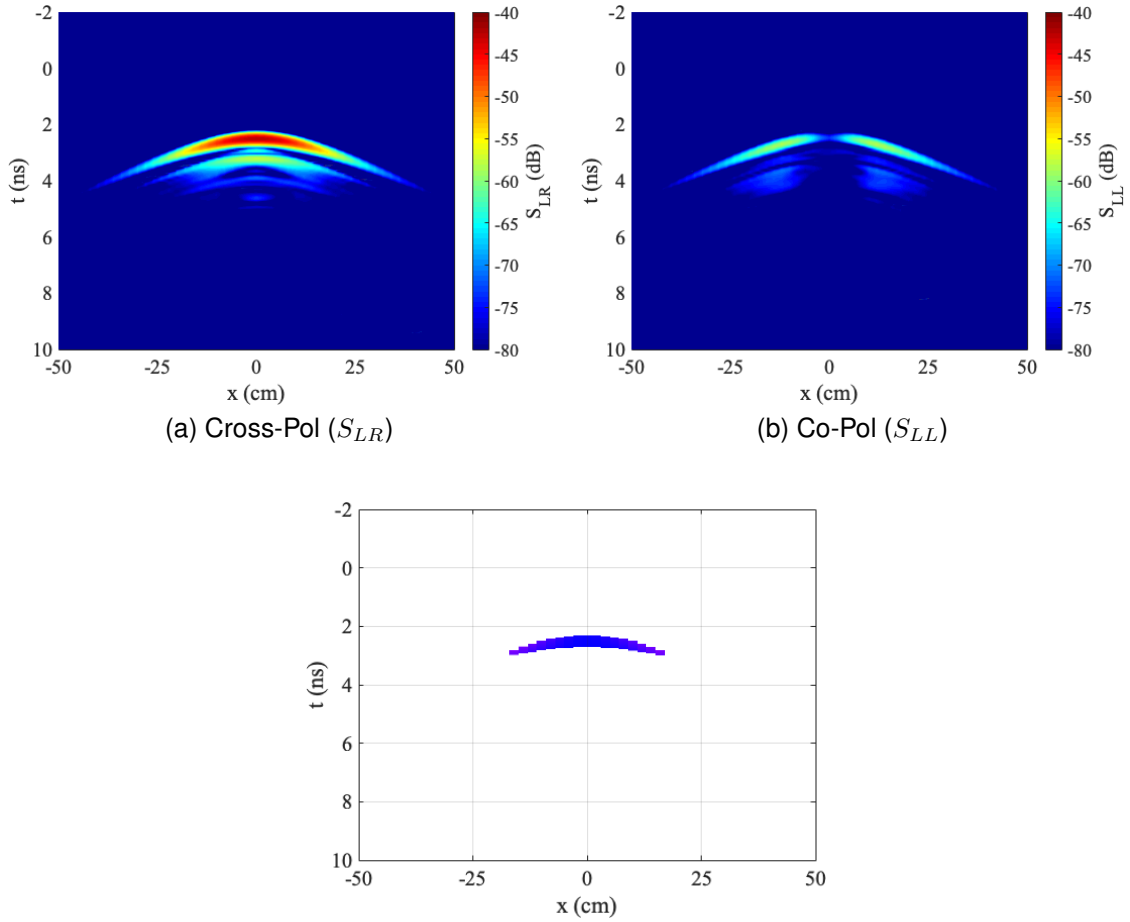

(a) Cross-Pol (S_{LR})

(b) Co-Pol (S_{LL})

(c) False Color Map

Figure 6.8: Measured cross-polarized CP response (a), co-polarized response (b), and false color map (c) for the 7.62 cm sphere in the air.

color maps are blue—indicating a symmetric target.

The wire target was measured at multiple orientations, starting aligned with the $\hat{y}$-axis (perpendicular to the scan-axis) and then rotated in a clock-wise fashion about the $\hat{z}$-axis to 22.5°, 45°, and 90°. The coordinate system is defined in Figure 5.1. The results are shown in Figures 6.11 and 6.12. The wire will produce equal co- and cross-polarized CP responses, which results in a red false-color map indicating target asymmetry. The B-scans change shape as the wire rotates since the wire's pattern is being rotated off of the scan axis.

This set of targets demonstrates the usefulness of the antenna's polarimetric capability

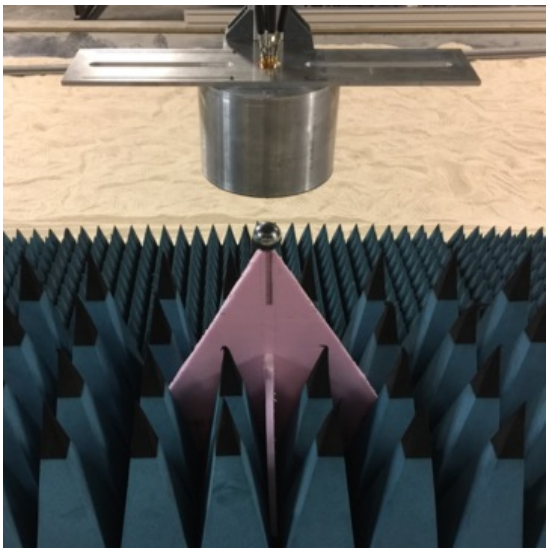

(a) 5.08 cm Sphere

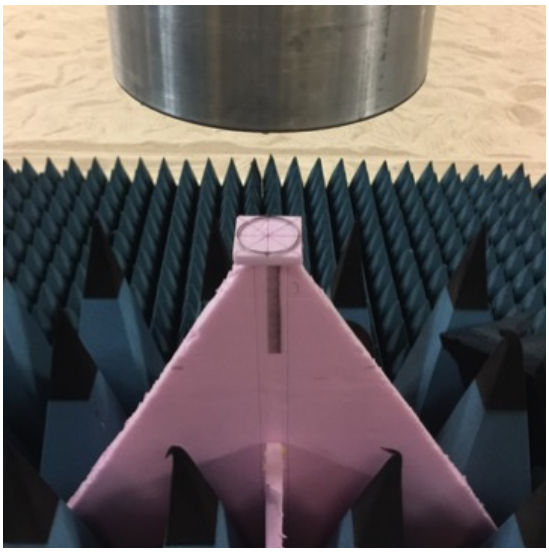

(b) 4.8 cm Wire Loop

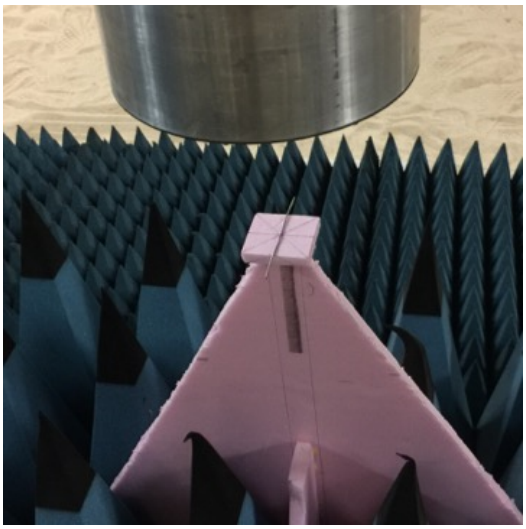

(c) 10.1 cm Straight Wire, rotated 0°

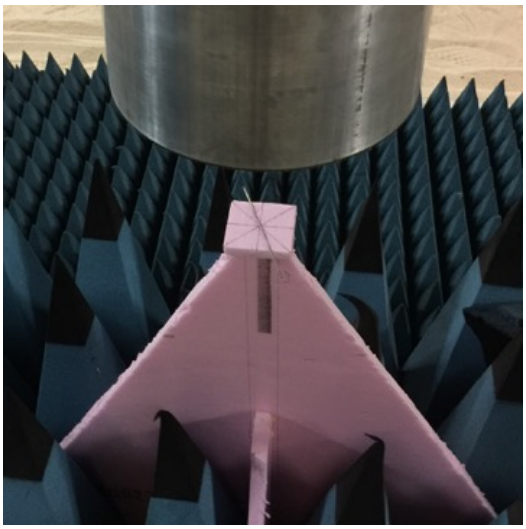

(d) 10.1 cm Straight Wire, rotated 22.5°

Figure 6.9: Targets measured in the air: (a) 5.08 cm diameter sphere, (b) 4.8 cm diameter wire loop, (c) 10.1 cm long wire aligned perpendicular to scan axis (0° off of $\hat{y}$-axis), and (d) 10.1 cm long wire rotated 22.5°.

as it can identify the various symmetries correctly. Furthermore, the algorithm correctly identifies the wire (red false-color map) regardless of its orientation. Next, the system is tested with targets buried in the sand.

6.3 Targets Buried in the Sand

With the system performance verified by measuring targets in the air, a subset of the targets was then measured after being buried in dry sand. Figure 6.13 shows the targets measured, which consists of two spheres (symmetric targets) and a straight segment of wire at multiple orientations (asymmetric targets). During the measurements, the antenna was placed 5 cm above the surface of the smoothed sand. Both B-scan and C-scan measurements were performed.

6.3.1 Data Processing

The measured data from the buried targets were processed similar to those from the targets measured in the air (see Section 6.2). The background subtraction was performed using the sample at $x = 50$ cm. Similarly, the C-scan data, which may be considered a set of B-scans, used the first sample of each row (B-scan) as the background. The time alignment procedure described in Section 6.2.1 was performed at each location to improve the removal of the mutual coupling in the antenna. The background subtraction also removed a significant amount of the response from the surface of the sand. However, the smoothed surface is not perfectly level, which leaves a remnant of the surface return in the data. A second phase alignment could be used to improve the removal of the surface via subtraction; however, the remnant of the surface is left in the results as another target for discrimination. Dual linear data is collected, which is then used to synthesize CP responses, as described in Section 6.2.3. An IFFT was used to transform the frequency domain data to the time domain after weighting with a Taylor window having parameters $\bar{n} = 15$ and $PSR = -80$ as defined in [102]. The CP responses are then used to generate false-color maps for target

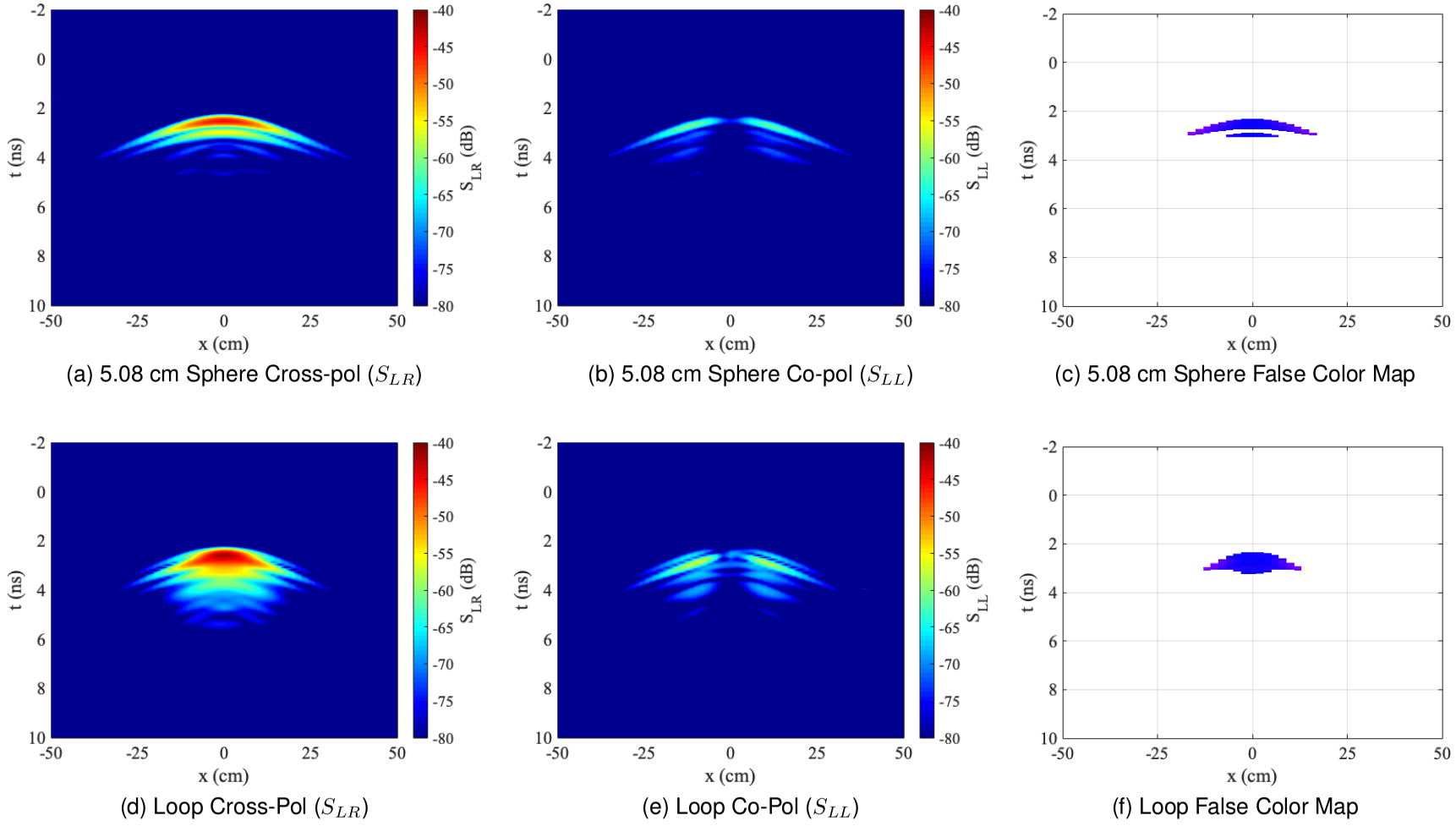

(a) 5.08 cm Sphere Cross-pol (S_{LR})

(b) 5.08 cm Sphere Co-pol (S_{LL})

(c) 5.08 cm Sphere False Color Map

(d) Loop Cross-Pol (S_{LR})

(e) Loop Co-Pol (S_{LL})

(f) Loop False Color Map

Figure 6.10: Cross-polarized CP response (a), co-polarized CP response (b), and false color map (c) for the 5.08 cm sphere measured in the air. Cross-polarized CP response (d), co-polarized CP response (e), and false color map (f) for the wire loop measured in the air.

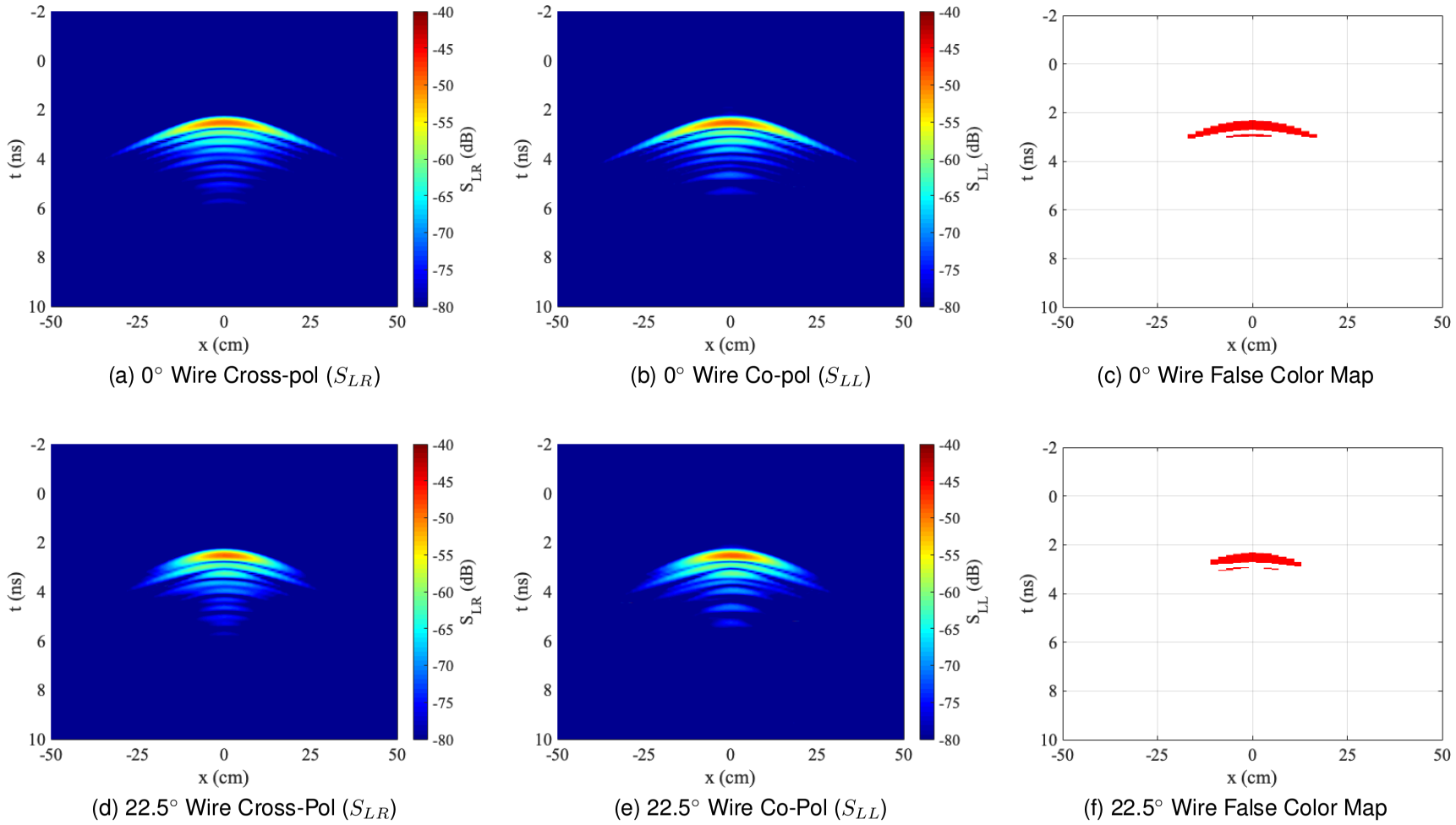

(a) 0° Wire Cross-pol (S_{LR})

(b) 0° Wire Co-pol (S_{LL})

(c) 0° Wire False Color Map

(d) 22.5° Wire Cross-Pol (S_{LR})

(e) 22.5° Wire Co-Pol (S_{LL})

(f) 22.5° Wire False Color Map

Figure 6.11: Cross-polarized CP response (a), co-polarized CP response (b), and false color map (c) for the 10.1 cm long straight wire aligned perpendicular to the scan axis (0° off of $\hat{y}$-axis) and measured in the air. Cross-polarized CP response (a), co-polarized CP response (b), and false color map (c) for the 10.1 cm long straight wire rotated 22.5° and measured in the air.

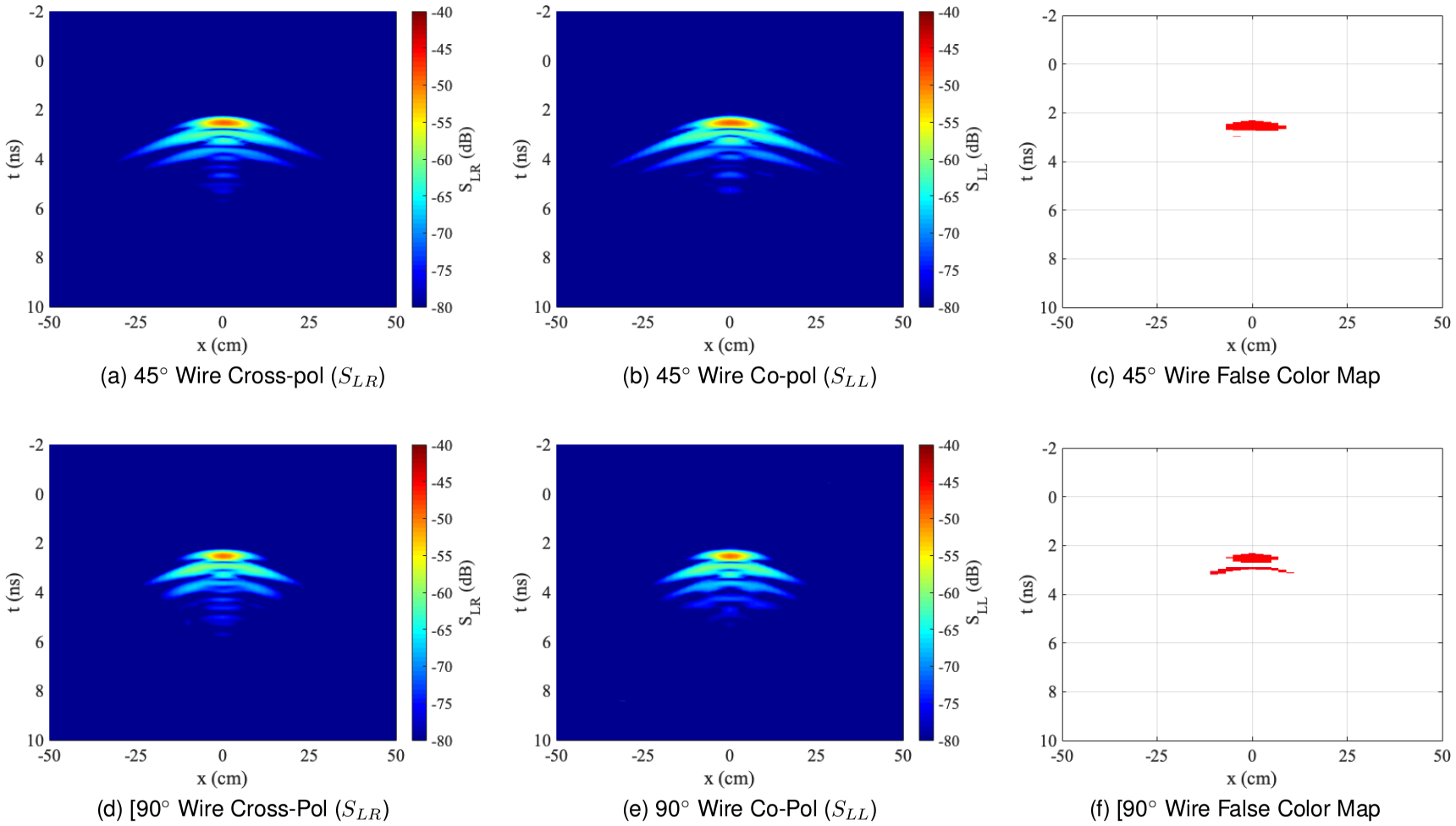

(a) 45° Wire Cross-pol (S_{LR})

(b) 45° Wire Co-pol (S_{LL})

(c) 45° Wire False Color Map

(d) [90° Wire Cross-Pol (S_{LR})

(e) 90° Wire Co-Pol (S_{LL})

(f) [90° Wire False Color Map

Figure 6.12: Cross-polarized CP response (a), co-polarized CP response (b), and false color map (c) for the 10.1 cm long straight wire rotated 45° and measured in the air. Cross-polarized CP response (a), co-polarized CP response (b), and false color map (c) for the 10.1 cm long straight wire rotated 90° (aligned with the scan axis) and measured in the air.

(a) 7.62 cm Sphere

(b) 5.08 cm Sphere

(c) 10.1 cm Straight Wire, rotated 45°

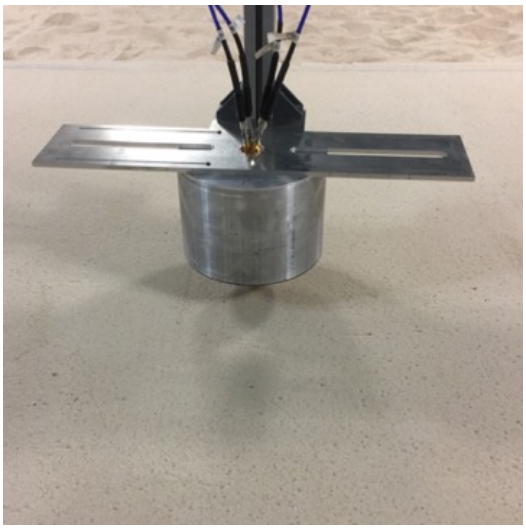

(d) Smoothed Sand

Figure 6.13: Targets measured when buried in the sand: (a) 7.62 cm diameter sphere buried 10 cm deep, (b) 5.08 cm diameter sphere buried 5 cm deep, (c) 10.1 cm long wire rotated 45° off of the $\hat{y}$-axis buried 5 cm deep, and (d) smoothed sand after burying the target.

discrimination—similar to what was done in Section 6.2.4.

6.3.2 B-scan Measurement Results

The processed measurement results are shown in Figure 6.14 and Figure 6.15 for the symmetric and asymmetric targets, respectively. The results indicate that targets may be correctly identified when buried in the sand. The co-polarized response is not zero for the symmetric targets; however, it is sufficiently small to identify the target as symmetrical. For all the rotations of the wire target, the co- and cross-polarized responses are essentially equal as expected. The residual reflection from the surface of the sand is located at approximately 1.8 ns in all the graphs. The return from the surface of the sand is mainly cross-polarized, since the surface is symmetric, which allows for the wire targets to be easily distinguished from the surface response. Notice that the residual of the surface response is significantly less for the 5.08 cm sphere (see Figure 6.14), which indicates the sand was leveled better for that particular measurement allowing for an improved complete subtraction of the background.

6.3.3 C-scan Measurement Results

Two-dimensional C-scans were made of the buried 5.08 cm sphere and 10.1 cm wire segment; the results are displayed in Figure 6.16. The data is essentially sets of multiple x-axis B-scans made at different y-axis locations. The background was subtracted by removing the $x = 40$ cm sample from each B-scan. Since the C-scan represents a three-dimensional volume of data, it can be challenging to visualize effectively. For the results shown in Figure 6.16, the peak response in time was taken for each (x,y) sample. The peak search began after 2.2 ns in order to avoid the primary response from the surface. The two-dimensional data obtained in this manner was then used to create the false-color maps shown. As can be observed, the false-color maps accurately distinguish the target symmetries. The peak-search is not a particularly useful method for processing real-world data—especially when

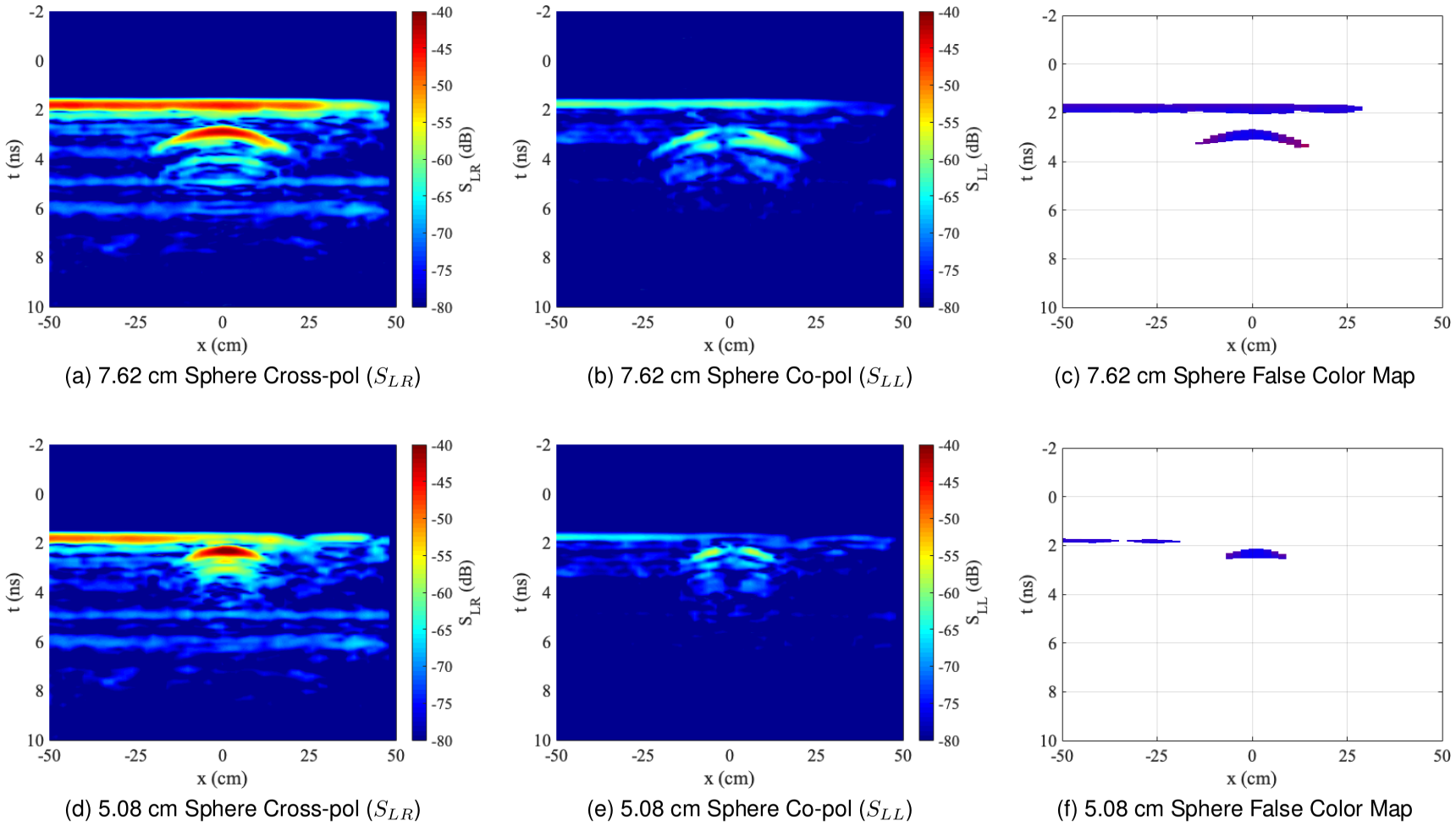

(a) 7.62 cm Sphere Cross-pol (S_{LR}) (b) 7.62 cm Sphere Co-pol (S_{LL}) (c) 7.62 cm Sphere False Color Map

(d) 5.08 cm Sphere Cross-pol (S_{LR}) (e) 5.08 cm Sphere Co-pol (S_{LL}) (f) 5.08 cm Sphere False Color Map

Figure 6.14: Cross-polarized CP response (a), co-polarized CP response (b), and false color map (c) for the 7.62 cm sphere measured when buried 10 cm in the sand. Cross-polarized CP response (d), co-polarized CP response (e), and false color map (f) for the 5.08 cm sphere measured when buried 5 cm in the sand.

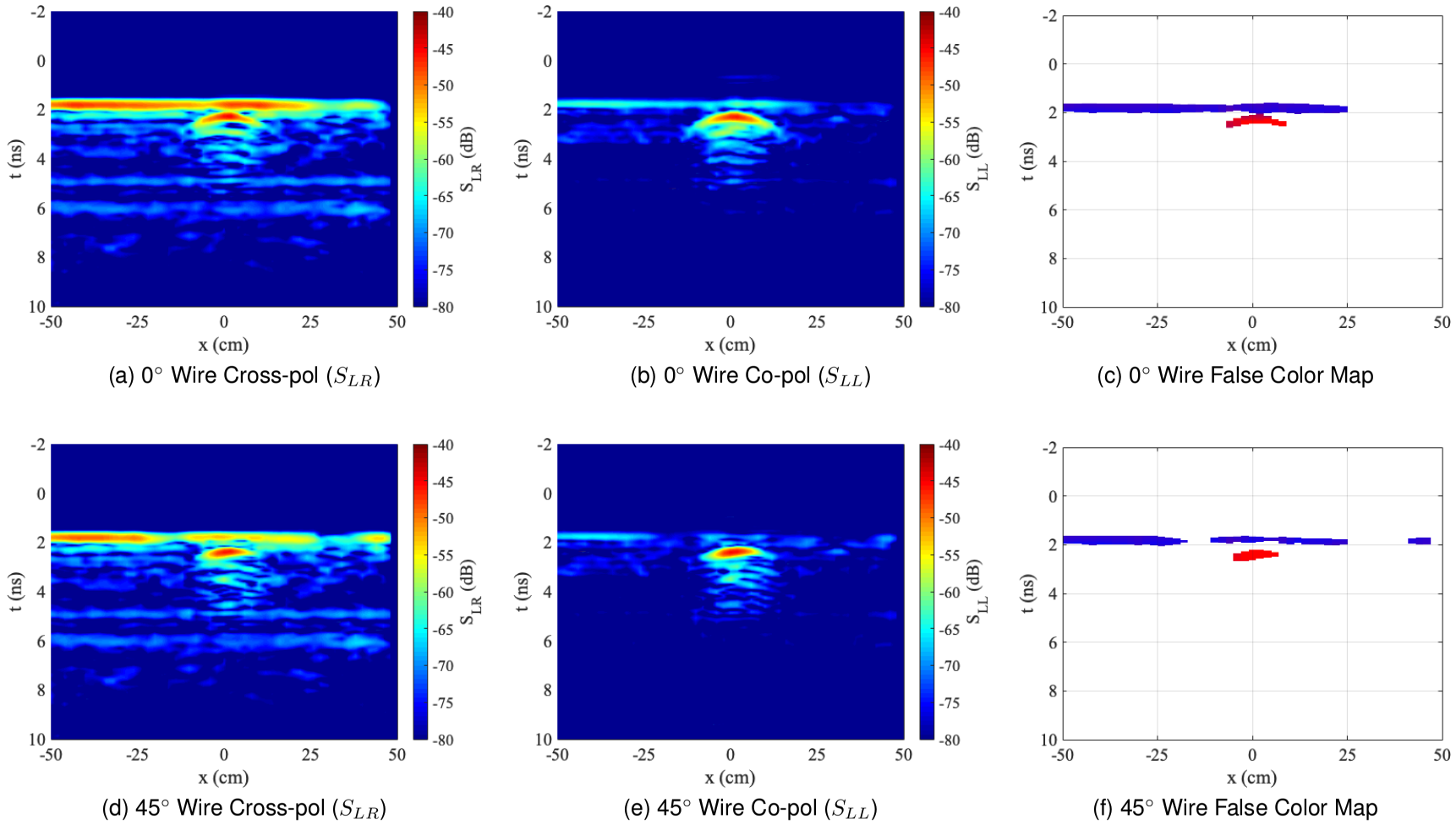

(a) 0° Wire Cross-pol (S_{LR})

(b) 0° Wire Co-pol (S_{LL})

(c) 0° Wire False Color Map

(d) 45° Wire Cross-pol (S_{LR})

(e) 45° Wire Co-pol (S_{LL})

(f) 45° Wire False Color Map

Figure 6.15: Cross-polarized CP response (a), co-polarized CP response (b), and false color map (c) for the 10.1 cm long wire rotated 0° off of the $\hat{y}$-axis measured when buried 5 cm in the sand. Cross-polarized CP response (d), co-polarized CP response (e), and false color map (f) for the 10.1 cm long wire rotated 45° off of the $\hat{y}$-axis measured when buried 5 cm in the sand.

the scene contains multiple targets. However, the technique was adequate for the simple case analyzed. In more complicated scenes, two-dimensional slices of the data or three-dimensional iso-surfaces [115] may be used for more effective visualizations.

6.4 Summary

The four-port sinuous antenna developed in Chapter 5 was integrated with a GPR testbed and used to measure targets in the air as well as buried in dry sand. Dual linear data was acquired and then used to generate circularly-polarized (CP) responses. The CP responses were successfully used to discriminate between symmetric and asymmetric targets by comparing the ratio of co- and cross-polarized returns.

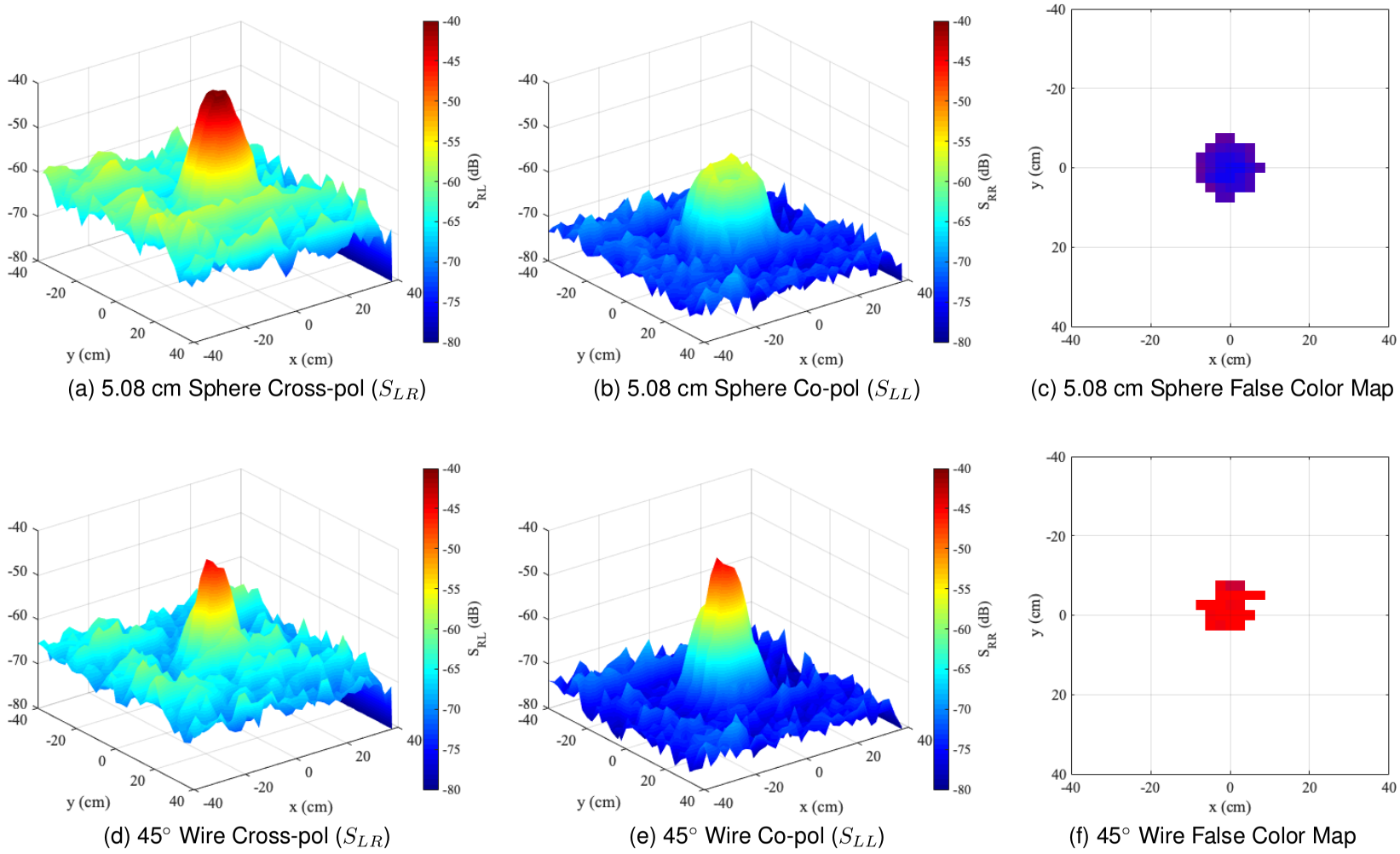

(a) 5.08 cm Sphere Cross-pol (S_{LR})

(b) 5.08 cm Sphere Co-pol (S_{LL})

(c) 5.08 cm Sphere False Color Map

(d) 45° Wire Cross-pol (S_{LR})

(e) 45° Wire Co-pol (S_{LL})

(f) 45° Wire False Color Map

Figure 6.16: C-scan measurement results for the 5.08 cm sphere measured when buried 5 cm in the sand: cross-polarized peak CP response (a), co-polarized peak CP response (b), and false color map (c). C-scan measurement results for the for the 10.1 cm long wire rotated 45° off of the $\hat{y}$-axis measured when buried 5 cm in the sand: cross-polarized peak CP response (d), co-polarized peak CP response (e), and false color map (f).

CHAPTER 7
CONCLUSION AND FUTURE WORK

The research presented in this dissertation analyzes the operation of the sinuous antenna and provides guidance for overcoming practical design challenges when utilizing the antenna for pulsed radar applications. The specific application investigated was the detection of close-in targets, e.g., landmines, with polarimetric ground-penetrating radar (GPR). The sinuous antenna is a desirable candidate for such applications since it is ultra-wideband, can produce multiple polarizations, has relatively flat gain over frequency, and has a low height profile.

Often GPR systems utilize multiple antennas to achieve increased isolation between transmit and receive channels and obtain polarization diversity. This configuration results in increased size as well as large bistatic angles when utilized for close-in targets. It was shown herein that the sinuous antenna could be operated as an array of closely spaced independent antennas that act as a quasi-monostatic antenna while providing polarimetric data. The ability to operate a single antenna for polarimetric sensing in a low-profile form factor is especially desirable for hand-held sensors.

The following sections outline the primary contributions of this dissertation, suggest follow-on research, and list the publications derived from this work.

7.1 Contributions

The primary contributions of this research are summarized below.

7.1.1 Detailed Analysis of the Excitation and Mitigation of Unintended Resonant Modes

The sinuous antenna may suffer from unintended resonant modes which distort the radiation and will produce ringing when the antenna is used to transmit pulses. An investigation

was performed to determine the correlation between design parameters and these resonant modes. Design guidance was presented, which mitigates the excitation of these modes merely by the selection of design parameters—no additional empirical design steps are required.

7.1.2 Novel Sinuous Antenna Outer Truncation Technique

A new sinuous antenna outer truncation technique was presented, which prevented low-frequency resonances. This technique avoids the additional empirical design step of clipping off the shape ends, as is common in the literature.

7.1.3 Simplistic Model for the Compensation of Dispersion in Sinuous Antennas

Dispersion in sinuous antennas is an undesirable characteristic when radiating pulses. Since the active region on the antenna moves with frequency, the spectral content of the radiation is spread out over time, i.e., dispersed. The original pulse may be reconstructed by applying a phase correction that compensates the dispersive effects. A simple dispersion model that is suitable for a fieldable system was proposed and implemented for both simulated and measured sinuous antennas. However, the dispersion is dependent on sinuous antenna design variables not accounted for by the model. Therefore, an optimization procedure was used to improve the dispersion correction model for each specific sinuous antenna. With the developed dispersion model, the sinuous antenna can be successfully used to transmit and receive temporally short pulses.

7.1.4 Development of an Unbalanced Sinuous Antenna for Close-in Sensing

When attempting to detect targets close to the ground surface, GPR systems often employ a bistatic antenna configuration. Such an arrangement is used to improve the isolation between the transmit and receive channels and decrease size; however, this leads to extreme bistatic angles that can reduce system performance. The operation of the sinuous

antenna as an array of closely spaced yet independent arms was presented as a potential quasi-monostatic antenna with a low height profile. The quasi-monostatic configuration significantly reduced the bistatic angles, which substantially improved performance for close-in targets while keeping the isolation to a manageable level. A prototype antenna was fabricated and integrated into a GPR testbed. The polarimetric nature of the antenna allows for the discrimination between linear and circular targets, which was demonstrated with measured data.

7.2 Future Work

The research presented in this dissertation enabled the practical utilization of sinuous antennas for pulsed radar applications. Also, a compact, quasi-monostatic, antenna design concept for close-in GPR was developed based on the unbalanced operation of a sinuous antenna. With these developments, future work will focus on expanding the application-specific design guidance as well as improving the performance of the new antenna concept.

7.2.1 Sinuous Antenna Design Guidance

In this work, many cases of the sinuous antenna were simulated and measured. Future work will seek to expand this analysis and develop general design graphs relating performance to design variables similar to what was done with the spiral antenna in [92].

7.2.2 Improved Sinuous Antenna Dispersion Model

The simple dispersion model presented in this work was able to compensate for the sinuous antenna dispersion successfully. However, the model required an optimization process for each antenna design to achieve the best results. It is desired to improve the model derivation to no longer require the optimization process. This improvement might be made by expanding the analytical expression to include other sinuous antenna design parameters, e.g., the angular width α. Another avenue may be the use of machine learning techniques

to build a dispersion prediction model that accounts for all design parameters.

7.2.3 Improved Feed for the Unbalanced Sinuous Antenna

A bundle of 50 Ω coaxial cables fed the prototype unbalanced sinuous antenna, which produced a considerable reflection at the antenna terminals while not achieving the degree of port isolation theoretically possible. Furthermore, such cable bundles may be difficult to phase align and represent mechanical difficulties. A new, robust, feeding structure capable of driving each arm independently while transforming the impedance from 50 Ω to that desired is a future research topic.

7.2.4 Unbalanced Eight-Arm Sinuous Antenna

In this work, an eight-arm unbalanced sinuous antenna was proposed, which improved the isolation between arms of the sinuous antenna when operating the arms independently. However, the initial investigation of the eight-arm antenna showed some disadvantages when compared to the four-arm version, such as off-boresight near-field radiation and reduced low-frequency performance. Future research may continue the study of this antenna to explore the possibility of mitigating the issues while achieving increased port isolation.

7.2.5 Improvement of Off-Boresight Performance

The sinuous antenna polarization was shown to degrade from linear on boresight to elliptical off of boresight, which produced undesired cross-polarized responses. An area of future study may be the possible improvement of isolation between polarization channels through signal processing, similar to what was done in [67].

7.2.6 Inversion with Full-Wave Forward Model

With the recent improvements in computing architecture for full-wave simulations, e.g., the acceleration of time-domain methods with large graphical processing units. Detailed

models of the antennas and their surrounding materials may be accurately simulated. The use of the forward-modeled channel may be able to improve the accuracy of inversion algorithms such as back projection while also accounting for undesirable effects of the antenna, e.g., dispersion, mutual coupling, etc. Future work will seek to improve the accuracy of inversion for targets close-in to the antenna with full-wave simulation results.

7.3 Publications

Subsets of the research presented herein have been published, with some still in preparation for submission, to peer-reviewed journals and refereed conferences. The publications are listed below.

7.3.1 Peer-Reviewed Journal Articles

- D. A. Crocker and W. R. Scott, "An Unbalanced Sinuous Antenna for Near-Surface Polarimetric Ground-Penetrating Radar," in IEEE Open Journal of Antennas and Propagation, 2020 (In Preparation).
- D. A. Crocker and W. R. Scott Jr. "Compensation of Dispersion in Sinuous Antennas for Polarimetric Ground Penetrating Radar Applications." Remote Sensing, vol. 11, no. 16: 1937, August 2019.
- D. A. Crocker and W. R. Scott, "On the Design of Sinuous Antennas for UWB Radar Applications," in IEEE Antennas and Wireless Propagation Letters, vol. 18, no. 7, pp. 1347-1351, July 2019.

7.3.2 Refereed Conference Proceedings and Presentations

- D. A. Crocker and W. R. Scott, "An Unbalanced Sinuous Antenna for Ultra-Wideband Polarimetric Ground-Penetrating Radar," *2020 IEEE International Geo-*

science and Remote Sensing Symposium, Waikoloa, Hawaii, USA, 2020 (In Preparation)

- D. A. Crocker and W. R. Scott Jr., "Sinuous Antenna Design for UWB Radar," *2019 IEEE International Symposium on Antennas and Propagation & USNC/URSI National Radio Science Meeting*, Atlanta, GA, 2019

- D. A. Crocker and W. R. Scott Jr., "Exploiting Polarization Wobble in Sinuous Antennas for the Detection of Linear Scatterers in Ground Penetrating Radar Applications," *2018 IEEE International Symposium on Antennas and Propagation & USNC/URSI National Radio Science Meeting*, Boston, MA, 2018, pp. 837–838.

Appendices

APPENDIX A
FULL-WAVE SIMULATION TOOLS

The analysis of the sinuous antenna presented in this work consisted of a significant amount of full-wave simulations. The simulation tool chosen for this work was CST Microwave Studio [86]. The choice of this tool was motivated by its availability (Sandia National Laboratories maintains licenses to this software) and the author's familiarity with it. In this appendix, some important aspects of simulating the sinuous antennas using CST are considered.

A.1 Drawing the Sinuous Antenna Geometry

The initial difficulty encountered when attempting to simulate the sinuous antenna was that of drawing the antenna's geometry with the computer-aided drafting (CAD) capability provided in the CST software. The final method utilized required drawing a single sinuous antenna arm as a point-by-point polygon, rotating the arm to produce the full antenna, and finally exporting the model as a CAD file for use in other simulation models. MATLAB code was developed to automate this process. The code for generating a sinuous antenna arm as a list of points is provided in Listing A.1. The CST automation script is provided in Listing A.2.

A.2 Solver Comparison

CST Microwave Studio provides a suite of solvers for electromagnetic analysis [86]. The three solvers considered for this work were the time-domain solver based on the Finite Integral Technique (FIT) [116], the frequency-domain solver based on the Finite Element Method (FEM) [117], and the frequency-domain Integral Equation (IE) [117] solver. Cer-

tain aspects of each solver, such as the mesh generation and run time, will be considered.

A.2.1 Mesh Generation

The sinuous antenna can be challenging to appropriately mesh since the details of the geometry vary substantially in size. The small part of the antenna near the feed requires a decreased mesh size when compared to the larger sections at the outer diameter. If a constant mesh size is used, the mesh will get very big, and the larger parts of the antenna will be meshed unnecessarily fine. The FEM solver has an adaptive meshing capability that will refine the mesh at specified frequencies. The IE solver does not have such a capability, and the mesh had to be adjusted manually. The FIT solver uses a grid-type mesh which required a small step width to model the small parts of the antenna accurately. Defining a good mesh was essential to compute the input impedance accurately.

Example meshes for the improved sinuous antenna (see Figure 2.34c) with parameters $P = 8$, $R_T = 5$ cm, $\alpha = 45°$, and $\tau = 0.7628$ are shown for each solver in Figure A.1. The FEM mesh was obtained via the adaptive meshing procedure applied at 4 and 10 GHz. The FIT mesh cell step size was set, such that the smallest trace width contained multiple mesh cells. Finally, the IE mesh was manually controlled by defining a step size in two regions. The mesh sizes are shown along with the run times in Table A.1.

These example meshes were used to compute the input impedance of the antenna, as discussed in the following section. The mesh size also directly impacts the simulation run time, which is discussed in Section A.2.3.

A.2.2 Input Impedance

A comparison of the input impedance for a balanced sinuous antenna simulated with the three different solvers is shown in Figure A.2. The meshes for the antenna are depicted in Figure A.1. Above 2 GHz, the results show an input impedance near the theoretical value of 267 Ω. The results diverge from the theoretical below 2 GHz due to the antenna's

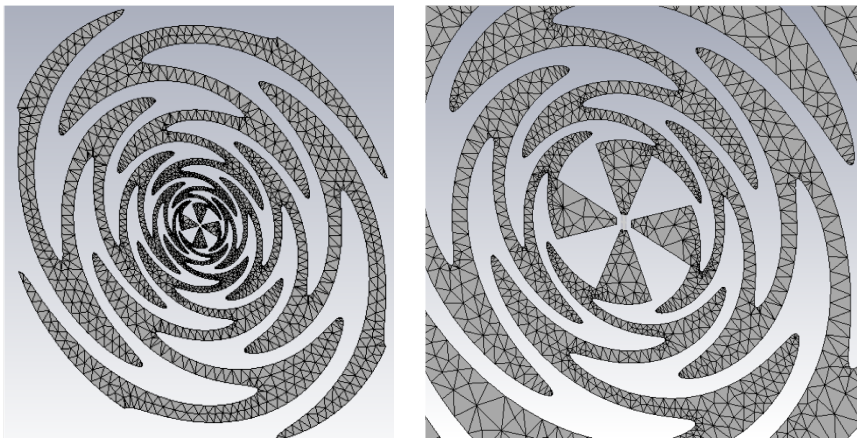

(a) FEM Mesh (b) FEM Mesh (Zoomed)

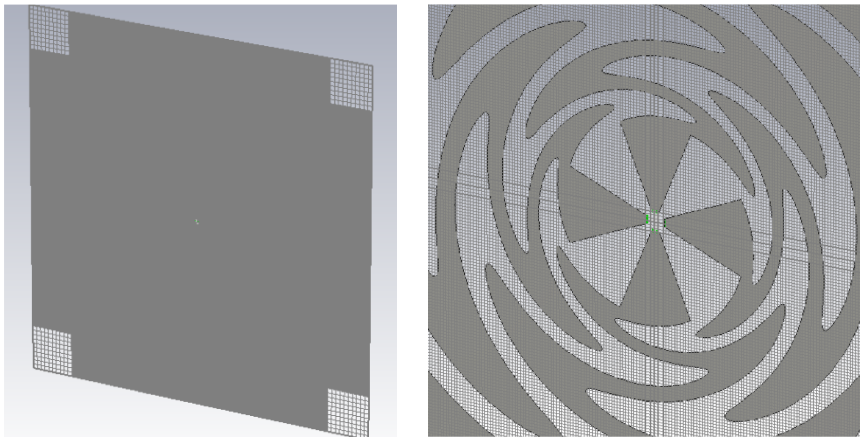

(c) FIT Mesh (d) FIT Mesh (Zoomed)

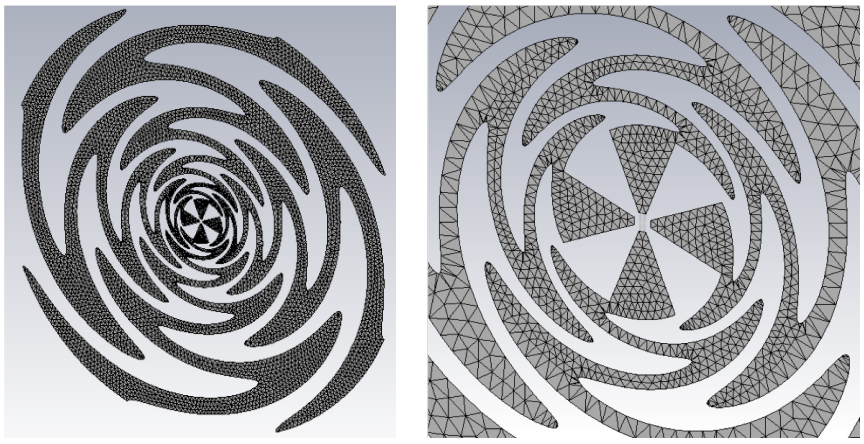

(e) IE Mesh (f) IE Mesh (Zoomed)

Figure A.1: Depictions of meshes generated by CST for the different solvers for the improved sinuous design ($P = 8$, $R_T = 5$ cm, $\alpha = 45^\circ$, and $\tau = 0.7628$). Note that the FEM and FIT meshes are three-dimensional but only two-dimensional cuts are shown.

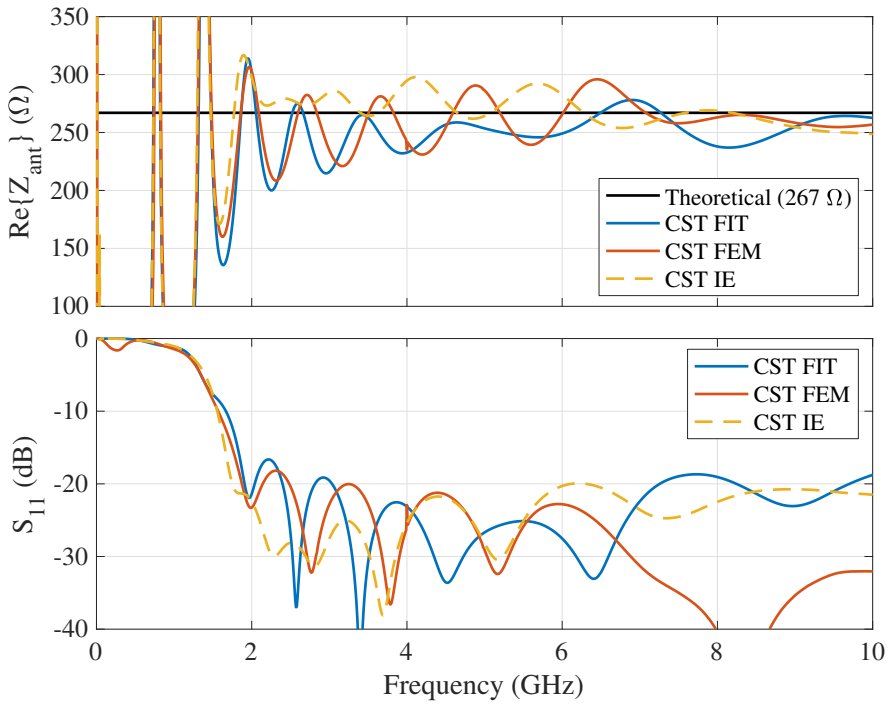

Figure A.2: Comparison of input impedance Z_{ant} and match S_{11} to 267 Ω for the improved sinuous design when simulated with different CST solvers: time domain (FIT), frequency domain (FEM), and integral equation (IE) [86].

finite size. The IE solver gives a result closest to the theoretical input impedance. This simulation comparison is further discussed in Chapter 4. The run times of each solver for this particular simulation are compared in the next section.

A.2.3 Simulation Run Time

The run times of each solver for the simulation discussed in the previous sections are summarized in Table A.1. All the simulations were run on a Linux machine with dual Intel® Xeon® CPUs (36 physical cores 2.30GHz), and dual NVIDIA® Tesla® K80 compute GPUs. The FIT solver had GPU acceleration enabled.

Additional comparison of the FEM and FIT solver simulation times are provided in Table A.2. These solvers were used more in this research since the antenna needed to be simulated on a substrate and with the absorber loaded cavity, which required either the FIT or FEM solvers. Three antennas are considered, each having the traditional outer

Table A.1: Comparison of the simulation run times for the improved sinuous antenna considered using the three different solvers.

Solver	Time (Hours)	Mesh Size	Frequency Samples
FEM	1.04	87,360 tetrahedrons	201
FIT	0.71	10,682,880 cells	N/A
IE	2.63	10,500 edges	201

Table A.2: Comparison of the simulation run times for the improved sinuous antenna considered using the three different solvers.

	FIT		FEM		
Antenna	Time (Hrs)	Mesh Cells	Time (Hrs)	Tetrahedrons	Samples
1	0.17	6,967,728	31	212,476	1000
2	0.28	14,138,460	37	261,851	1000
3	14.45	171,284,520	191	775,808	1000

truncation. Antenna #1 parameters are $P = 8$, $R_1 = 5$ cm, $\alpha = 50^\circ$, and $\tau = 0.75$. Antenna #2 parameters are $P = 12$, $R_1 = 5$ cm, $\alpha = 45^\circ$, and $\tau = 0.773$. And finally, antenna #3 has parameters $P = 16$, $R_1 = 5$ cm, $\alpha = 90^\circ$, and $\tau = 0.866$. Antennas 1 and 2 were simulated with the FIT method using a Tesla® C2075 GPU.

As can be seen, the FIT solver with GPU acceleration was significantly faster. The smaller run times allowed for the successful completion of some simulations that would have otherwise been prohibitively slow, e.g., the antenna with substrate and absorber loaded cavity.

A.2.4 Absorbing Boundaries

Another advantage of the FIT solver over the FEM was the performance of the open boundary conditions at low frequencies. The FIT solver implements a perfectly matched lay (PML) boundary while the FEM solver implements both a PML and a surface impedance boundary condition (SIBC) [118]. The performance of each combination of solver and boundary is shown in the realized gain plots of the improved sinuous antenna described above. As can be seen, the FIT solver produces higher gain at the lower frequencies. The

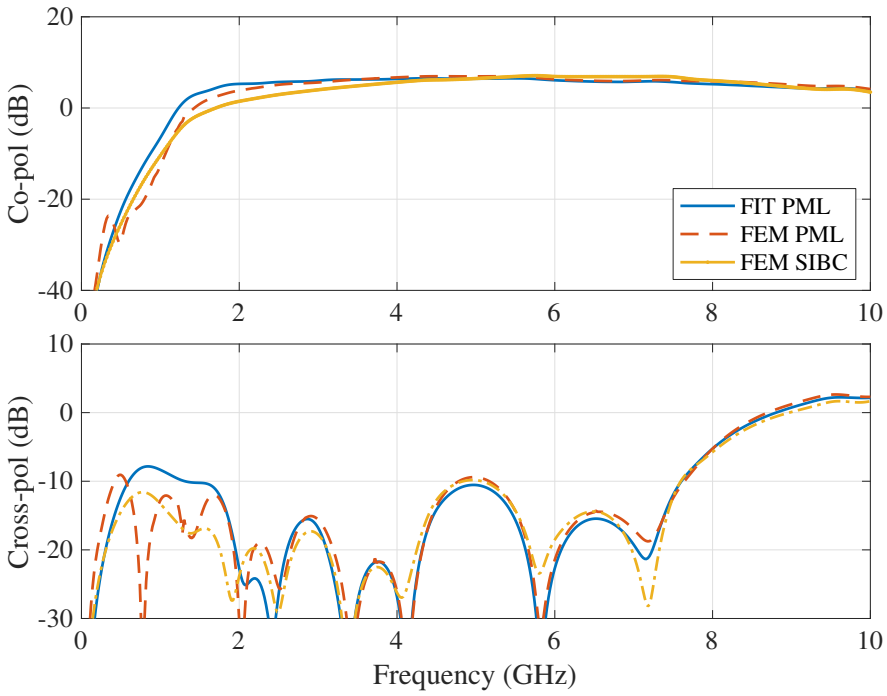

Figure A.3: Comparison of realized gain for the improved sinuous design when simulated with different CST solvers and open boundary conditions. The time-domain solver (FIT) with a PML boundary, frequency-domain (FEM) with both PML and SIBC boundaries.

FEM solver with the SIBC has the smallest gain. The PML with the FEM solver has a higher gain, but some additional instabilities may be observed below 1 GHz. Results from the FIT simulation are trusted since measurements validated the solver in Chapters 2 and 3.

A.3 Code

```
function [ x, y ] = sinuousArm( p, alpha, tau, delta, r1 )
%SINUOUSARM Draws a sinuous arm based on the specified parameters.
%   The return values are a set of x,y coordinates for drawing the arm.

% Validation of inputs omitted.

% Handle the vector inputs: if they are scalars create vectors for the
% correct indexing in the loop. If they are already vectors make sure they
% are the correct size.
if isscalar(alpha)
    alpha = ones(p, 1)*alpha;
elseif length(alpha) ~= p
```

```
    error('Alpha must be either a scalar or vector of length p.');
end
if isscalar(tau)
    tau = ones(p, 1)*tau;
elseif length(tau) ~= p
    error('Tau must be either a scalar or vector of length p.');
end

% Define a function for converting polar coordinates to Cartesian.
pol2cart = @(r,p) deal(r.*cos(p), r.*sin(p));

pts = 31; % Points per cell... this may need to be an optional input.

rEnd = r1;
rStart = r1*tau(end);
x = zeros(pts + (p - 1)*(pts - 1), 2); % allocate storage
y = zeros(pts + (p - 1)*(pts - 1), 2);
for n = p:-1:1 % Build the curve
  % Get the alpha and tau values for the cell
  alpha_p = alpha(n);
  tau_p = tau(n);

  % Calculate the sinuous curve in polar coordinates
  r = linspace(rStart, rEnd, pts);
  phi = ((-1)^n)*alpha_p*sin(pi*log(r/rEnd)/log(tau_p));

  if n == 1
    % Calculate the upper curve
    [xt, yt] = pol2cart(r, phi + delta);
    x(1:pts,1) = xt;
    y(1:pts,1) = yt;

    % Calculate the lower curve
    [xt, yt] = pol2cart(r, phi - delta);
    x(1:pts,2) = xt;
    y(1:pts,2) = yt;
  else
    % For all but the first arm, do not keep the first point to avoid
    % overlapping nodes.
    idx = (pts + (pts - 1)*(n - 2) + 1):(pts + (pts - 1)*(n - 1));

```

```
54      % Calculate the upper curve
55      [xt, yt] = pol2cart(r(2:end), phi(2:end) + delta);
56      x(idx,1) = xt;
57      y(idx,1) = yt;
58
59      % Calculate the lower curve
60      [xt, yt] = pol2cart(r(2:end), phi(2:end) - delta);
61      x(idx,2) = xt;
62      y(idx,2) = yt;
63    end
64
65    % Reset the radius limits for the next cell
66    rEnd = rStart;
67    rStart = rStart*tau_p;
68  end
69
70  % Circular curve to close the ends of the arm
71  xr = r1*cos(linspace(delta, -delta, 11));
72  yr = r1*sin(linspace(delta, -delta, 11));
73
74  % Add the feed taper (bow-tie)
75  xf = [feedGap/2 x(1,1)];
76  yf = [0.0       y(1,1)];
77
78  % Create column vector outputs
79  x = [x(:,1); xr(2:end-1).'; flipud(x(:,2)); xf(:)];
80  y = [y(:,1); yr(2:end-1).'; flipud(y(:,2)); yf(:)];
81  end
```

Listing A.1: MATLAB function to generate the outline of a sinuous arm as a list of points.

```
% Sinuous antenna design parameters
n = 8;
p = 13;
alpha = 45;
tau = 0.773;
delta = 90/n;
rt = 0.1;
r1 = rt/sqrt(tau);

%% Open the template CST project
studio = actxserver('CSTStudio.Application.2018');
mws = studio.NewMWS;

%% Draw the antenna arm curve (units of mm)
[x, y] = sinuousArm(p, alpha, tau, delta, r1);

% Draw a polygon curve in the open project.
curveName = 'curve1';
curve = mws.invoke('curve');
curve.invoke('NewCurve', curveName);

% Create the new polygon
polygonName = 'polygon1';
polygon = mws.invoke('polygon');
polygon.invoke('Reset');
polygon.invoke('Name', polygonName);
polygon.invoke('Curve', curveName);
for ii = 1:length(x) % Add the points to the polygon
  if ii == 1
    polygon.invoke('Point', x(ii)*1e3, y(ii)*1e3);
  else
    polygon.invoke('LineTo', x(ii)*1e3, y(ii)*1e3);
  end
end
polygon.invoke('Create');

%% Cover the curve to make a surface
cover = mws.invoke('CoverCurve');
cover.invoke('Reset');
cover.invoke('Name', 'armSurf');
cover.invoke('Curve', [curveName ':' polygonName]);
```

```
cover.invoke('Component', 'antenna');
cover.invoke('Material', 'PEC');
cover.invoke('Create');

%% Rotate the first arm to make four arms
tx = mws.invoke('Transform');
tx.invoke('Reset');
tx.invoke('Name', 'antenna:armSurf');
tx.invoke('Repetitions', n - 1);
tx.invoke('Component', 'antenna');
tx.invoke('Material', 'PEC');
tx.invoke('Origin', 'Free');
tx.invoke('Center', 0, 0, 0);
tx.invoke('Angle', 0, 0, 360/n);
tx.invoke('MultipleObjects', true);
tx.invoke('Transform', 'Shape', 'Rotate');

%% Export as a 3D drawing file
sat = mws.invoke('SAT');
sat.invoke('Reset');
sat.invoke('FileName', [pwd '\new_antenna_1.sat']);
sat.invoke('WriteAll');
```

Listing A.2: MATLAB script to automate drawing a sinuous antenna in CST and exporting as a .sat file.

APPENDIX B

GAUSSIAN PULSE EXCITATIONS

Gaussian pulses are often used as source waveforms in wideband applications. Such applications include Ground-Penetrating Radar (GPR) [119] and time-domain electromagnetic simulations like the Finite-Difference Time-Domain (FDTD) method [117]. Details of the pulses used in this research are described below.

B.1 Gaussian Pulse

A Gaussian function (or pulse) may be defined as

$$a \ \exp\left[\frac{-(x-b)^2}{2c^2}\right], \tag{B.1}$$

where a is the amplitude scaling factor ($a =$ peak amplitude), b determines the location of the curve on the x-axis, and c controls the width of the curve. Note that in this definition, all variables are real-valued. Many will recognize this as the bell curve in statistics. The equation for the bell curve is [120]

$$\frac{1}{\sigma\sqrt{2\pi}} \exp\left[\frac{-(x-\mu)^2}{2\sigma^2}\right], \tag{B.2}$$

which is the same as Equation B.1 but with differences in the scaling factor and variable notation. The scaling factor

$$a = \frac{1}{\sigma\sqrt{2\pi}} \tag{B.3}$$

is necessary to keep the integral (area under the curve) equal to unity. In statistics, μ is the average, i.e., defines the value around which the curve is centered, and σ is the standard deviation, i.e., controls the curve width or spread.

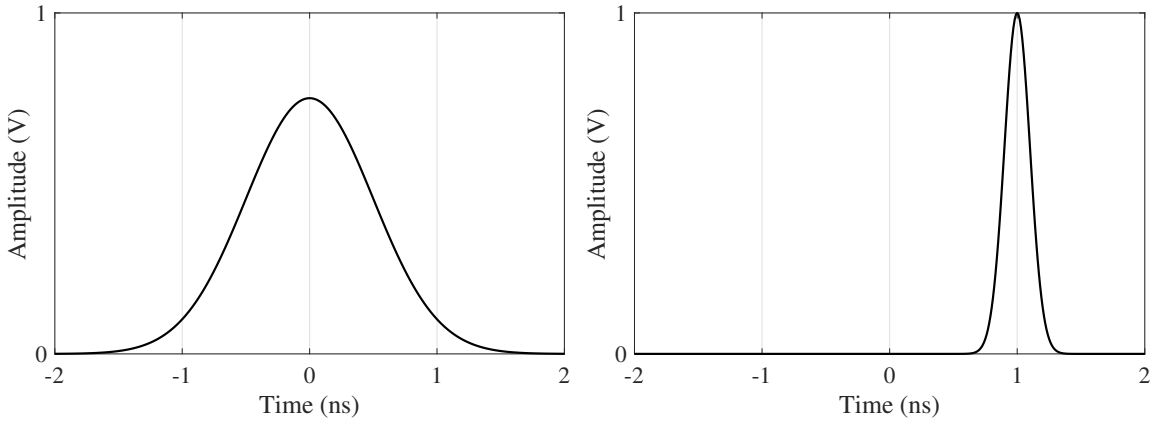

Figure B.1: Gaussian pulse with different parameters: $v_{max} = 0.75$ V, $\mu = 0$ ns, and $\sigma = 1$ ns (left); and $v_{max} = 1$ V, $\mu = 1$ ns, and $\sigma = 0.5$ ns (right).

When Gaussian pulses are used as waveforms in engineering, they often represent a voltage in the time domain. Therefore we will change x to t and a to v_{max} which, when combined with statistical notation, gives

$$v_{pulse,G}(t) = v_{max} \exp\left[\frac{-(t-\mu)^2}{2\sigma^2}\right] \tag{B.4}$$

as the equation for a Gaussian voltage pulse. Figure B.1 displays two examples of a Gaussian pulse.

As illustrated in Figure B.1, μ can be used to shift the pulse in time. One particular use of this parameter is to move the pulse entirely into positive time. To do this, specify a minimum allowable voltage v_0 at $t = 0$ and then solve for μ which gives

$$\mu = \sigma\sqrt{-2\ln\left(\frac{v_0}{v_{max}}\right)}, \tag{B.5}$$

where $\ln$ represents the natural logarithm. The pulse can then be shifted entirely into positive time using μ obtained from Equation B.5.

One of the unique things about the Gaussian pulse is that its Fourier transform is also a Gaussian function. The frequency-domain representation of a time-domain Gaussian Pulse

is given in [117] as

$$\exp\left(\frac{-t^2}{2\sigma^2}\right) \overset{FT}{\Rightarrow} \sqrt{2\pi}\sigma \exp\left[\frac{-(\omega\sigma)^2}{2}\right]. \tag{B.6}$$

Notice that the width of the pulse in the frequency domain (pulse bandwidth) is now controlled by $1/\sigma$. We can then derive the half-power bandwidth (HPBW) or 3 dB bandwidth by solving

$$\frac{1}{2} = \exp\left[\frac{-(\omega\sigma)^2}{2}\right] \tag{B.7}$$

for ω which gives

$$\omega_{\pm 3\text{dB}} = \pm\frac{\sqrt{2\ln 2}}{\sigma}. \tag{B.8}$$

Given that the full 3 dB bandwidth ω_{BW} is equal to $\omega_{+3\text{dB}} - \omega_{-3\text{dB}}$, we can define σ for our pulse as

$$\sigma = \frac{2\sqrt{2\ln 2}}{\omega_{BW}} \approx \frac{2.3548}{2\pi f_{BW}}. \tag{B.9}$$

A similar derivation is shown in [120].

The frequency-domain analysis of the Gaussian pulse presented above reveals a limitation in the use of a Gaussian pulse as a voltage source. Specifically, the Gaussian pulse contains a significant DC ($f = 0$ Hz) component. For many applications, such as numerical simulations [117], a DC component is undesirable. Further, in Radar applications, one would not be able to correctly transmit the pulse since an antenna cannot radiate DC. Therefore, in practice, modified versions of the Gaussian pulse that do not have DC components are used. The most popular are discussed in the following sections.

B.2 Differentiated Gaussian Pulse

A straightforward way to remove the DC component of the Gaussian pulse is to take the derivative with respect to time [117]. Such waveforms are referred to in the literature as differentiated Gaussian pulses or Neumann pulses [117]. We begin by solving the time

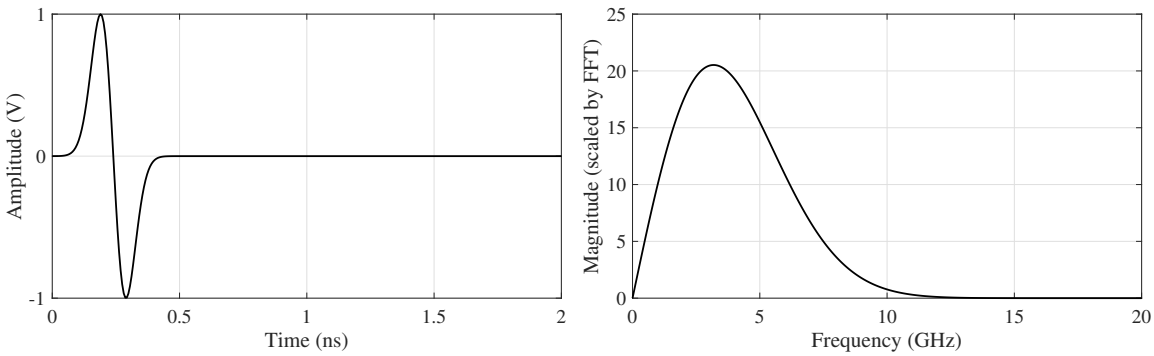

Figure B.2: Example Differentiated Gaussian pulse with 1 V peak voltage and maximum spectral energy at 3.2 GHz. The pulse is shown in both the time domain (left) and frequency domain (right).

derivative

$$v_{max}\ \frac{\partial}{\partial t} \exp\left[\frac{-(t-\mu)^2}{2\sigma^2}\right], \tag{B.10}$$

which results in

$$-\ v_{max}\ \frac{(t-\mu)}{\sigma^2} \exp\left[\frac{-(t-\mu)^2}{2\sigma^2}\right]. \tag{B.11}$$

However, this result is now scaled in amplitude such that the peak voltage is no longer v_{max}. In the literature [119], the following modified form is often used

$$v_{pulse,DG}(t) = -v_{max}\ \frac{t-\mu}{\sigma} \exp\left[\frac{1}{2} - \frac{(t-\mu)^2}{2\sigma^2}\right], \tag{B.12}$$

where v_{max} represents the peak voltage, μ an arbitrary time shift and σ, defined as $2.3548/(2\pi f_{BW})$, controls the width of the pulse. Other variations of this pulse may also occur, e.g., the negative sign is often dropped. The example pulse shown in Figure B.2 has v_{peak} and f_{BW} set to 1 V and 7.5 GHz respectively. These values result in a pulse with peak spectral energy at 3.2 GHz.

Additionally, the pulse has been shifted into positive time by selecting $\mu = 0.24$ ns. In order to select the appropriate time shift, Equation B.12 must be solved for μ at $t = 0$—similar to what was done to derive Equation B.5—however, the solution is complicated, so Equation B.5 was solved with $v_0 = 0.00001$ V as an approximation. Although there is

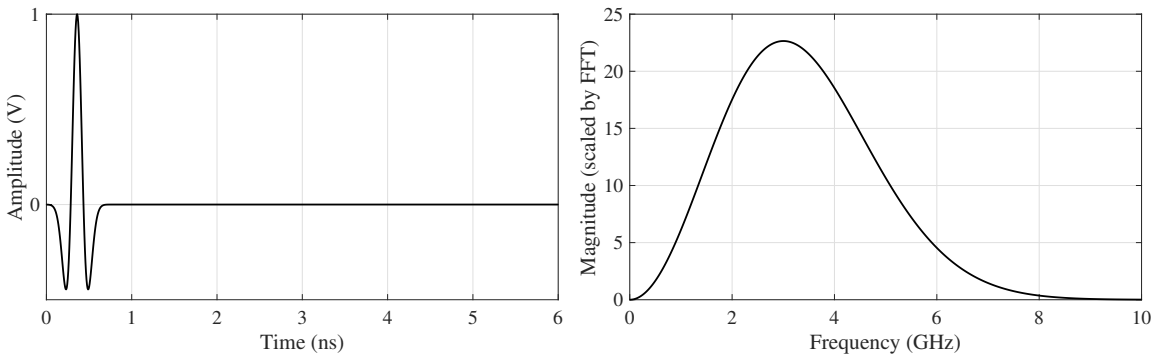

Figure B.3: Example double-differentiated Gaussian pulse. The time-domain representation of the signal (left) shows a peak amplitude of 1 V at 0.36 ns, while the frequency-domain (right) shows maximum spectral energy at 3 GHz.

no longer a DC component, the spectrum contains non-trivial energy at frequencies near to 0 Hz.

B.3 Double-Differentiated Gaussian Pulse

In order to shift spectral energy further away from 0 Hz while still maintaining a relatively low-frequency pulse, a double-differentiated Gaussian can be used. Such a pulse may be desirable for GPR applications since lower operating frequencies are often utilized for good ground penetration; however, due to their finite size, the antenna(s) have some "turn-on" frequency above 0 Hz.

The double-differentiated Gaussian pulse may be defined as

$$v_{pulse,DDG}(t) = -v_{max}\left[\frac{(t-\mu)^2}{\sigma^2} - 1\right]\exp\left[\frac{(t-\mu)^2}{2\sigma^2}\right], \tag{B.13}$$

where, again, μ represents an arbitrary time shift, and the width of the pulse is controlled by σ. The double-differentiated Gaussian presented here is derived by multiplying the Gaussian function [120] with the second-order Hermite polynomial [121, 122]. The coefficients are changed to produce a positive peak voltage at v_{max}. An example pulse is shown in Figure B.3 where $v_{max} = 1$ V, $\mu = 0.36$ ns, and $f_{BW} = 5$ GHz.

Although the double-differentiated Gaussian can reduce spectral energy at frequencies

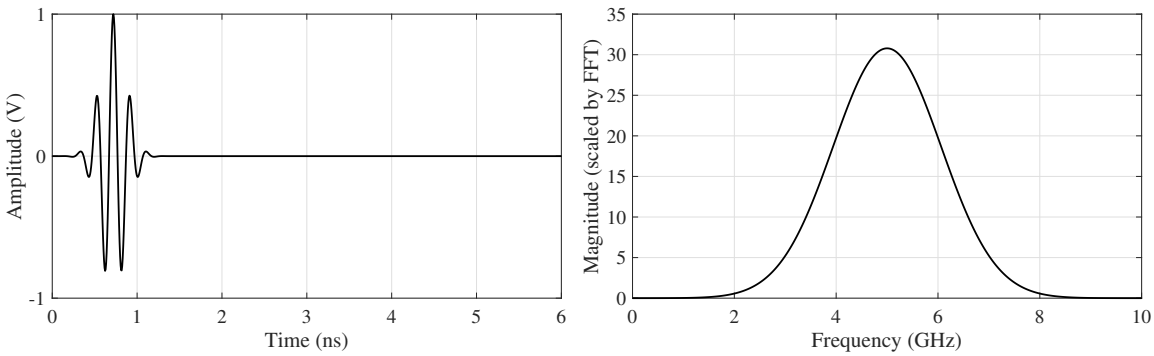

Figure B.4: Example sinusoidally-modulated Gaussian pulse. The time-domain representation of the signal (left) shows a peak amplitude of 1 V at 0.72 ns, while the frequency-domain (right) shows maximum spectral energy at 5 GHz.

near DC, it is often desired to utilize the Gaussian pulse at even higher frequency bands, which may be accomplished via modulating the pulse.

B.4 Sinusoidally-Modulated Gaussian Pulse

Multiplication of a Gaussian pulse by a sinusoid at frequency f_c shifts the pulse's spectrum from zero Hz to f_c. Another way to think of this is to recall that multiplication in the time domain is equivalent to convolution in the frequency domain. The expression for sinusoidal modulation is

$$v_{pulse,SMG}(t) = v_{max} \exp\left[\frac{-(t-\mu)^2}{2\sigma^2}\right] \sin(2\pi f_c t), \tag{B.14}$$

where σ has been determined by Equation B.9 for some bandwidth centered at f_c. We can also modulate by a cosine

$$v_{pulse,SMG}(t) = v_{max} \exp\left[\frac{-(t-\mu)^2}{2\sigma^2}\right] \cos(2\pi f_c t) \tag{B.15}$$

which is demonstrated in Figure B.4. The example pulse in Figure B.4 has $v_{max} = 1$ V, $\mu = 0.72$ ns, $f_{BW} = 2.5$ GHz, and $f_c = 5$ GHz.

A potential pitfall to avoid when using sinusoidally-modulated Gaussian pulses is an unintended DC component. A DC component can occur if the modulation frequency is

not high enough to completely shift the pulse's spectrum away from zero. In this situation, a narrower pulse may be considered or possibly a differentiated/double-differentiated Gaussian pulse.

B.5 Code

A MATLAB [101] function for generating the Gaussian pulses described in this Appendix is provided in Listing B.1. The function computes f_{BW} by $f_c * P_{BW}/100$ where P_{BW} indicates percent bandwidth. Such notation is more relevant to the sinusoidally-modulated Gaussian function; however, for the other Gaussian pulse types, specify f_{BW} in terms of f_c and P_{BW}.

```
function [ pulse, mu, sigma ] = gaussianPulse( t, fc, pBW, vmax, ptype )
%GAUSSIANPULSE Generates Gaussian pulses in the time domain.
%
%   INPUTS:
%   time - Time vector in seconds
%   fc - Pulse center frequency (Hz)
%   pBW - Percent (of fc) bandwidth (%)
%   vmax - The maximum voltage of the pulse (defaults to 1 V)
%   ptype - Pulse type:
%       normal (Gaussian) [default]
%       diff (Differentiated Gaussian)
%       doublediff (Double-Differentiated Gaussian)
%       sinmod (Sinusoidally-Modulated Gaussian)

% Validation of inputs omitted.

% Maximum voltage allowed at t = 0
v0 = vmax*0.00001;

% Compute sigma (set pulse width)
sigma = 1/(2*pi*(fc*bw/100)/2.354820045030949);

% Compute mu (time offset)
% Note that this is only approximate for the Differentiated and
```

```
% Double-Differentiated pulses.
mu = sigma*sqrt(-2*log(v0/vmax));

if strcmp(ptype, 'normal')
    pulse = vmax*exp(-(t - mu).^2/(2*sigma^2));
elseif strcmp(ptype, 'diff')
    pulse = -vmax/sigma*(t - mu).*exp(0.5 - (t - mu).^2/(2*sigma^2));
elseif strcmp(ptype, 'sinmod')
    pulse = vmax*exp(-(t - mu).^2/(2*sigma^2)).*cos(2*pi*fc*(t - mu));
elseif strcmp(ptype, 'doublediff')
    % Based on second-order Hermite function
    pulse = -vmax*(((t - mu)/sigma).^2 - 1).*exp(-(t - mu).^2/(2*sigma^2));
else
    error('Unsupported pulse type')
end

if nargout == 0 % If no output arguments, plot the pulse
    figure()
    plot(t*1e9, pulse)
    xlabel('Time (ns)')
    ylabel('Amplitude (Volts)')
    grid on
end

end % gaussianPulse
```

Listing B.1: Gaussian Pulse MATLAB Function

B.6 Summary

In this appendix, a mathematical description of Gaussian pulses was presented in the context of voltage waveforms for applications in electrical engineering, e.g., GPR voltage sources. Three variants of the Gaussian pulse, the differentiated Gaussian pulse, double-differentiated Gaussian pulse, and the sinusoidally-modulated Gaussian pulse, were also described. These modified forms of the Gaussian pulse serve to remove the DC component present in the unmodified version. Graphs, as well as example MATLAB code, were also provided.

REFERENCES

[1] "Ieee standard for radar definitions," *IEEE Std 686-2017 (Revision of IEEE Std 686-2008)*, pp. 1–54, Sep. 2017.

[2] R. B. Colton, "Radar in the United States Army History and Early Development at the Signal Corps Laboratories, Fort Monmouth, N.J.," *Proceedings of the IRE*, vol. 33, no. 11, pp. 740–753, Nov. 1945.

[3] D. Giuli, "Polarization diversity in radars," *Proceedings of the IEEE*, vol. 74, no. 2, pp. 245–269, Feb. 1986.

[4] C. F. Barnes, *Synthetic Aperture Radar, Wave Theory Foundations*. Powder Springs, Georgia: C. F. Barnes, 2014, ISBN: 9780692313732.

[5] V. Kabourek, P. Černý, and M. Mazánek, "Landmine detection using ground penetrating radar and polarimetric synthetic aperture radar," in *Proceedings of the 5th European Conference on Antennas and Propagation (EUCAP)*, Apr. 2011, pp. 34–38.

[6] Y. Yu, C. Chen, X. Feng, and C. Liu, "Application of entropy classification method to the detection of subsurface linnear targets in polarimetric gpr data," in *Geoscience and Remote Sensing Symposium (IGARSS), 2016 IEEE International*, IEEE, 2016, pp. 7438–7441.

[7] J. W. Sustman and W. R. Scott, "A resistive-vee dipole based polarimetric antenna," in *2013 IEEE Antennas and Propagation Society International Symposium (APSURSI)*, Jul. 2013, pp. 888–889.

[8] J. W. Sustman and W. R. Scott, "Polarimetric antenna for ground penetrating radar based on the resistive-vee dipole," in *Detection and Sensing of Mines, Explosive Objects, and Obscured Targets XVIII*, International Society for Optics and Photonics, vol. 8709, 2013, p. 870 912. [Online]. Available: `https://doi.org/10.1117/12.2018099`.

[9] X. Feng, M. Sato, and C. Liu, "Subsurface Imaging Using a Handheld GPR MD System," *IEEE Geoscience and Remote Sensing Letters*, vol. 9, no. 4, pp. 659–662, Jul. 2012.

[10] I. T. McMichael, W. R. Scott, E. C. Nallon, V. P. Schnee, and M. S. Mirotznik, "EBG antenna for GPR co-located with a metal detector for landmine detection,"

in *2013 IEEE International Geoscience and Remote Sensing Symposium - IGARSS*, Jul. 2013, pp. 3915–3918.

[11] L3 Security & Detection Systems, *AN/PSS-14 handheld standoff mine detection system*, `www.sds.l3t.com/military-first-responders/ANPSS-14.htm` (Accessed March 25, 2019).

[12] R. H. DuHamel, "Dual polarized sinuous antennas," US4658262A, Apr. 14, 1987.

[13] D. A. Hofer, O. B. Kesler, and L. L. Loyet, "A compact multi-polarised broadband antenna," in *International Symposium on Antennas and Propagation Society, Merging Technologies for the 90's*, May 1990, 522–525 vol.1.

[14] T. W. Hertel and G. S. Smith, "On the dispersive properties of the conical spiral antenna and its use for pulsed radiation," *IEEE Transactions on Antennas and Propagation*, vol. 51, no. 7, pp. 1426–1433, Jul. 2003.

[15] S. Zheng, S. Gao, Y. Yin, Q. Luo, X. Yang, W. Hu, X. Ren, and F. Qin, "A broadband dual circularly polarized conical four-arm sinuous antenna," *IEEE Transactions on Antennas and Propagation*, vol. 66, no. 1, pp. 71–80, Jan. 2018.

[16] J. J. H. Wang, G. D. Hopkins, and V. K. Tripp, "A new class of wideband low-profile, conformal antennas-its impact to wireless telecommunications," in *1992 IEEE International Conference on Selected Topics in Wireless Communications*, Jun. 1992, pp. 115–117.

[17] C. Waldschmidt and W. Wiesbeck, "Compact wide-band multimode antennas for mimo and diversity," *IEEE Transactions on Antennas and Propagation*, vol. 52, no. 8, pp. 1963–1969, Aug. 2004.

[18] H. S. Zhang, K. Xiao, L. Qiu, and S. L. Chai, "Four-arm sinuous antenna for direction finding system," in *2014 IEEE International Wireless Symposium (IWS 2014)*, Mar. 2014, pp. 1–4.

[19] A. Bellion, C. L. Meins, A. Julien-Vergonjanne, and T. Monediere, "A new compact dually polarized direction finding antenna on the uhf band," in *2008 IEEE Antennas and Propagation Society International Symposium*, Jul. 2008, pp. 1–4.

[20] C. Xu, F. lina, W. Xianfeng, and H. Chunjiu, "Design of an ultra-wideband sinuous antenna applied for respiratory monitor," in *2016 Asia-Pacific International Symposium on Electromagnetic Compatibility (APEMC)*, vol. 01, May 2016, pp. 256–258.

[21] R. S. Gawande and R. F. Bradley, "G/t sensitivity comparison of different topologies using ultra wide band, active, conical sinuous antenna," in *2009 IEEE Antennas and Propagation Society International Symposium*, Jun. 2009, pp. 1–4.

[22] R. Gawande and R. Bradley, "Towards an ultra wideband low noise active sinuous feed for next generation radio telescopes," *IEEE Transactions on Antennas and Propagation*, vol. 59, no. 6, pp. 1945–1953, Jun. 2011.

[23] M. V. Ivashina, R. Bradley, R. Gawande, M. Pantaleev, B. Klein, J. Yang, and C. Bencivenni, "System noise performance of ultra-wideband feeds for future radio telescopes: Conical-sinuous antenna and eleven antenna," in *2014 XXXIth URSI General Assembly and Scientific Symposium (URSI GASS)*, Aug. 2014, pp. 1–4.

[24] D. I. L. de Villiers, "Initial study of a pyramidal sinuous antenna as a feed for the ska reflector system in band-1," in *2017 IEEE International Symposium on Antennas and Propagation USNC/URSI National Radio Science Meeting*, Jul. 2017, pp. 555–556.

[25] R. O'Brient, J. Edwards, K. Arnold, G. Engargiola, W. Holzapfel, A. T. Lee, M. Myers, E. Quealy, G. Rebeiz, P. Richards, *et al.*, "Sinuous antennas for cosmic microwave background polarimetry," in *Millimeter and Submillimeter Detectors and Instrumentation for Astronomy IV*, International Society for Optics and Photonics, vol. 7020, 2008, 70201H.

[26] L. Liu, H. Xu, R. R. Percy, D. L. Herald, A. W. Lichtenberger, J. L. Hesler, and R. M. Weikle, "Development of integrated terahertz broadband detectors utilizing superconducting hot-electron bolometers," *IEEE Transactions on Applied Superconductivity*, vol. 19, no. 3, pp. 282–286, Mar. 2009.

[27] L. Liu, J. L. Hesler, H. Xu, A. W. Lichtenberger, and R. M. Weikle, "A broadband quasi-optical terahertz detector utilizing a zero bias schottky diode," *IEEE Microwave and Wireless Components Letters*, vol. 20, no. 9, pp. 504–506, Sep. 2010.

[28] O. Y. Volkov, Y. Y. Divin, V. N. Gubankov, I. I. Gundareva, and V. V. Pavlovskiy, "Spectral analysis of subterahertz resonant system by josephson admittance spectroscopy," in *35th International Conference on Infrared, Millimeter, and Terahertz Waves*, Sep. 2010, pp. 1–2.

[29] R. O'Brient, P. Ade, K. Arnold, J. Edwards, G. Engargiola, W. Holzapfel, A. T. Lee, M. Myers, G. Rebeiz, P. Richards, and A. Suzuki, "A log-periodic channelizer for multichroic antenna-coupled tes-bolometers," *IEEE Transactions on Applied Superconductivity*, vol. 21, no. 3, pp. 180–183, Jun. 2011.

[30] Z. Jiang, S. M. Rahman, P. Fay, S. T. Ruggiero, and L. Liu, "Lens-coupled dual polarization sinuous antenna for quasi-optical terahertz balanced mixers," in *2012 Asia Pacific Microwave Conference Proceedings*, Dec. 2012, pp. 52–54.

[31] Y. Chen and P. Li, "Design and simulation of a novel sinuous antenna for gps," in *Proceedings of 2014 3rd Asia-Pacific Conference on Antennas and Propagation*, Jul. 2014, pp. 11–13.

[32] A. H. Stults, "Impulse loading of sinuous antennas by ferroelectric generators," in *2008 IEEE International Power Modulators and High-Voltage Conference*, May 2008, pp. 156–158.

[33] P. Baldonero, A. Manna, F. Trotta, A. Pantano, and M. Bartocci, "UWB double polarised phased array," in *2009 3rd European Conference on Antennas and Propagation*, Mar. 2009, pp. 556–560.

[34] A. Manna, P. Baldonero, and F. Trotta, "Novel UWB low-profile sinuous slot antenna," in *Proceedings of the 5th European Conference on Antennas and Propagation (EUCAP)*, Apr. 2011, pp. 783–786.

[35] D. J. Blejer, S. M. Scarborough, C. E. Frost, H. R. Catalan, K. H. McCoin, J. Roman, and D. M. Mukai, "Ultra-wideband polarimetric imaging of corner reflectors in foliage," in *IEEE Antennas and Propagation Society International Symposium 1992 Digest*, Jun. 1992, 587–590 vol.1.

[36] G. P. Pochanin, N. M. Kaluzhny, S. A. Masalov, and I. Y. Pochanina, "Ultrawideband linearly polarized antennas of vivaldi type for ground penetrating radar," in *2015 International Conference on Antenna Theory and Techniques (ICATT)*, Apr. 2015, pp. 1–3.

[37] Y. Kang, K. Kim, and W. R. Scott, "Modification of sinuous antenna arms for UWB radar applications," *IEEE Transactions on Antennas and Propagation*, vol. 63, no. 11, pp. 5229–5234, Nov. 2015.

[38] P. R. Lacko, W. W. Clark, K. Sherbondy, J. M. Ralston, and E. Dieguez, "Studies of ground penetrating radar antennas," in *Proceedings of the 2nd International Workshop onAdvanced Ground Penetrating Radar, 2003.*, May 2003, pp. 24–29.

[39] J. M. Edwards, R. O'Brient, A. T. Lee, and G. M. Rebeiz, "Dual-polarized sinuous antennas on extended hemispherical silicon lenses," *IEEE Transactions on Antennas and Propagation*, vol. 60, no. 9, pp. 4082–4091, Sep. 2012.

[40] T. Chen and G. H. Huff, "Re-visitation on the input impedance of two-arm frequency-independent antennas in free space," in *2013 IEEE Antennas and Propagation Society International Symposium (APSURSI)*, Jul. 2013, pp. 2137–2138.

[41] T. Samson and T. Cencich, "Low profile, minimally absorptive cavity backed non-complimentary sinuous antenna," in *2016 IEEE International Symposium on Antennas and Propagation (APSURSI)*, Jun. 2016, pp. 1833–1834.

[42] N. Mutonkole and D. I. L. de Villiers, "A 3:1 bandwidth planar, lossless cavity backed sinuous antenna for reflector feed applications," in *2013 Africon*, Sep. 2013, pp. 1–5.

[43] M. C. Buck, J. Burford, and D. S. Filipovic, "Multiband two arm slot sinuous antenna," in *IEEE Antennas and Propagation Society Symposium, 2004.*, vol. 1, Jun. 2004, 165–168 Vol.1.

[44] M. C. Buck and D. S. Filipovic, "Two-arm sinuous antennas," *IEEE Transactions on Antennas and Propagation*, vol. 56, no. 5, pp. 1229–1235, May 2008.

[45] Z. Chen and Q. Cao, "Study of a two-arm sinuous antenna and the relevant wideband balun," in *2008 International Conference on Microwave and Millimeter Wave Technology*, vol. 4, Apr. 2008, pp. 1837–1840.

[46] D. Li and J. Mao, "Investigation on dual-armed sinuous antenna," in *2012 International Conference on Microwave and Millimeter Wave Technology (ICMMT)*, vol. 2, May 2012, pp. 1–4.

[47] R. Sammeta and D. Filipovic, "Quasi-frequency independent high power sinuous antenna," in *Proceedings of the 2012 IEEE International Symposium on Antennas and Propagation*, Jul. 2012, pp. 1–2.

[48] R. Sammeta and D. S. Filipovic, "Improved efficiency lens-loaded cavity-backed transmit sinuous antenna," *IEEE Transactions on Antennas and Propagation*, vol. 62, no. 12, pp. 6000–6009, Dec. 2014.

[49] R. DuHamel and D. Isbell, "Broadband logarithmically periodic antenna structures," in *1958 IRE International Convention Record*, vol. 5, Mar. 1957, pp. 119–128.

[50] W. N. Kefauver, "Multi-Polarized Spiral Antennas for RF Sensing," PhD thesis, University of Colorado, Boulder, CO, Jan. 2011.

[51] Y. Kang and K. Kim, "Polarization improvement through sinuous antenna arm modification," in *2016 International Symposium on Antennas and Propagation (ISAP)*, Oct. 2016, pp. 386–387.

[52] S. Palreddy, A. I. Zaghloul, and R. Cheung, "An optimized lossy back cavity loaded four arm sinuous antenna," in *2010 IEEE Antennas and Propagation Society International Symposium*, Jul. 2010, pp. 1–4.

[53] Y. Kang and K. Kim, "Investigation of the effects of sharp-ends removal in the sinuous antenna arms on the radiation patterns," in *2015 IEEE International Symposium on Antennas and Propagation USNC/URSI National Radio Science Meeting*, Jul. 2015, pp. 1989–1990.

[54] M. J. DeVincentis, S. Ulker, and R. M. Weikle, "A balanced hemt doubler for quasi-optical applications," *IEEE Microwave and Guided Wave Letters*, vol. 9, no. 6, pp. 239–241, Jun. 1999.

[55] X. Zhang, G. Fu, and Z. Zhang, "A planer sinuous antenna and the relevant balun," in *2013 International Workshop on Microwave and Millimeter Wave Circuits and System Technology*, Oct. 2013, pp. 109–112.

[56] J. Edwards and G. Rebeiz, "Dual-polarized sinuous antennas on silicon dielectric lenses," in *2010 IEEE Antennas and Propagation Society International Symposium*, Jul. 2010, pp. 1–4.

[57] R. Balakrishnan, K. Mouthaan, I. Hinostroza, and R. Guinvarc'h, "Dual-circular polarized planar array of connected sinuous antennas," in *2014 IEEE Antennas and Propagation Society International Symposium (APSURSI)*, Jul. 2014, pp. 941–942.

[58] Y. Kang and K. Kim, "Experimental validation of removal of sharp ends in sinuous antenna arms," in *2013 Asia-Pacific Microwave Conference Proceedings (APMC)*, Nov. 2013, pp. 212–214.

[59] E. Agastra, L. Lucci, G. Pelosi, and S. Selleri, "High gain compact strip and slot UWB sinuous antennas," *International Journal of Antennas and Propagation*, vol. 2012, 2012.

[60] N. Lorho, G. Lirzin, A. Bikiny, S. Lestieux, A. Chousseaud, and T. Razban, "Miniaturization of an UWB dual-polarized antenna," in *2015 IEEE International Conference on Ubiquitous Wireless Broadband (ICUWB)*, Oct. 2015, pp. 1–5.

[61] S. Lizhong, "Performance simulation of a kind of conformal sinuous antenna with four arms," in *2010 IEEE International Conference on Wireless Communications, Networking and Information Security*, Jun. 2010, pp. 169–172.

[62] H. R. Fang, R. Balakrishnan, R. Guinvarc'h, and K. Mouthaan, "Quad-polarized wideband phased array with reduced sidelobes by interstitial-packing," in *2015 9th European Conference on Antennas and Propagation (EuCAP)*, May 2015, pp. 1–5.

[63] S. Lizhong, C. Guojin, and H. Huanfeng, "Simulation and analysis of a hemispherical conformal sinuous antenna with four arms," in *2010 IEEE International Conference on Ultra-Wideband*, vol. 1, Sep. 2010, pp. 1–4.

[64] K. S. Saini and R. F. Bradley, "The sinuous antenna-a dual polarized element for wideband phased array feed application," *NRAO Electronics Division Internal Memo no. 301*, p. 5, 1996.

[65] M. Vahdani and X. Begaud, "Wideband integrated feeding system for a dual polarisation sinuous antenna," *IET Microwaves, Antennas Propagation*, vol. 4, no. 11, pp. 1704–1713, Nov. 2010.

[66] R. H. DuHamel and J. P. Scherer, "Frequency-independent antennas," in *Antenna Engineering Handbook*, R. C. Johnson and H. Jasik, Eds., 3rd ed., New York: McGraw-Hill, 1993, ch. 14, ISBN: 007032381X.

[67] B. T. Walkenhorst and D. Tammen, "Correcting polarization distortion in a compact range feed," in *AMTA 2016 Proceedings*, Oct. 2016, pp. 1–6.

[68] D. A. Crocker and W. R. Scott, "Exploiting polarization wobble in sinuous antennas for the detection of linear scatterers in ground penetrating radar applications," in *2018 IEEE International Symposium on Antennas and Propagation USNC/URSI National Radio Science Meeting*, Jul. 2018, pp. 837–838.

[69] I. M. Alotaibi, J. Hong, and S. K. Almorqi, "Cavity-backed dual linear polarization sinuous antenna with integrated microstrip balun feed," in *2015 IEEE 15th Mediterranean Microwave Symposium (MMS)*, Nov. 2015, pp. 1–4.

[70] Y. Yan and Q. Cao, "Microwave absorbing properties of sinuous antenna filled with absorbing material," in *2010 IEEE International Conference on Ultra-Wideband*, vol. 1, Sep. 2010, pp. 1–4.

[71] J. H. Cloete and T. Sickel, "The planar dual-polarized cavity backed sinuous antenna - a design summary," in *2012 IEEE-APS Topical Conference on Antennas and Propagation in Wireless Communications (APWC)*, Sep. 2012, pp. 1169–1172.

[72] A. I. Zaghloul, S. Palreddy, and S. J. Weiss, "A concept for a broadband electromagnetic band gap (ebg) structure," in *Proceedings of the 5th European Conference on Antennas and Propagation (EUCAP)*, Apr. 2011, pp. 383–387.

[73] T. R. Holzheimer and J. C. Holloway, "Investigation of sinuous performance over tightly spaced ground planes," in *Proceedings of IEEE Antennas and Propagation Society International Symposium and URSI National Radio Science Meeting*, vol. 2, Jun. 1994, 1310–1313 vol.2.

[74] Buck and Filipovic, "Split-beam mode four-arm slot sinuous antenna," *IEEE Antennas and Wireless Propagation Letters*, vol. 3, pp. 83–86, 2004.

[75] M. A. Elmansouri, J. Ha, and D. Filipovic, "Multioctave antenna array for simultaneous transmit and receive applications," in *2018 International Applied Computational Electromagnetics Society Symposium (ACES)*, Mar. 2018, pp. 1–2.

[76] N. Steenkamp, D. I. L. de Villiers, and N. Mutonkole, "Wideband pyramidal sinuous antenna for reflector antenna applications," in *2017 11th European Conference on Antennas and Propagation (EUCAP)*, Mar. 2017, pp. 2291–2295.

[77] S. Zheng, Z. Wang, X. Ren, and S. Gao, "A conical four-arm sinuous antenna," in *2015 IEEE International Symposium on Antennas and Propagation USNC/URSI National Radio Science Meeting*, Jul. 2015, pp. 1986–1987.

[78] R. Sammeta and D. S. Filipovic, "A low-profile sinuous antenna," in *2014 IEEE Antennas and Propagation Society International Symposium (APSURSI)*, Jul. 2014, pp. 1333–1334.

[79] K. M. P. Aghdam, R. Faraji-Dana, and J. Rashed-Mohassel, "Optimization of microstrip tapered balun for sinuous antenna feeding circuits," in *2004 10th International Symposium on Antenna Technology and Applied Electromagnetics and URSI Conference*, Jul. 2004, pp. 1–4.

[80] M. Vahdani and X. Begaud, "A directive ultra wideband sinuous slot antenna," in *2006 First European Conference on Antennas and Propagation*, Nov. 2006, pp. 1–6.

[81] V. K. Tripp and G. D. Hopkins, "A new tapered double balun for spiral-mode 2," in *2007 IEEE Antennas and Propagation Society International Symposium*, Jun. 2007, pp. 1981–1984.

[82] I. M. Alotaibi and J. Hong, "Sinuoua antenna with dual linear polarization and a notch characteristic," in *2016 16th Mediterranean Microwave Symposium (MMS)*, Nov. 2016, pp. 1–4.

[83] P. Salem, C. Wu, and M. C. E. Yagoub, "Non-uniform tapered ultra wideband directional coupler design and modern ultra wideband balun integration," in *2006 Asia-Pacific Microwave Conference*, Dec. 2006, pp. 803–806.

[84] H. Emami, N. Sarkhosh, E. R. L. Lara, and A. Mitchell, "Reconfigurable photonic feed for sinuous antenna," *Journal of Lightwave Technology*, vol. 30, no. 16, pp. 2725–2732, Aug. 2012.

[85] X. Begaud, P. Poey, J. P. Daniel, and G. Dubost, "Design of wideband dual polarized slot antenna," in *AP2000 Millennium Conf. Antennas and Propagation*, Apr. 2000.

[86] Dassault Systèmes, *CST STUDIO SUITE 2018*, www.3ds.com/products-services/simulia/products/cst-studio-suite (Accessed July 25, 2019).

[87] C. A. Balanis, *Antenna Theory, Analysis and Design*, 3rd ed. Hoboken, New Jersey: John Wiley & Sons, 2005, ISBN: 047166782X.

[88] Dylan A. Crocker and W. R. Scott, "Compensation of dispersion in sinuous antennas for polarimetric ground penetrating radar applications," *Remote Sensing*, vol. 11, no. 15, 2019. [Online]. Available: https://www.mdpi.com/2072-4292/11/15/1829.

[89] LPKF Laser & Electronics AG, *LPKF Laser & Electronics*, www.lpkf.com/en/ (Accessed January 29, 2019).

[90] Rogers Corporation, *RT/duroid 5880 Laminates*, www.rogerscorp.com/acs/products/32/rt-duroid-5880-laminates.aspx (Accessed January 29, 2019).

[91] MVG, *StarLab*, www.mvg-world.com/en/products/field_product_family/antenna-measurement-2/starlab (Accessed January 29, 2019).

[92] M. McFadden, "Analysis of the equiangular spiral antenn," PhD thesis, School of Electrical and Computer Engineering, Georgia Institute of Technology, Nov. 2009. [Online]. Available: http://hdl.handle.net/1853/31726.

[93] C. Knop, "On transient radiation from a log-periodic dipole array," *IEEE Transactions on Antennas and Propagation*, vol. 18, no. 6, pp. 807–808, Nov. 1970.

[94] J. McLean, H. Foltz, and R. Sutton, "The quantitative assessment of the UWB performance of log-periodic dipole antennas with fixed equalization," in *2004 International Workshop on Ultra Wideband Systems Joint with Conference on Ultra Wideband Systems and Technologies. Joint UWBST IWUWBS 2004 (IEEE Cat. No.04EX812)*, May 2004, pp. 317–321.

[95] A. D. J. F. Olvera, U. Nandi, J. Norman, A. C. Gossard, H. Roskos, and S. Preu, "Dispersive properties of self-complementary log-periodic antennas in pulsed THz systems," in *2017 42nd International Conference on Infrared, Millimeter, and Terahertz Waves (IRMMW-THz)*, Aug. 2017, pp. 1–2.

[96] Marshall R. Bradley, Thomas R. Witten, Michael Duncan, and Robert McCummins, "Mine detection with a forward-looking ground-penetrating synthetic aperture radar," in *Detection and Remediation Technologies for Mines and Minelike*

Targets VIII, International Society for Optics and Photonics, vol. 5089, 2003. [Online]. Available: https://doi.org/10.1117/12.487054.

[97] William W. Clark, Peter R. Lacko, James M. Ralston, and Elvis Dieguez, "Wideband 3d imaging radar using archimedean spiral antennas," in *Detection and Remediation Technologies for Mines and Minelike Targets VIII*, International Society for Optics and Photonics, vol. 5089, Sep. 2003. [Online]. Available: https://doi.org/10.1117/12.485714.

[98] J. R. R. Gary D. Sower Roger Kilgore, "Gstamids ground-penetrating radar: Data processing algorithms," in *Detection and Remediation Technologies for Mines and Minelike Targets VI*, International Society for Optics and Photonics, vol. 4394, 2001. [Online]. Available: https://doi.org/10.1117/12.445532.

[99] T. Jin and Z. Zhou, "Refraction and Dispersion Effects Compensation for UWB SAR Subsurface Object Imaging," *IEEE Transactions on Geoscience and Remote Sensing*, vol. 45, no. 12, pp. 4059–4066, Jan. 2007.

[100] D. Crocker and W. Scott, "On the Design of Sinuous Antennas for UWB Radar Applications," *IEEE Antennas and Wireless Propagation Letters*, vol. 18, no. 7, pp. 1347–1351, Jul. 2019.

[101] The MathWorks, Inc., *MATLAB R2018 Optimization Toolbox*, www.mathworks.com/products/optimization.html (Accessed July 25, 2019).

[102] M. A. Richards, J. A. Sheer, and W. A. Holm, Eds., *Principles of Modern Radar, Basic Principles*, ser. 3. Edison, NJ: SciTech, Jul. 2010, vol. 1, pp. 797–800.

[103] G. Deschamps, "Impedance properties of complementary multiterminal planar structures," *IRE Transactions on Antennas and Propagation*, vol. 7, no. 5, pp. 371–378, Dec. 1959.

[104] R. Sivan-Sussman, "Various modes of the equiangular spiral antenna," *IEEE Transactions on Antennas and Propagation*, vol. 11, no. 5, pp. 533–539, Sep. 1963.

[105] C. A. Balanis, *Advanced Engineering Electromagnetics*, 2nd ed. Hoboken, New Jersey: John Wiley & Sons, 2012, ISBN: 9780470589489.

[106] Rogers Corporation, *RT/duroid 6002 Laminates*, www.rogerscorp.com/acs/products/34/RT-duroid-6002-Laminates.aspx (Accessed September 7, 2019).

[107] Laird Technologies, *ECCOSORB LS*, www.eccosorb.com/products-eccosorb-ls.htm (Accessed September 9, 2019).

[108] ——, *ECCOSORB AN*, www.eccosorb.com/products-eccosorb-an.htm (Accessed September 9, 2019).

[109] D. M. Pozar, *Microwave Engineering*, 4th ed. Hoboken, New Jersey: John Wiley & Sons, 2012, ISBN: 9780470631553.

[110] M. Elmansouri, D. Filipovic, and P. Hoover, "Performance of multi-arm sinuous antenna in analog and digital angle of arrival estimation," in *2019 IEEE International Symposium on Antennas and Propagation USNC/URSI National Radio Science Meeting*, Jul. 2019.

[111] S. J. Orfanidis, *Electromagnetic waves and antennas*. New Brunswick, New Jersey: Rutgers University, 2016. [Online]. Available: https://www.ece.rutgers.edu/~orfanidi/ewa/.

[112] D. J. Daniels, Ed., *Ground Penetrating Radar*, 2nd ed., ser. Electromagnetics and Radar Series. Institution of Engineering and Technology, 2004, ISBN: 9780863413605.

[113] J. Kleinberg and É. Tardos, *Algorithm Design*. Pearson/Addison-Wesley, 2006, ISBN: 9780321295354.

[114] J. W. Sustman, "Analysis of resistive-vee dipole antennas for producing polarization diversity," PhD thesis, School of Electrical and Computer Engineering, Georgia Institute of Technology, Jun. 2014. [Online]. Available: http://hdl.handle.net/1853/52283.

[115] T. Counts, A. C. Gurbuz, W. R. Scott, J. H. McClellan, and K. Kim, "Multistatic ground-penetrating radar experiments," *IEEE Transactions on Geoscience and Remote Sensing*, vol. 45, no. 8, pp. 2544–2553, Aug. 2007.

[116] C. Warren, S. Sesnic, A. Ventura, L. Pajewski, D. Poljak, and A. Giannopoulos, "Comparison of time-domain finite-difference, finite-integration, and integral-equation methods for dipole radiation in half-space environments," *Progress In Electromagnetics Research*, vol. 57, pp. 175–183, 2017.

[117] J. Jin, *Theory and Computation of Electromagnetic Fields*. IEEE, 2010, ISBN: 9780470874257. [Online]. Available: https://ieeexplore.ieee.org/servlet/opac?bknumber=5628376.

[118] S. Yuferev and N. Ida, "Selection of the surface impedance boundary conditions for a given problem," *IEEE Transactions on Magnetics*, vol. 35, no. 3, pp. 1486–1489, May 1999.

[119] D. Uduwawala, "Gaussian vs differentiated gaussian as the input pulse for ground penetrating radar applications," in *2007 International Conference on Industrial and Information Systems*, Aug. 2007, pp. 199–202.

[120] E. W. Weisstein, *Gaussian function. From MathWorld—A Wolfram Web Resource*, `http://mathworld.wolfram.com/GaussianFunction.html`, Accessed on 1 September 2019.

[121] ——, *Hermite polynomial. From MathWorld—A Wolfram Web Resource*, `http://mathworld.wolfram.com/HermitePolynomial.html`, Accessed on 25 July 2019.

[122] S. Lee, "Approximation of gaussian by scaling functions and biorthogonal scaling polynomials.," *Bulletin of the Malaysian Mathematical Sciences Society*, vol. 32, no. 3, 2009.

VITA

Dylan Andrew Crocker was born in Rolla, Missouri, in May of 1988. He grew up on a small farm in southern Missouri and was homeschooled until graduating high school in 2006. Dylan received the B.S. (*summa cum laude*) and M.S. degrees in electrical engineering from the Missouri University of Science and Technology, Rolla, Missouri, in 2011 and 2014, respectively. His M.S. research was conducted with the Applied Microwave Nondestructive Testing Laboratory (*amntl*). He received the Ph.D. in electrical engineering from the Georgia Institute of Technology, Atlanta, Georgia, in 2019.

Dylan joined Sandia National Laboratories in 2012, where he is presently a Senior Member of the Technical Staff. From 2015 he has been a member of the Department of ISR EM & Sensor Technologies, where he has focused on antenna design and radar-cross-section analysis. His current research interests include radar system design, antenna design, and the application of machine learning to electromagnetic problems.

Dylan and his wife Grace married in May of 2010. They live in Albuquerque, New Mexico, with their four children.